ENGINEERING NEXT-GENERATION MYCELIA-BASED MATERIALS AND COMPOSITES FOR ENVIRONMENTAL AND BIOMEDICAL APPLICATIONS.

JUWON SAMUEL AFOLAYAN

A thesis submitted in partial fulfilment of the requirements of Nottingham Trent University for the degree of Doctor of Philosophy

October 2021 – March 2025

Abstract

This thesis investigates the use of six category 1 fungal strains; *Aspergillus niger, Botrytis cinerea, Mucor rouxii, Rhizopus oryzae, Schizophyllum commune,* and *Trametes versicolor*, to develop next-generation materials for environmental and biomedical applications. These strains were gifted or sourced from the culture collection at Nottingham Trent University. The research explores functionalization with nanomaterials, structural modifications using carbohydrates, and evaluations of nutrient-sensing properties. Key findings indicate that fungi-based materials can serve as sustainable alternatives aligned with several Sustainable Development Goals (SDGs). A significant breakthrough was the natural self-deposition of surface-stabilized gold nanoparticles onto *A. niger* mycelia without harmful chemicals, with the composite able to remove mercury from wastewater below World Health Organization (WHO) standards (2 ppb) with reusability up to five times. Additionally, the functionalization of *M. rouxii and R. oryzae* mycelia with TiO_2 nanoparticles offered protection from UVA and UVB radiation, delayed thermal degradation, and increased hydrophobicity, although it adversely affected mechanical properties. This research opens new avenues for utilizing mycelium-based materials in previously untapped applications. Using various carbohydrate nutrients, I achieved superhydrophobicity in some strains including *A. niger and B. cinerea,* enhancing surface properties and improving mycelial mechanical properties. The study also developed innovative characterization methods, including spatial mapping of mycelial homogeneity and a new fungal sensing technique, both yielding useful results. The research presented herein contributes to the fields of applied mycology and materials science by presenting sustainable bio-composites with diverse applications, emphasizing the importance of fungi-based materials for environmental sustainability. I recommend that future research focus on optimizing carbohydrate concentrations, exploring new fungal strains, and assessing long-term durability for large-scale use, setting the stage for the next generation of sustainable materials.

DEDICATION

To My Dear Parents

Mr. Jame Ade Afolayan and Mrs. Theresa Idowu Afolayan,

You are the golden threads in the fabric of my life, woven with love, sacrifice, and unwavering support. Your dreams lifted me higher; your wisdom guided me through the darkest nights.

In every challenge, your strength anchored me, your faith illuminated my path. You gave everything, with hearts full of hope, to see me succeed in my educational journey.

This thesis is a testament to your boundless love, A tribute to your sacrifices and the dreams you nurtured. With deepest gratitude and eternal love, I dedicate this work to you.

Acknowledgment

I extend my deepest gratitude to my supervisor, Professor Carole C. Perry (Distinguished), whose unwavering support, counsel, and mentorship have been instrumental in my training and daily progress throughout the PhD program. From my very first day in the laboratory, she has deployed every possible means to ensure my success. Her dedication and commitment have been the cornerstone of my academic journey. I also wish to acknowledge the invaluable contributions of my co-supervisor, Dr. Samatha McLean, and my Independent Assessor Dr. Cave Gareth. Their insightful guidance and support have significantly enhanced the quality of my work.

I am grateful to Nottingham Trent University (NTU) for providing a Vice-Chancellor's studentship, and I gratefully acknowledge the support from the Air Force Office of Scientific and Research (AFOSR) FA9550-20-1-0206.

Special thanks to everyone at the Biomolecular and Material Interface Research Group, including Dr. Dave Belton, Dr. Tom Warwick, Dr. Ayesha Sadaf, Dr. Xin Zhang, and Dr. Rajeharish Rajendran, whose assistance in troubleshooting, training, and collaboration has been invaluable during my PhD program. I also appreciate the support of the excellent technicians at the Medical Technologies Innovation Facility (MTIF) at NTU, Dr. Graham Hickman and Dr. Dominic Eberl-Craske.

A heartfelt shoutout to my colleague Dooshima, a fellow compatriot with whom I shared many library sessions and experimental discussions. Your companionship has been a source of strength.

Finally, I express my sincere appreciation to the Almighty God, the source of my strength every single day. I am grateful to my external support network, including the British Mycological Society (BMS) for the awards that supported my career development, Prof. Paul Dyer of the University of Nottingham, and the community at The Redeemed Christian Church of God, Rehoboth House Nottingham.

I confirm that all experimental work presented in this thesis was carried out by me, the candidate, unless otherwise indicated. The use of 'we' in any part of the thesis reflects the input and guidance from my supervisory team.

Table of Contents

Abstract

LIST OF FIGURES

LIST OF TABLES

LIST OF APPENDICES

Appendix 3

Appendix 4

Appendix 5

LIST OF ABBREVIATIONS

Abbreviation	Definition
AFHEA	Associate Fellow of the Higher Education Academy
AFOSR	Air Force Office of Scientific and Research
ANOVA	Analysis of Variance
ARGs	Antimicrobial Resistant Genes
AuNPs	Gold Nanoparticles
BMS	British Mycological Society
CHS-AuNPs	Chitosan-Stabilized Gold Nanoparticles
DDA	Degree of Deacetylation
DLS	Dynamic Light Scattering
DMEM	Dulbecco's Modified Eagle Medium
EDX	Energy Dispersive X-ray Spectroscopy
FTIR	Fourier Transform Infrared Spectroscopy
GF	Growth Face (of mycelia)
HaCaT	Human Immortalized Keratinocyte Cells
HEK 293	Human Embryonic Kidney 293 Cells
HR-TEM	High-Resolution Transmission Electron Microscopy
ICP-MS	Inductively Coupled Plasma Mass Spectrometry
LMW	Low Molecular Weight
MAC	Maximum Allowable Concentration
MF	Media Face (of mycelia)
MM	Minimal Media
MMW	Medium Molecular Weight
MTIF	Medical Technologies Innovation Facility
MTT	3-(4,5-dimethylthiazol-2-yl)-2,5-diphenyltetrazolium bromide
NPs	Nanoparticles
PBS	Phosphate Buffered Saline
PDB	Potato Dextrose Broth
PDI	Polydispersity Index
SAED	Selected Area Electron Diffraction
SDGs	Sustainable Development Goals
SEM	Scanning Electron Microscopy
SFE	Surface Free Energy
SPR	Surface Plasmon Resonance
TEM	Transmission Electron Microscopy
TGA	Thermogravimetric Analysis
TiO_2	Titanium Dioxide
TTIP	Titanium Tetraisopropoxide
UPF	Ultraviolet Protection Factor
USEPA	United States Environmental Protection Agency
UV-Vis	Ultraviolet-Visible Spectroscopy
WHO	World Health Organization
XRD	X-ray Diffraction
ZP	Zeta Potential

CHAPTER 1

INTRODUCTION

1.1. Background

The increasing demand for cost-effective and sustainable materials has driven research into environmentally friendly alternative sources (Raghunathan, et al. 2024). With their unique overall physicochemical, mechanical, and biological properties, fungi have emerged as promising candidates for developing new materials (Sharma et al., 2024). This research explores the innovative use of fungi in developing next-generation materials for environmental and biomedical applications. By functionalizing fungi with nanoparticles, either through a nature inspired system for gold nanoparticles (AuNPs) assembly or an in-situ approach for TiO_2 nanoparticles, composite microstructures were created. These structures were then applied to applications including heavy metal (mercury, Hg^{2+}) bioremediation, UV radiation protection, non-wettable surfaces, and thermal stable scaffolds. Additionally, organic nutrients, such as carbohydrates, were used to tune the mycelia properties of various fungal strains on different substrates (solid or liquid). The impact of these carbohydrate variations on the mechanical properties (strength, stiffness, elongation potential, and thickness) and surface properties (wettability and surface free energy) of the fungal materials was thoroughly investigated, yielding interesting results. Beyond material development, this research introduces new methods for characterizing fungal materials and manipulating their growth. A system has been developed for spatially characterizing the homogeneity of single mycelia, providing insights into the uniformity of fungal growth. The effects of the drying process on material outcomes were also evaluated, highlighting the importance of drying conditions on the final properties of the materials. Notably, the natural biomimetic process (using nature's designs and processes as inspiration to solve human problems), in which gold is passively deposited on the surface of certain fungi without the use of intrusive chemicals, was successfully replicated at the laboratory scale, demonstrating the potential for environmentally friendly material synthesis. Furthermore, a novel nutrient-sensing model for glyconanoparticles is presented, offering an independent system for characterizing the biology and chemistry of surface materials on nanoparticles and how these contribute to nutrient-sensing in fungi. This comprehensive approach not only advances the field of fungal materials and applied mycology but also provides valuable methodologies for future research.

1.2 Significance of the Study

Research in this thesis contributes to the advancement of fungal biology, nanotechnology, polymer chemistry, and applied mycology. It introduces novel and insightful approaches in the engineering of fungal-based materials and composite nanostructures, following nature-inspired principles or other innovative methods sustainably. This study also demonstrates the interplay between the nature of nanomaterials, including their surface chemistry and synthesis methods, and their effectiveness in various applications. Additionally, it establishes new methods in fungal morphometrics, creating a needs-based model to guide the processing of fungal mycelia. New materials were engineered that show great promise in environmental and biomedical domains resulting from novel applications of nanoparticles, carbohydrate monomers, polymers, and fungal-based composite microstructures. These materials have the potential to address challenges related to heavy metal contamination, and the development of biodegradable materials for UV protection, water repellence, thermal stability, and general sustainable designs enshrined in the Sustainable Development Goals (SDGs). Specifically, this research aligns with SDG 3 (Good Health and Well-being) by promoting healthy lives through biodegradable biomedical materials; SDG 6 (Clean Water and Sanitation) by using fungal-based materials for heavy metal bioremediation; SDG 9 (Industry, Innovation, and Infrastructure) by fostering sustainable industrialization and innovation; SDG 12 (Responsible Consumption and Production) by supporting sustainable consumption and production patterns; SDG 13 (Climate Action) by contributing to climate change mitigation through eco-friendly materials; SDG 14 (Life Below Water) by reducing marine pollution with biodegradable materials; and SDG 15 (Life on Land) by promoting sustainable use of terrestrial ecosystems and biodiversity conservation.

1.3 The Potential of Fungi in Sustainable Material Engineering

Fungi are multicellular, macroscopic organisms that have been exploited in diverse applications over the years (Sanchez and Demain, 2017; Paul and Joshi, 2022). Their structures are made up of tiny filaments called hyphae, and a collection of these forms the mycelium (Riquelme, et al. 2018). Mycelium consists of a network of fine filaments known as hyphae. These hyphae create diverse and intricate networks with varying structures and functions. Mycelia are essential for nutrient absorption, decomposition, and forming symbiotic relationships with plants. Their design enables efficient nutrient transport and adaptation to environmental changes, making them crucial for maintaining ecosystem health and resilience (Wang et al., 2022). By exploring the literature, I established that current research has

demonstrated the tremendous potential of fungi in material science, but significant gaps remain in understanding their full capabilities, and their translation from conceptualization to actual usage. This study aims to fill these gaps by introducing novel methods and applications. Generally, fungal biology, at the intersection of chemistry, physics, nanotechnology, and engineering has proven to be a ground-breaking field over the years, with transformative potential, opportunity for developments, and innovative applications across several industries and the general society (Meyer). Generating materials from fungi (mycomaterials) is one of the innovative and modern approaches being used to explore the beneficial properties of different fungal strains (Rashdan and Ashour 2023). Notably, some fungi, such as Mucorales (e.g., *Mucor* and *Rhizopus* species), which have roles in the etiology of mucormycosis, can occasionally be pathogenic (Challa 2019), and their mycelial network can grow abundantly over a large area within a very short time (Hoffmann, et al. 2013). Fungi have long been primarily associated with public health concerns and food spoilage, yet this narrow lens overlooks their indispensable roles in ecology, nutrient cycling, symbiosis, and pathogenesis (Botha and Botes 2014). As Nicholas Money (2024) highlights in *Molds, Mushrooms, and Medicines*, fungi are essential agents of life, intertwined with biological systems from decomposition to medicine. However, with the growing human population, the need for more sustainable materials that can grow in a controlled manner, at a low cost, and within a short time frame has brought fungal-based materials into the spotlight (Alemu, Tafesse and Mondal 2022). This provides an opportunity to explore their beneficial properties in addressing some of the persistent and emerging global challenges in material production (Haneef, et al. 2017). As materials enthusiasts and scientists, I are eager to determine whether fungal-based materials truly have the qualities for their vast potential. By reviewing existing literature and recent findings, I can uncover insights that help answer this question.

Aside from the admirable physicochemical and mechanical properties of fungal microstructures which are well documented, they could easily grow on cheap substrates or agricultural waste materials such as wheat, corn, and other remnant carbohydrates (Jiang, et al. 2017, Girometta, et al. 2019). This system is efficient for waste recycling, and it aligns with the global track for green and circular economy (Alemu, Tafesse and Mondal 2022). This establishes the possibility of growing their materials across all economies, representing a huge potential for global adaptation. Similarly, existing data shows that almost 10% of the total carbon emission has its source from industrial processes (Italia, Patel and Shah 2016), and the final products that are fabricated from this in most cases are not recyclable (Alemu, Tafesse

and Mondal 2022). Aside from the fact that this already constitutes a huge environmental threat as pollutants (air, soil, water), demand is also expected to increase with increasing urbanization and human population (Alemu, Tafesse and Mondal 2022). The emission of greenhouse gases due to material exploration could exceed 18% of the global gas emission where it stood as of 2010 (Penaloza 2017). Exploring materials from fungi could be a sustainable alternative that provides excellent output in a much safer manner. Fungal biology at the intersection with other fields is an evolving interdisciplinary research area, with promising potential. Most importantly, it offers opportunities for the management of economically significant fungi strains, and for the development of novel bioactive fungal materials (Abo Elsoud and El Kady 2019). This thesis reports a holistic use of fungal materials by conducting experiments with diverse strains, combining fungi with different bioactive under various conditions, and uses different components of the mycelium (either the mycelium itself or it's bioactive components). However, a journey into the literature leading up to this thesis on how these fungal structures could be tuned or combined with different bioactive and organic molecules makes their development even more fascinating. This helps to better understand the dimensions of the current study and to appreciate the depth of materials design I can achieve with fungi.

1.3.1 Engineering Mycelia-Based Composites by Combining Living or Non-Living Fungal Microstructures with Nanoparticles.

From their structural and biological characterization, I know that fungal cells which form the bulk mycelia are matrices containing varying biopolymers. These biopolymers (such as chitin, glucans, glycoproteins, etc.) have functional groups and chemical constituents to which different external functional materials can be combined with or coupled to to form composite materials. An example of these external bioactives that can be combined with fungal materials are nanoparticles (Mukherjee, et al. 2001). From this process, structural modifications could be made to fungal materials, especially at their outer surface. Nanoparticles are tiny materials with dimensions between 1-100 nm (Murthy 2007). They can be inorganic (such as gold or titanium oxide nanoparticles), organic (such as chitosan nanoparticles), or hybrid, where the inorganic component has an organic surface (such as chitosan-coated gold nanoparticles). For hybrid nanoparticles with surface coatings, there is also the possibility of surface modification to achieve desired surface properties, which can include antibiotics, nutrients, ions, etc. (Kim, et al. 2023a). When nanoparticles (NPs) are coupled with fungi, they form highly functional mycelia-based nanocomposites (Mukherjee, et al. 2001). The mycelial network serves as the matrix for functionalization, and the interaction between the nanoparticles and the charged

group on the mycelia also offers the possibility of chemical adhesion (Mukherjee, et al. 2001). This interaction can occur in living mycelia, where the fungi direct the assembly of the nanomaterials onto their microstructure, forming living templated materials. This phenomenon was first reported for *A.niger* by (Li, Z., et al. 2003)in 2003. A new global discussion emerged in 2019 when the redox interaction between fungi and nanomaterials was reported (Bohu, et al. 2019). Since then, more research on different templated materials has been published ((Joy, et al. 2023, Birdsong, et al. 2025). Alternatively, composite materials from fungal mycelia and nanoparticles can be engineered in situ on non-living mycelia. Here, the mycelia are dried and used directly or processed to form a stable, non-living matrix suitable for nanoparticle incorporation (Sivaprasad, et al. 2021). Either way, the goal is to ensure the successful assembly of nanomaterials on the fungal mycelia at a concentration sufficient for use in the desired area of application. When these nanocomposites are formed, their overall properties differ from those of the original mycelia due to functionalization. As a result, the composite becomes a unique entity that integrates the characteristics of both the mycelia and the incorporated nanoparticles (Sharma, R., Jafari and Sharma, 2020). Such nanocomposites exhibit distinct properties compared to the native matrix, including variations in mechanical strength, thermal stability, optical responsiveness, and other functional attributes (Sharma, R., Jafari and Sharma, 2020). The potential application of the materials formed also depends on the properties of the overall composite (Sharma, R., Jafari, and Sharma, 2020).

1.3.2 Modifications in Living Mycelium at the Fundamental Level

Across fungal strains, thousands of microscopic threadlike materials called hyphae combine to form a bulk structure known as the mycelium (Islam, et al. 2017). These hyphae can vary in their organization (degree of branching or interconnections), partition patterns (septate or non-septate), or biochemical profiles (polymer compositions) (Islam, et al. 2017). Generally, the individual hyphae are made of cellular structures, whose properties can be tuned in specific ways (Haneef, et al. 2017). Modifying each cell's characteristics (tuning) contributes to the overall structure of the mycelium, which is the bulk material formed from thousands of hyphae. For example, in how these cells can be tuned, the cell walls are made of structural carbohydrates and proteins like chitin and glucans (Gow and Lenardo, 2022, Gow 2025). In the presence of carbohydrate-rich nutrients (such as monosaccharides or disaccharides), which are monomers to these structural carbohydrates, more of these structural carbohydrates are rapidly synthesized (Hamad, et al. 2014). This impacts the overall physical and mechanical properties (filament thickness, strength, elasticity, flexibility, and load-bearing capacity), surface chemistry (surface

energies and wettability), and biochemistry (biomolecular constituents and polymer profile) of the bulk materials. These systems can be leveraged to engineer materials with desired properties in a very green manner by tuning from the fundamental level. Unlike other classes of materials like textiles or plastics, this form of materials engineering is done on the living fungus by controlling its properties right from inoculation. Interestingly, because of the sensitivity of fungi to various external changes such as temperature, pressure, nutrients, pH, and the presence of other bioactive materials, the tuning of living fungal structures can be tailored toward numerous applications by understanding how these changes impact the overall Structures (Schoder, et al. 2024, Haneef, et al. 2017). Because some of these processes are very cheap (including using waste materials) and easy to control, engineering materials from fungi offers an excellent modern approach to coupling novel materials development with profound sustainability (Girometta, et al. 2019).

1.3.3 Fungal Polymers

While I look at material engineering from the functionalization of the bulk materials to the tuning of growth at fundamental levels, there is also the importance of looking at subcellular levels where I can focus on trends in the exploration of polymers from natural and non-renewable sources, and why fungal polymers have modern relevance. Modern industrialization utilizes different kinds of polymers across fields and processes, and for every single year, it is estimated that about 180m tons of these are consumed in different industries (Castillo, Valdez and Fariña 2015). The world is blessed with a huge range of plant species and other living organisms, and these have been a major source of useful biopolymers (Biswas, et al. 2022, Shankar et al., 2024). A common example is cellulose which has been extracted from plants (e.g. bamboo) and used in the paper industries for many years (Li, X., et al. 2024). Similarly, polyisoprene also called 'natural rubber' from *Hevea brasiliensis* has been extracted and used in many synthetic products such as common car tyres (Distler 2001). However, it is believed that the primary role of plants is to recycle oxygen, so when polymers are extracted via processes that lead to deforestation or subject the plants to the possibility of disease infestation, they are exploitative and environmentally non-friendly (Amer, et al. 2024). The increasing climate effect today is also believed to be a result of some of these activities, and caution has been recommended in their utilization (Gutti, Aji, and Magaji 2012). On the other end, petrochemicals derived from petroleum refining, or their derivatives, are another alternative source to generate building blocks for synthetic polymers (Speight 2020). For example, when olefins (e.g., ethylene and propylene) which are derived from petroleum are refined, their

polymeric form (such as polyethylene) has a very vast application as a synthetic resin to produce plastics (Speight 2020). Petroleum is found naturally as crude oil in underground reservoirs, and its exploration accounts for some of the most severe disruptions to natural habitats, loss of biodiversity (Ribeiro, et al. 2013), air and water pollution (Falih, et al. 2024), Greenhouse gas emission (Ma, et al. 2023), land degradation (Buzmakov and Khotyanovskaya 2020), Public health risk and transportation accidents (Nisbet, Maibach and Leiserowitz 2011), and threat to ecosystem safety (Henry, Singh and Oyedotun 2023). In fact, there is emerging global consensus on the need for a drastic reduction in the use of non-renewable forms of material sources in the production process (Danish and Khan 2019). Some classes of animals such as Arthropods and reptiles also offer good structural polymers as part of their skeletal or integumentary system, and the use of these also dates to time immemorial (Liu, X., Zhang and Zhu 2019). For example, collagen has been extracted from marine creatures and ungulates (Chen, et al. 2023), and chitins from insects and crustaceans (Liu, X., Zhang and Zhu 2019). There is an increased call for the protection of biodiversity because, over the years, some species that once roamed the earth have gone into extinction due to human activities (Pulido-Chadid, Virtanen and Geldmann 2023). With these realities, the need for alternatives was birthed, and the exploration of microbial options became a sustainable alternative (Suryanarayanan and Azevedo 2023).

There are many useful fungal-derived polymers, including chitin, pullulan chitin, cellulose, mannans, and glucans, which are used for a variety of purposes (Manan, et al. 2021). Relevant to our choice in this thesis are chitin (made of repeating units of N-acetylglucosamine (GlcNAc) linked together by β-(1→4) glycosidic bonds), deacetylated chitin (chitosan), which is comprised of repeating units of glucosamine molecules, and glucan (a polysaccharide of glucose) (Sánchez-Machado, et al. 2019, Alemu, Tafesse and Mondal 2022). These structural polymers have excellent applications due to their biocompatibility, biodegradability, and antibacterial properties. In biomedicine, they are used in wound dressings, drug delivery systems, and tissue engineering (Patrulea, et al. 2015). The food industry benefits from chitosan's use in food preservation and as a natural additive, and it has been approved as safe for use by the United States Food and Drug Administration (USFDA) (Yan, et al. 2021). In agriculture, chitosan-based biopesticides and seed coatings enhance plant growth and disease resistance (Riseh, Vazvani and Kennedy 2023). Cosmetics utilize chitosan in skin and hair care products for its hydrating and strengthening effects (Lu, et al. 2015). Medical applications include the use of chitosan as dissolvable suture threads in surgery (Da Silva et al., 2020).

Environmental applications include water treatment for removing heavy metals and dyes, and biodegradable packaging as a sustainable alternative to plastics (Kumari and Kishor 2020). In addition, these fungal polysaccharides can also induce immune responses. For example, beta-glucan is widely used as a food additive (Edo et al., 2024). These versatile applications highlight the potential of chitin and chitosan in creating innovative and sustainable solutions across various industries. Being bioactive, chitosan has also been processed to synthesize nanomaterials for a variety of applications (Bandara, et al. 2020). In summary, fungi present excellent pathways to material generation across their structural complexities, whether in bulk materials or polymers.

1.4 Current Trends and Novelties in Materials Engineering from Fungi

Although applied mycology is an emerging field, trends in research outputs from the literature show that it offers many opportunities for material development. By understanding the progression of these trends, I can highlight the uniqueness of the works reported in this doctoral thesis and their innovative contributions to fungal materials design and applications. While the scope of research is broad, I focus on pioneering and novel studies in the environmental and biomedical niches of fungal materials engineering. In the past few years, over 100 fungal strains have been reported in various publications for use in fungal-based materials or composites (Sydor, et al. 2022). Additionally, numerous patents related to fungal materials have been documented since the first filings in the United States in 2007 (Sydor, et al. 2022, Bayer and McIntyre 2016). Recently, researchers have explored fungal-based materials and composites, including the use of nanomaterials. Below, I outline a few examples of these innovative studies.

1.4.1. Fungal-Mediated Self-Healing Concrete and Bio-Cementation (PF)

Before 2018, the process of bio-cementation was predominantly associated with bacteria and was exclusive of fungi until researchers at Binghamton University, New York, made a breakthrough. The study, led by Professor Congrui Jin, explored fungi believed to have the potential to heal concrete cracks (Menon, et al. 2019). By inoculating fungal spores embedded into the concrete, the hypha of the fungal would grow into an interconnected three-dimensional network within the concrete. This network serves as a nucleation site for the precipitation of calcium carbonate ($CaCO_3$), which helps to heal cracks in the concrete. In addition, germination produces calcium carbonate upon the appearance of cracks, effectively sealing them, this is due to longer spore viability. This method also addresses the limitations associated

with using bacterial spores (Menon, et al. 2019). Interestingly, the group found that *A. nidulans* (MAD1445) can grow on concrete plates and promoting the precipitation of calcium carbonate, marking an excellent breakthrough (Luo, et al. 2018, Menon, et al. 2019). The process of biocementation is straightforward: fungal spores and nutrient media are incorporated during the concrete mixing. The fungi grow and precipitate calcium carbonate with their filaments, leveraging the nutrients in the mixture (Van Wylick, et al. 2021). The three-dimensional interwoven network of fungal filaments serves as the nucleation site for the precipitation of calcium carbonate ($CaCO_3$). This system is especially effective for crack healing (Van Wylick, et al. 2021).This promising application also presents challenges. According to a review by Konwarh, Palanisamy and Jogi (2020), fungi used in biocementation have specific environmental requirements, such as moisture, temperature, and pH levels, which can be hindered by concrete's high alkalinity and low nutrient availability. The long-term durability of fungal-based bio-cementation is still under investigation, and some fungi can produce acids that degrade concrete, requiring careful management (Konwarh, Palanisamy and Jogi 2020).

1.4.2 Super-Amphiphilic Janus Membrane

In another pioneering study on fungal structures, the use of hydrophobins for the development of Janus membranes was reported by (Cavalcante and Szekely 2023) using *Pleurotus ostreatus*. The differential variation in the wettability profiles of different sides of *P. ostreatus* mycelium was established. The researchers discovered that surface wettability on the two sides of a mycelium grown under certain conditions differed significantly, with different records of surface contact angles. These are the side in contact with the growth media and the side with aerial growth. Owing to these surface chemistry differences; the authors proposed the utilization of the resulting mycelium as a Janus membrane filter suitable for selectivity in oil-water separation. By definition, Janus membranes are a group of emerging materials that have contradictory surface properties, allowing for selective or novel transport properties (Yang, H., et al. 2016). This debut holds excellent potential in future environmental bioremediation. Despite the promising potential of fungal-based Janus membranes for applications like oil-water separation, their efficiency still requires verification in real-world conditions. Real-world testing is essential to confirm their practical performance and address any challenges that may arise during actual use (Yang, J., et al. 2019).

1.4.3 Fungal Biobattery (Myco-energy)

As the world continues to decarbonize and shift from non-renewable energy towards net zero, fungal materials have found a novel application in energy generation (Reyes, et al. 2024). In modern society, energy availability is one of the most pressing environmental challenges affecting people and industries across all regions of the world. With resource scarcity and ongoing conflicts, affected zones can now leverage the utilization of fungi for energy generation. This is possible because, in a novel study published in 2024 by (Reyes, et al. 2024), it was reported that when cellulose (a natural polymer) is used for the 3D printing of fungal electrodes, it could repurpose the metabolic activities of fungi for use in electrochemical devices. Interestingly, the study found that a 'fungal biobattery generated between 300 and 600 mV for several days, delivering 3–20 µA for external loads between 10 and 100 kΩ'. This biobattery was also reported to power a small sensor for up to 65 h. With the limitless availability of fungal materials, the possibilities seem endless, offering the potential for waste conversion to sustainable use.

1.4.4 Mycelia-Based Packaging and Insulation Materials.

Sustainable packaging has a lot of benefits, and so do eco-friendly insulation materials (Li, K., et al. 2022). In 2012, the first fungal-processed cotton materials that were used in packaging were reported and sent for use in a factory; the outcome materials surpassed expectations even when compared to the properties of polystyrene foam, making it suitable as a biodegradable packaging material (Holt, et al. 2012). Because of low density and thermal conductivity, mycelia-based polymers have been used in thermal insulation and bio-foam (Li, K., et al. 2022). The principle is that polymers with lower thermal conductivity are better thermal insulators, and this was shown in the study by (Jones, et al. 2018), where mycelia composites were found to have excellent flame-retardant properties, making them less prone to fire. There is a plethora of opportunities offered by fungi in materials development, and this will have a huge role in next-generation sustainable materials for diverse applications (Sun 2024). More studies to unravel the physicochemical (mechanical, thermal response, etc.), biochemical (e.g., oxidative stress), and physiological changes (e.g., sporulation and production of secondary metabolites) that occur when a composite microstructure is formed from either living or dead mycelia, there will be better clarity and standardization that will be required for sustained production for translational application (Sun 2024). The niche of applied mycology at the intersection of chemistry, physics, and nanotechnology will continue to evolve with promising outcomes (Elsacker, De Laet and Peeters 2022).

Table 1. Summary of Fungal-Based Material Applications in Recent Literature (2020–2025)

Application Area	Fungal Strains Used	Material/Composite Type	Functional Benefit	Key Reference(s)
Bio-cementation / Self-healing Concrete	*A. nidulans*	Fungal spores in concrete	$CaCO_3$ precipitation, crack self-healing	Menon et al., 2019
Janus Membrane for Oil–Water Separation	*Pleurotus ostreatus*	Natural mycelium membrane	Amphiphilic surface, selective permeability	Cavalcante & Szekely, 2023
Biobatteries (Myco-energy)	*S. commune*	Cellulose-printed fungal electrodes	Powers sensors, sustainable low-voltage energy generation	Reyes et al., 2024
Biodegradable Packaging & Insulation	*Ganoderma lucidum, T. versicolor*	Mycelium biofoam and packing structures	Flame-retardant, biodegradable, thermal insulator	Jones et al., 2018; Holt et al., 2012

1.5 Current Areas in the Application of Mycelia-Based Materials in this Thesis and Literature Records

This thesis explores main areas (other than method developments): the formation of fungal composite microstructures with nanomaterials for applications such as heavy metal removal, bioremediation, biodegradable scaffolds, UV-radiation protection, non-wettable surfaces, and thermal stability; the tuning of fungal morphometrics using various sugars and sugar alcohols; the sensitivity, tuneability, and potential for self-control in Mucorales when exposed to glyconanoparticles, including those formed from polymers extracted from these fungi. Below I give an overview of the current state of knowledge and progression in these areas, establishing the depth of new contributions made by this doctoral research, with further detailed discussions in each results chapter.

1.5.1 Environmental Monitoring for Heavy Metal Detection and Removal

The safety of humans and the ecosystem is a global necessity, and monitoring the environment to detect and remove harmful contaminants is crucial for sustaining this (Zulkifli, Rahim and Lau 2018). Various classes of toxicants can be found in the environment, including persistent heavy metals (e.g., Pb, Hg, Cd, Cr), pesticides, oil residues, and antimicrobial-resistant organisms (ARGs) (Alengebawy, et al. 2021). Removing these contaminants is of public health

importance, and the methods adopted must not introduce new classes of contaminants, as has been seen in some situations (Sharma, S. and Bhattacharya 2017). Given that environmental contamination is a global problem, the toxicant removal system must be globally adaptable and readily available across all economies (Cutrupi, et al. 2024). Additionally, it must be highly effective and sensitive, suitable for use even with low concentrations of contaminants (Alves and Alves 2022). The growing human population exacerbates these issues, necessitating urgent and sustainable responses (Sharma, S. and Bhattacharya 2017). As an example, various nano or biomaterials methods (adsorption, solvent extraction, chemical precipitation, photocatalytic, flotation, inn exchange, Phyto remediation, etc.) have been tried for the removal of mercury down to 0.002 mg L^{-1} maximum acceptable standard (Sarma, Sen Gupta and Bhattacharyya 2019, Vikrant and Kim 2019, Gore, C. T., et al. 2016, Kumar, Smita and Flores 2017), and previous research has identified their challenges, especially the reduced mercury adsorption rate by the adsorbing materials (Goci, et al. 2023). The application of fungi in a process called mycoremediation has also been well researched and documented (Gadd, 2001). Chitosan-based nanocomposites have been introduced but face challenges in forming a self-sustained matrix (Goci, et al. 2023). Traditional biochar offers a low-cost solution, but depending on the starting materials, it can constitute a pollution channel to the environment (Gelardi, Li and Parikh 2019). Alginate seaweed, which can also be derived from biochar, offers efficient mercury filtration platforms with a highly sustainable natural matrix but is costly (Chaouay, et al. 2024). The new goal is to develop an effective filtration system, offers a good adsorption matrix, is highly sustainable in its production process, and is less likely to constitute environmental contaminants. This thesis focuses on mercury detection, modelling its detection and removal using fungal-mediated composite microstructures inspired by nature. This approach aims to provide an effective and globally adaptable solution to environmental contamination. By leveraging the unique properties of fungal structures, I can develop innovative methods for sensing and bioremediation, addressing the pressing need for efficient and sustainable environmental monitoring and cleanup. This research not only contributes to scientific knowledge but also offers practical solutions for mitigating the impact of toxic contaminants on our environment.

1.5.2 Multifunctional Scaffold: UV-Shielding, Thermal Protection, and Water Repellence of Fungal-Based Composite Materials

Climate change impacts have greatly increased in recent years, as evidenced by record-breaking environmental data recently published (Bais, et al. 2018). For example, January 2025

recorded the highest global temperatures for the month, with an average ERA5 surface air temperature of 13.23°C, which is 0.79°C above the January average from 1991-2020 and 1.75°C above pre-industrial levels (National Centers for Environmental Information 2025). Additionally, the period from February 2024 to January 2025 was 0.73°C above the 1991-2020 average and 1.61°C above the estimated 1850-1900 pre-industrial average (National Centers for Environmental Information, 2025). Due to the depleting ozone layer, UV radiation reaching the earth does so with increased intensity, posing significant health risks and necessitating the development of UV-radiation-protective materials (Bais, et al. 2018). UV-blocking materials vary in protection levels based on their Ultraviolet Protection Factors (UPF) (Rabiei, et al. 2022). Biopolymer-based nanocomposites have shown remarkable potential in UV-radiation protection, with UPF values greater than 30. Fungal melanin has also been deployed as an ionizing radiation shield (Dadachova et al., 2008). Other Examples include lignin (UPF 50+), chitosan (UPF 50+), cellulose (UPF 30-50), and textile fabrics (UPF 15-50) (Gore, A. H. and Prajapat 2022, Kim, et al. 2023b, Lv, et al. 2023, Saha, et al. 2024). Nanomaterials such as titanium and zinc oxide nanoparticles, combined with biopolymers, offer excellent opportunities for UV protection. UV radiation (100-400 nm) is divided into UV-A, UV-B, and UV-C, with UV-C being the most damaging but fully absorbed by the ozone layer. UV-A and UV-B contribute to health issues like cancer and DNA damage. This thesis redefines this niche by introducing mycelia as a possible sustainable alternative. Guided by the optical and biological properties of mycelia and their ability to survive in extreme conditions, I believe this can be utilized for human benefits in UV radiation protection. This approach aims to provide effective and globally adaptable solutions to environmental contamination, leveraging the unique properties of fungal structures for innovative methods in sensing and bioremediation. This research not only contributes to scientific knowledge but also offers practical solutions for mitigating the impact of toxic contaminants on our environment.

Beyond UV-radiation protection, composite structures from biomaterials are increasingly used in smart applications due to their desirable properties (Dave, et al. 2024). For instance, TiO_2 NPs provide hydrophobic surfaces, thermal stability, and antibacterial properties (Yang, M., et al. 2018). Starch-based films, chitosan-based nanocomposites, and polyhydroxyalkanoates (PHA) are examples of biodegradable materials used in smart packaging for monitoring food quality, extending shelf life, providing antimicrobial properties, and offering real-time freshness detection (Yang, M., et al. 2018). These materials either have the desired surface properties for non-wettability or are thermally suitable for their intended use. Hydrophobic

materials can be used in sustainable packaging to reduce contamination (Frota, et al. 2022). Certain nanomaterials like TiO_2 nanoparticles confer hydrophobicity by interacting with hydrophilic groups or through nano-hierarchical structures, creating air pockets that prevent water adhesion (Liu, S., Wang and Yang 2024, Zhang, et al. 2016). Additionally, they enhance thermal stability in polymers through mechanisms such as kinetic stabilization, which hinders phase transformation and particle growth by arranging particles at particle boundaries to slow diffusion rates (Andrievski 2014). Oxidation resistance is another mechanism, where nanomaterials absorb energy and shield the matrix, making them suitable for use under varying conditions (Chrissafis and Bikiaris 2011). These properties make fungal-based composite materials a promising solution for UV-shielding, thermal protection, and water repellence in various applications, as proposed and researched in this doctoral thesis. The increasing use of nanomaterials in smart and sustainable applications is opening opportunities to enhance current technologies and create entirely new ones (Dave, et al. 2024).

1.5.3 Harnessing Fungal Sensing and Nanotechnology for Environmental Monitoring and Biocontrol.

Beyond what I can do with fungi or fungi-based composites, there is also a lot that can be done to control fungal growth. This includes studying their environmental sensitivity and using chemicals introduced to their environment to direct their growth and structural properties (Mukherjee, et al. 2001). Fungi play a crucial role in environmental sensing and biocontrol due to their unique biological mechanisms and sensing abilities (Gohel, et al. 2022). Bioactive polymers derived from fungi, such as chitosan and others, have demonstrated antimicrobial properties and are widely used in nanoparticle synthesis for diverse applications. (Lopez-Moya, Suarez-Fernandez and Lopez-Llorca 2019). This study introduces a novel agar-bridge model to investigate nutrient-sensing in Mucorales species, specifically *M. rouxii* and *R. oryzae*. This model allows for advancements, characterizations, and real-time observation of fungal responses to glucose- and chitosan-capped gold nanoparticles (AuNPs).

1.6 Research Objectives

This thesis explores the multifaceted applications of nanoparticles and mycelia-composite structures in addressing pressing environmental and biomedical challenges. Specific areas covered are:

1. **Method Developments in Fungal Morphometrics**: Determining the effect of spatial variation and processing methods on material outcomes.

2. **Synthesis and Characterization of AuNPs**: Determining the physicochemical and optical properties, stability, and toxicity of gold nanoparticles (AuNPs) with different surface functionalizations on various cell lines *in vitro*.

3. **Colorimetric Sensing of Mercury Ions**: Investigating the use of gold nanoparticles capped with glucose, citrate, cefaclor, etc., in colorimetric sensing, particularly their effectiveness in detecting mercury.

4. **Engineering Novel Composite Microstructures for Wastewater Bioremediation**: Forming nanoparticle-mycorrhizal composites using *A. niger* (via a biomimetic system) and evaluating their potential as bioactive matrices for mercury filtration from wastewater.

5. **Correlation of Fungal Morphometrics to Carbohydrate Variation**: Using carbohydrate variation to tune the mechanical properties and surface chemistry of five fungal strains (*A. niger*, *B. cinerea*, *S. commune*, *T. versicolor*, and *R. oryzae*).

6. **Developing Multifunctional Titania Nanoparticle-Modified Materials**: Characterizing *M. rouxii* and *R. oryzae* mycelia, and in situ deposition of Titania nanoparticles on the mycelia. Examining the resulting composites for their potential as biodegradable scaffolds in UV-shielding, water repellence, and thermal stability.

7. **Chitosan Biopolymer from Shrimp and Fungal Origins**: Comparing their application in AuNP synthesis and their nutrient-sensing effect in fungal control. This involves the extraction and characterization of the polymer, determining the physicochemical and optical properties of the respective AuNPs, and their application for fungal growth control using a novel agar bridge model.

CHAPTER 2

Experimental Methods

This chapter contains information about the methods that were used in sample preparation, the condition and mode of characterization of samples, and all other analyses used. In addition to detailing the technical processes, this chapter directly addresses Objective 1: Method Developments in Fungal Morphometrics, by establishing the methodological framework used to assess how spatial variation and processing methods influence fungal material properties, supporting the development of morphometric techniques.

2.1. Spectroscopy Based characterization.

2.1.1 Ultra-Violet Visible Light (UV-Vis) Spectrophotometry

Ultra-violet visible light spectrophotometry (UV-Vis) is an analytical technique that can be used for the quantitative or qualitative determination of analytes within the ultraviolet and visible electromagnetic radiation regions (190 - 800 nm) (Passos and Saraiva 2019). The instrument for this method is the spectrophotometer. Depending on its type, it can be used for samples either in solid state, or the determination of analyte in solution following the Beer Lambert Principle ($A = \varepsilon \times b \times c$; A: absorbance, ε: molar absorbance coefficient, and b: is the path length). The amount of the light that is absorbed by the analyte correlates with its concentration in the solution (Tissue 2002).

2.1.1.1 Operational Principle

When an analyte is placed on the light path of an incident electromagnetic radiation (λ) within the UV-Vis region, it interacts with the light thus creating measurable attenuation because of absorption, reflection, scattering, or interference (Passos and Saraiva 2019). This phenomenon can be used in quantitative determination of analytes such as measuring the concentration of a molecule in solution, stability of a material over time (qualitative), or the presence of a certain molecule in solution (Akash, et al. 2020).

2.1.1.2 Instrument Description and Application in this Thesis.

In this study, a Cary-50 Bio UV-Vis spectrophotometer (Agilent Technologies) and a JASCO V-670 double-beam spectrophotometer were used to determine the surface plasmon resonance (SPR) properties of colloidal gold nanoparticles, as well as the UV-radiation absorption of fungal mycelia. For liquid samples, the method provided information about the unique absorbance regions of the nanoparticles, indicated by distinct SPR peaks. Au NPs exhibit SPR,

where surface electrons oscillate in response to light, enhancing absorption and scattering at specific wavelengths (Huang and Yang, 2004). A polystyrene cuvette (SARSTEDT 10×10×45 mm) was used as the sample holder along the light path, and measurements were taken at 25°C within the 300–800 nm wavelength range. For solid samples, UV measurements were conducted between 200–800 nm for pigment characterization and UV absorption analysis of fungal mycelia.

2.1.1.3 Limitations of instrument and method within the scope of this thesis

This method is suitable for the quantitative and qualitative determination of the properties of NPs in colloidal states. However, it could be insensitive to slight variations in NPs size especially when the colloidal properties are retained (Tomaszewska, et al. 2013). UV-Vis is also a bulk characterization technique and does not give information about individual NPs, creating the need for complementary characterization methods (e.g., TEM or DLS) (Mourdikoudis, Pallares and Thanh 2018). In this study, UV-Vis was used in conjunction with other methods to ensure accurate interpretation of nanoparticle behaviour and material performance.

2.1.2. Fourier Transform Infrared Spectroscopy

Fourier transform infrared (FTIR) Spectroscopy is a non-destructive technique detailing the interaction between a matter and electromagnetic radiation within $4000 - 400$ cm^{-1} wavelength region (Xiang 2018). It can be used in structural elucidation, identification of compounds (Daéid 2005), monitoring the role of biomolecules in a reaction (Padhi and Behera 2022), mapping of cellular components (Berthomieu and Hienerwadel 2009), and for the investigation of the nature and behaviour of substances under specific conditions. Information is   revealed through the characteristic IR spectra of the bonds in that sample (Tranter 2017).

2.1.2.1. Operational Principle

In principle, an IR Spectrophotometer produces a beam of IR irradiation ($4000 - 400$cm^{-1}) which is interfered with and recombined by the interferometer creating constructive and destructive interference (interferogram) (Mohamed, et al. 2017). When the interferogram reaches the sample at the sample compartment, the frequency of its energy is selectively absorbed according to the analyte's distinct properties Mohamed, et al. (2017). The signal from this versus all the frequencies is then simultaneously measured by the detector to give a unique IR vibration indicative of the analyte (Mohamed, et al. 2017). For a molecule to exhibit IR absorption, it must have a changing electric dipole moment during its vibrations. These

vibrations should have resonant frequencies within the IR region to absorb infrared radiation (Malik and Kumar 2016).

2.1.2.2. Instrument Description and Application in this Thesis.

All IR measurements for vibrational assignment in this thesis were done using a Thermo Scientific NICOLET iS50 FT-IR, with a DTGS detector and a KBr beam splitter. Spectral source is IR, optical velocity is 0.47, Aperture is 87, maximum wavelength range is 4000 cm^{-1} and minimum range is 500 cm^{-1}, with a total of 120 scans for each of the materials. The instrument is connected to Thermo Scientific OMNIC software, which is used for processing data from IR experiments before export. This technique was applied to:

1. Confirm the presence of capping agents (e.g., glucose, chitosan) on AuNPs.
2. Identify functional groups in fungal mycelia and their composites.
3. Assess chemical interactions between nanoparticles and fungal matrices.

2.1.2.3 Limitations of instrument and method within the scope of this thesis

This instrument is environmentally sensitive and multiple background scans before sample scans are required to avoid spectra variations (Faghihzadeh, et al. 2016). The method is also susceptible to temperature variation and samples must be run under similar conditions(Cadet, et al. 2006). Generally, homonuclear molecules such as O_2, Cl_2, and H_2, do not have IR spectra due to a lack of dipole (American Chemical Society, Tyner and Francis 2016). In the context of this thesis, FTIR was effective for identifying functional groups, but it does not provide spatial resolution or detailed structural information, making it necessary to complement it with techniques like XRD or SEM for full material characterization.

2.1.3. Nuclear Magnetic Resonance Spectroscopy

Nuclear magnetic resonance spectroscopy is a powerful and versatile method for compositional, interactions, and structural elucidation at the atomic level in chemical and physical science (Levy and Craik 1981, Simpson, Simpson and Soong 2012). The change of phase, solubility and diffusion patterns, and alterations in the configuration and conformation of a sample can also be monitored via NMR (Singh, M. K. and Singh 2022a).

2.1.3.1 Operational Principle

The principle guiding the NMR technique has been outlined to better under understand it operationality, and this works based on charged nuclei of an atom which have multiple spins (Singh, M. K. and Singh 2022b) (. When an external magnetic field is created around this, there

is transfer of energy usually from lower to higher levels (Hodgkinson and Emsley 2000) . According to Pykett, et al. (1982) , radio frequency makes the absorption of these energy transfer possible, and it is distinct to the type of nuclei (e.g., proton or carbon relevant for this study) and the chemical environment of the nucleus (Koshani, Jafari and van de Ven 2020). This absorption has been recorded to depend on location of the nuclei in the magnetic field (Singh, M. K. and Singh 2022c). By returning to rest, the nuclei spin generates and energy emission within the same frequency, which is then transferred, detected, and processed to produce the NMR spectrum (Johnson and Schmidt-Rohr 2014) NMR application in colloid analysis and materials chemistry has been significant over the years, for example, it has been extensively used in the determination of the interaction between molecules and nanomaterials (Pestov, et al. 2015) , as well as their bioactivity and chemical status. In this study it was important in, determining the degree of deacetylation of Chitin (Lavertu, et al. 2003).

2.1.3.2. Instrument Description and Application in this Thesis.

Nuclear magnetic resonance (NMR) spectra for samples were obtained using a Jeol ECX-400 spectrometer (1H: 400 MHz and 13C: 100.6 MHz. Chemical shifts (δ) are quoted in ppm and coupling constants (J) in Hz). Sample solutions were made in DCl and D_2O and transferred to an NMR tube (5 mm × 8 in. Sigma Aldrich® ColorSpec® NMR tubes, 0.38 mm thick). The NMR procedure was done at 70 °C and the spectra were analysed with ACDLabs Spectrus Processor 2023.2 (From Nottingham Trent University Software Hub)**.**

2.1.3.3. Limitations of the instrument and method within the scope of this thesis

This method processes samples in solution, and because of the limitation with chitin solubility, the extensive use of this method in characterizing the chemical structure of chitin was limited.

2.1.4. Inductively Coupled Plasma Mass Spectrometry (ICPMS)

Inductively Coupled Plasma Mass Spectrometry (ICPMS) is a very sensitive analytical technique that can detect, quantify, and report the elemental composition of samples at trace levels (Mazarakioti, et al. 2022). Unlike graphite furnace atomic absorption spectroscopy (GFAAS), ICPMS is quite advanced, capable of multielement analysis at a single run, equal or better detection limits (Al-Hakkani 2019) , and it is isotope specific (Vincent 2016) .

2.1.4.1 Operational Principle

The sample to be analysed is introduced into the instrument and converted into an aerosol mist (Singh, A. K. 2016a). Solutions are vaporized using a nebulizer, solids are sampled using laser ablation, and gaseous samples are used directly. This aerosol is then transferred to a high-

energy argon plasma, where atomization occurs, leading to ionization of the sample. In the plasma, which contains electrons and positively charged argon ions, the atoms lose electrons and become positively charged. The positive ions from the sample are extracted from the plasma into a mass analyser, where they are separated based on their mass-to-charge ratio. After mass separation, the ions strike a detector that identifies them across a range of masses (Singh, A. K. 2016b).

2.1.4.2 Instrument Description and Application in this Thesis.

In this study, a NexION 100 ICP Mass Spectrophotometer was used in the quantification of Au metal from AuNPs-Mycelia Composite Microstructure. The sample was run (in ppm) with the known concentration of Au from the internal standard.

2.1.4.3 Limitations of the instrument and method within the scope of this thesis

1. The detection limits in ICP-MS typically fall within the nanomolar (nmol/L) range for most elements (Wilschefski and Baxter 2019).

2. Potential for interference due to matrix effects, depending on the nature of the sample (Beauchemin 2017).

2.2.0 Dynamic Light Scattering and Zeta Potential

Dynamic Light Scattering (DLS) also known as Photon Correlation Spectroscopy (PCS) or Quasi-Elastic Light Scattering (QELS) (Malm and Corbett 2019a, Stetefeld, McKenna and Patel 2016), and zeta potentials are non-destructive light-based measurement techniques for the size (hydrodynamic) and surface charge of dispersed nano- and micro-scale particles respectively (Bhattacharjee 2016a, Malm and Corbett 2019b).

2.2.1. Operational Principle

The principle of hydrodynamic size measurement via DLS is guided by the measurement of the intensity of fluctuation of scattered light due the Brownian motion of the molecule in solution(Stetefeld, McKenna and Patel 2016). Light scattering in all directions is a result of interaction between monochromatic beam of light and the solution in a cell on the light path containing the macromolecule, and this is a function of the size and shape of the molecule (Stetefeld, McKenna and Patel 2016). DLS allows for the direct measurement of samples, and it is very sensitive to the state of agglomeration or clustering behaviour of particles in solution, a phenomenon which may be undetected in some instances under an electron microscope because of drying (Brydson, et al. 2015). However, the method measures hydrodynamic size

including the solvent layer around the particle (Eaton, et al. 2017). The Zeta or electrokinetic potential (ZP) is the shear/slip plane potential of a colloid moving under an electric field (Bhattacharjee 2016b) . ZP provides information about the electric state of charged surfaces (Pochapski, et al. 2021). Though not directly measurable, ZP can be experimentally determined from the electrophoretic mobility of the nanomaterial (Pochapski, et al. 2021), reflecting potential differences between the electric double layer (EDL) of the particle under electrophoretic mobility and the layer of the surrounding dispersant (Bhattacharjee 2016c).

2.2.2. Instrument Description and Application in this Thesis.

The overall surfaces charge and *zeta* potential of the NPs colloidal solutions were measured by Zetasizer Nano-S Zen 600 (Malvern Instruments Ltd.) with DTS1070 folded capillary cells (Malvern Instruments Ltd.). Both size and zeta potential measurements were taken at 25°C after 120 sec equilibrations with water as the dispersant (η 0.8872 cP, n 1.33 and ε_r 78.5) and gold (n 0.2 and absorbance 3.32) as the material. This instrument only measures hydrodynamic size.

2.2.3. Limitations

DLS is a bulk technique, and the instrument measures the hydrodynamic radius of multiple particles within a colloidal sample. With a few aggregates, the overall average size of the NPs can be greatly influenced, creating the need for complementary size measurement with electron microscopes (Mourdikoudis, Pallares and Thanh 2018). In this study, these limitations were mitigated by using complementary techniques such as XRD and electron microscopy to validate particle and crystallite size and morphology.

2.3. X-ray related characterization techniques.

2.3.1. X-Ray Diffraction

X-Ray diffraction (XRD) is a non-destructive analytical technique through which the detailed crystallographic structure, material components, and the physicochemical nature of materials can be determined (Titus, James Jebaseelan Samuel and Roopan 2019). The technique offers complementary information about the purity, size, morphology, and the phase of a materials, complementing other microscopic and spectroscopic techniques (Holder and Schaak 2019).

2.3.1.1. Operational Principle

The principle guiding the operation of this technique is based on the constructive interference between monochromatic incident x-Ray radiation and a crystallite sample along the light path which generates a diffracted x-ray which is processed and counted. To obtain a diffraction pattern, the diffraction intensity at different angles (2θ) region is plotted. Each material has a unique diffraction pattern due to its specific crystal structure, which is defined by the arrangement of atoms in the unit cell, the type of atoms present, and the interatomic distances. These structural features determine the angles and intensities at which X-rays are diffracted, producing a characteristic pattern (Raja, et al. 2022).

2.3.1.2 Instrument Description and Application in this Thesis.

X-ray diffraction diffractograms for the sample to determine crystalline and domain properties were determined using a Rigaku Ultima IV X-Ray Diffractometer. Samples were run (on a Rigaku silicon low background specimen holder at 40 kV and 50 mA (λ=1.540593 Å) between 5 – 80 2θ, scans were obtained in step mode; step size was 0.002º and scan speed 0.5 deg./ min.

2.3.1.3 Limitation

The instrument is highly phase-sensitive (amorphous or crystalline), and post-synthesis modification (calcination) of some samples such as TiO_2 NPs was required before their crystal structure could be determined (anatase or rutile).

2.4. Microscopy-based Characterization Techniques

2.4.1. Scanning Electron Microscopy

The scanning electron microscopy (SEM) is an advanced electron-based microscopy technique suitable for imaging the microstructural arrangements and morphological orientation of materials (Omidi, et al. 2017).

2.4.1.1 Operational Principle

In principle, when an electron beam which a low energy is scanned across the surface, there are a lot of different interactions, and the sample emits photons and electrons near its surface (Sampath Kumar 2013a). For imaging, the photon and electron signals (e.g., the secondary electrons, backscattered electrons, and cathodoluminescence) from the sample are detected by the instruments' detectors (Omidi, et al. 2017a). The secondary electrons are usually emitted from the material surface, and they are important in surface analysis (Koga, et al. 2021).

2.4.1.2 Instrument Description and Application in this Thesis.

For this study, a scanning electron microscopy (JSM-7100F LV FEG-SEM) with an EDX detector (JEOL JED-SDD 30 mm^2 window) was used in evaluating the detailed morphological structure of the fungal biomass, fungal polymers, and nanoparticle functionalized mycelia microstructures. Prior to imaging, the samples were fixed on a coverslip (AmScope 100pc pre-cleaned 18mm Diameter Round Microscope Glass Cover Slides Coverslips) already attached to am SEM stub (JEOL Ø9.5 x 9.5mm cylinder SEM sample stub – aluminium), and then carbon coated through a pulse cord (10 nm) using a Quorum Q150R ES Sputter Coater. Imaging was done at an accelerating voltage of 5-20 kV with a working distance of 10 μm at a magnification range between 40 – 50000X.

2.4.1.3 Limitations

SEM uses a focused electron beam; this can be highly destructive to samples, especially soft or dielectric materials. This leads to issues like electron charge build-up and deformation due to absorption-based heating thereby limiting their use on some biological samples and natural polymers (de Haan, et al. 2019). Similarly, SEM has a resolution limit about 1.2 nm, and HRTEM offers a better alternative to characterize extremely small nanomaterials (Barhoum and Luisa García-Betancourt 2018).

2.4.2. High-Resolution Transmission Electron Microscopy (HR-TEM)

Transmission electron microscopy (TEM) is another electron-based microscopy technique that is used for the determination of the morphological orientation, crystal structure, and composition of materials at a higher resolution than the SEM (Omidi, et al. 2017b).

2.4.2.1 Operational Principle

The principle guiding the operation of the HR-TEM is as follows. According to Omidi, et al. (2017) and Sampath Kumar (2013), The electron gun located vacuum chamber emits electrons which are directed towards the sample by electrostatic lenses. The interaction between the electrons and the sample leads to absorption (or scattering) while some are transmitted through the sample to hit the electron detectors at the bottom of the microscope thus forming the image. The output of the sample image is not only a function of the instrument, the properties of the material such as density play an important role. A dense material absorbs more electrons making the output darker (Ong, Appleford and Mani 2014).

2.4.2.3 Instrument Description and Application in this Thesis.

The NP size and morphological orientation in these were assessed through digital micrographs obtained with a JEOL JEM-2100Plus transmission electron microscopy (TEM) fitted with a LaB_6 filament operating at an accelerating voltage of 200 kV. Samples were prepared by depositing 5 µL of colloidal NP samples onto 200 mesh carbon-coated grids (Quantifoil Micro Tools GmbH), and micrographs were taken with an Orius SC200 CCD camera (Gatan Inc.).

2.4.2.3 Limitations

Conventional TEM can only be used in analysing thin-sectioned samples (especially biomaterials), owing to the design of the instrument, resulting in two-dimensional images (Malatesta 2021). Even when tomographic approaches are used, the samples are still sectioned, but 3D images are obtained (Malatesta 2021).

2.4.3. SEM/EDX – HRTEM/EDX

The X-ray detector used in this study is a JEOL JED-SDD 30 mm^2 window attached to either the Scanning or the Transmission electron microscope. For each sample, 100 scans at 5 scans per/ min were run to obtain an EDX map and for elemental detection and quantification. Electron voltage or current was adjusted to hit the Kα or Lα of the element of interest. Mapping the elemental composition of a sample is very essential for qualitative and confirmatory assessment, Energy Dispersive Xray is a technique that works in association with electron microscopy to reveal this (Scimeca, et al. 2018). EDX can be used in endogenous or exogenous mapping and detection across various analyte groups (Golding, et al. 2016). When an electron beam is radiated on a sample, it generates X-rays which are unique to the nature and characteristics of the material's elemental composition. This can be intercepted by the attached X-ray detector and converted to a voltage pulse once it enters the detector. The voltage pulse depends on the X-ray energy, and samples with low energy can be increased by increasing the current of the beam and scanning period (Raval, et al. 2019).

For each sample, 100 scans at 5 scans per/ min were run to obtain an EDX map and for elemental detection and quantification. Electron voltage or current was adjusted to hit the Kα or Lα of the element of interest. Mapping the elemental composition of a sample is very essential for qualitative and confirmatory assessment, Energy Dispersive Xray is a technique that works in association with electron microscopy to reveal this (Scimeca, et al. 2018). EDX can be used in endogenous or exogenous mapping and detection across various analyte groups

(Golding, et al. 2016). However, EDX is primarily a qualitative technique, and may not be very effective for the analyses of elements with low atomic numbers (Soldado, et al. 2022).

2.4.4. Light/Fluorescence Microscopy

These microscopes are powerful instruments that use glass lenses to magnify objects, allowing direct observation through binocular eyepieces. They can visualize objects and archive total magnification by the dual roles of objective and eyepiece magnifications, with a range from 04 to 1000 X (Holgate and Webb 2003).

2.4.4.1 Operational Principle

The light generated from a light source (within 400 -700 nm range) passes through a sample on the stage and is then submitted to the lenses of the microscope to obtain magnified images that correspond to the area of the sample being focused on (Exbrayat 2016). The quality of the image that is seen on a screen or within the objective lenses may differ, depending on if the image is created from visible light or from fluorescence generated within the sample.

2.4.4.2. Instrument Description and Application in this Thesis.

A THUNDER fluorescence Imager -Live Cell & 3D Assay- from Leica was used in this study to image the growth pattern of mycelia in the agar-bridge nutrient-sensing of *M. rouxii* and *R. oryzae* with Chitosan-AuNPs. The equipment is built on a fully motorized DMi8 microscope, in a Quantum Stage, and has a K8 camera which is highly sensitive. The fluorescence is produced from a multi-line, high-intensity fluorescence LED light source. It is designed for simultaneous imaging of multiple points within a single analysis.

2.4.4.3. Limitations

1. Simultaneous imaging of samples at different contrast areas can be difficult.

2.5. Tensiometry-Surface Wettability

This method determines the ability of a solid (mycelia) to be wet by a liquid (water or diiodomethane), and it is used as a measure of their liquid repellence as a function of interacting surface energies (Gulfam and Chen 2022).

2.5.1 Operational Principle

The static contact angle of a solid surface, determined using the sessile drop method, involves placing a droplet on a solid surface and capturing an image using an attached optical microscope. The contact angle of the droplet on the solid surface is then calculated by fitting

the Young-Laplace equation around the droplet (Quetzeri-Santiago, Castrejón-Pita and Castrejón-Pita 2020), although alternative fitting methods like circle or polynomial can also be employed (Quetzeri-Santiago, Castrejón-Pita and Castrejón-Pita 2020)**.**

2.5.2 Instrument Description and Application in this Thesis.

In this study, the contact angle was recorded by an Attention Theta Lite Tensiometer (connected to a Navitar Zoom 6000® Lens System with a magnification range of 0.09-393X), via the OneAttension software. A volume of 4 µL of double deionized water or diiodomethane was used as the fluid (polar and non-polar respectively) for the experiment at different points on the mycelia surface, and this was done three times. The experiment followed the procedure described by (Mourdikoudis, Pallares and Thanh 2018a). The Surface free energies of the surfaces were calculated using the (Fowkes 1964).

2.5.3. Limitations

1. Experimentally, mycelia do not grow to have uniformly flat or planar surfaces, therefore more samples are required to get enough flat surfaces suitable to data collection (Marie and Torbjörn 2007).
2. Contact angles from a tensiometer cannot directly give information about the surface energies without further processing.

2.6. Thermogravimetric Analysis (TGA)

Thermogravimetric Analysis is type of thermal analysis technique that can be used in the determination of material composition, quantification, and change in the physical or chemical properties along a temperature region (Parameshwaran, et al. 2018).

2.6.1 Operational Principle

The method involves the determination of change in mass of a sample under controlled isothermal condition or a linearly changing temperature in a given atmosphere (Wunderlich 2001). For materials, this method can be used to determine thermal stability of materials, fibres and polymers (Gomes, et al. 2018), as well as the biomolecule constituent of bioactive nanomaterials (Rami, et al. 2021), by giving their qualitative or quantitative thermal weight loss kinetics with change in temperature of time (Jing, Zhang and Wu 2002).

2.6.2 Instrument Description and Application in this Thesis.

TGA measurements were conducted using a TGA/DSC 3+ (Mettler-Toledo International Inc.), with samples heated in air at 10°C/min from 30°C to 900°C in 1 mL cylindrical alumina crucibles. This method was used to:

1. Assess the thermal stability of fungal biomass and extracted biopolymers (chitin and chitosan).
2. Quantify the organic content in gold nanoparticle formulations.
3. Evaluate the degradation behaviour of fungal–nanoparticle hybrid materials (e.g., TiO_2 and AuNP composites).

2.6.3 Limitations

The limitations of TGA as a characterization method have been discussed, and according to Moseson, et al. (2020), these include:

1. TGA relies on the measurement of mass loss as a function of temperature. However, if the sample undergoes decomposition or chemical reactions during heating, the results may be inaccurate.
2. TGA experiments often require an inert atmosphere (e.g., nitrogen) to prevent oxidation or other reactions. This limitation restricts the applicability of TGA.
3. The rate at which the sample is heated affects the TGA curve. Different rates may yield different results, as can sample size, and conditions (e.g., moisture content).
4. TGA can't reliably tell how much degradation has occurred based solely on mass loss from volatile substances. This limitation affects its ability to give consistent and universally applicable indicators of degradation extent.

2.8. METHOD DEVELOPMENT

Mycelial Mechanics: Unveiling Spatial Variations and Effects of Processing Methods on Mycomaterial from *M. rouxii* and *R. oryzae*.

This section presents findings from method development experiments conducted to assess spatial variation and the effects of processing methods on the mechanical properties of mycelial materials. These results are included here to justify the methodological choices made in later chapters and to demonstrate the rationale behind selecting specific fungal strains and drying techniques for material fabrication.

2.8.1. Summary of Results

In this study, the inhomogeneity of the mycelia of *M. rouxii* and *R. oryzae,* and how different drying conditions impact various mechanical parameters (width, elongation potentials, strength, and flexibility) were investigated. The mycelia of both species exhibited spatial non-homogeneity by mechanical characterization (variations in mechanical properties, such as stiffness and elasticity, observed within different regions of the mycelia). Interestingly, the mechanical properties were influenced by the specific location from which the samples were cut from the mycelia (either the point of inoculation, the midpoint, or a random edge). This spatial variation highlights the importance of considering local differences within the mycelial network especially for developing the use of such materials as biomaterials. The results indicated that the drying conditions played a significant role in shaping the mechanical behaviour of the mycelia. When conventionally frozen at -44°C before drying, the mycelia were significantly thicker comparatively. However, using liquid nitrogen (-196 °C) for freezing led to physical tearing, affecting their overall structure. In contrast, air-dried (25 °C) or oven-dried (90 °C) mycelia showed increased stiffness but reduced flexibility. Despite this, both groups demonstrated high load-retaining strength. The mechanical response varied based on the drying method and the specific strain (*M. rouxii* or *R. oryzae*).

2.8.2. Introduction and Problem Description

Fungal mycelia consist of a network of intertwining hyphae filaments as revealed from their morphological characterization, but due to the growth patterns of these hyphae, the overall properties of mycelia are often described as inhomogeneous (Lehmann et al, 2019). Understanding these variations, particularly the mechanical properties, can inform decisions on which parts of the mycelia are best suited for specific applications. This is because there is a growing global demand for sustainable materials that are biodegradable, readily available,

and environmentally friendly (Abdur Rahman, et al. 2023). Mycelia-based materials have emerged as a promising solution to meet this demand with their unique physicochemical and mechanical properties (Sharma, et al. 2024). Their unique properties and eco-friendly nature make them ideal candidates for various applications, filling a crucial gap in the market for sustainable materials. This study aims to provide clarity and guidance for scientists and industrialists who use mycelium-based materials in their work or production processes. I developed a method to demonstrate the existence of spatial variation within a single mycelium. To accomplish this, I set the objectives below.

1. Establishing the mechanical inhomogeneity of the mycelia of *M. rouxii* and *R. oryzae.*
2. Establishing the effect of different preparation processes on the mycelia's mechanical properties (thickness, elongation potentials, stiffness, as strength).

2.8.3. Growth Condition and Preparation of *M. rouxii and R.s oryzae*

The fungal strains *M. rouxii* indexed NTUCC 244/ATCC 44260, and *R. oryzae* indexed NTUCC 260 (Unknown strain) were sourced from the Nottingham Trent University Culture Collection (NTUCC). The fungi cultivation on potatoes dextrose broth (PDB; P6685), from Sigma Aldrich-Merck Life Science UK Limited)) was achieved by introducing 1×1 cm freshly cut pieces of mycelium (using a sterile scalpel on actively growing cultures) into 200 mL of the media (24 g/L) already autoclaved at 121°C for 30 min (Crystal – MP25, Rodwell Scientific, UK), and then incubated for 10 days at 25 °C (Labnet international 211DS Shaking Incubator, Appleton Woods Ltd., Birmingham, UK). Freshly harvested mycelia were washed (10 x in 600mL of DDH$_2$O) to remove all extracellular components adhering to the mycelia surface.

2.8.4. Drying the Mycelia of *M. rouxii and R. oryzae* under Different Conditions

The freshly washed mycelia were dried on a Teflon sheet under different conditions as described below.

1. **Air Drying**: The mycelia were left to dry at room temperature (25°C) for 8 h.
2. **Oven Drying**: The mycelia were dried in an oven at 90°C for 4 h using a Memmert UNB400 Oven with the following specifications: Power 230V, 50/60Hz, and a temperature range of 0-200°C.
3. **Conventional Freezing and Freeze-Drying**: The mycelia were initially frozen at -45°C in a conventional freezer (TEFCOLD SE-45 Series) 8 h. Subsequently, they were dried using a BT4KZL dryer-VirTis freeze-drier for 48 h.

4. **Cryogenic Freezing and Freeze-Drying**: The mycelia were cryogenically frozen at -196°C using liquid nitrogen before drying. Samples from both conditions 3 and 4 were dried under the same conditions.

2.8.5. Evaluation of Mechanical Properties

The mechanical properties (thickness, stiffness, endurance, and elasticity) of 5 mm by 35 mm (width by length) mycelia strips were measured using a Zwick/Roell machine with a 0.5 N load. The software used was testXpert II v2.2. The mycelia thickness for both *M. rouii* and *R. oryzea* was determined using an adjustable vernier caliper (RS PRO 0-150 mm Digital Caliper with 0.01 mm resolution). Additionally, the mycelium area was divided into three distinct regions, as illustrated in Figure 2.1 below.

Figure 2.1: Spatial division of fungal mycelia for mechanical evaluation showing (A) the point of the mycelia that has the inoculant; (B) the other edge of the mycelia (A random edge); and (C) the mid portion of the mycelia.

2.8.6. Data Analysis

Experiments were conducted in triplicate, and the mean values along with their standard deviations reported in plots. Two-way analysis of variance (ANOVA) was used to assess significant differences among various treatment factors and their levels. Subsequently, Tukey's Post hoc test was used for multiple comparisons of means across different groups (with a significance level of $P < 0.05$). GraphPad Prism 10.0 for statistical analysis.

2.8.7. Results and Discussion

2.8.7.1 Preliminary Evaluation of Inhomogeneity of Mycelia with *M. rouxii*

Data in Figure 2 represents the preliminary mechanical test results for the mycelia of *M. rouxii* at different areas and widths. I observed variations in strength across different areas of the mycelium. Interestingly, these mechanical differences were not correlated with the width of the mycelia strip. The applied force was kept constant, this caters for so differences in length of the different areas of the mycelia. This observation prompted a more detailed study, where various portions of the mycelium were investigated using four different drying methods. It is noteworthy that I included another Mucorales (*R. oryzae*) in the experiment due to some variations observed in morphological Structures.
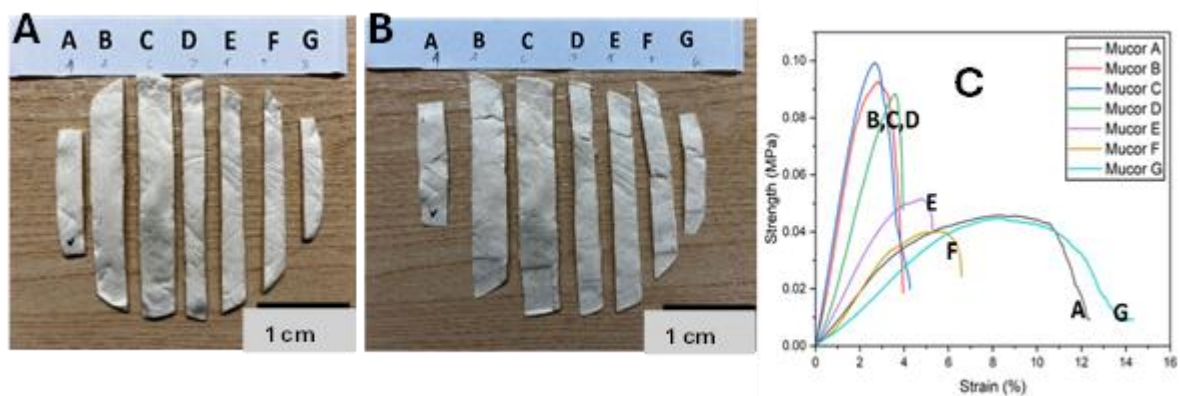
Figure 2.2: Representative image from the preliminary evaluation of mycelia strength (A) intact mycelia; (B) Breaking pattern of the mycelia (C) the strength of different areas of the mycelia.

2.8.7.2 Effects of Drying Methods on the Mechanical Properties of *M. rouxii*

I investigated the mechanical properties of *M. rouxii* mycelia under different drying processes (Table S1). My results reveal significant effects on mycelial thickness, strength, elongation potential, and flexibility. Figure 3 below illustrates these findings. Regardless of the location where the mycelia were cut, conventional freezing at -45°C resulted in thicker mycelia mat. There was no observable difference in thickness across other groups. Drying the mycelia either at room temperature (25°C) or in an oven (90°C) significantly increased their strength (load-bearing capacity). However, this also led to increased stiffness and reduced elongation potential. Despite the mycelia's inherent inhomogeneity, the impact of the drying process was consistent across different portions of the mycelia. Notably, cryogenic freezing using liquid nitrogen (-196°C) caused physical damage to the mycelia. Therefore, pre-freezing with a conventional freezer (-45°C) prior to drying yielded moderately thick, flexible, and biodegradable materials.
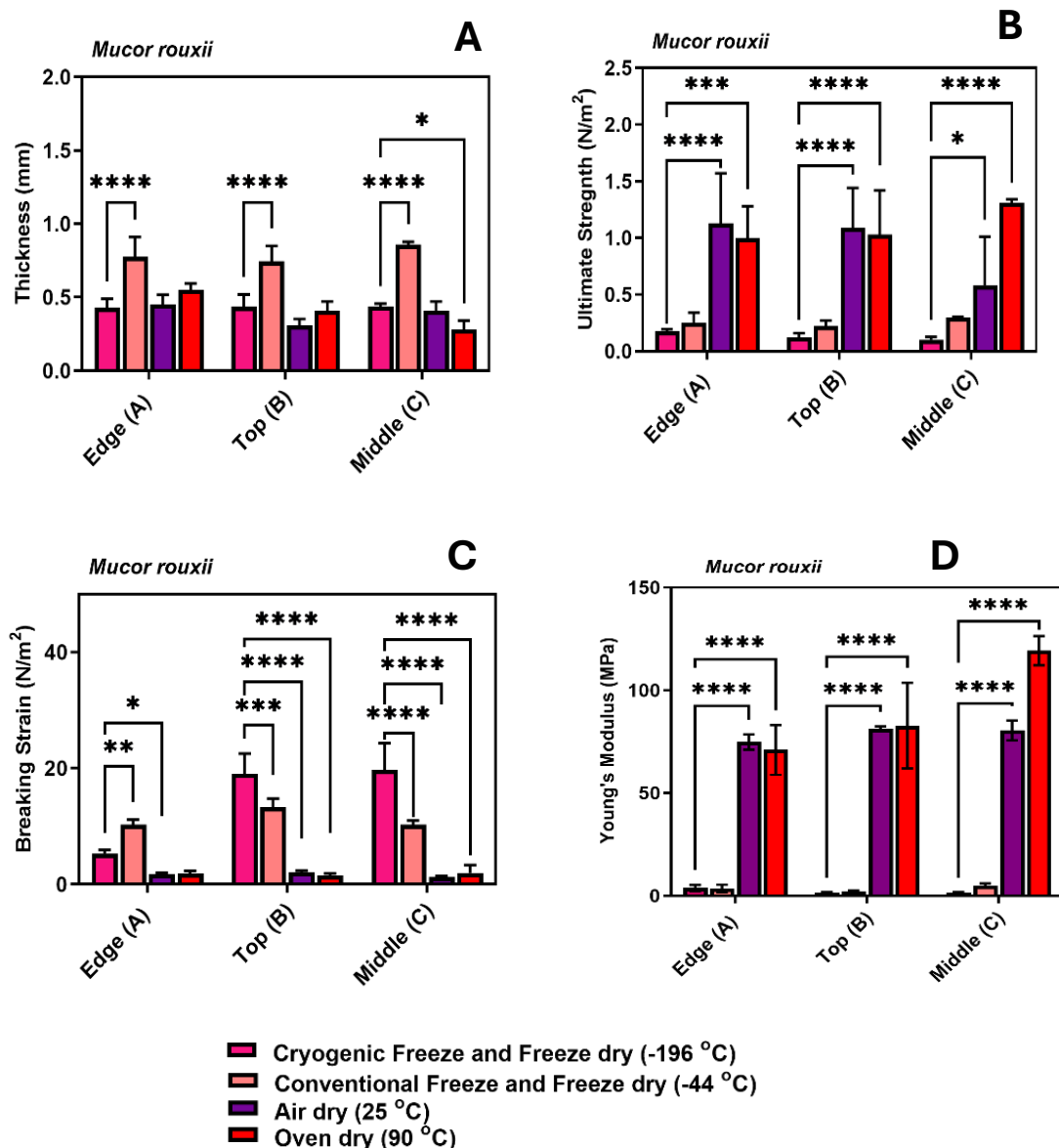
Figure 2.3: Mechanical Properties of *M. rouxii* Mycelia (A) Thickness (B) Ultimate Strength (C) Breaking Strain (D) Young's Modulus. Asterisks denote the level of significance (* P ≤ 0.05, ** P ≤ 0.01, *** P ≤ 0.001, **** P ≤ 0.0001).

2.8.7.3 Effects of Drying Methods on the Mechanical Properties of *R. oryzae*

I also investigated the mechanical properties of *R. oryzae* mycelia under varying drying conditions. My findings revealed significant effects on mycelial thickness, strength, elongation potential, and flexibility (Figure 4). Like *M. rouxii*, the mycelia of *R. oryzae* exhibited trends in response to different drying methods. However, the inhomogeneity of the mycelial area was more pronounced with the various drying processes. Conventional freezing at -45°C preserved the highest mycelial thickness. Drying the mycelia either at room temperature (25°C) or in an

oven (90°C) significantly increased their strength and stiffness (ability to withstand load), but at the expense of elongation potential. Notably, the midpoint of the mycelia was thinner and less flexible compared to other areas. This observation may be attributed to the organization of hyphal filaments in *R. oryzae* and the growth patterns of the fungus. In liquid media, *R. oryzae* grows from the flask's edge toward the centre, resulting in varying mycelial thickness. New shoots are thinner, as they originate from the centre. Therefore, the observed reduction in thickness at the midpoint aligns with this growth behaviour.
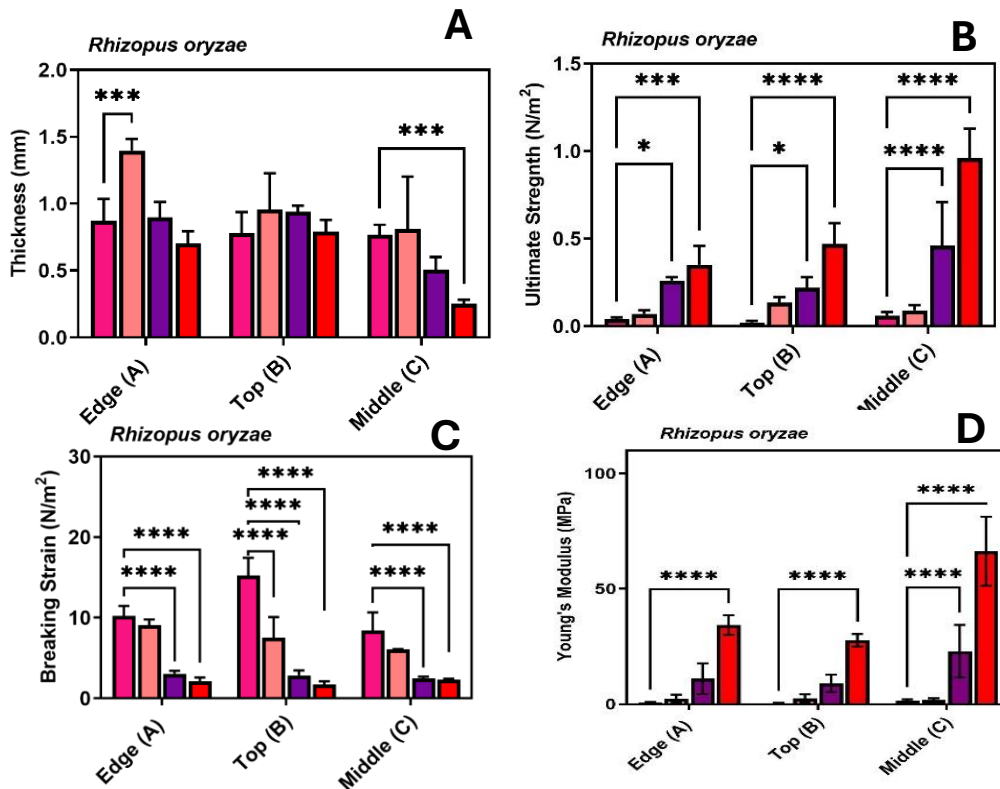
Figure 2.4: Mechanical Properties of *R. oryzae* Mycelia (A) Thickness (B) Ultimate Strength (C) Breaking Strain (D) Young's Modulus. Asterisks denote the level of significance (* $P \leq 0.05$, ** $P \leq 0.01$, *** $P \leq 0.001$, **** $P \leq 0.0001$).

2.8.8. Conclusion and Recommendation

Based on my investigation into the spatial variation of the mycelia of *M. rouxii* and *R. oryzae*, I conclude that the mechanical properties of mycelium-based materials are significantly influenced by both the specific location within the mycelium and the drying conditions applied. My findings highlight the non-homogeneous nature of mycelia, with mechanical properties varying depending on whether samples were taken from the point of inoculation, the midpoint, or a random edge. This spatial variation underscores the importance of considering local differences within the mycelial network when developing these materials for applications.

Furthermore, my results demonstrate that drying conditions play a crucial role in determining the mechanical behaviour of mycelia. Conventional freezing at -44°C resulted in thicker mycelia mat, while freezing with liquid nitrogen at -196°C caused physical tearing, compromising structural integrity. Air-dried (25°C) and oven-dried (90°C) mycelia exhibited increased stiffness but reduced flexibility, yet both methods maintained high load-retaining strength. The mechanical response varied not only with the drying method but also between the two strains studied, *M. rouxii* and *R. oryzae*. These insights are vital for optimizing the use of mycelium-based materials in various industrial and scientific applications, ensuring that the unique properties of mycelia are effectively harnessed.

2.8.9. Challenges Encountered and Solutions Adopted

During preliminary experiments, the mycelia adhered to aluminium foil and Petri dishes when air-dried or oven-dried. This adhesion made it impossible to remove the samples without causing damage. To overcome this issue, I introduced Teflon sheets as drying platforms. This adjustment allowed for complete drying and easy removal of the samples, effectively addressing the initial challenges.

2.8.8.10 Reproducibility of Method

To ensure reproducibility, I maintained constant experimental conditions and carefully avoided errors due to human handling. Multiple samples were analysed from each group to validate the results and ensure consistency.

2.8.8.11 Limitations of the Study

This experiment was conducted in liquid media (PDB) using cut pieces of mycelia. To ensure comprehensive validation, the results should also be tested under conditions where spores are used or on different substrates, particularly solid media.

CHAPTER 3

3.0 Synthesis, Characterization, and Application of Surface Functionalised Gold Nanoparticles (AuNPs)

In this chapter, gold nanoparticles (AuNPs) with different surface modifications (ionic-citrate, nutrient-glucose, antibiotic-cefaclor, and conventional reductant-sodium borohydride) were synthesized and characterized using multiple techniques. The characterization focused on their chemistry, morphology, stability, and interactions with biological systems, specifically human immortalized keratinocyte (HaCaT) and Human Embryonic Kidney 293 (HEK 293) cells. Transmission Electron Microscopy (TEM) revealed that the nanoparticles were predominantly spherical, with some triangular glucose-stabilized particles, all measuring less than 100 nm in diameter, while hydrodynamic sizes diameters were determined via Dynamic Light Scattering (DLS). Chemical analysis confirmed that the nanoparticles were composed of gold (Au) and crystalline in nature (XRD/EDX). The reducing agents used in the synthesis were found to stabilize the nanoparticles in solution, as indicated by their respective surface characteristics (FTIR). Thermogravimetric Analysis (TGA) showed that the amount of reducing material associated with the nanoparticles varied, with glucose being the most incorporated. The AuNPs significantly impacted cell viability in HaCaT (epidermal) and HEK 293 (kidney) cells, exhibiting either proliferation effects in a concentration-dependent manner. There was no significant cytotoxicity recorded on cells at the concentration at which the materials were used especially via the intended area of application being biofiltration. The nanoparticles remained stable for over 30 days post-synthesis, with no significant changes in size as monitored by DLS. Purifying the NPs using membrane dialysis tubing significantly stabilized NPs Notably, the nanoparticles exhibited well-defined surface plasmon resonance properties, allowing them to be used in rapid colorimetric sensing, with mercury detection being used as an exemplar application. Mercury ions could be detected within less than 5 s, with a registered detection limit for each type of surface functionalised NP system. These nanoparticles demonstrated excellent morphological and functional characteristics, and biological compatibility, making them ideal for forming reusable composite biofilters for mercury.

Key words: Gold nanoparticles (AuNPs); Surface modifications; Characterization; Stability; Biological systems; Surface plasmon resonance; Colorimetric sensing; Biofilters

3.1 Introduction

Gold nanoparticles (AuNPs), with sizes ranging from 1-100 nm, are synthesized from a gold precursor (typically a gold salt) and a reducing and stabilizing agent (Gimeno 2008). In its pure form, gold appears slightly reddish-yellow due to absorption at 2.4 eV, attributed to orbital absorption transitions from the filled 5d to the Fermi level, which is essential in the 6s band (Gimeno 2008). Gold is known for its stability and corrosion resistance, even in the presence of organic mineral acids (except selenic acid) (Yannopoulos 2012). It is a monovalent metal with an electronic configuration of [Xe] $4f^{14}$ $5d^{10}$ $6s^1$ for ^{197}Au (Wani, et al. 2021). The chemistry of gold reveals its interactions and changes in oxidation states in aqueous or colloidal solutions. In aqueous solutions, gold exists as a complex in Au^{+1} or Au^{+3} oxidation states, but as Au^0 in its neutral state, explaining its switch in chemical reactivity (Saldan, et al. 2018). The formation of the Au^{+3} oxidation state is due to the destabilization of the 5d orbitals (Gimeno 2008). In colloidal solutions, gold typically exists as Au^0, forming very fine coloured nanoparticles in a suspension known as colloidal gold (De Souza, Nogueira and Rostelato 2019). Gold is considered nontoxic, and this property has been reported in various colloidal forms (Sani, Cao and Cui 2021). The use of colloidal gold for different applications (e.g. for diagnostics or therapeutics) dates to the 1850s when Michael Faraday introduced it, and the formation of gold nanoparticles has been a significant breakthrough in the use of gold materials (Hutchings, Brust and Schmidbaur 2008). In 1951, (Turkevich, Stevenson and Hillier 1951) developed a novel method for synthesizing citrate-stabilized AuNPs by treating hydrogen tetrachloroauric acid with citrate, which acts as both the reducing and stabilizing agent. This system has undergone numerous modifications over the years, such as size and dispersity-controlled synthesis achieved by altering the gold-to-citrate ratio (Frens 1973). Further advancements include the adoption of alternative reducing and stabilizing agents such as $NaBH_4$ (Brust, et al. 1994, Giersig and Mulvaney 1993), controlled synthesis of AuNPs under varying temperature and pH conditions (Kim, et al. 2021), and the introduction of functional monomers (Lang, Liu and Liu 2014), polymers (Mohan, Gunasekaran and Ravishankar 2019), crude extracts from living organisms (Boruah, et al. 2021), antibiotics (Rai, Prabhune and Perry 2010), or other bioactive moieties into the AuNP Structures. These modifications aim to synthesize AuNPs suitable for specific applications as desired by scientists. This chapter addresses Objectives 2 and 3 by examining how different surface functionalizations affect the physicochemical, optical, and biological properties of gold nanoparticles (AuNPs), and by evaluating their effectiveness in colorimetric sensing of mercury ions. The overall properties
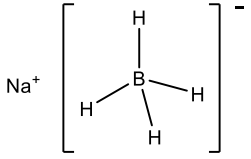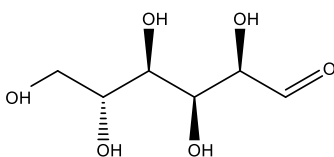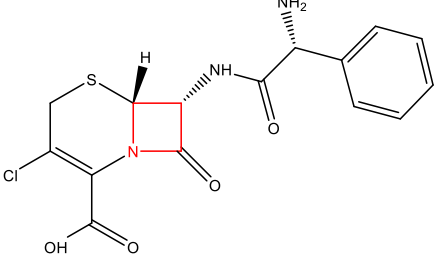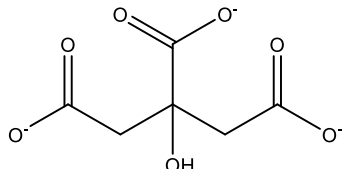
of AuNPs depend on the entire component structure, particularly the capping and stabilizing material, which influences physicochemical properties such as stability, surface charge, surface plasmon properties (Kumar, et al. 2019), and efficacy (Bolaños, Kogan and Araya 2019). The primary objective of synthesizing AuNPs with various surface modifications ($NaBH_4$, glucose, cefaclor, or citrate; Table 3.1) in this study is to examine how these reducing and stabilizing agents influence structural changes and their subsequent impact on the nanoparticles' physicochemical and biological properties. Additionally, the study explores their potential application in forming composite microstructures and reusable biofilters, which is presented in the next chapter.

$$HAuCl_4 + 3e^- \rightarrow Au + H^+ + 4Cl^- \quad \cdots\cdots\cdots\cdots\cdots\cdots\cdots\cdots\cdots\cdots\cdots\cdots\cdots\cdots \qquad \text{Equation 3.1}$$
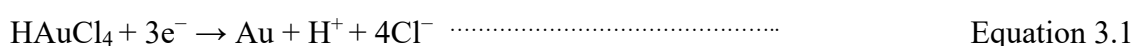
The half-reaction for the reduction of $HAuCl_4$ to Au.

The reducing agents used in this study differ in strength and mechanism, ranging from strong inorganic reducers like sodium borohydride to mild organic and multifunctional agents like glucose, citrate, and cefaclor.

Table 3.1: Chemical and Structural Descriptions of Various Reducing and Stabilizing Agents for AuNPs Synthesis (Structures from ChemOffice Suite 2020 v20.1).

Name	Description	Molecular Structure
Sodium borohydride ($NaBH_4$)	Ionic borate	
β-D-Glucose ($C_6H_{12}O_6$)	Carbohydrate Nutrient	
Cefaclor ($C_{15}H_{14}ClN_3O_4S$)	Antimicrobial	
Sodium citrate tribasic dihydrate	Ionic- citrate	

3.2 Materials and Methods

3.2.1 Materials

Gold (III) chloride trihydrate ($HAuCl_4.3H_2O$) (204390), 14 kDa cellulose dialysis tubing (D9527), sodium hydroxide (S/4880/60) were purchased from Fisher Scientific UK Ltd. Cefaclor (C6895-1G), sodium citrate tribasic dihydrate (S4641-500G), D-(+)-glucose (G-7528) were purchased from Sigma- Aldrich UK, and sodium borohydride (9984980L) was sourced from General purpose reagents. All chemicals were used without further purification. Purification involving dialysis tubing has been described in the relevant section of the methods below.

3.2.2 Methods

3.2.2.1. Synthesis of Surface-Functionalized Gold Nanoparticles

Gold nanoparticles were prepared whose outer surface was coated with borohydride, glucose, citrate, or an antibiotic, in this case, cefaclor was synthesized. For the conventional synthesis of Au NPs with sodium borohydride ($NaBH_4$), 1 mL of freshly prepared ice-cold 0.01 M $NaBH_4$ was added dropwise (50 µL per/ s) to 5 mL of 2.5×10^{-4} M $HAuCl_4$ and gently stirred (Stuart CB162) until a ruby red colour was observed, signifying the synthesis of gold NPs. The procedure is a modification of the method adopted by (Kwon, K., et al. 2007). For the glucose-mediated synthesis of Au NPs, 1 mL of 1M D-glucose was added to 9 mL of 2.5×10^{-4} M $HAuCl_4$ in a flask, and the solution was heated to 60 °C, followed by the addition of 20 µL 1 M NaOH. The resulting solution was rapidly stirred for 10 s when a ruby red colour was confirmed (Suvarna, et al. 2017). Antibiotic-mediated synthesis of Au NPs was achieved by adding equal volumes (100 µL) of the 0.01 M cefaclor and 0.01M $HAuCl_4$ solutions to 9.8 mL of water in a one-pot synthesis. The resulting solution was kept at 60 ^{0}C for 2 h until a stabilized ruby red colour was observed (Rai, Prabhune and Perry 2010) For the synthesis of citrate stabilized Au NPs, 19 mL of 2.5×10^{-4} M $HAuCl_4$ and 1 mL of 1×10^{-4} M citrate to form a 20 mL solution, then 60 µL of freshly prepared ice-cold 0.1 M $NaBH_4$ solution was added while still stirring vigorously. The resulting solution was transferred into a sample tube and wrapped in a foil until a red colour was formed (Turkevich, Stevenson and Hillier 1953).

3.2.2.2. Characterization of synthesized AuNPs ($NaBH_4$-AuNPs, Glc-AuNPs, Cit-AuNPs and Cef-AuNPs)

The surface plasmon resonance properties of the AuNP solutions by ultraviolet-visible light Spectroscopy were measured using a Cary 50 Bio UV-Vis spectrophotometer (Agilent

Technologies) between 300- 700 nm. The overall surface charge (*zeta* potential) by Zetasizer Nano-S Zen 600 (Malvern Instruments Ltd.) was performed at pH 7.0 using DTS1070 folded capillary cells (Malvern Instruments Ltd.). Both size and zeta potential measurements were taken at 25°C after 120 s equilibrations with water as the dispersant (η 0.8872 cP, n 1.33 and ε_r 78.5) and gold (n 0.2 and absorbance 3.32) as the material. The AuNP's size and morphological orientation were assessed through digital micrographs obtained with a JEOL JEM-2100Plus transmission electron microscopy (TEM) fitted with a LaB_6 filament operating at an accelerating voltage of 200 kV. Samples were prepared by depositing 5 µL of suspended AuNPs onto 200 mesh carbon-coated grids (Quantifoil Micro Tools GmbH), and micrographs were taken with an Orius SC200 CCD camera (Gatan Inc.). Elemental mapping of the AuNPs was done with a TEM-fitted EDS detector (JEOL JED-SDD 30 mm^2 window). TEM images were analysed using ImageJ 1.53t w/Adiposoft 1.16 Software. The composition of surface materials was determined by thermogravimetric analysis (TGA) with a TGA/DSC 3+ (Mettler-Toledo International Inc.) with samples heated in air at 10°C/ min over 30-900°C. Fourier transform infrared (FTIR) spectra were measured using a NICOLET iS50 FT-IR, with a DTGS detector and a KBr beam splitter. The spectral source was IR, optical velocity was 0.47, Aperture was 87, the range was between 600-4000 cm^{-1}, and Resolution was 0.09 cm-1, with 300 scans. X-ray diffraction using a Rigaku Ultima IV X-Ray Diffractometer was used to reveal the domain and crystallite properties of the AuNPs. Samples were run on a Rigaku silicon low background specimen holder at 40 kV and 50 mA (λ=1.540593 Å) between $5 - 80$ (2θ). Scans were obtained in step mode; step size was 0.02º, and scan speed 5.0 deg./ min. Before analysis, the instrument was calibrated, and background measurements were taken. The blends of each sample were analysed in powdered form.

3.2.2.3. Nanoparticle Purification and Stability Study

The removal of extraneous organic moieties not bound to the AuNPs solution was done using 14KDa membrane dialysis tubing. The NP solution formed was dialyzed against DDH_2O (pH 5.5, <10 µS) to remove excess residual reactants. Dialysis lasted for 48 h. The DDH_2O was changed after 8 h within the process, and stirring was kept constant using a magnetic stirrer. The purified NPs were then studied for changes in the size distribution properties for 6 months.

3.2.2.4. Cell viability via MTT Assay on Human Immortalized Keratinocyte (HaCaT) and Human Embryonic Kidney (HEK) 293 cells.

The 3-(4,5-dimethylthiazol-2-yl)-2,5-diphenyltetrazolium bromide (MTT) assay used to test the cytotoxicity status of the synthesized AuNPs followed the procedure described by

(Carnovale, et al. 2019) using MTT reagents (Sigma Aldrich, CT01-5). In summary, 100 µL of the HaCat cells (passage 9) were seeded into a 24-well plate at a seeding density of 50,000 cell/ mL (TC-10 Bio-Rad Automated cell counter). Incubation (Panasonic-IQ MCO-170AICUV-PA Dual-Chamber Air-Jacketed CO_2 Incubators) conditions were 37 °C, 5% CO_2, 85% RH, 24 h in an incubator). Dulbecco's Modified Eagle Medium (DMEM) plus 10% FBS and 1% Pen/was used. All other manufacturers' recommendations were adhered to. The cells were left to recover from handling for 24 h before treatment. The medium was then gently aspirated and replaced with fresh medium containing different concentrations of AuNPs (0.1, 0.5, 1, 5, 10, 15, 20, 40 µg/ mL). After 24 h of the treatment durations, 50 µl of MTT solution (3 mg/ ml in PBS, Sigma Aldrich, UK) were added to each well, and the cells were incubated at 37°C for 1 h. After incubation, the MTT solution was gently aspirated and DMSO (500 µl) was added to each well and left on a plate shaker for 10 min protected from light to solubilize the formed formazan crystals. Absorbance readings were taken at 570 nm using a plate reader (Synergy LX Multi-Mode Reader). AuNPs were incubated with MTT solution in the absence of cells and no formazan crystal formation was observed. For HEK 293 (Passage 11), the standard protocol for culturing by Thermo-scientific was followed. The final Eagle's minimum essential medium was modified to contain Earle's Balanced Salt Solution (110 mg/ L), non-essential amino acids (6 mM L-glutamine), Fetal Bovine Serum (10% of culture) and penicillin (1U/ mL/100 µg/ mL). The viability assessment for HEK 293 – HCL4517 Thermo Scientific, followed the same procedure as HaCaT (where) as described above. HaCaT 293 (ThermoFisher Scientific) was sourced from the biosciences department, and HEK-293 (ThermoFisher Scientific) was gifted by the John van Geest Cancer Research Centre, both at Nottingham Trent University, United Kingdom. All experiments were conducted in triplicates.

3.2.2.3. Colorimetric Sensing of Mercury (Hg^{2+})

The colorimetric sensing of mercury (Hg^{2+}) was accomplished using a spectrophotometric method (Cary 50 Bio UV-Vis Agilent Technologies). The mercury standard (1g/1000 mL) was sourced from Sigma -Aldrich: Pcode 101740455. Different concentrations of the heavy metal (1, 2, 10, 20, 30, 40, 50 µM) were prepared using the respective AuNPs as diluent. The absorbance of the resulting solution (2 mL) transferred into a polystyrene cuvette (SARSTEDT 10×10×45mm) was measured at 25 °C between 300 – 800 nm.

3.3. Results And Discussion

3.4.1. Surface Plasmon Resonance Properties

The surface plasmon resonance (SPR) peaks, which indicate the absorption properties of the surface-functionalized gold nanoparticles (Au NPs), are illustrated in Figure 3.1. The synthesized gold NPs exhibit a brick-red colour. Distinct SPR peaks were observed at 520 nm, 525 nm, 530 nm, and 534 nm for $NaBH_4$-AuNPs, Glc-AuNPs, Cit-AuNPs, and Cef-AuNPs, respectively. These peaks confirm the successful synthesis of the Au NPs. The maximum absorbance values align with previous studies(Rai, Prabhune and Perry 2010, Turkevich, Stevenson and Hillier 1951, Silva, et al. 2021, Liu, et al. 2006). The synthesis, stabilization, and capping of the Au NPs were facilitated by the reducing agents used during the synthesis process. Consistent with the findings of (Rai, Prabhune and Perry 2010) regarding the use of cefaclor in Au NP synthesis, (Suvarna, et al. 2017) demonstrated that glucose and citrate, when used as reductants, effectively reduced Au^{3+} to Au^0. Additional stabilization was achieved through the biomolecular constituents, such as the hydroxyl (-OH) group present in glucose.
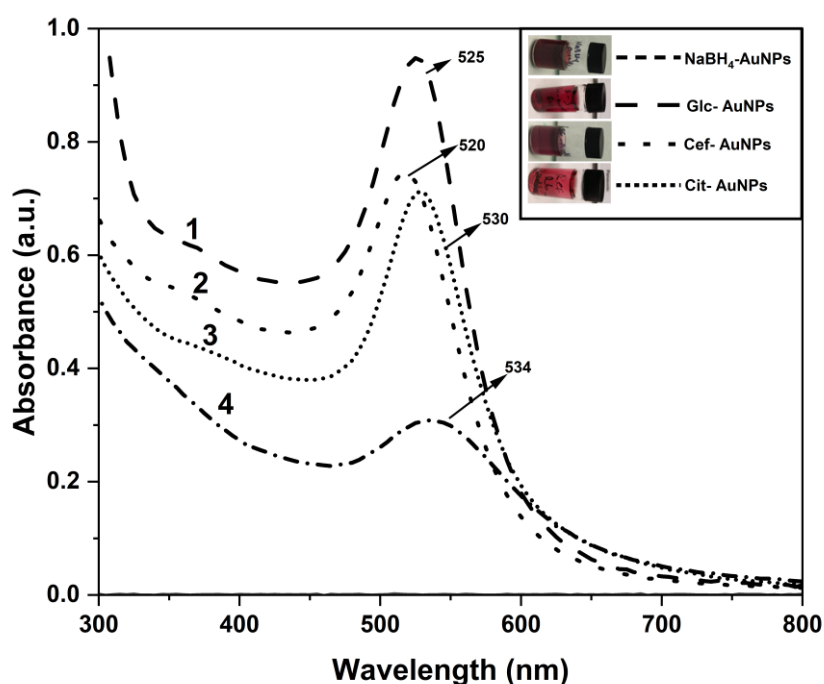
Figure 3.1: UV-visible absorption spectra of AuNPs at a nominal concentration of 47 µg/ mL (measured by Au content). Line 1: Glc-AuNPs; Line 2: $NaBH_4$-AuNPs; Line 3: Cit-AuNPs; Line 4: Cef-AuNPs. Inset images display the corresponding AuNP solutions, illustrating visual differences in colour and dispersion.

3.4.2. Hydrodynamic Size Distribution

The nanoparticles exhibit distinct hydrodynamic size distributions in their colloidal solution state, along with respective zeta potentials, as presented in Table 3.2 below. Generally, the AuNPs are less than 100 nm, fitting the description of ideal nanomaterials (Gimeno 2008). All groups display very high zeta potential values, which are either negative (NaBH$_4$-AuNPs, Glc-AuNPs, Cit-AuNPs) or positive (Cef-AuNPs) suggesting high stability (Öztürk, Kaplan and Çalış 2024). These values align well with previous literature reports (Table 3.2). Notably, except for Cef-AuNPs, which have a polydispersity index of around 0.25, the other AuNP groups exhibit very low polydispersity indexes, less than 0.1 which is indicative of homogeneous size distribution (Danaei, et al. 2018).

Table 3.2: Comparison of AuNP Size Properties from Different Methods and Zeta Potential. DLS size and zeta potential data were obtained directly from the instrument. TEM and XRD values were analysed using Scherrer's equation and ImageJ, respectively.

Sample	Size from DLS (nm)	Crystallite domain size XRD (nm)	TEM Size (nm)	Zeta potential (mV)	Literature Comparison (mV)
NaBH$_4$-AuNPs	16.1 ± 2.2	16.0 ± 3.9	14.0 ± 3.3	-35.7 ± 8.4	-27 to -37 (Karimi, Moshaii and Nikkhah 2019)
Glc-AuNPs	25.2 ± 3.0	8.9 ± 2.0	24.0 ± 3.7	-38.5 ± 6.1	-19 to -38.7 (Boitor, et al. 2015, Suvarna, et al. 2017)
Cef-AuNPs	27.9 ± 8.4	6.1 ± 1.9	5.6 ± 0.7 (small particles) 21.3 ± 3.9 (Big particle)	41.5 ± 12.0	(Rai, Prabhune and Perry 2010)
Cit-AuNPs	47.0 ± 6.5	18.0 ± 4.7	17.5 ± 2.9	-41.3 ± 8.5	-24 to -53 (Karimi, Moshaii and Nikkhah 2019)

3.4.3. Transmission Electron Microscopy

The morphological structure, particulate interactions (physical), and dispersity properties of the gold nanoparticles (AuNPs) are illustrated through transmission electron microscopy (TEM) images in Figure 3.2 A-C. The TEM analysis shows a characteristic spherical shape for each of the nanoparticles, with occasional triangular Glc-AuNP appearing (Fig. 3.2A). The particles exhibit high monodispersity, with Cef-AuNPs distributed across two distinct size categories: small and large particles (Table 3.2). Except for the Glc-AuNPs, the data indicate that the AuNPs predominantly exist as single-domain, highly crystalline nanospheres. These nanoparticles demonstrate either high positive or negative zeta potentials, signifying substantial stability. The nanocrystalline nature of the particles was further validated by their selected area diffraction pattern (SAED), which confirms their purity (Cheng and Hight Walker 2010). The Representative EDX Spectra of the NPs can be found in Appendix 3.1.
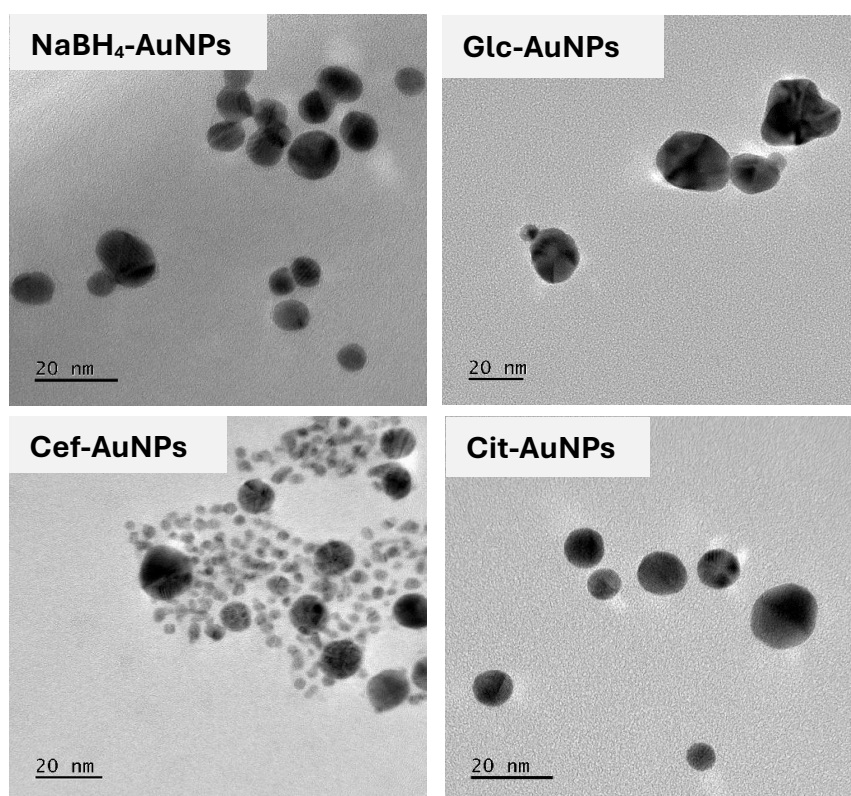
Figure 3.2A. Representative transmission electron microscopy (TEM) images of gold nanoparticles (AuNPs) synthesized using different reducing agents. Each panel shows the morphology and size distribution of AuNPs produced with a specific agent: NaBH4 (top left), Glucose (Glc, top right), Cefaclor (Cef, bottom left) and Citrate (bottom right). Scale bars represent 20 nm.

Measurements were taken for 100 particles of each type of nanoparticle (NP), except for the Cef-AuNPs, where 150 particles were analyzed, 100 for the small particles and 50 for the large particles. This analysis resulted in distinct particle sizes, which are compared to the hydrodynamic size and crystallite size shown in Table 3.2. Histograms illustrating the particle sizes for each category of AuNPs can be found in Figure 3.2B below.
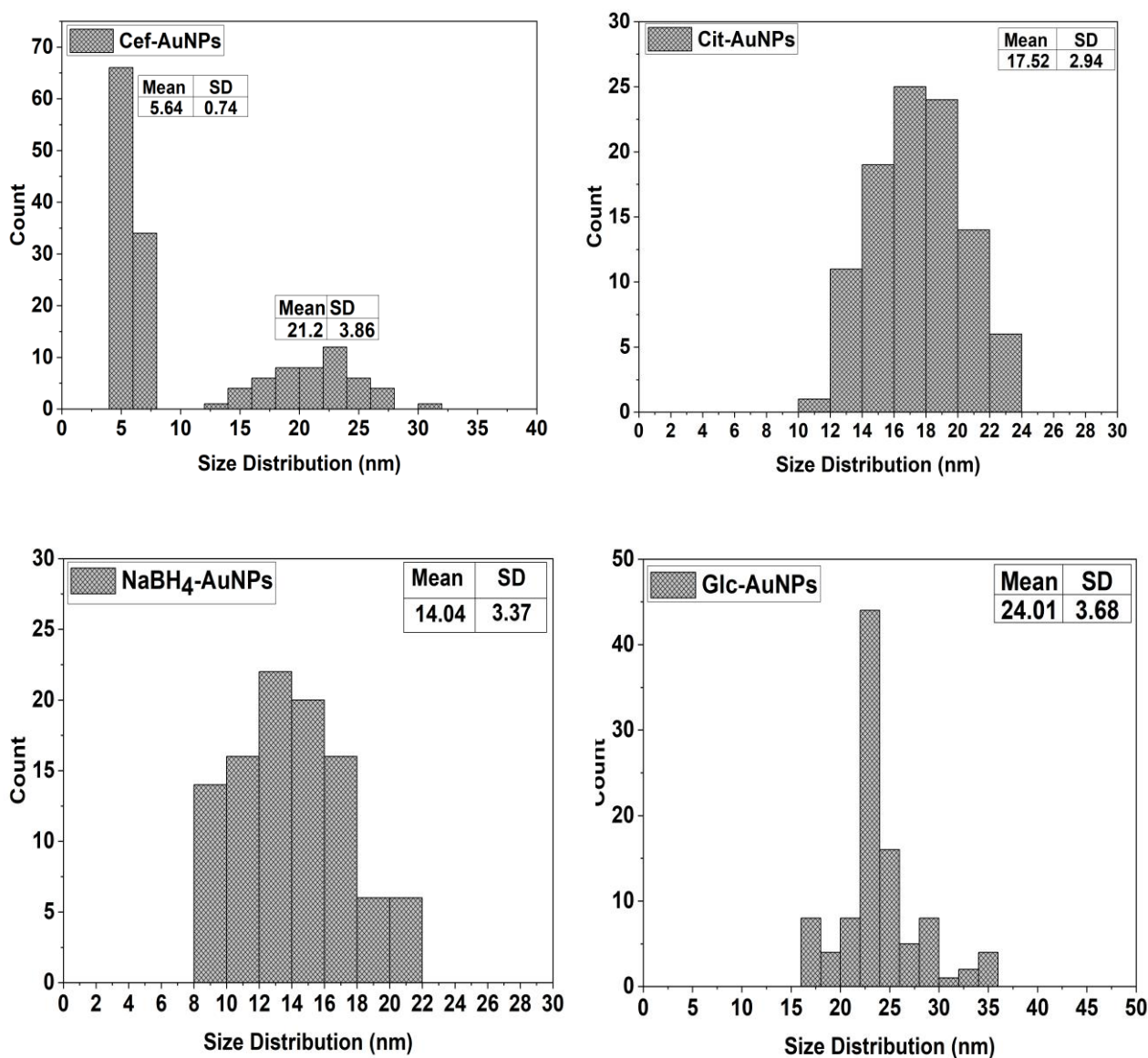
Figure 3.2B: Histograms showing the distribution obtained from the TEM measurement for each of the AuNP synthesized using different reducing agents. The histograms illustrate the variation in particle size distributions influenced by the choice of reducing agent.

The HRTEM images of the AuNPs (Figure 2C) showed fringe spacings corresponding to both the Au (220) and Au (311) planes, recorded as 0.113 ± 0.003 nm for NaBH$_4$-AuNPs, 0.140 ±

0.007 nm for Glc-AuNPs, 0.079 ± 0.009 nm for Cef-AuNPs, and 0.118 ± 0.007 nm for Cit-AuNPs (Figure 2Aii -2Dii).
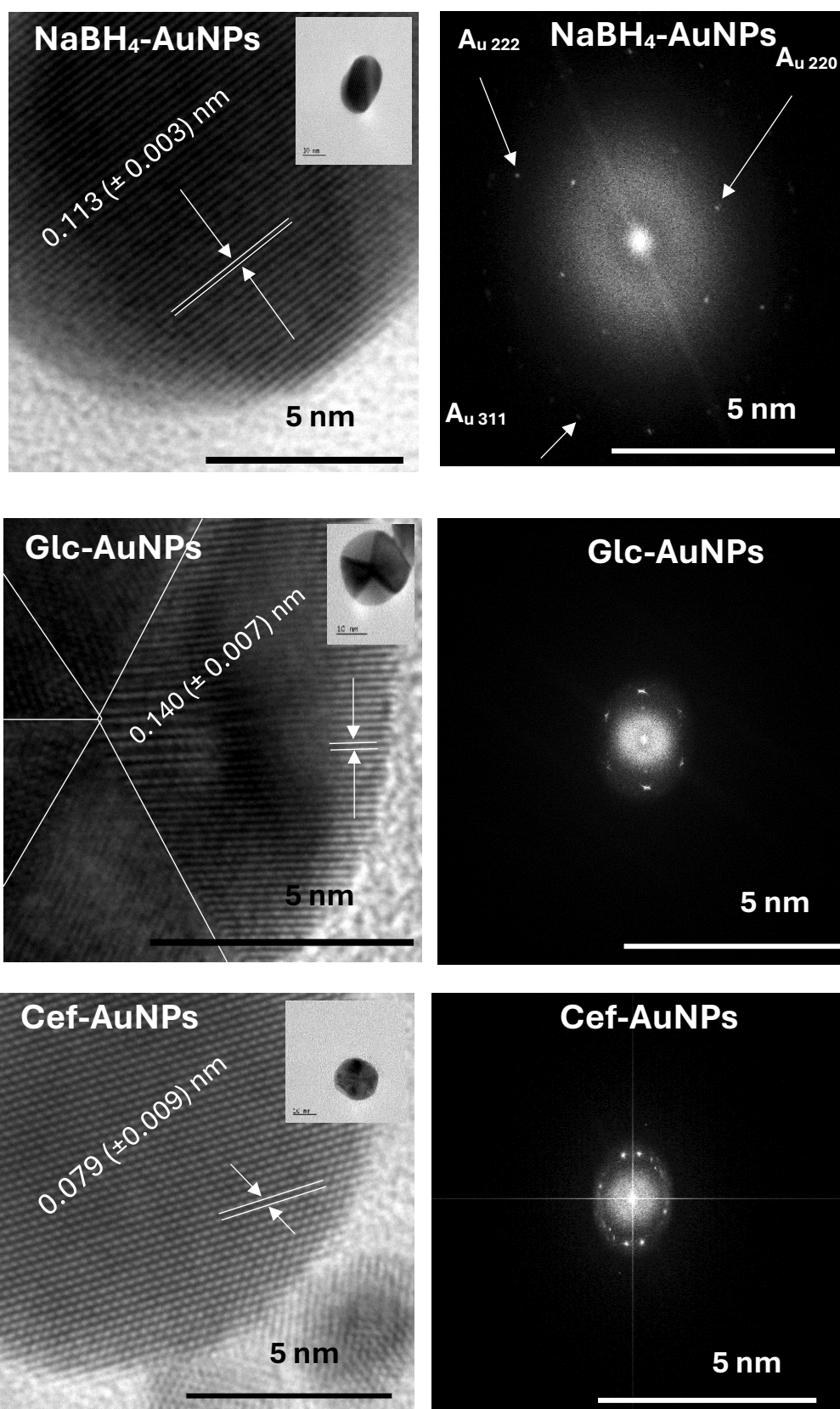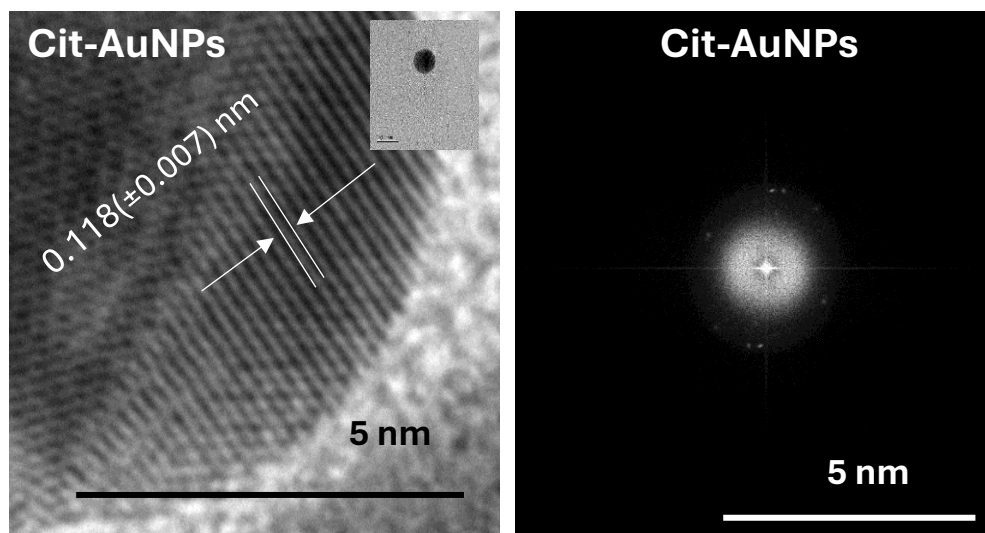
Figure 3.2C: High-resolution transmission electron microscopy (HRTEM) images (showing the fringe spacing) and corresponding diffraction patterns of gold nanoparticles (AuNPs) synthesized using different reducing agents. Each set includes a nanoparticle image (left) and its selected area electron diffraction (SAED) pattern (right) for $NaBH_4$-AuNPs, Glc-AuNPs, Cef-AuNPs and Cit-AuNPs. The insert at the top right corner of the HRTEM are single particles of the respective AuNPs (views at a scale of 10 nm).

HRTEM image of Au Nanostructures showing the fringe spacing and their corresponding FFT image for each of the AuNPs.

3.4.4. X-ray Diffraction for Crystallinity Assessment

The crystallinity and domain properties of the synthesized AuNPs were characterized via powder X-ray diffraction; they exhibit well-defined X-ray diffraction patterns within the 5–80-2θ region, as shown in Figure 3.3. For each group of AuNPs, the results indicate the presence of gold with Miller indices corresponding to the (111), (200), (220), and (311) planes of the face-centered cubic (FCC) structure of gold (JCPDS, File No. 04-0784;(Philip 2010)). Compared to the fringe spacing from the HRTEM images of the Au_{220} and Au_{311} planes, recorded as 0.113 (±0.003) nm for $NaBH_4$-AuNPs, 0.140 (±0.007) nm for Glc-AuNPs, 0.079 (±0.009) nm for Cef-AuNPs, and 0.118 (±0.007) nm for Cit-AuNPs (Figure 2), the corresponding d-spacing values from XRD are 0.24 nm, 0.20 nm, 0.14 nm, and 0.12 nm for the (111), (200), (220), and (311) planes of the FCC structure, respectively. Crystallite sizes reported in Table 3.2 were determined from the most intense XRD peak, corresponding to the (111) plane. The results of the three size measurements (particle sizes from TEM,

hydrodynamic sizes from DLS, and crystallite sizes from XRD) are compared in Table 3.2. Generally, the NPs are relatively small, with diameters ranging from 5.64 to 24.01 nm (Table 3.2). The size of the crystallites was determined using the Scherrer formula equation $D = \frac{K\lambda}{\beta Cos\Theta}$ In this equation, λ indicates the wavelength of the incoming X-ray beam (expressed in Angstroms-Å), K is Scherrer's constant, generally accepted as 0.9, β is the full width at half maximum (FWHM) of the peak, and θ represents the Bragg angle (Scherrer 1918, Debye and Scherrer 1917).
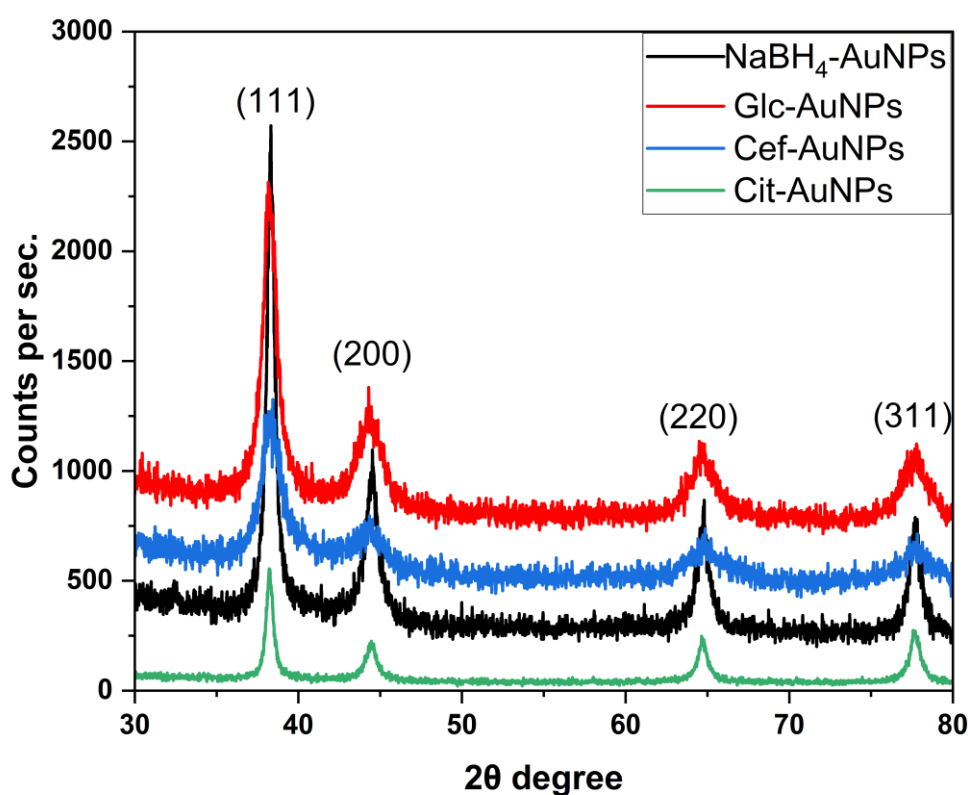
Figure 3.3: X-ray diffraction (XRD) patterns of gold nanoparticles (AuNPs) synthesized using different reducing agents. The samples include NaBH4-AuNPs (black), Glc-AuNPs (red), Cef-AuNPs (blue), and Cit-AuNPs (green), showing consistent crystalline structures across all synthesis methods.

3.4.5. Fourier Transform Infrared (FTIR) Analysis of Synthesized AuNPs

FTIR spectroscopy was performed to analyse the binding of the reducing and stabilizing agents on the surface of the synthesized Au NPs, showing the interaction between the particles and

the reducing agents. as shown in Figure 3.4A-D. Curves in Figure 4A represent the FTIR spectra of NaBH$_4$ compared to NaBH$_4$-reduced AuNPs. Typical borohydride split bands were observed between 2300 - 2200 cm^{-1}, 1430 – 1322 cm^{-1}, and 931 – 877 cm^{-1}; denoting B-H bond for borohydride, B-H bending, and the deformation of the BH band (Renaudin, et al. 2004). The designated peaks denoting BH$_4^-$ notably shifted to higher vibrations in the NaBH$_4$-reduced AuNPs.

Curves in Figure 3.4B present the FTIR spectra of glucose compared to Glc-AuNPs. The Glc-AuNPs show a strong absorption peak at 3268 cm^{-1} denoting the OH group. The presence of an O-H stretching band at 3268 cm^{-1} for Glc-AuNPs confirms that glucose is an essential component of the Glc-AuNPs (Suvarna, et al. 2017). Explanations have been given for the shift in the band from 3305 cm^{-1} in pure D-glucose to 3268 cm^{-1} in the Glc-AuNPs. According to Sylvestre, et al. (2004) and (Xu, Wu and Zhu 2008), the dominant high-frequency shift for D-glucose-stabilized NPs suggests the presence of intermolecular hydrogen bonding, whereas (Liu, et al. 2006)suggests that this represents an intimate association between the glucose molecule and the surface of the Au NPs (Xu, Wu and Zhu 2008). Other glucose peaks within 4000 – 500cm^{-1} were confirmed on the Glc-AuNPs.

Curves in Figure **3.**4C present the characteristic FTIR spectra of cefaclor compared to Cef-AuNPs. Cefaclor has characteristic peaks at 1768 cm^{-1} (C=O group of the four-membered ring lactams and the COOH functional group), 1691 cm^{-1} (C=O group), 1600 cm^{-1} (C-N primary amine), and 1510 cm^{-1} (C=C ring stretches), consistent with previous reports(Bouhedja, et al. 1997, Devi, Basha and Sailaja 2020). As a member of the β-lactam antibiotic family, cefaclor has characteristic β-lactam ring vibrations recorded at 1361, 1251, and 1172 cm^{-1}, as presented in**,** which aligns with the report by (Gil, et al. 2001). The Cef-AuNPs exhibit a distinct vibration at 1645 cm^{-1}**,** which can be assigned to an amine group, excited to a higher wavenumber compared to the primary amine of pure cefaclor (1605 cm^{-1}). Previous studies have linked this primary group of cefaclor with the reducing and capping role in the synthesis of Cef-AuNPs (Rai, Prabhune and Perry 2010). The consistent position of the β-lactam ring vibrations in pure and Cef-AuNPs implies that the functional component of cefaclor responsible for antimicrobial activities is present on the Cef-AuNPs surface, agreeing with (Rai, Prabhune and Perry 2010).

Curves in Figure **3.**4D present the characteristic FTIR spectra of sodium citrate compared to the Cit- AuNPs. Like sodium citrate at 1595 cm^{-1} and 1388 cm^{-1}, the Cit-AuNPs showed characteristic intense carboxylate peaks at 1637 cm^{-1}, corresponding to COO$^-$ symmetric

stretching, and a band at 1340 cm⁻¹ assigned to C–H stretching vibration. This indicates a slight shift in the COO⁻ symmetric stretching to a higher wavelength in the Cit-AuNPs compared to the ordinary sodium citrate. According to Max and Chapados (2004), the carboxylate group exhibits asymmetric and symmetric stretching vibrations around 1500–1630 and 1305–1415 cm⁻¹, respectively. The carboxylate band for pure citrate was observed at 1595 cm⁻¹, but there was a transition to 1637 cm⁻¹ in the Cit-Au NPs. This confirms the role of the carboxylate moiety in the chemical interactions that mediate the synthesis and stability of the Cit-AuNPs (Park and Shumaker-Parry 2014a).
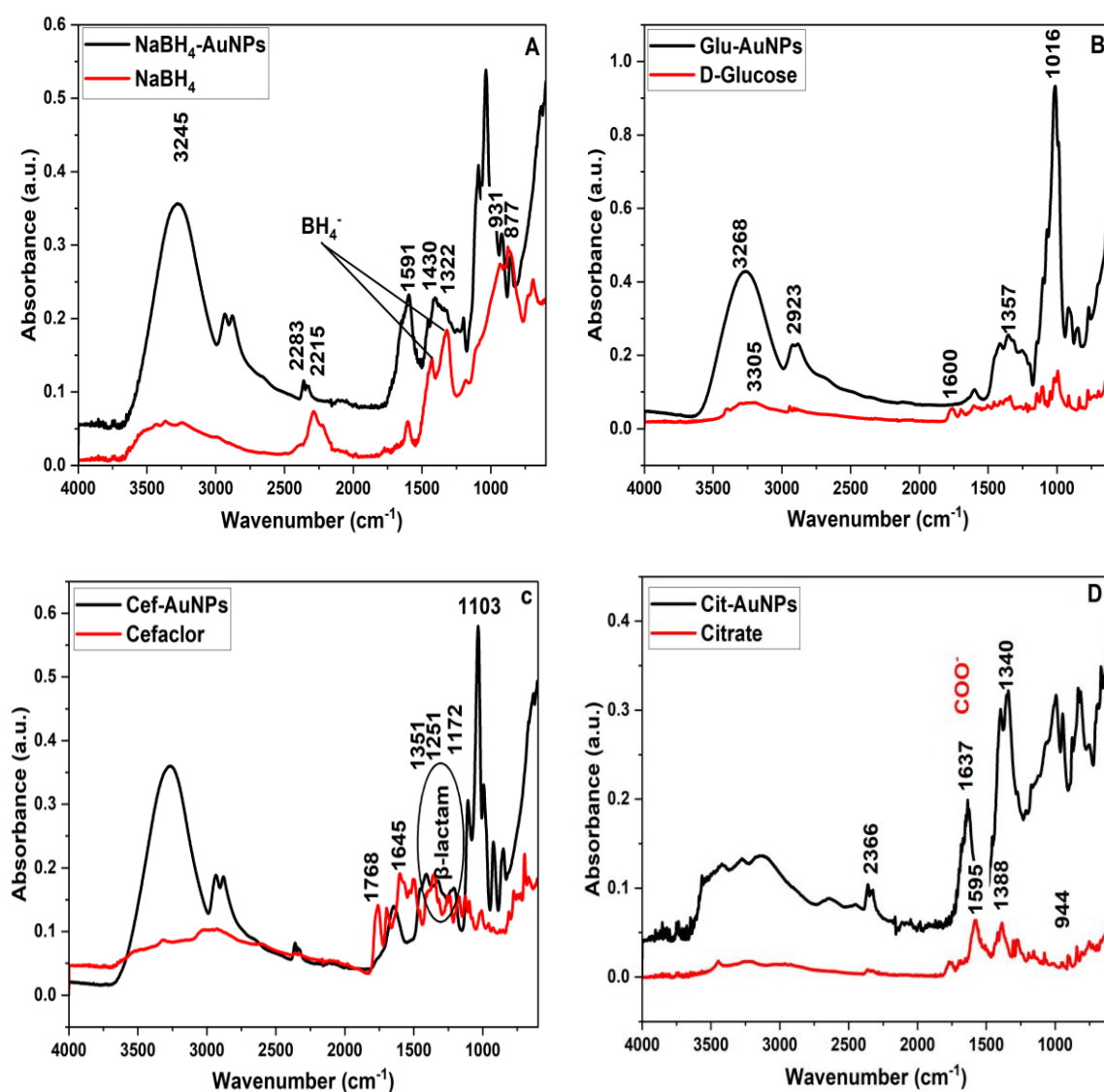
Figure 3.4. Fourier-transform infrared (FTIR) spectra of gold nanoparticles (AuNPs) synthesized using different reducing agents compared to their respective precursors. (A) NaBH₄-AuNPs vs. NaBH₄, (B) Glc-AuNPs vs. D-Glucose, (C) Cef-AuNPs vs. Cefaclor, (D) Cit-AuNPs vs. Citrate.

3.4.6. Thermogravimetric Analysis of Reducing and Stabilizing Agent Bound to Gold Nanoparticles

Quantitative information on the amount of the reducing and stabilizing agent bound to the Au NPs was determined using thermogravimetric analysis (TGA). Thermograms illustrating the weight changes (TGA), temperature differences (DTA), and heat flow (DSC) during the digestion of the capping agents are shown in Figure 5 below. Compared to other NP groups, citrate and $NaBH_4$-AuNPs exhibit greater thermostability, with distinct digestion regions. Each NP system is now discussed in detail.

Figures 3.5A represent the thermograms in air for $NaBH_4$ and $NaBH_4$-reduced AuNPs, respectively. $NaBH_4$ alone shows three distinct heat change regions, five distinct temperature change regions, and six regions of weight change (loss or gain). This is comparable to the $NaBH_4$-reduced AuNPs. The initial weight loss, denoted by *, between 70-100°C is believed to be due to the dehydration of the moisture content in the sample (Park and Shumaker-Parry 2014b). Between 150-330°C, there are four distinct regions of reactions, indicated by heat absorption and rapid pyrolysis of $NaBH_4$, leading to rapid weight losses. In the first 35-150°C, about 17.3% of the sample was digested, while a further 10.94%, 16.9%, and 6% of the sample were digested at 150-191°C, 220-225°C, and 279-330°C, respectively, with over 50.5% of the total sample already digested. These changes are suggested to be due to the rapid thermolysis of $NaBH_4$, forming byproducts such as sodium metaborate ($NaBO_2$) (Park and Shumaker-Parry 2014b). Interestingly, further heating between 350-500°C led to a weight gain of about 1.57%. This phenomenon is believed to be due to an exothermic effect from the oxidation of products (Park and Shumaker-Parry 2014b). Generally, there was delayed degradation of components and reduced mass loss in the $NaBH_4$-reduced AuNPs (Figure 1B) compared to ordinary $NaBH_4$. Additionally, the distinct effect leading to weight gain upon oxidation was not observed in the $NaBH_4$-reduced AuNPs. At 900 °C, borate constitutes about 51 % of the $NaBH_4$-reduced AuNPs.
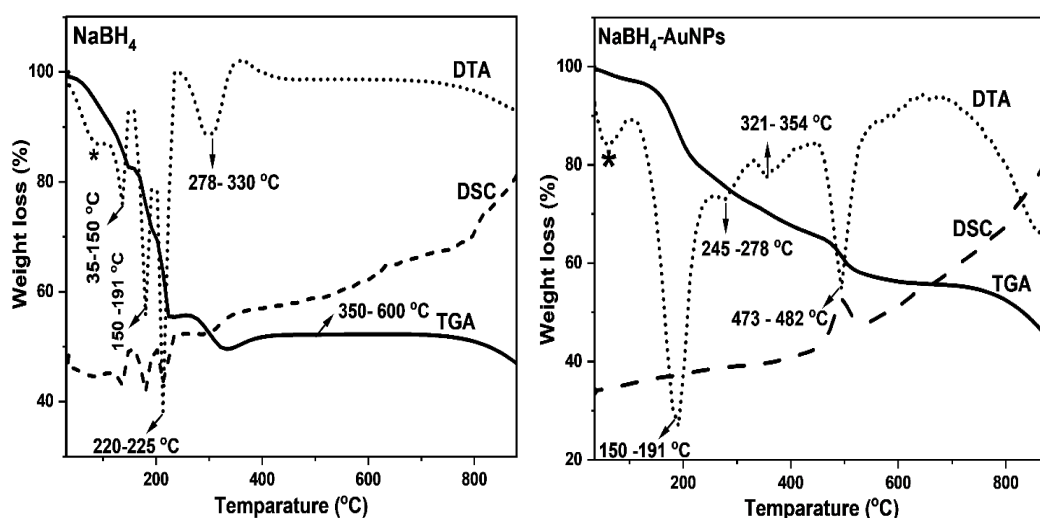
Figure 3.5A: Thermogravimetric analysis (TGA), differential scanning calorimetry (DSC), and differential thermal analysis (DTA) curves of NaBH₄ and NaBH₄-AuNPs. The left graph shows the weight loss percentage as a function of temperature for NaBH₄, while the right graph shows the same for NaBH₄-AuNPs.

For the Glc-AuNPs, the TGA curve is comparable to that of pure D-glucose (Figure 3.5B). The Glc-AuNPs exhibit three distinct regions of mass loss from room temperature to around 600°C . Stability was observed in the digestion of pure glucose up to 200°C, with no mass loss recorded. For the Glc-AuNPs, about 4% to 6% of the weight was lost, assumed to be due to the desorption of water from the surface of the NPs. Between 200°C and 355°C, the Glc-AuNPs show a rapid weight loss of up to 67% of the initial weight. (Farajollah, et al. 2021)recorded that the carbonation of glucose mainly occurs around 200-400°C, explaining the rapid weight loss observed within this temperature range. Further weight loss of the Glc-AuNPs continued until 600°C, when the core of the glucose on the surface of the Glc-AuNPs was suggested to have been digested (Guo, Finne-Wistrand and Albertsson 2010). At 600°C, the Glc-AuNPs have lost 90.6% of their initial weight, whereas the ordinary glucose has lost 99.7% of its initial weight. I calculated the glucose component to be 91.4% of the Glc-AuNPs.
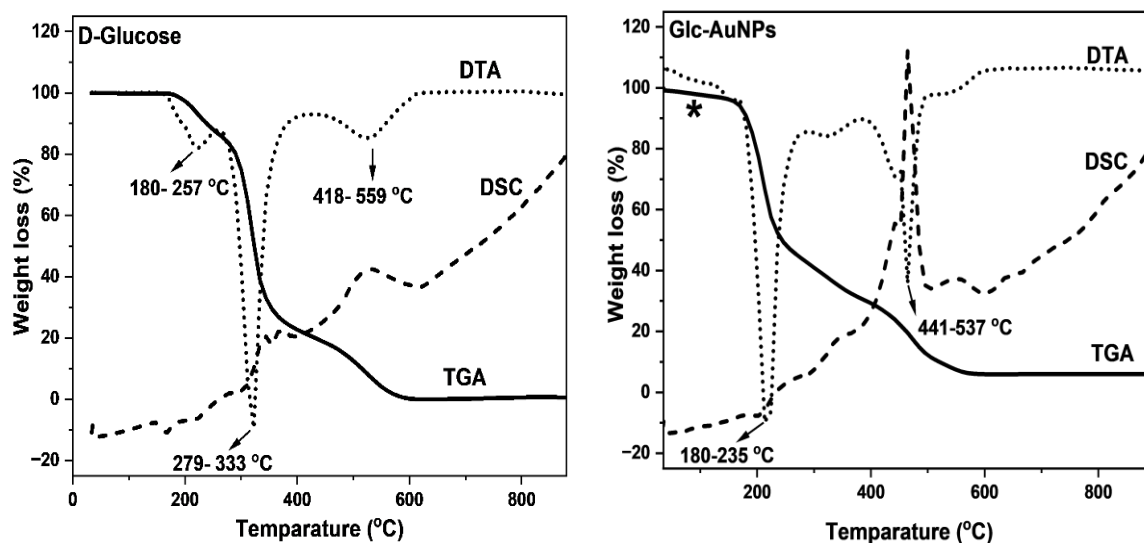
Figure 3.5B: Thermogravimetric analysis (TGA), differential scanning calorimetry (DSC), and differential thermal analysis (DTA) curves of glucose and Glc-AuNPs. The left graph shows the weight loss percentage as a function of temperature for Glucose, while the right graph shows the same for Glc-AuNPs.

Figure 3.5C represents the thermogram of this digestion between 0 – 900 °C. The initial 3% to 7% weight loss of the Cef-AuNPs observed within the region of 40-200 °C is due to the desorption of water molecules from the surface of the Cef-AuNPs. For pure cefaclor, a 100% weight loss was observed, but the digestion followed multiple distinct steps as shown in Figure 5C. The Cef-AuNPs exhibited an overall 27.2% weight loss in two distinct steps at 200-408°C and 408-670°C. This suggests that a substantial quantity of pure cefaclor was used in the reduction of gold ions and subsequent surface binding during and after synthesis (Rai, Prabhune and Perry 2010). The distinct regions of weight loss observed in the digestion of Cef-AuNPs have been described in previous studies and may indicate different modes of interaction between cefaclor and the AuNPs(Rai, Prabhune and Perry 2010, Bhattacharya, et al. 2007). The recorded weight loss within the low-temperature region (40-200 °C) has been linked to the desorption of water molecules and the physical adsorption of cefaclor on the surface of the Au NPs, mediated by the arrangement of bound cefaclor molecules (Nayak and Shin 2006). The second maximum weight loss observed at 200-408 °C is suggested to be due to the covalent interaction of the amine group with the Au NPs, requiring higher energy for the decomposition or desorption of the AuNPs-bound cefaclor molecule (Bhattacharya, et al. 2007). According to

Chen, et al. (2007) and Rai, Prabhune and Perry (2010), the third observable loss between 408-678 °C is most likely due to the electrostatic interaction of the AuNPs surface-bound amine group, donated by cefaclor, and the negatively charged gold chloride ($AuCl_4^-$) ions present on the nanoparticle surface. The observations from the TGA experiment are consistent with the FTIR results, where the bond stretches indicating the functional component of cefaclor were confirmed on the surface of the Cef-AuNPs. From TGA analyses, I estimated that cefaclor is 25% of the Cef-AuNPs.
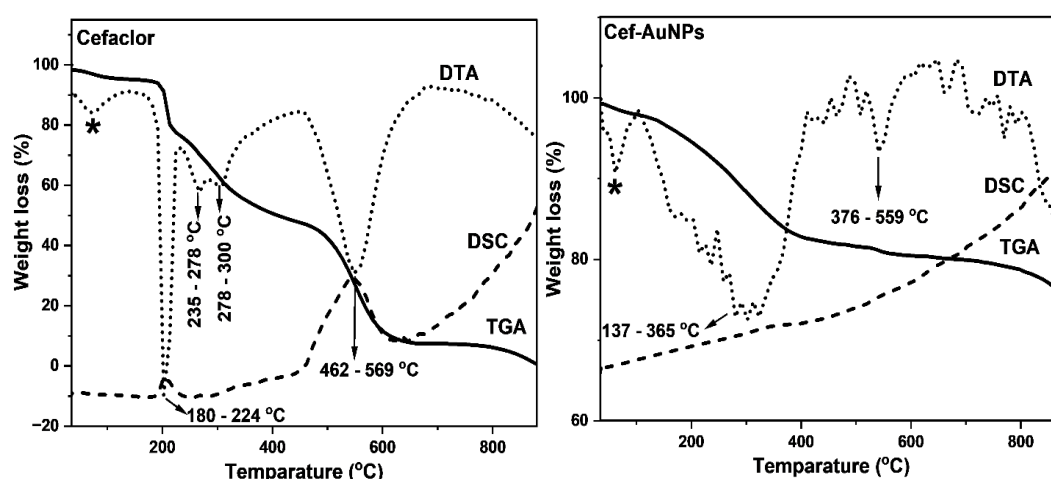
Figure 3.5C: Thermogravimetric analysis (TGA), differential scanning calorimetry (DSC), and differential thermal analysis (DTA) curves of cefaclor and Cef-AuNPs. The left graph shows the weight loss percentage as a function of temperature for cefaclor, while the right graph shows the same for Cef-AuNPs.

The thermograms for the pyrolysis of sodium citrate and citrate stabilized AuNPs in air between 0 - 900°C shown in Figure 5D, indicates weight loss at four distinct phases. An initial weight loss due to dehydration was observed around 100-200°C is due to dehydration (Gao, Wang and Hao 2012). Further thermal decomposition occurs at 310 – 332 °C and 494 °C, representing the partial breakdown of citric acid into smaller compounds and the release of gases like CO_2 and the complete breakdown of residue respectively (Marcilla, et al. 2018). A final process was noted around 797 °C, this indicates that oxygen significantly enhances the gasification of the carbonaceous residue (Marcilla, et al. 2018). Compared to ordinary sodium citrate, the pyrolysis of citrate-stabilized gold nanoparticles (AuNPs) exhibited similar digestion patterns but with less intense degradation at each stage. The digestion of these nanoparticles progressed through an endothermic process, whereas the digestion of ordinary citrate involved both endothermic and exothermic processes. These differences are likely due to the interaction

between the gold and the citrate on the nanoparticle surface, which stabilizes the nanoparticles. In total, only about 56% of the initial mass of sodium citrate trihydrate was burned at 900 °C, which indicates the presence of the organic component. My calculations show that sodium citrate constitutes approximately 46% of the Cit-AuNPs.
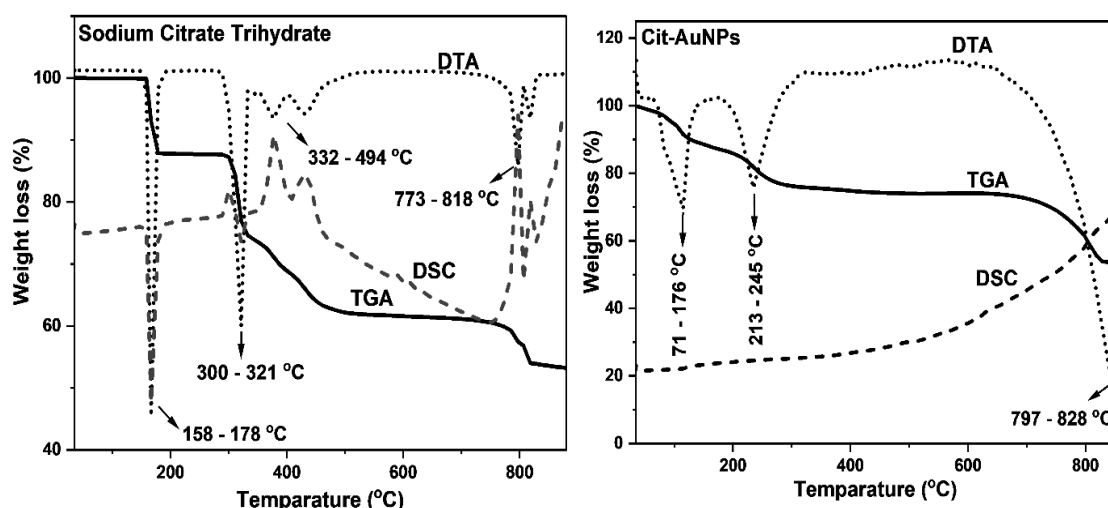
Figure 3.5D: Thermogravimetric analysis (TGA), differential scanning calorimetry (DSC), and differential thermal analysis (DTA) curves of citrate and Cit-AuNPs. The left graph shows the weight loss percentage as a function of temperature for Citrate, while the right graph shows the same for Cit-AuNPs.

3.4.7. Impact of Dialysis on the Stability and Size Distribution of Colloidal AuNPs Over 60 Days.

Figure 3.6 illustrates colloidal AuNPs size distribution changes over 60 days from synthesis. It was assumed that the AuNPs would retain their characteristic spherical shape, which is why the dynamic light scattering (DLS) method was chosen for size characterization. Purification through 14kDa membrane dialysis tubing was also performed for the NP groups, and the impact of this on size stability was monitored. The size distribution of the colloidal AuNPs solution at synthesis is presented in Table 3.2 and shown as Day 1 in Figure 3.6. Except for Cit-Au NPs, all dialyzed groups showed a noticeable increase in size compared to the reference samples after 24 h of dialysis. Generally, NPs have surface charges that promote gradual aggregation

through Van der Waals forces (Zare 2016). It can be suggested from this observation that consistent stirring during dialysis might contribute to the surface interaction of AuNPs. Further characterization by monitoring the size distribution by intensity and the polydispersity index (PI) over 60 days showed that aggregation progressed faster in the un-dialyzed samples. For example, within the first 60 days, the solution of the un-dialyzed Glc-AuNPs already had visible sediments that required agitation to dissolve. A size difference of about 15 and 25 nm was recorded between the dialyzed and un-dialyzed groups of NaBH$_4$-AuNPs and Cef-AuNPs, respectively. This highlights the significant importance of the dialysis purification process as an essential phase that promotes nanoparticle stability. NPs for future works were stored at low temperatures (8 ^{o}C) in clean, dark containers to prevent aggregation and degradation (Velgosova, et al. 2024).
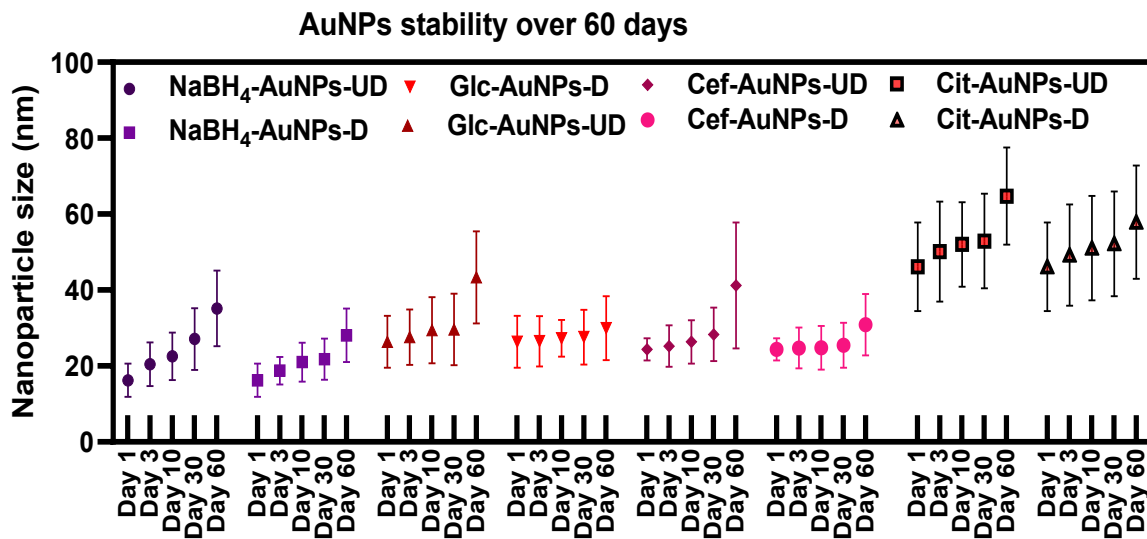
Figure 6: Dynamic light scattering (DLS) analysis of gold nanoparticles (AuNPs) stability over 60 days under purified (D) and unpurified (UD) conditions. NaBH$_4$-AuNPs-UD (purple circles), NaBH$_4$-AuNPs-D (purple squares), Glc-AuNPs-UD (red downward triangles), Glc-AuNPs-D (red upward triangles), Cef-AuNPs-UD (pink diamonds), Cef-AuNPs-D (pink circles), Cit-AuNPs-UD (black squares with red outline), and Cit-AuNPs-D (black triangles) The level of significance * (p $\leq$ 0.05), ** (p $\leq$ 0.01), and *** (P $\leq$ 0.001).

3.4.8. Cell Viability Assessment Using MTT Assay on HaCaT and HEK 293 Cells

In this research, surface-functionalized gold nanoparticles (AuNPs) were utilized to create composite nanoparticle-mycelia microstructures. One intended application is to use the functionalized mycelia as reusable heavy metal chelators for wastewater purification (biofiltration). This approach takes advantage of the chemical properties of coated AuNPs to

form complexes with heavy metals (He, et al. 2020). The application also reveals potential human exposure routes, specifically through the skin and kidneys, along with the types of cells that may be affected, namely epithelial and renal cells, for toxicity assessment. Human immortalized keratinocytes (HaCat) and embryonic kidney 293 (HEK 293) cells were chosen for this study because they represent significant avenues for potential exposure or uptake of nanoparticles in humans. HaCat cells, being major components of the epidermis, are used to evaluate the effects of exposing the skin to bioactive nanoparticles (Kundu, et al. 2018). In the case of AuNP-treated water samples, the kidney pathway serves as a crucial route for ultrafiltration, and HEK 293 cells are utilized for cytotoxicity assessment along this pathway (Tlotleng, et al. 2016).

An in vitro toxicity evaluation was conducted on HaCaT and HEK 293 cells using an MTT assay. The cells were treated with $NaBH_4$-AuNPs, Glc-AuNPs, Cef-AuNPs, and Cit-AuNPs at concentrations ranging from 0.1 to 40 µg/ mL for 24 h. The results, shown in Figures 3.7A and 3.7B, indicated significant effects on cell viability that varied between the two cell types. For HaCaT cells, increasing the concentration of AuNPs, particularly at the maximum concentration of 40 µg/ mL, notably affected cell viability. This effect was most pronounced with Cit-AuNPs, where cell viability decreased to 67.15% after 24 h at this highest concentration (far above the concentrations later used in applications). In contrast, HaCaT cells exhibited less sensitivity to Cef-AuNPs, a broad-spectrum beta-lactam antibiotic, up to a concentration of 15 µg/ mL (Rai, Prabhune and Perry 2010). The effects of AuNPs on HaCaT cells have been well documented, demonstrating dose-dependent cytotoxic effects. (Vechia, et al. 2020). For instance, (Lu, et al. 2017) demonstrated that HaCaT cells could be sensitive to AuNPs at concentrations as low as 10 µg/ mL, with sensitivity also being size-dependent (Lu, et al. 2017, Coradeghini, et al. 2013). The survival rate of HaCaT cells is likely to be significantly reduced by very small nanoparticles (1-3 nm), while larger nanoparticles (10-15 nm) may have a lesser impact. Additionally, Cit-AuNPs around 30 nm have been shown to elicit cytotoxicity in non-cancerous cells at concentrations above 8.5 µg/ mL (Vechia, et al. 2020). These findings are consistent with the observations from this study where NP size is between 5-30 nm.

For cytotoxicity assessment on HEK 293 cells, a different phenomenon was observed within the same timeframe of AuNPs administration under the same conditions. With increasing AuNPs concentration, cell proliferation significantly increased, particularly with $NaBH_4$-AuNPs and Glc-AuNPs (Figure 3.7B). Initially at lower doses (0.1-10 µg/ mL) for Cit and Cef

AuNPs, there was a progressive decline in viability, which halted, then proliferation set in with further increased concentration. Previous reports have documented the cytotoxic effects of AuNPs on HEK 293 cells. For example, (Tlotleng, et al. 2016) showed that Cit-AuNPs induced significant toxicity on HEK 293 cells even at 0.1 µg/ mL. In this study, I also observed a progressive drop in cell viability between 0.1-1.0 µg/ mL, but it was not significant at the experiment's termination. Notably, my experiment lasted 24 h, while the referenced study lasted 52 h. Additionally, (Pardhiya, Priyadarshini and Rajamani 2020) observed no significant changes at 50 µg/ mL in their study on the cytotoxicity of MnO_2 NPs on HEK 293 cells, but after 72 h, there was a significant increase in cell proliferation, suggesting that NPs acted as antioxidants, which created a favorable environment for cell proliferation. I suggest that this could be a possible explanation for the observed proliferation since the stabilizing materials are mostly good reducing agents. Sodium borohydride ($NaBH_4$) is a strong reducing agent capable of donating hydride ions (H^-) to reactive oxygen species (ROS) such as superoxide and hydrogen peroxide, converting them into water and oxygen (Kawamoto and Ryu 2014). This process reduces oxidative stress and enhances cell viability (Perillo, et al. 2020). Similarly, glucose has a significant reducing potential and effectively scavenges ROS, thereby lowering their production (Braissant, et al. 2020). Citrate is unique in its ability to modulate enzymes involved in oxidative stress management, leading to the depletion of ROS or free radicals (Machi, Ono and Iwahashi 2024). The toxicity index and sensitivity to gold nanoparticles (AuNPs) vary between HaCaT and HEK 293 cells within the tested concentration range. Although previous studies have shown that these cells can exhibit comparable tolerance levels to test compounds, their differences in cellular origin and function affect their nanoparticle uptake, processing, susceptibility to oxidative changes, and regulatory mechanisms (Kwon, Y., et al. 2022). A previous study comparing the cytotoxic effects of AuNPs on various cell types yielded results consistent with my findings. The authors reported dose-dependent toxicity in HaCaT cells, while HEK 293 cells exhibited no significant toxicity, aside from changes in gene expression (Niżnik, et al. 2024).

I infer from this study that the NP groups are suitable for use if their overall concentration on the mycelia is less than the concentration at which any significant effect was observed.
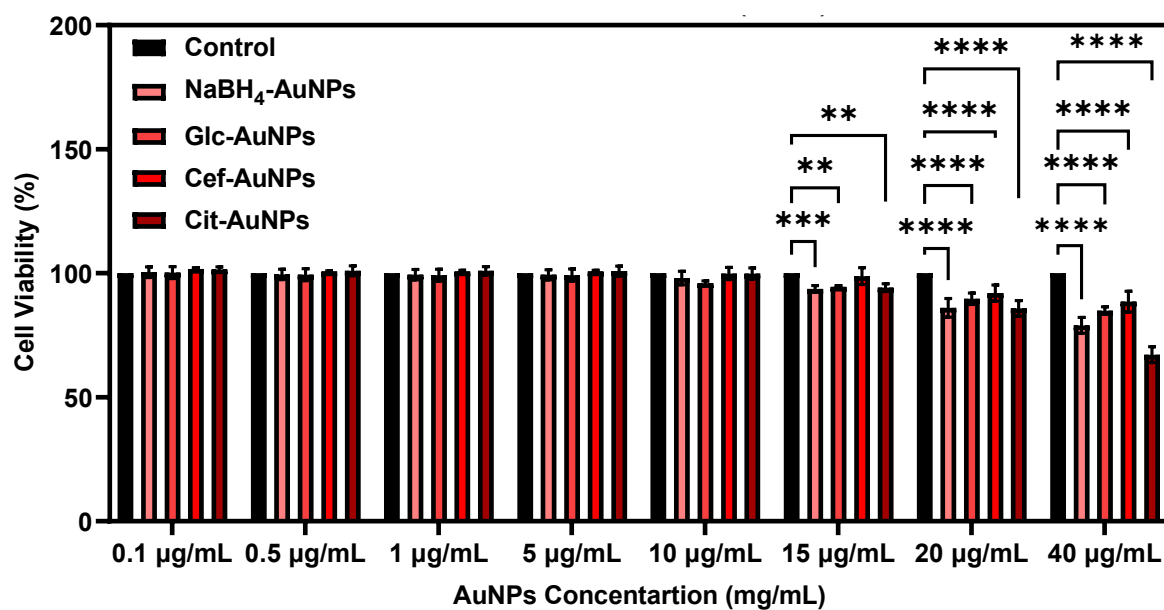
Figure 3.7A: *In vitro* toxicity evaluation of surface-functionalized gold nanoparticles on human immortalized keratinocyte (HaCaT). The level of significance * (p ≤ 0.05), ** (p ≤ 0.01), and *** (P ≤ 0.001).
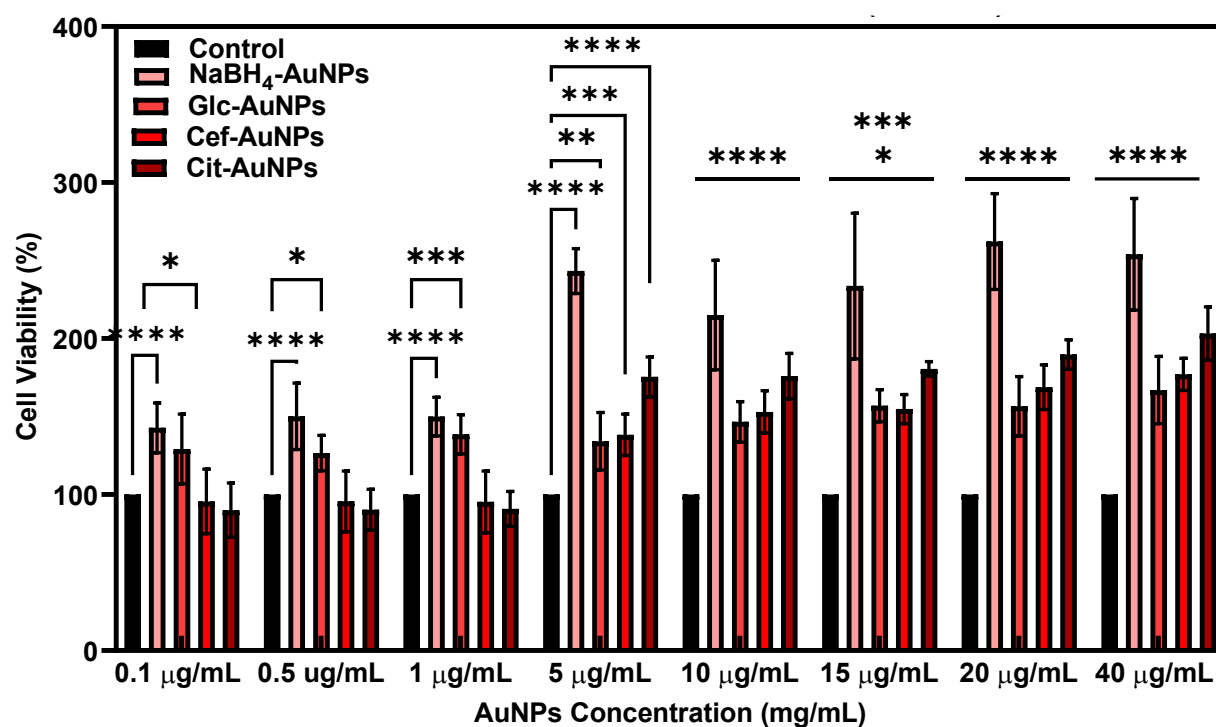
Figure 3.7B: In vitro toxicity evaluation of surface-functionalized gold nanoparticles on human embryonic kidney (HEK) 293 cells. The level of significance * (p ≤ 0.05), ** (p ≤ 0.01), and *** (P ≤ 0.001).

3.4.9. Colorimetric Sensing of Mercury with Surface Functionalized AuNPs

The sensitivity of surface-functionalized gold nanoparticles (AuNPs) to mercury (Hg^{2+}) was assessed using UV-spectrophotometry within the concentration range of 1–50 µM. The AuNPs were dispersed in a phosphate buffer solution at a pH of 7.4. The samples were thoroughly mixed using gentle stirring before measurements. This was done to establish the potential for the AuNPs to interact with Hg, understand the nature of these interactions, and determine the detection limits. Hg^{2+} was selected due to its global importance in environmental bioremediation, given its very toxic effects even at low concentrations (World Health Organization 2017, Zulkifli, Rahim and Lau 2018).

The sensitivity of surface-functionalized gold nanoparticles (AuNPs) to mercury (Hg^{2+}) was assessed using UV-spectrophotometry within the concentration range of 1–50 µM. This was done to establish the potential for the AuNPs to interact with Hg, understand the nature of these interactions, and determine the detection limits. Hg^{2+} was selected due to its global importance in environmental bioremediation, given its very toxic effects even at low concentrations (World Health Organization 2017, Zulkifli, Rahim and Lau 2018). The results revealed rapid detection of Hg^{2+} (within 5 s) by the AuNPs, as shown by changes in surface plasmon resonance (SPR) properties in unique patterns that related to the surface functionalisation (Figure 3.8A-D). Notably, each type of AuNP exhibited a distinct response. Among all the groups studied, glucose-stabilized gold nanoparticles (Glc-AuNPs) and sodium borohydride-reduced gold nanoparticles ($NaBH_4$-AuNPs) were the most sensitive, detecting mercury ions ($Hg^{2+)}$ at concentrations as low as 5 µM. The Glc-AuNPs demonstrated a structural shift of the initial peak at 535 nm and a subsequent regeneration at 691 nm, while the $NaBH_4$-reduced AuNPs exhibited a broad shift in absorption from 524 nm to 605 nm. These chemical differences and varying sensitivities highlight the potential of AuNPs, especially those derived from glucose and $NaBH_4$, for environmental Hg^{2+} monitoring. For Cef-AuNPs, the detection limit was 20 µM, but the band position (528 nm) did not shift with increasing SPR absorption correlating to Hg^{2+} concentration. Cit-AuNPs were sensitive down to 10 µM, but contrary to Cef-AuNPs, the absorption band decreased with increasing Hg concentration at the SPR (544 nm) without significant band shifts.

Many gold nanoparticle (AuNP)-based sensors display visible colour changes that result from nanoparticle aggregation or size alterations. For examples like $NaBH_4$-AuNPs, Glc-AuNPs, and Cit-AuNPs, the solution transitioned from brick red to purple. In contrast, Cef-AuNPs appeared slightly pink compared to the original brick red colour. These colour changes are

consistent with nanoparticle aggregation induced by the binding of metal ions (Lou, et al. 2012). My results showed high sensitivity to Hg^{2+} by the AuNPs and unique detection patterns for each type, indicating how the surface characteristics of nanomaterials influence their chemical reactions. The shift in SPR peaks is indicative of changes in the local dielectric environment and surface electron density, as documented by Nanda(Nanda, et al. 2024). The binding of Hg^{2+} to surface-functionalized groups likely causes aggregation or changes in nanoparticle morphology, leading to observable shifts in absorption (Nanda, et al. 2024). These findings demonstrate the chemical specificity of gold nanoparticles (AuNPs) for detecting mercury ions (Hg^{2+}). Additionally, they highlight the potential for customizing surface functionalization to enable rapid, visible, and sensitive mercury monitoring. Future studies could focus on improving detection times and colour changes to make these methods suitable for field applications.
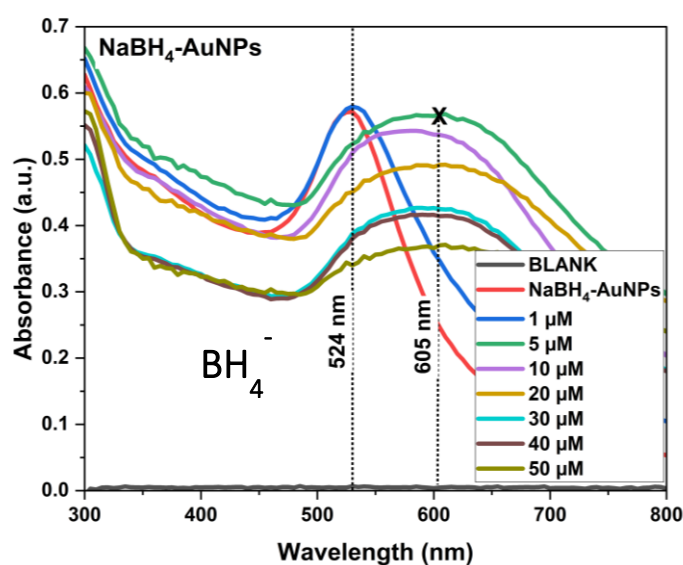
Figure 3.8A: UV-Vis spectroscopy of NaBH$_4$ reduced AuNPs on interacting with mercury at different concentrations.
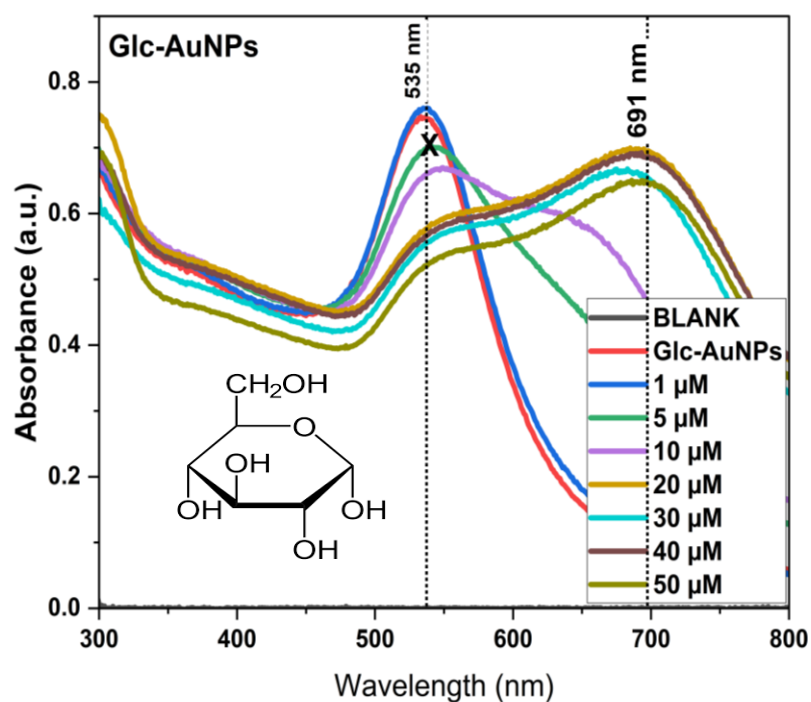
Figure 3.8B: UV-Vis spectroscopy of Glucose reduced Glc-AuNPs on interacting with mercury at different concentrations.
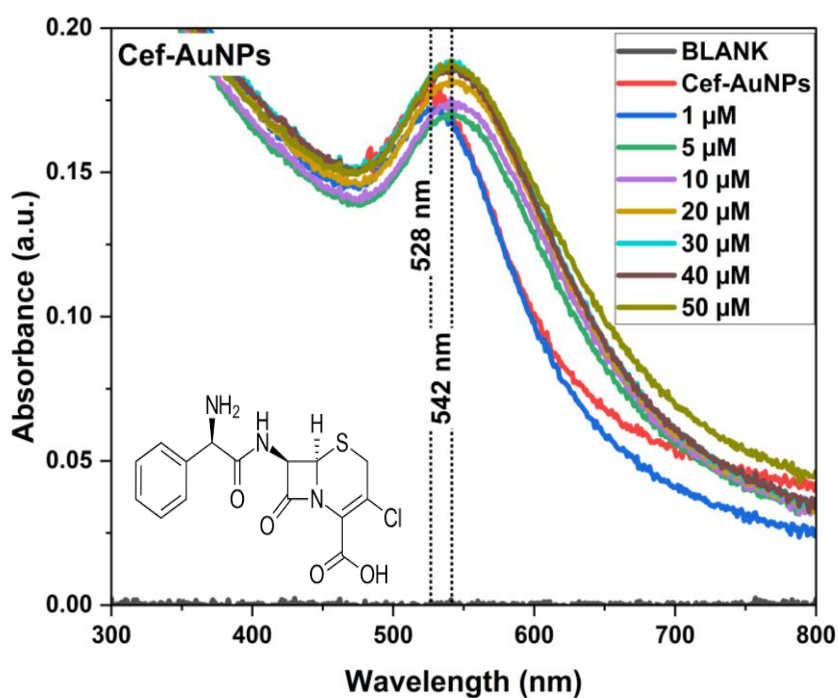
Figure 3.8C: UV-Vis spectroscopy of Cefaclor reduced Cef-AuNPs on interacting with mercury at different concentrations.
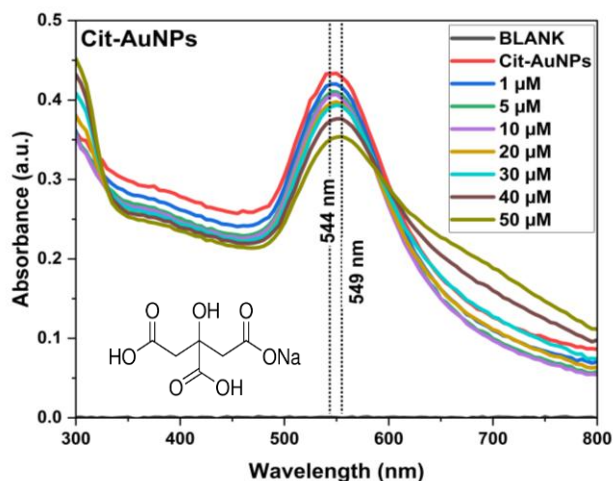
Figure 3.8D: UV-Vis spectroscopy of Citrate reduced Cit-AuNPs on interacting with mercury at different concentrations.

3.4.10 Conclusion

This chapter focuses on the synthesis and detailed characterization of gold nanoparticles (AuNPs) modified by four different agents: sodium borohydride, glucose, cefaclor, and sodium citrate. The primarily spherical nanoparticles, which are under 100 nm in size, were characterized using various techniques, including Transmission Electron Microscopy (TEM), X-ray diffraction (XRD), Fourier Transform Infrared Spectroscopy (FTIR), and UV-visible spectroscopy. These analyses confirmed the crystalline nature of the gold and the well-defined properties of the nanoparticle surfaces. The nanoparticles demonstrated excellent characteristics that are particularly beneficial for environmental applications, such as mercury detection, where rapid and sensitive colorimetric responses were observed. Regarding biological interactions, toxicity assays conducted with HaCaT and HEK 293 cells indicated that the AuNPs were generally non-toxic, causing only a minimal negative impact on cell viability, particularly at their synthesis concentrations which are far above the concentration of use. This low toxicity, combined with excellent stability in solution over 30 days, highlights the potential of AuNPs for biological applications. Their ability to maintain structural stability and functionality under various conditions makes them ideal candidates for environmental remediation efforts, especially in composite biofilters designed to efficiently capture heavy metals like mercury. These findings showcase the versatility, stability, and safety of the nanoparticles in both biological and environmental contexts.

CHAPTER 4

4.0 Engineering Gold Nanoparticle-Integrated Fungal Microstructures: A Novel Reusable Biofilter for the Bioremediation of Mercury.

In this chapter, I report that *Aspergillus niger* can form a living template for gold nanoparticle (AuNPs) functionalization in situ using four different categories of AuNPs with chemically distinct surfaces. The synthesis and characteristics of these NPs (physicochemical, surface properties, and morphology) were reported in detail in the previous chapter. The findings from these experiments illustrate the significant influence of varying concentrations of gold nanoparticles (AuNPs) on the formation of a composite material with the mycelium of *A. niger*. Notably, optimal results were observed at a concentration of 30 µg/ mL of AuNPs. Depending on the surface coat of the NPs, their chemistry affects the levels to which they are associated with the mycelium. I also replaced the nitrogen source of the fungus (sodium nitrate) with glutamine and investigated its effect on AuNP binding to the mycelia using inductively coupled plasma mass spectrometry (ICPMS). The fungus preferred sodium nitrate for some AuNP surface functionalization, but glutamine for both growth and AuNP functionalization in more groups, implying that nitrate-based nitrogen seemed to favour AuNP binding, while glutamine resulted in higher material yields. Physiological characterization also showed interesting outcomes. It was revealed that functionalizing *A. niger* with AuNPs significantly influenced fungal sporulation, regardless of the nitrogen source. Scanning electron microscopy (SEM) and energy-dispersive X-ray spectroscopy (EDX) revealed well-distributed NPs on the mycelia, with notable differences in the distribution site of the AuNPs on the mycelia or patterns across the NPs-Mycelia according to the surface functionalisation of the gold NPs. Gold peaks were observed from spot and map scanning of these particles, indicating that they were indeed AuNPs. As reported in the previous chapter, the AuNPs on their own exhibited remarkable sensitivity to mercury, detecting it within 5 s at concentrations as low as 5 µM. I leveraged these unique properties and repurposed mycelia-AuNP composites for eco-friendly heavy metal (mercury) filtration. Interestingly, the mycelia-based composite, whether grown in nitrate or glutamine, proved to be an efficient reusable heavy metal filter, significantly removing mercury below the World Health Organization (WHO) 2 ppb maximum allowable concentration. Remarkably, the mycelia alone outperformed conventional industrial filters and can be used up to five times before losing efficiency or requiring replacement. Interestingly, though repeated runs may be required, the filtered mercury bonded to the mycelia can also be

collected to be reused via a non-intrusive natural system using ddH$_2$O at pH 8.0. Though the two groups of filters (either from nitrate or glutamine as a nitrogen source) were effective, they also exhibited different surface chemistries (wettability and surface-free energies) offering insight into the differences in their level of efficacy. This study underscores the potential of *A. niger* mycelia and AuNPs for sustainable environmental applications. I offer new insights into the utilization of mycelia-based materials in innovative applications, advancing from detection to removal of heavy metals, and contribute to new knowledge of species-specific fungal-gold interactions, showing the possibility of this in a new species.

Keywords: *A. niger,* Mycelia-based composite, gold nanoparticles (AuNPs), Nitrate, Glutamine, Mercury detection, Heavy metal filtration
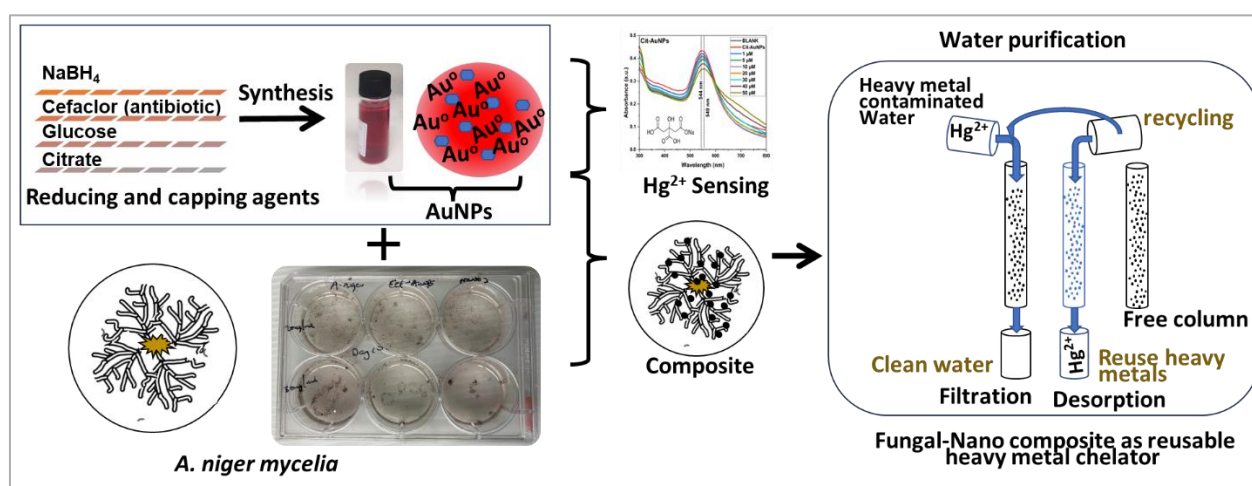
Graphical Abstract

4.1. Introduction

Environmental monitoring for the detection and removal of contaminants plays a crucial role in the safety of humans and the general ecosystem (Zulkifli, Rahim and Lau 2018). Common environmental toxicants include chemical contaminants such as heavy metals (e.g lead (Pb), mercury (Hg), cadmium (Cd), chromium (Cr), etc.), pesticides (e.g. organophosphates, carbamates, triazines, etc), oil and exploration and mining residues, and antimicrobial resistant organisms/genetic (ARGs) materials (Alengebawy, et al. 2021). Many of these are discharged as effluents or wastes and washed into water bodies, which may end up in general circulation or large aquifers (Parida, et al. 2022). Chemical contaminants such as Hg^{2+} could be very toxic even at low concentrations slightly above their minimum acceptable limits of 2 ppb, this

remains a modern environmental and public health threat that should be managed efficiently (Zaynab, et al. 2022). Nanomaterials have been used as novel sensors to detect chemical contaminants in the environment, leveraging on the possibility of transition in optical properties and selective detection (Wang, et al. 2010). They have been used in remediating environmental pollutants including total petroleum hydrocarbons (Roy, et al. 2021) from wastewater because they offer very high surfaces which contaminants could be adsorbed for subsequent degradation (de Araujo Scharnberg and Ravanello 2022). The chemistry of metal-based nanoparticles (NPs) shows that some have heavy metal adsorption potentials (Wawata and Fabiyi 2024) leading to my hypothesis that they can serve as novel filters for metals like Hg^{2+} in wastewater when assembled within a matrix that holds them together. In 2019, a natural phenomenon reported in Australia inspired new insights into how this matrix could be formed sustainably, ultimately yielding a biodegradable composite nanostructure for biofiltration. Briefly, the fungus *Fusarium oxysporum* was discovered to naturally accumulate gold on its surface within its ecosystem, demonstrating excellent gold biogeochemistry. This prompted researchers to argue the existence of redox interactions between natural gold and fungi, focusing on the biogeochemical cycle of gold (Bohu, et al. 2019). While some researchers have tailored this study as an innovative system to track gold ores leveraging the fungal affinity for gold, I focused on mimicking this system in the lab to form a novel composite. However, this comes with challenges. First, the natural gold reported in this study is chemically inactive and therefore cannot be used in applications where bioactivity is required (e.g., heavy metal filtration via metal adsorption). Another challenge is that the global utilization and scalability of this system in biofiltration could be limited if this phenomenon is only applicable to *F. oxysporum*, hence the need to try other genera. My hypothesis is that a biomimetic system where *F. oxysporum* is replaced by *A. niger*, and the natural gold is replaced by gold nanoparticles, would yield similar outcomes but with improvements. In this system, the fungal structure forms the matrix, the gold nanoparticles provide bioactivity, and the entire structure is deployed as a reusable mercury filter in wastewater treatment. No coupling agents will be used to retain the natural system being mimicked. *Aspergillus* is a fungus of choice because existing studies have shown that its ecological functions are also guided by metabolites, some of which are also found in *F. oxysporum* (Yu, et al. 2021). By leveraging a biomimetic approach to develop fungal-templated gold nanoparticle-mycelia composite microstructures for environmental applications (biofiltration), I intend to contribute to sustainable environmental bioremediation, innovative use of fungal materials, and novelty in applied mycology. My goal is to establish the different responses with different gold nanoparticles having different surfaces.

I will also document physiological changes or fungal responses observed during the growth process under different concentrations of gold nanoparticles and nitrogen sources (nitrate or glutamine). From the previous chapter, I have documented the sensitivity of gold nanoparticles with different surfaces to mercury. Biofiltration will be a further step that takes the system beyond detection to removal, creating a balanced monitoring system suitable for any economy globally. This chapter addresses Objective 4 by developing and evaluating bioinspired nanoparticle–fungal composites using *A. niger* for mercury removal from wastewater.

4.2. Materials and Methods

4.2.1. Materials

A. niger (ATCC 1015) was sourced from Dr. Matthias Brock of the University of Nottingham, United Kingdom. NPs were lab-synthesized, and their properties were reported in the previous chapter. Sodium nitrate (7631-99-4), and glutamine (56-85-9), were sourced from Sigma-Aldrich UK. All chemicals were prepared as per the manufacturer's instructions as aligned with my methods.

4.2.2. Methods

4.2.2.1 Fungal Culture Condition

The *A. niger* used in this study was sub-cultured on a slant of potato dextrose agar (PDA) and incubated (Labnet international 211DS Shaking Incubator; Appleton Woods Ltd., Birmingham, UK) at 25 °C. The newly grown fungi were then stored as a mother culture at 4 °C (Lec Freestanding Lab Refrigerator, G334M.02L). For subsequent experiments, spores were harvested from the fungus after 3-5 days of growing it on PDA. Once washed using phosphate-buffered saline (PBS), the number of spores is determined from a hemocytometer (NanoEntek C-Chip disposable) to prepare the desired concentration of spores.

4.2.2.2. Gold Nanoparticle Deposition on Fungal Mycelium

To evaluate the incorporation of AuNPs by *A. niger,* the method previously tested via preliminary evaluation (at 22 and 41 µg/ mL of the AuNPs; randomly selected) was adopted with slight modifications (concentration change). The experiment was conducted in a 12-well plate (Eppendorf Cell Culture Plate 24-Well TC) with Hutner's minimal medium (containing 5 mM of KCl, KH_2PO_4, and K_2HPO_4, 2 mM $MgSO_4$, adjusted to pH 7.0). It was supplemented with a trace element solution, 1% (w/v) glucose as the carbon source, and 10 mM glutamine or sodium nitrate as the nitrogen source. The AuNPs were tested at two concentrations (20 and 30

µg/ mL) of sodium borohydride (NaBH$_4$-AuNPs), glucose-AuNPs (Glu-AuNPs), citrate-AuNPs (Cit-AuNPs), and cefaclor-AuNPs (Cef-AuNPs). The concentration (µg/ mL) for each of the NPs was calculated based on the gold content. The medium composition for group A consisted of 750 µL of the AuNPs (30 µg/ mL) and 200 µL of minimal medium with 10% glucose. Group B consisted of 460 µL of the AuNPs (20 µg/ mL) and 446 µL of minimal medium with 10% glucose as the nutrient source. The control comprised 900 µL of minimal medium and 100 µL of 10% glucose. Fungal inoculation was done by introducing a specific number of spores (10^6/ ml) into each well. The growth at 25°C lasted for either 7 or 10 days (to study the effect of time) before the mycelium was harvested, washed, and dried for further analysis. All experiments were carried out in triplicate.

4.2.2.3. Preparing the AuNPs- Mycelia Composite Sample for Analyses

To prepare the harvested mycelia for analysis, exactly 50 mg (Sartorius CPA2245) of fresh mycelium from each group was harvested and washed three times to remove non-bound AuNPs. The washing process was conducted in a 2 mL centrifuge tube for each wash. Exactly 1 mL of ddH$_2$O was added and hand-shaken (vigorous agitation) 10 times. This was centrifuged (Eppendorf AG 22331 Mini Spin) at 13,000 rpm for 3 min. The wash liquid was kept after each wash for further analysis. The washing process was repeated three times using the pellet obtained from the previous wash, yielding the first three samples per group (wash 1, wash 2, and wash 3). Another 0.05 g of the samples was also prepared without any washing and kept as the fourth sample from each group. The samples were then dried in a VirTis Freeze Drier 7.0L DBTEL after the equipment was built up to -64°C. Upon drying, the final weight of the dried samples was recorded.

4.2.2.4. Evaluation of Au NPs Incorporation into Fungal Mycelia by SEM/EDX

To determine if the Au NPs were incorporated and firmly bound on the dried mycelium of *A. niger,* A JEOL Scanning electron microscope (JEOL JEM-2100Plus) with a guaranteed resolution for secondary electron imaging (SEI) of 1.2 nm (30 kV) was used for high-resolution high surface mapping and imaging. Imaging was done at a working distance of 10 µm, accelerating voltages 5-20 kV, and probe current of 9-12 nA (depending on the composite interaction with the electron beam which led to charging effects). An EDS detector (Oxford X-Max^n EDS with 80 mm^2 window) was attached to the SEM and was employed in the morphological and elemental characterization of the mycelium as initially described above.

The SEM equipment used a field emission gun with a tungsten filament. Before SEM analysis, the Au NPs bound A. *niger* mycelium samples were carbon coated through a controlled pulse cord 10 nm using a Quorum Q150R ES Sputter Coater. Imaging was done at the highest possible magnification, where samples were not burnt by the electron beam (being biological samples with high electron interaction because of AuNPs surfaces). Complementarily, Infrared spectroscopy of the mycelial-AuNPs composite (NICOLET iS50 FT-IR) in comparison to the ordinary mycelia and Au NPs was obtained to ascertain the incorporation of the NPs.

4.2.2.5. Gold Concentration on Mycelium using ICPMS.

To support the obtained results, ICP-MS Spectroscopy which measured gold concentration in the samples was done (NexION 100 ICP Mass Spectrophotometer). Exactly 0.001g of the freeze-dried samples (Washed and unwashed), for each AuNPs and control group were digested for 8 h in 1 mL aqua regia (3 HCl: 1 HNO_3). Standard gold (Honeywell Fluka™) samples from 0.01 – 1.0 ppm were also prepared using 2 % HNO_3 for the dilution. The final dilution of the samples was 10^{-3} of the original concentration.

4.2.2.6. Physiological Studies of *A. niger* Under the Effect of AuNPs.

The study of physiological changes via sporulation was conducted using a hemacytometer (NanoEntek C-Chip disposable) and performed in triplicates. Mycelia were collected under each treatment condition and control, then centrifuged to collect the spores (Eppendorf AG 22331 Mini Spin). The spores were counted to determine the average number produced by the fungus under the different AuNPs treatment conditions.

4.2.2.7. Biofiltration of Mercury using AuNPs-Mycelia Composite Microstructure

The filtration column is a Pierce™ Centrifuge Column (Thermo-Scientific) with a polyethylene filter and pore size of 30 µM. A measured volume of 1 mL of 5 ppb of the Hg^{2+} (prepared using laboratory standard mercury 1g/1000 mL from Sigma -Aldrich: Pcode-101740455), was added to 0.01 g of the AuNP-Mycelia composite in the tube. The solution was infiltrated with the composite 30 min before centrifugation. The system was then centrifugated at 5000 rpm for 3 min. The filtrate was collected in a 2 mL centrifuge tube (Safeseal Microtube from SARSTEDT). This was digested in aqua regia (as described in 4.2.2.5), and the Au remaining was measured by ICPMS.

4.2.2.8. Testing Reusability of the AuNPs-Mycelia Biofilters

The reusability of the AuNPs-Mycelia composite was evaluated using ICP-MS analysis (NexION 100 ICP Mass Spectrophotometer). An experimental concentration of 5 ppb of

mercury in DDH$_2$O was prepared, and 1000 μL of this solution was run across 0.01 g of the composite five times. Each sample was collected via centrifugation after 30 min of interaction with the composite in a tube. To determine the effectiveness of mercury removal, the collected mercury solutions were diluted to 10 mL for ICP-MS analysis. Similarly, to assess if the attached mercury ions could be washed off the mycelia, DDH$_2$O at pH 8.0 was prepared (Jing, He and Yang 2007), and 1000 μL was run through the used biofiltration composite five consecutive times. The wash solutions were collected using a centrifuge after 30 min of interaction with the biofilter for each wash. The mercury concentration in these wash solutions was then determined via ICP-MS.

4.2.2.9. Role of Surface Chemistry in Composite Filtration Efficiency

To evaluate if the surface chemistry of the fungal mycelia was impacted by changing the nitrogen source (either nitrate or glutamate), and to highlight the observed differences in filtration efficiency, the surface-free energies of the mycelia grown under each condition and their corresponding wettability via contact angle were measured using a tensiometer (Attention Theta Lite Tensiometer connected to a Navitar Zoom 6000® Lens System with a magnification range of 0.09-393X), via the OneAttension software. A measured 4 μL of double deionized water or diiodomethane (polar and non-polar fluids, respectively) was used for the experiment at different points on the mycelia surface, and this was done three times. The experiment followed the procedure described by (Huang, et al. 2019). The surface free energies were calculated using the Fowkes & Extended Fowkes Model (Fowkes 1964). This experiment was done for the control groups (nitrate and glutamine); therefore, mycelia were grown under the same conditions as the other experiments for the controls, but in a 250 mL flask to allow for growing larger mycelia suitable for this experiment.

5.2.2.10 Analysis

The mean values and standard deviations from data analysis were reported in plots. One-way or two-way ANOVA was conducted to determine significant differences among various treatment factors and their levels. Tukey's post hoc test was used for multiple comparisons among the means across different groups ($P < 0.05$). All analyses were performed using GraphPad Prism 10.0 under a laboratory license. For each group, experiments were performed in triplicate, both technically and biologically.

4.3. Results and Discussion

4.3.1. Fungal Growth and Filament Characterization

The pictorial representation in solid and liquid media, and filaments characteristics of *A. niger* by SEM are presented in Figure 4.1 below. The fungal hyphae emerged from spores' inoculation within 24 h signalling the log phase of growth, the entire area of the Petri dish was covered with mycelia within 3-5 days of exponential growth. After this, there is intense sporulation which is characteristic of the fungus. Notably, on solid media, the fungus has characteristic dark patches indicating spore nucleation (Figure 4.1A, but these spores are more widely distributed on liquid media (Figure 4.1B). The mycelium of *A. niger* comprises interlaying and less branching filaments (Figure 4.1C) with a diameter of about 4.54 (±1.58) as shown in Figure 4.1D. The value from 100 filaments is comparable to existing literature records (Krijgsheld, et al. 2013).
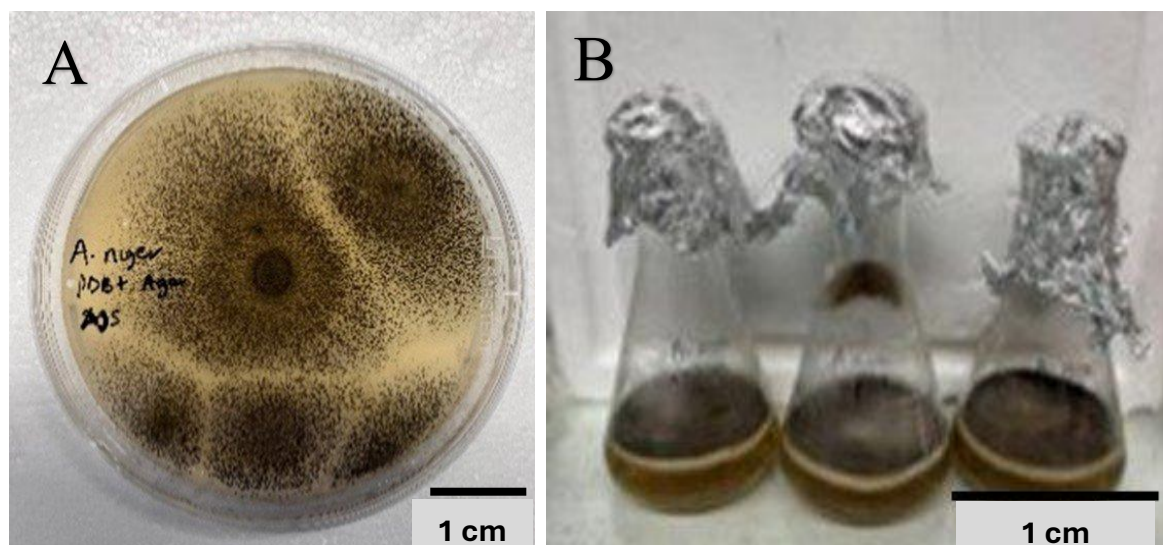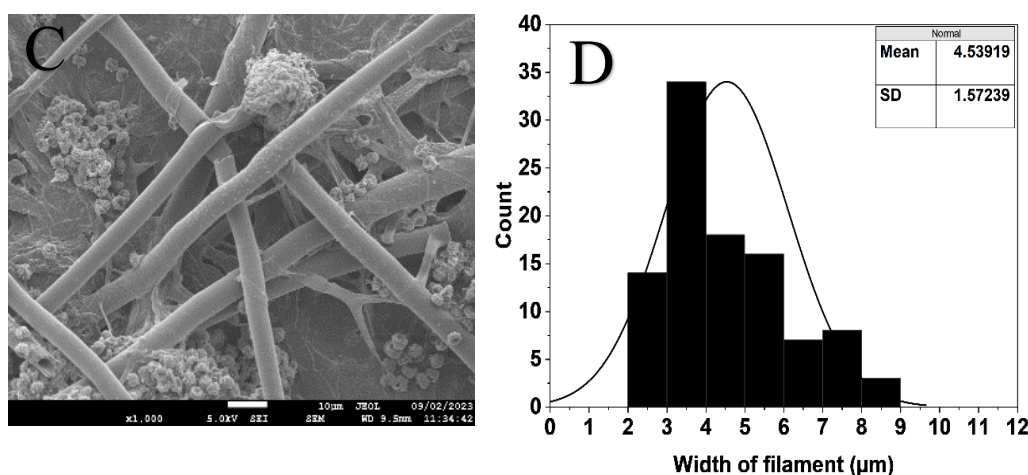
Figure 4.1: Illustrates the growth conditions and characteristics of *A. niger*. Panel (A) growth on slid media (PDB + agar); (B) growth on liquid media (PDB); (C Scanning Electron Micrograph (SEM) of *A. niger*, highlighting morphological features; and (D) Size distribution plot of *A. niger* spores, illustrating size variability.

4.3.2. Directed Au NPs Assembly on *A. niger* Mycelium (Preliminary evaluation).

Before the main experiments, a preliminary evaluation was conducted to establish a method suitable for AuNPs assembly on *A. niger* within the laboratory as a biomimetic system. Changes during growth were monitored and recorded, starting with two concentrations of the AuNPs (22 and 41 µg/ mL). These concentrations were randomly chosen to accommodate the synthesis concentration of the NPs, followed by a 2-fold dilution. Physical observation during the progression of Au NPs assembly on *A. niger* mycelium showed unique patterns (Figure 4.2 A). Firstly, all the freshly prepared fungi culture media had characteristic brick-red colors unique to the synthesized AuNPs added to the media. Within the first five days of initial growth, the characteristic brick-red color of the cefaclor and citrate AuNPs at 41 µg/ mL, which were initially conspicuous in the fungal culture media, changed to purple and pink, respectively. Interestingly, the *A. niger* in these groups picked up these colors in their filaments. While there was obvious growth inhibition, the alteration in the physical appearance (color changes) of the AuNPs solution could be suggested to be due to interaction with some media component. This suggestion is based on previous studies, where it was reported that the physicochemical properties of NPs could be altered by the matrix in which they are suspended, including biological matrices such as cell culture media (Kendall, et al. 2015, Moore, et al. 2015). However, the absence of similar observations in other groups at 41 µg/ mL and across 20 µg/

mL for the same AuNPs groups brought doubt to the initial suggestion. A further literature search revealed that some species of *Aspergillus* can secrete a special pigment called pyomelanin, which protects them against reactive oxygen intermediates, serves as a metal chelator, and protects them against wall-disturbing compounds. They secrete this during infection (Keller, et al. 2011, Koch, et al. 2023). However, previous reports on this have been on *A. fumigatus*. With my observation of distinct growth reduction in these two groups coupled with this understanding, I suggest that the observed color changes in the mycelium and media could be due to a severe stress response of the *A. niger* to the presence of the NPs at that concentration. The confirmation of the presence of Au NPs on the mycelium was then evaluated through Fourier transform infrared spectroscopy (FTIR) compared to the pure Au NPs.
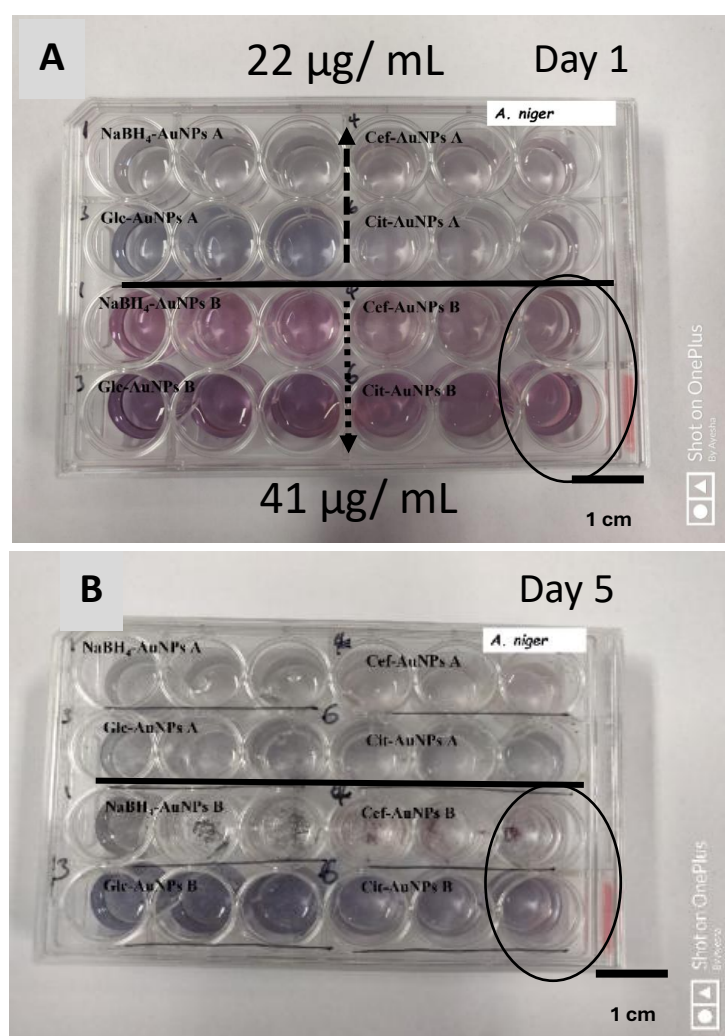
Figure 4.2: Physical observation of AuNPs assembly on *A. niger* mycelium at either 22 or 44 µg/ mL.

The self-assembly of AuNPs on *A. niger* mycelium was monitored after growing the fungus in nutrient media enriched with AuNPs. FTIR analysis recorded the self-organization of AuNPs after one week. Figure 4.2B (A-D) below compares the distinct AuNPs vibrations, indicating biomolecular constituents in pure AuNPs, AuNPs-bound mycelium, and control groups. Figure 4.2A shows FTIR spectra for NaBH$_4$-reduced AuNPs, with typical B-H bond bands between 2300 - 2200 cm^{-1}, 1430 – 1322 cm^{-1}, and 931 – 877 cm^{-1}(Renaudin, et al. 2004). Figure 4.2B highlights O-H vibrations in glucose (Liu, et al. 2006), observed in all treatment and control groups. *A. niger* mycelium is primarily a carbohydrate material composed of different carbohydrate polymers, some of which are rich in glucose. Figure 4.2C presents β-lactam ring vibrations in mycelium treated with Cef-AuNPs (Rai, Prabhune and Perry 2010), with consistent peaks at 22 and 41 µg/ mL. Figure 4.2D shows carboxylate peaks in Cit-AuNPs-treated mycelium, consistent with pure Cit-AuNPs. This indicates that the Cit-AuNPs assembled on the mycelium, and their functional properties after the assembly may not have been significantly altered. These observations were not recorded in the control groups (Hameed, Hamza and Kamal 2015). From preliminary evaluation, I concluded that 41 µg/ mL AuNPs induced stress responses in the fungus, affecting NP properties and growth (Figure 4.2B). Therefore, 20 and 30 µg/ mL concentrations were adopted for further experiments, examining deposition over varying days and nitrogen sources.
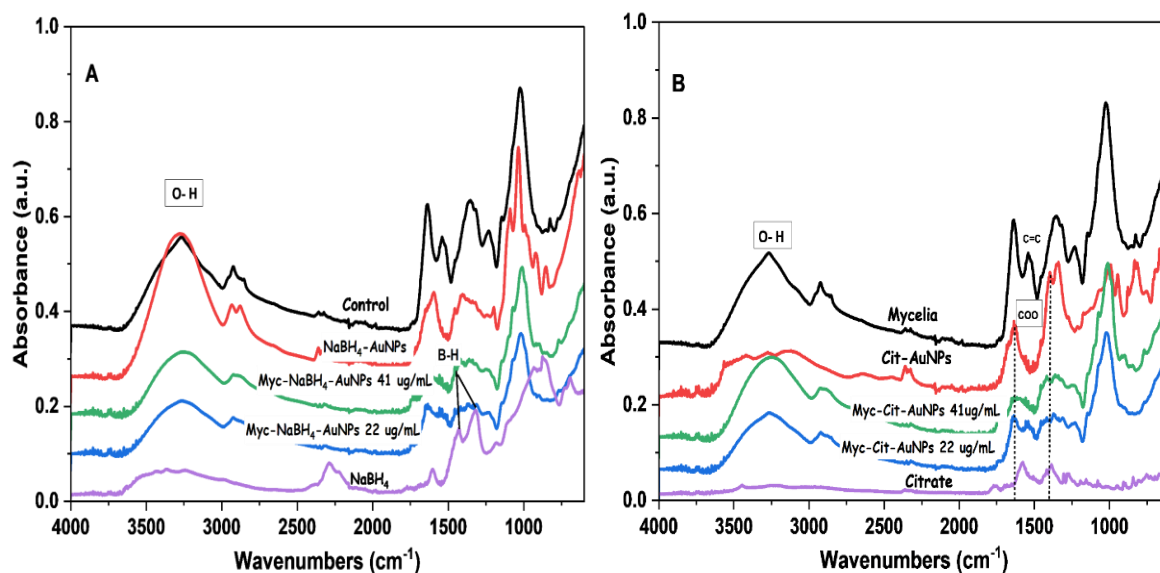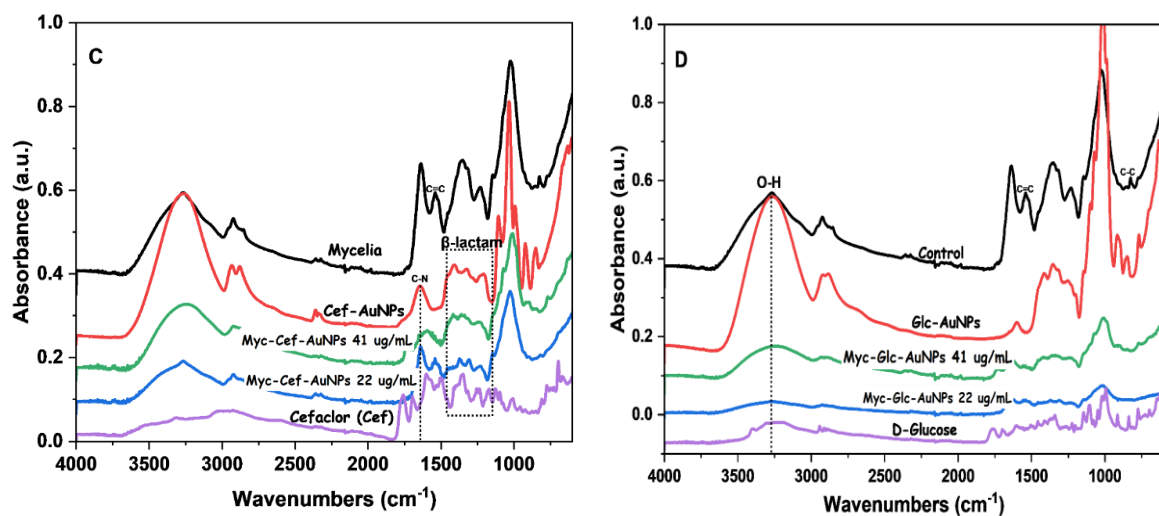
Figure 4.2B: The FTIR spectra of AuNPs-bound mycelia compared to their respective ordinary materials. Panel (A)NaBH₄-Reduced AuNPs; (B) Glc-AuNPs; (C)Cef-AuNPs; and (D) Cit-AuNPs.

4.3.3. Gold Nanoparticle Deposition on Fungal Mycelium (under Varying Conditions)

When gold nanoparticles (AuNPs) were introduced into the fungal culture of *A. niger*, observable changes were monitored, with images in (Figure 4.3 A-E) showing the culture's appearance during functionalization with AuNPs for either nitrate or glutamine (as nitrogen sources). The mycelia exhibited progressive physical and physiological changes, particularly in sporulation, indicating that successful AuNP deposition required the fungus to adjust, both for survival and NP assembly. After 10 days, the initial brick red colour of the AuNPs was only visible in the background due to the significant mycelial growth. Additionally, there was a concentration-dependent response, with fungal growth being proportional to the AuNP concentration (20 or 30 µg/ mL), consistent with preliminary studies.

A: PDB- Control

30 µg/ mL

20 µg/ mL

Glutamine

Nitrate

1 cm

B: Glc-AuNPs

30 µg/ mL

20 µg/ mL

Glutamine

Nitrate

1 cm
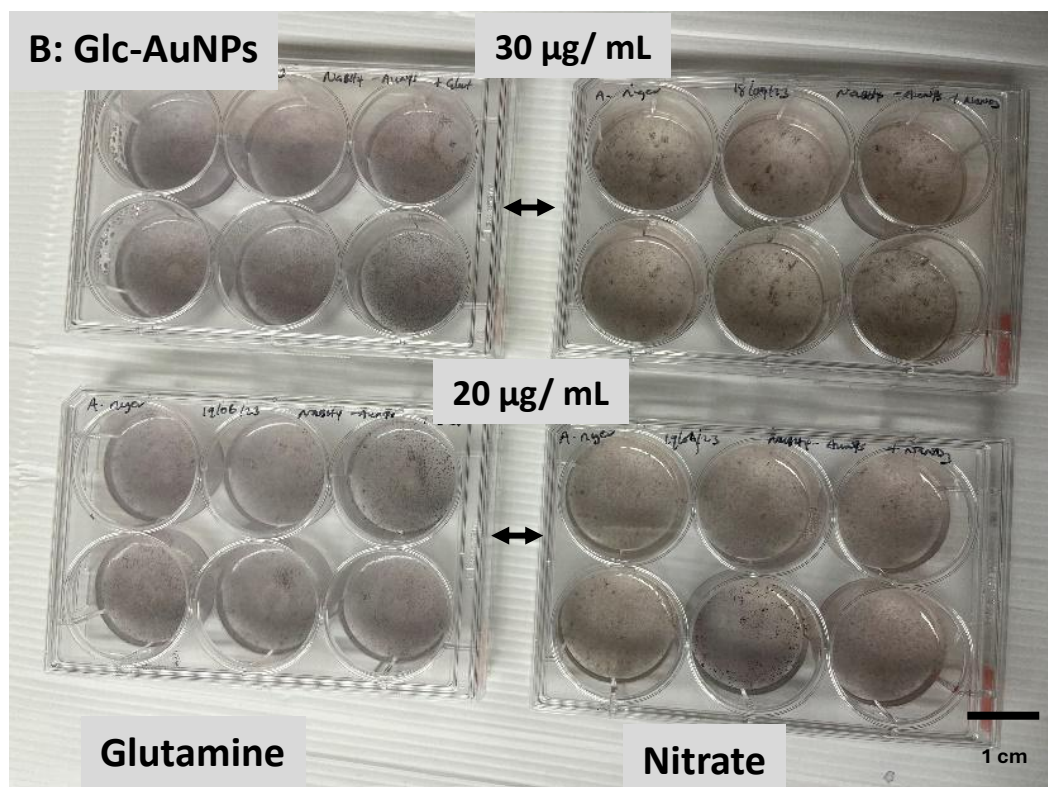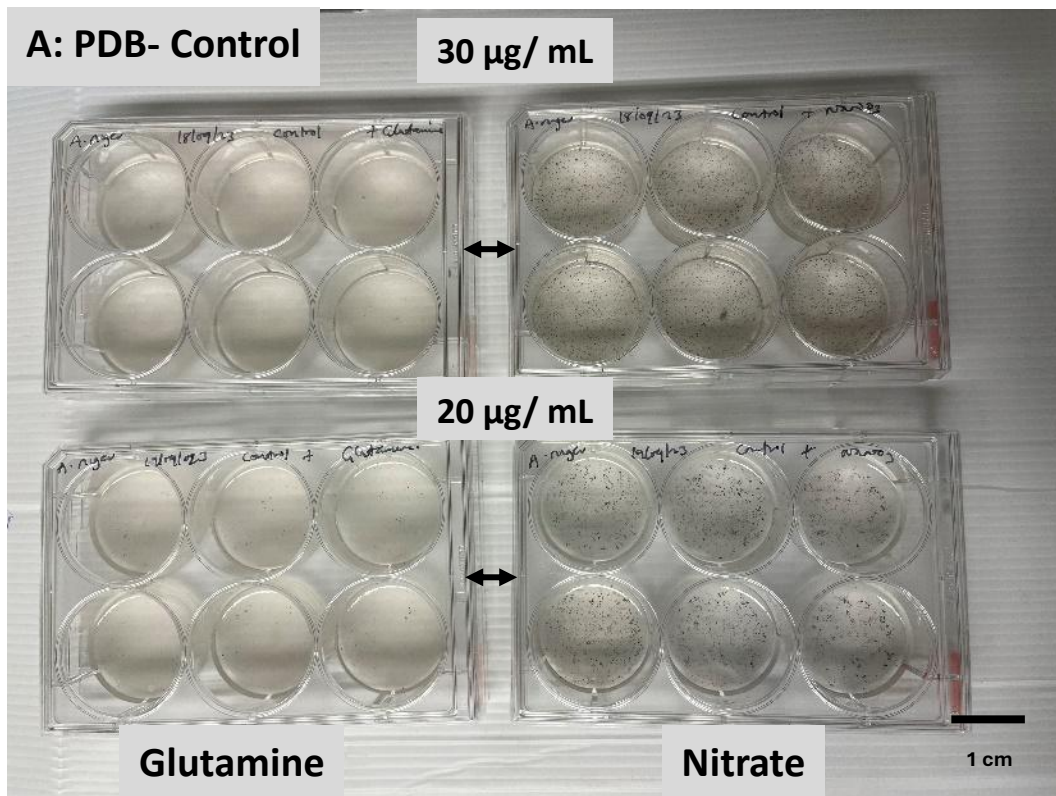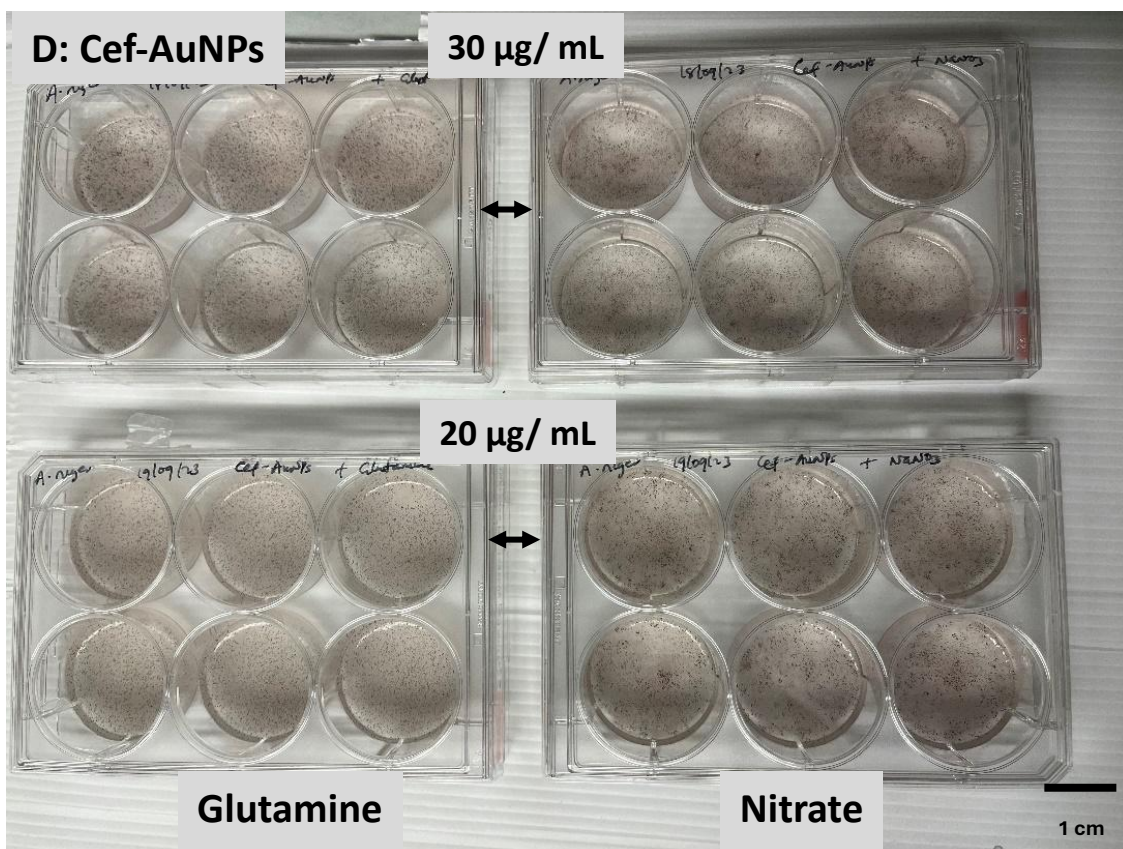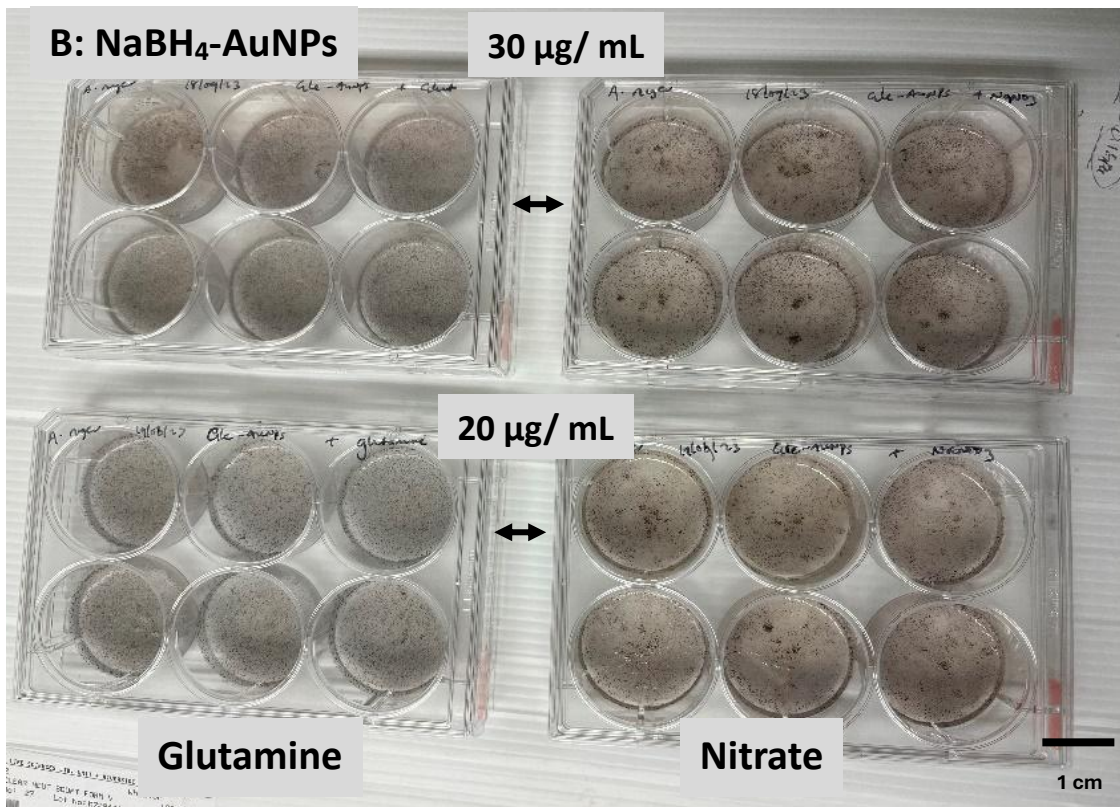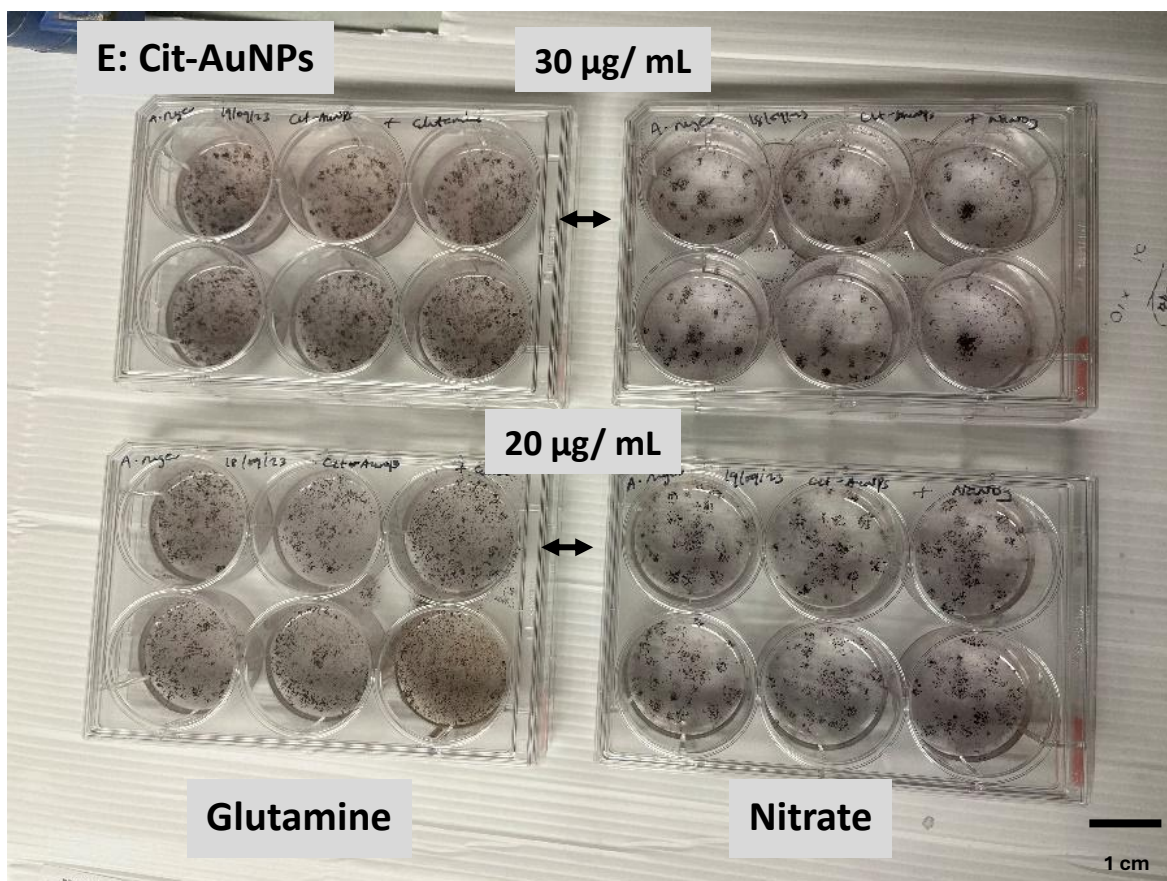
Figure 4.3: Picture of observable changes in *A. niger* culture during functionalization with AuNPs using nitrate or glutamine as nitrogen sources. Images A-E show the culture's appearance over 10 days, proportional to AuNP concentration (20 or 30 μg/ mL). (A) PDB-Control, (B) NaBH$_4$-reduced AuNPs, (C) Glc-AuNPs, (D) Cef-AuNPs, (E) Cit-AuNPs.

4.3.4. Impact of Varying Conditions on the Mycelial Yield of *A. niger*

4.3.4.1 Impact of Gold Nanoparticles Concentration (20 or 30 μg/ mL)

To determine how the mycelial yield of *A. niger* is affected by varying concentrations of AuNPs (20 or 30 μg/ mL) over different growth periods (7 or 10 days), I kept the nitrogen source constant and quantitatively evaluated the yield under different types of gold NPs used in functionalization. Significant variations in mycelia yield were recorded depending on the concentration, type of AuNPs, and growth duration, as shown in Figure 4.4 A–D. Generally, the yield of the AuNPs-mycelia composite varied with increasing AuNP concentrations, but lower yields were observed across NP groups compared to PDB, except for Glc-AuNPs where growth and yield were unaffected. The glucose on the AuNPs surface seems to offer additional nutrients. With glutamine as the nitrogen source (Figure 4.4 A), more mycelia were produced

at 30 µg/ mL if growth lasted 7 days, but no significant difference was noted with longer growth durations, except for Cef-AuNPs which favoured lower concentrations with increased growth duration (Figure 4.4 B). For nitrate as the nitrogen source, mycelia yield was unaffected by growth duration or AuNP concentration. Notably, lower concentrations of Cit-AuNPs resulted in higher yields, suggesting the possibility antifungal effect due to prolonged interaction with the fungus (Eid, et al. 2011).
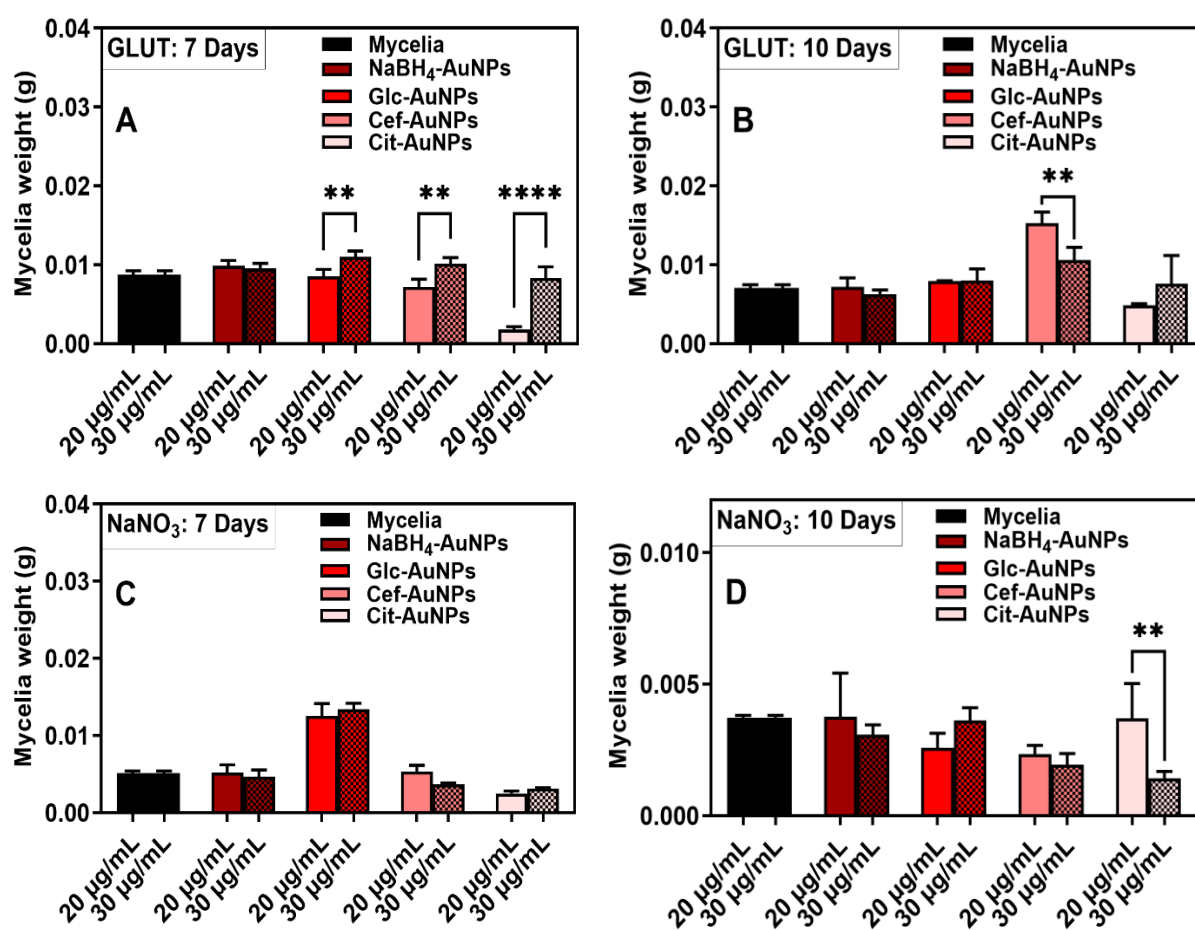
Figure 4.4: Mycelia yield of *A. niger* with varying AuNP concentrations (20 or 30 µg/ mL) over 7 or 10 days. (A) glutamine: 20 or 30 µg/ mL of AuNPs for 7 days; (B) glutamine: 20 or 30 µg/ mL of AuNPs for 10 days; (C) nitrate: 20 or 30 µg/ mL of AuNPs for 7 days; (D) nitrate: 20 or 30 µg/ mL of AuNPs for 10 days. The level of significance; * ($p \leq 0.05$), ** ($p \leq 0.01$), and *** ($P \leq 0.001$).

4.3.4.2. Impact of Different Nitrogen Sources (Nitrate or Glutamine)

To establish the optimal conditions for growing my composite, I evaluated how the fungus responded to different nitrogen sources while keeping the AuNP concentration and growth period constant. Significant connections were recorded between nitrogen sources, concentration, and growth duration, and these are presented in Figure 4.5 below. Figures 4.5 A and B denote the mycelia yield at 20 and 30 µg/ mL of the AuNPs, respectively, after 7 days of growth. The mycelia yield was significantly higher with glutamine as the nitrogen source compared to nitrate, indicating that the fungus thrived better with glutamine after 7 days of inoculation irrespective of the AuNPs concentration. Figures 4.5 C and D show the material yield at 20 and 30 µg/ mL respectively, after 10 days of growth. A similar trend of results was observed but with more interesting dynamics. Unlike glutamine, increasing the duration of growth from 7 to 10 days does not significantly impact the yields of the composite when nitrate is used as the nitrogen source. Compared to the other groups, Glc-AuNPs have a higher material yield especially when glutamine was the nitrogen source (Figures 4.4A and 4.3B). In the Glc-AuNPs groups, higher yields could be due to additional carbon sources from glucose on the NP's surface or the conversion of glucose to glutamine or glutamate, which are favoured by the fungus as nitrogen sources (Novodvorska, et al. 2013). Across both concentrations of AuNPs, glutamine was mostly preferred, resulting in higher mycelia yields. Thus, growing the composite under glutamine was best for mycelia yield, regardless of the AuNP concentration (20 or 30 µg/ mL), indicating that the nitrogen source had a greater impact on yield than concentration and growth duration.
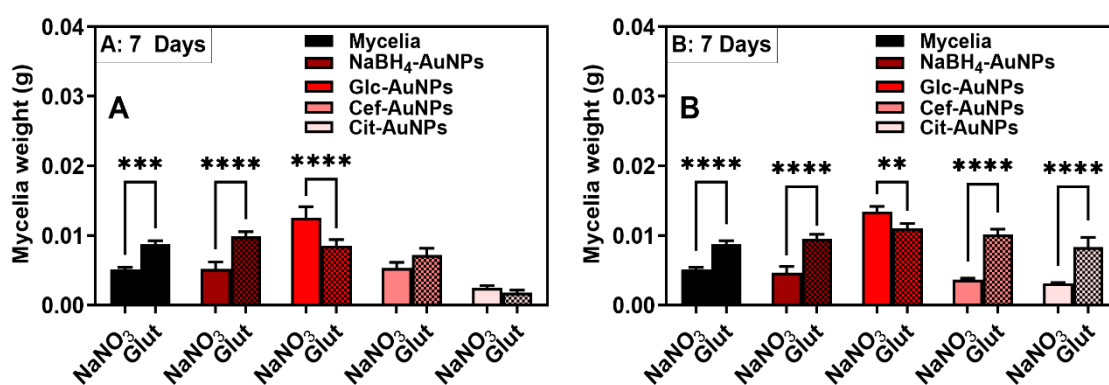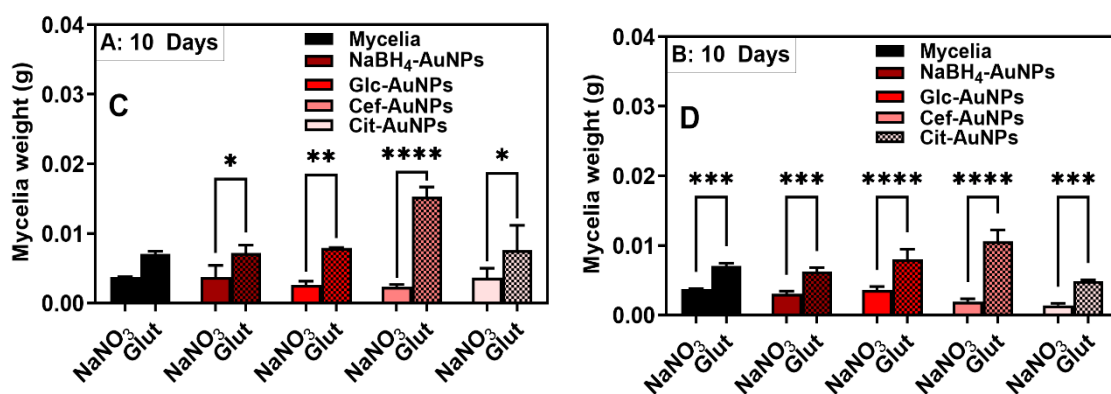
Figure 4. 5: Mycelia yield of *A. niger* with varying nitrogen sources (20 or 30 µg/ mL) over 7 or 10 days. (A) 7 days: 20 µg/ mL of AuNPs; (B) 7 days: 30 µg/ mL of AuNPs; (C) 10 days: 20 µg/ mL of AuNPs; (D) 10 days: 30 µg/ mL of AuNPs. The level of significance; * (p ≤ 0.05), ** (p ≤ 0.01), and *** (P ≤ 0.001).

4.3.5. Physiological Impact of AuNPs on Sporulation of *A. niger*

To understand how the introduction of AuNPs at 30 µg/ mL (being the highest selected concentration after preliminary evaluation) impacted physiological changes in *A. niger*, I evaluated the degree of sporulation under different types of AuNPs, recording significant differences, as shown in Figure 4.6. Sporulation is a crucial physiological response to stress in fungi and serves as a survival mechanism (Su, Qi and Cai 2012). In preliminary studies, *A. niger* thrived in AuNPs up to 41 µg/ mL, yielding high-quality mycelia composites in some groups, but with notable growth changes in others. These growth changes were not observed at 30 µg/ mL, leading us to focus my current investigation on the sporulation effects of AuNPs in growth media with either nitrate or glutamine as the nitrogen source at 30 µg/ mL. This is rather a physiological characterization other than physical growth changes. Apart from Glc-AuNPs, other groups exhibited significant sporulation due to AuNP exposure. Normally, *A. niger* is highly sporulating, but the introduction of NPs increased spore production. Spores from the 30 µg/ mL condition (10^{-1} dilution) showed that NaBH$_4$-AuNPs, Cef-AuNPs, and Cit-AuNPs significantly potentiated sporulation compared to Glc-AuNPs and control groups. Interestingly, sporulation was reduced with glutamine as the nitrogen source, consistent with previous studies showing that glutamine, along with glutamate and ammonia, are primary nitrogen sources for *A. niger* (Novodvorska, et al. 2013). This further supports the ideas well documented in the literature that while nitrate is preferred only as an alternative nitrogen source, glutamine is a primary nitrogen source for *A. niger* (Novodvorska, et al. 2013). Results showed

clear indications that the fungus though stressed, was still able to produce enough material suitable for composite formation under the treatment conditions explored.
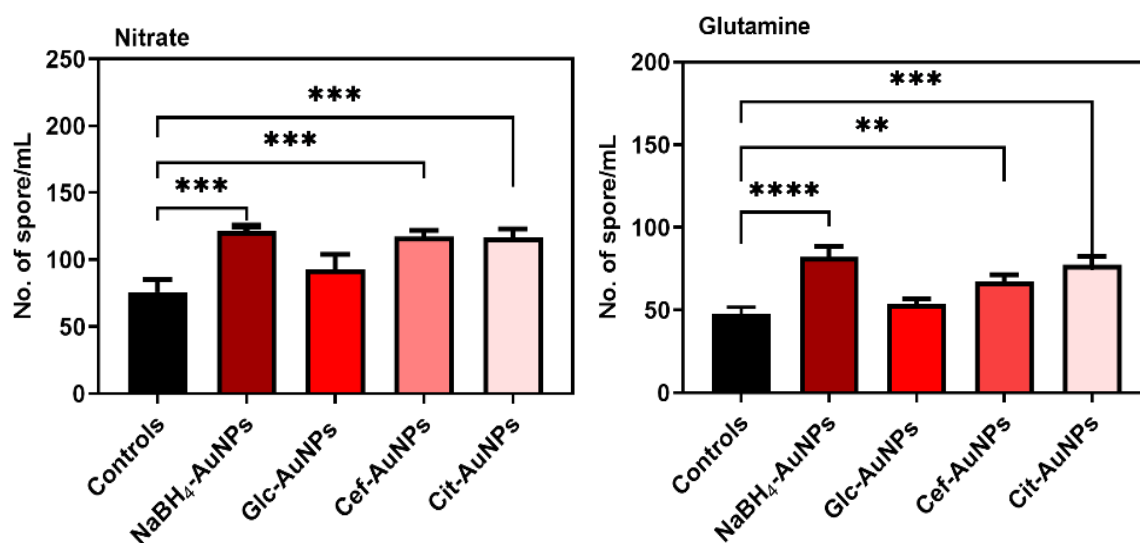
Figure 4.6: Quantitative comparison of the physiological response of *A. niger* by sporulation mycelia (A) 20 µg/ mL and (B) 30 µg/ mL in when either nitrate or glutamine was used as nitrogen source. The level of significance * ($p \leq 0.05$), ** ($p \leq 0.01$), and *** ($P \leq 0.001$).

4.3.6 Morphological Characterization and Elemental Mapping of AuNPs-Functionalized *A. niger* Mycelia

The morphological characterization and elemental mapping of the functionalized mycelia by SEM/EDX further confirmed the successful AuNPs functionalization of *A. niger* mycelia, providing additional structural information. These are presented in Figure 4.7 A-D below for the materials grown at 30 µg/ mL of the AuNPs for either 7 (Figure 4.7 A and B) or 10 days (Figure 4.7 C and D). The Figure for the materials grown at 20 µg/ mL of the AuNPs is in the appendix, labelled as Figure Appendix 4.1. For a comprehensive morphological analysis, scanning electron microscopy (SEM) images of the gold nanoparticle-mycelia (AuNP-mycelia) composites were captured at various magnifications. The SEM images demonstrated that the mycelia in each experimental group were effectively coated with gold nanoparticles, even after washing. However, a few filaments displayed fewer nanoparticles. The mycelia of *A niger* across all AuNP groups (NaBH4-AuNPs, Glc-AuNPs, Cef-AuNPs, and Cit-AuNPs) exhibited significant functionalization, as evidenced by the uniform distribution of AuNPs on the mycelia. This uniformity was consistent at both 20 and 30 µg/ mL concentrations when cultivated for either 7 or 10 days, using glutamine or nitrate as the nitrogen source. In terms of spatial distribution, the AuNPs were primarily observed as non-aggregates, with only a few clusters

noted in the Glc-AuNPs group. This suggests that the interaction between the nanoparticles, the media, and the fungal mycelia did not significantly alter the distribution. of their physicochemical and morphological properties (e.g. shape, and agglomeration). Complementary EDX analysis through spot and map scanning of the areas observed to have the NPs showed an intense optical absorption band peak for Au at approximately 2.2 keV, further confirming the presence of the AuNPs. Well-defined optical absorption bands designated to carbon (from the mycelia, AuNPs, and the 10 nm carbon coating), silica (from borosilicate glass that was used as sample holder), oxygen (from mycelia and Au NPs component), sulphur (for the groups with cefaclor coated AuNPs) and Au were also detected. Like the results from physiological characterization via sporulation, the SEM micrographs also showed intense sporulation on the filaments in the Cit-AuNPs-Myc group, especially when the fungus had nitrate as the nitrogen source (Figure 4.7D). However, the morphology of the fungal spores themselves did not seem to be affected, as no damage was observed. Generally, being a biological sample, images could not be taken under conditions that further exposed the sample to burning by the electron beam at high accelerating voltage. Similarly, there was a charging effect from some groups (especially citrate), likely due to the interaction between the electron beam and the electrons from the coating materials on the AuNPs surface. From SEM micrographs, clear distinctions could not be made on the effects of the nitrogen source on AuNPs deposition, indicating the need for further evaluation using more quantitative methods. However, the SEM/EDX characterization shows that the use of a natural coupling process without intrusive chemicals is adequate for the formation of AuNPs composites with *A. niger*.
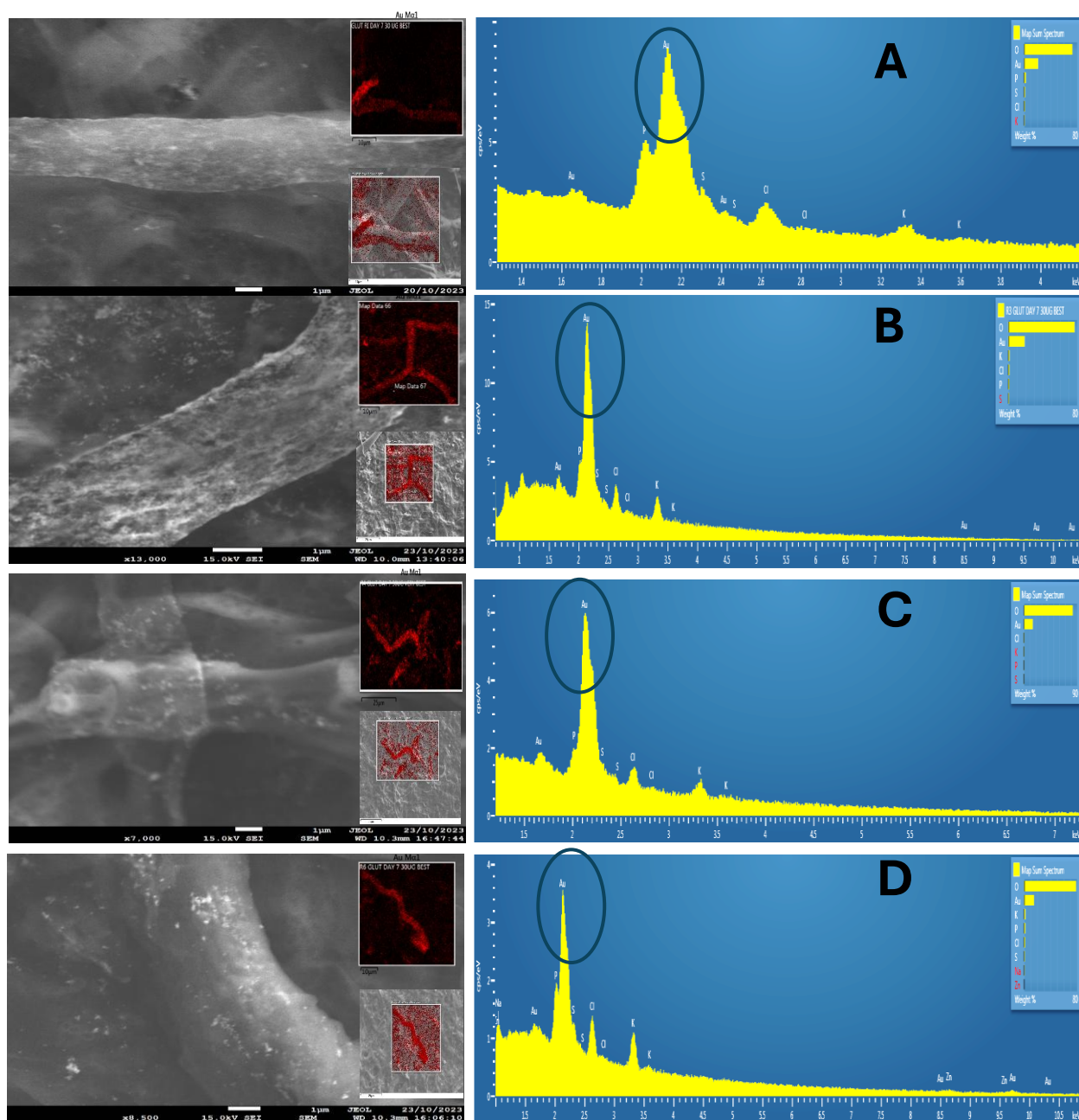
Figure 4.7A: Representative scanning electron microscopy (SEM) image, and elemental analysis (EDX) showing the distribution (A): NaBH$_4$-AuNPs; (B): Glc-AuNPs; (C): Cef-AuNPs; (D): Cit-AuNPs; on *A. niger* hyphae after 7 days of growth (nitrogen source: glutamine). The insert at the top right corner is the mapped area on the mycelia while that at the bottom right corner is the corresponding EDX signal for Au atoms. This signal is denoted by the area within the circle for the SEM/EDX image. All SEM images include a scale bar representing 1 μm.
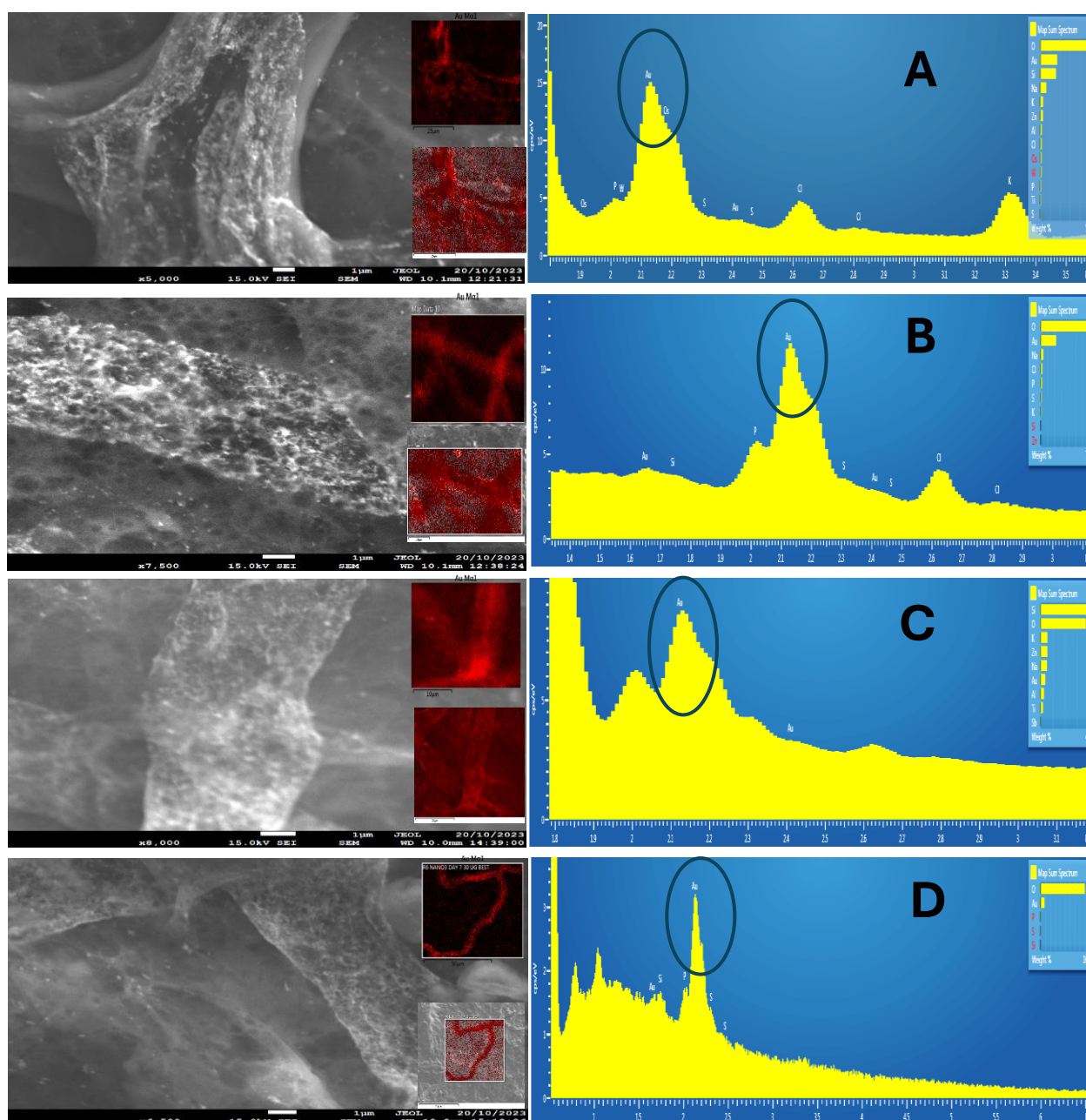
Figure 4.7B: Representative scanning electron microscopy (SEM) image, and elemental analysis (EDX) showing the distribution (A): NaBH$_4$-AuNPs; (B): Glc-AuNPs; (C): Cef-AuNPs; (D): Cit-AuNPs; on *A. niger* hyphae after 7 days of growth (nitrogen source: nitrate). The insert at the top right corner is the mapped area on the mycelia while that at the bottom right corner is the corresponding EDX signal for Au atom. This signal is denoted by the area within the circle for the SEM/EDX image. All SEM images include a scale bar representing 1 µm.
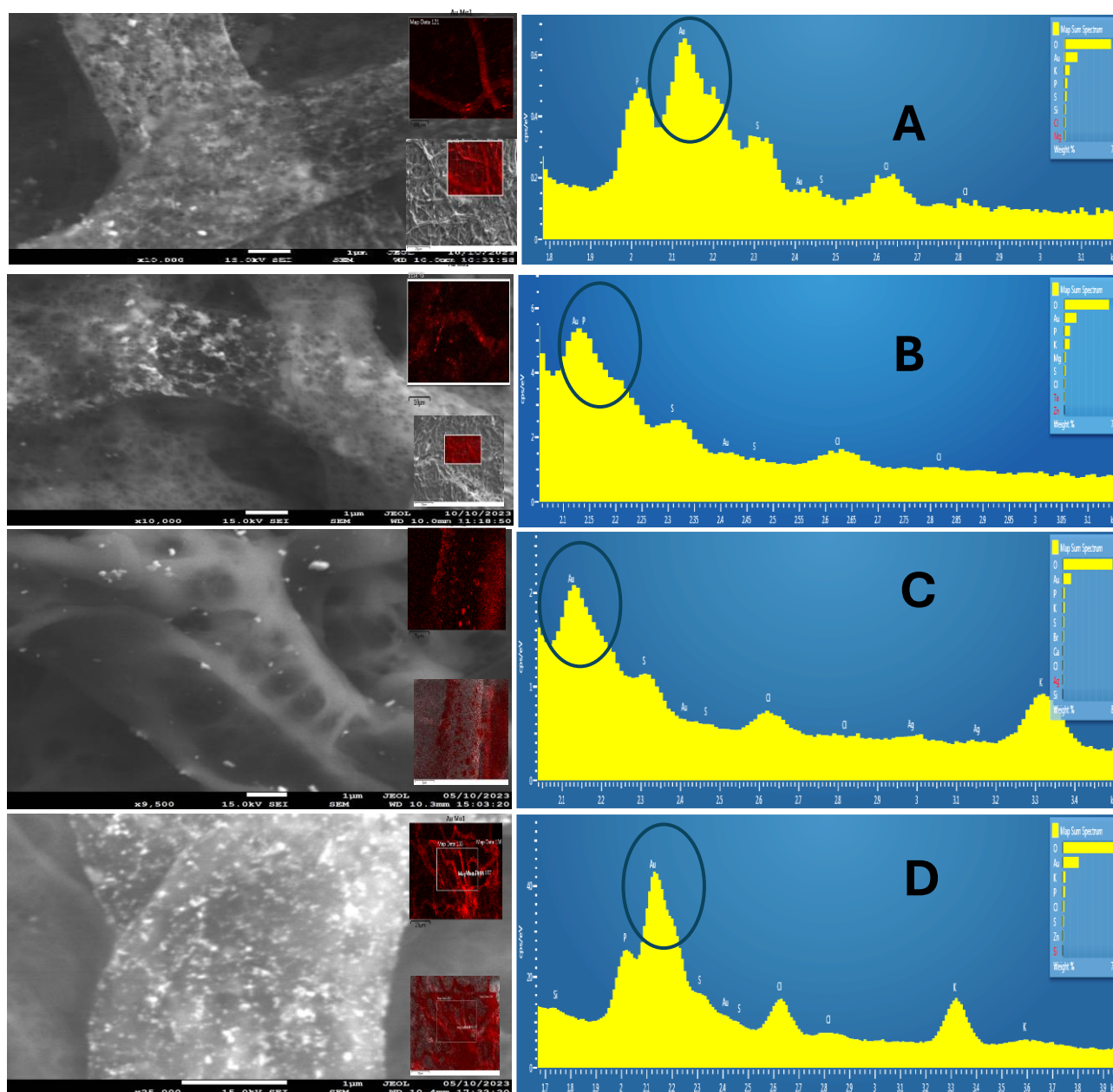
Figure 4.7C: Representative scanning electron microscopy (SEM) image, and elemental analysis (EDX) showing the distribution (A): NaBH$_4$-AuNPs; (B): Glc-AuNPs; (C): Cef-AuNPs; (D): Cit-AuNPs; on *A. niger* hyphae after 10 days of growth (nitrogen source: glutamine). The insert at the top right corner is the mapped area on the mycelia while that at the bottom right corner is the corresponding EDX signal for Au atom. This signal is denoted by the area within the circle for the SEM/EDX image. All SEM images include a scale bar representing 1 μm.
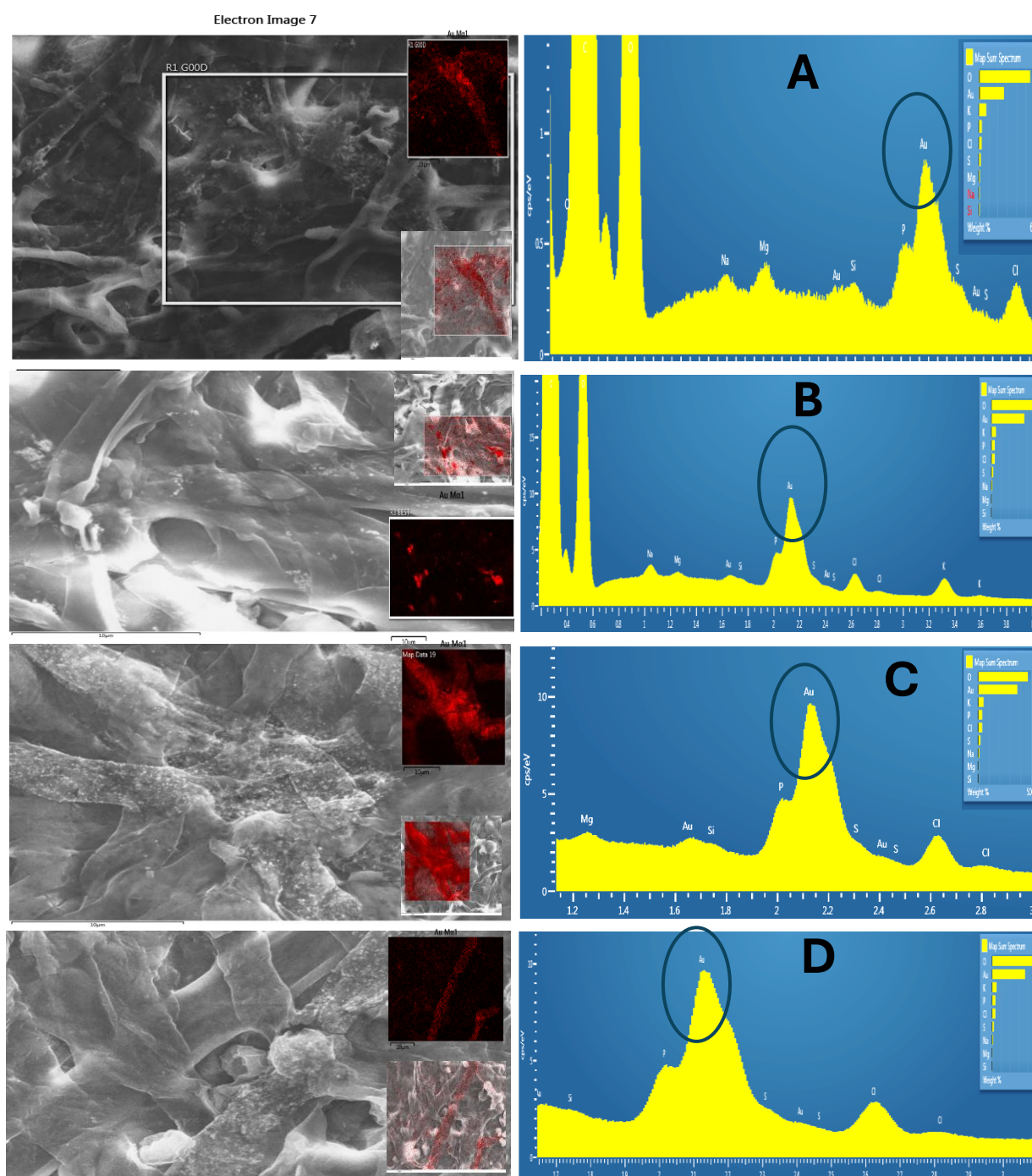
Figure 4.7D: Representative scanning electron microscopy (SEM) image, and elemental analysis (EDX) showing the distribution (A): NaBH4-AuNPs; (B): Glc-AuNPs; (C): Cef-AuNPs; (D): Cit-AuNPs; on *A. niger* hyphae after 10 days of growth (nitrogen source: nitrate). The insert at the top right corner is the mapped area on the mycelia while that at the bottom right corner is the corresponding EDX signal for Au atom. This signal is denoted by the area within the circle for the SEM/EDX image. All SEM images include a scale bar representing 10 µm.

4.3.7. Effects of Varying Conditions on the Deposition of AuNPs on *A. niger* Mycelia

4.3.7.1. Effect of AuNPs Concentrations (20 or 30 µg/ mL)

I quantitatively investigated the implications of using varying concentrations of AuNPs (20 or 30 µg/ mL) on their deposition dynamics on *A. niger*, and how this is further affected by growth duration. Understanding the deposition dynamics of the AuNPs on *A. niger* mycelia provides better insight into the chemical nature and usability of the AuNPs-mycelia composite. Inductively Coupled Plasma Mass Spectrometry (ICP-MS) is recognized as an effective elemental quantification technique for various nanoparticles, including metallic NPs (Laycock, et al. 2022). The standard calibration curves for gold (0.01-0.1 ppm) and extrapolations of Au:In counts for the AuNPs functionalized mycelia fractions, with curves Y (Au:In) = 45.84X + 0.45931 for glutamine and Y (Au:In) = 92.21X + 0.45931 for NaNO$_3$, indicate the concentration (ppm) of Au bound to the mycelia. Results, presented in Figure 4.8 A-D, show that more NPs are deposited at 30 µg/ mL (Fig 4.8 B, C, and D), indicating that concentration played a pivotal role. Similarly, increasing the growth duration from 7 to 10 days significantly contributed to AuNPs deposition at 30 µg/ mL, whether the nitrogen source was glutamine (Fig 4.8 A and B) or nitrate (Fig 4.8 C and D).
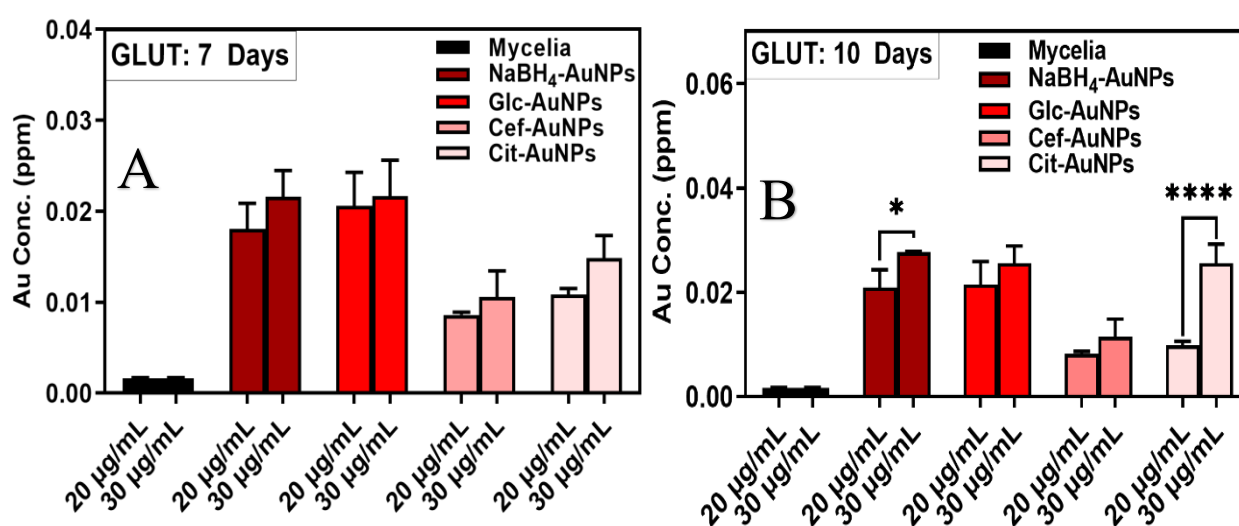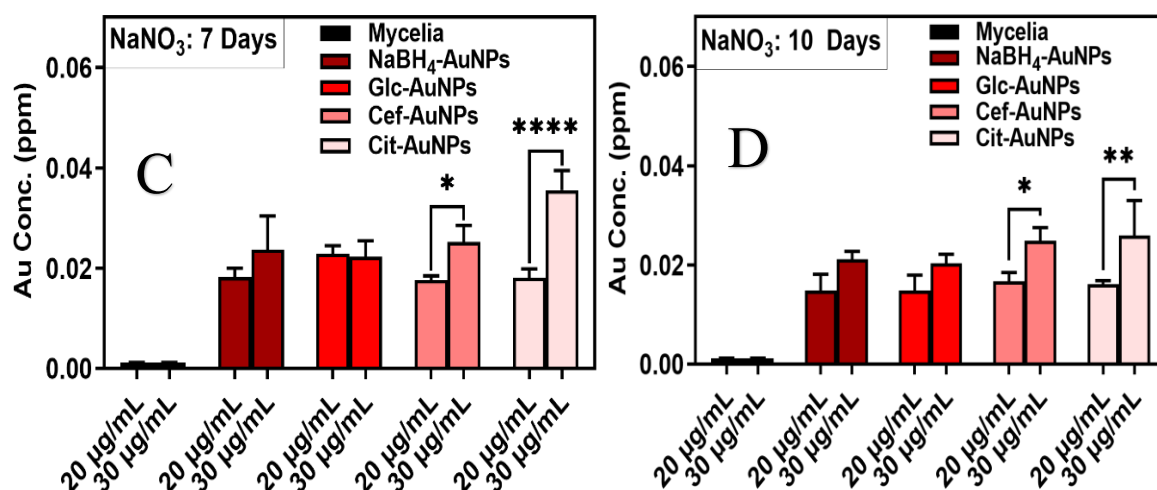
Figure 4.8: AuNPs deposition on *A. niger* with varying AuNPs concentration (20 or 30 μg/ mL) over 7 or 10 days. (A) glutamine: 20 or 30 μg/ mL of AuNPs for 7 days; (B) glutamine: 20 or 30 μg/ mL of AuNPs for 10 days; (C) nitrate: 20 or 30 μg/ mL of AuNPs for 7 days; (D) nitrate: 20 or 30 μg/ mL of AuNPs for 10 days. The level of significance; * (p ≤ 0.05), ** (p ≤ 0.01), and *** (P ≤ 0.001).

4.3.7.2. Effect of Nitrogen Sources (Nitrate or Glutamine)

For further clarification, Figure 4.9 A-D illustrates the AuNP deposition dynamics between the two nitrogen sources at the same growth duration and concentration. This was done to provide more details on how changing nitrogen sources affects AuNPs deposition, and which is preferred by the fungus (*A. niger*) for this. When the growth duration was 7 days, gold NPs deposition was favoured with nitrate as the nitrogen source (Figure 4.9A and B). However, for 10 days, the fungus preferred glutamine for Glc-AuNPs and NaBH4-AuNPs deposition, while nitrate was preferred for Cef-AuNPs and Cit-AuNPs deposition (Figure 4.9C and D). This implies that Cef-AuNPs and Cit-AuNPs showed a preference for NaNO3 as their nitrogen source for AuNP deposition but not for growth. Interestingly, both groups (Cef and Cit-AuNPs) retained at least 50% of the initial gold bound to the mycelia at both concentrations (20 and 30 μg/ mL) after three washes. Notably, these two groups have the highest zeta potentials, suggesting better stability and reduced NP-NPs aggregation, allowing for strong interaction between the fungal mycelia and the AuNPs (Rasmussen et al., 2020). This observation is consistent with SEM results showing more homogeneously distributed and unagglomerated microstructures for these groups. *A.* strains are versatile in utilizing a wide array of organic or inorganic nitrogen sources (Krappmann and Braus, 2005), but this versatility comes with

consequences. The triggering of conidia germination and subsequent outward growth to form the mycelia network, required for functionalization, can be affected by the nitrogen source (Hayer, Stratford and Archer 2014). Unlike nitrate, glutamine plays important roles in both stages (conidia activation and outward growth) within the first 24 h of inoculation, contributing to the early growth of *A. niger* without the need for complementary activators (Hayer, Stratford and Archer 2014). These differences may be responsible for the observed impact on growth patterns and the nature of deposition. I concluded that the composite is best formed at 30 µg/ mL of the AuNPs but retained both nitrogen sources in my further studies due to differing preferences. This also gives a platform to study how the fungus assembles the NP under different nitrogen sources.
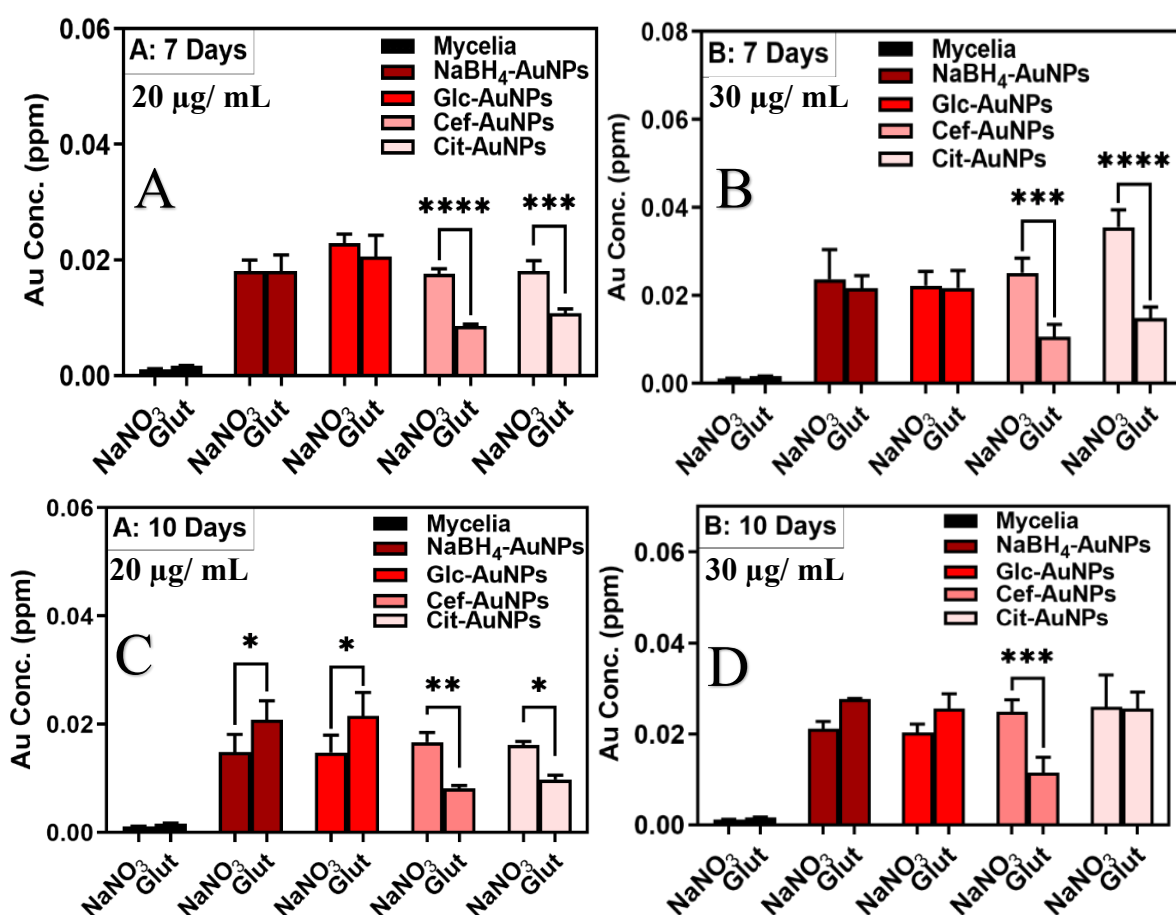
Figure 4.9: Mycelia yield of *A. niger* with varying nitrogen sources (20 or 30 µg/ mL) over 7 or 10 days. (A) 7 days: 20 µg/ mL of AuNPs; (B) 7 days: 30 µg/ mL of AuNPs; (C) 10 days: 20 µg/ mL of AuNPs; (D) 10 Days: 30 µg/ mL of AuNPs. The level of significance; * ($p \leq$ 0.05), ** ($p \leq 0.01$), and *** ($P \leq 0.001$).

4.3.8. Potential of AuNPs-Functionalized Fungal Composites in an Environmental Application

4.3.8.1. AuNPs-Functionalized Fungal Composites for Mercury Removal

Having understood the AuNPs deposition dynamics under different conditions and developed the composite, I explored the potential of fungal composites created at 30 µg/ mL of AuNPs using either nitrate or glutamine as nitrogen sources as novel, reusable filters for mercury removal. The previous chapter (chapter 3) established the sensitivity of these AuNPs to mercury, including their detection limits. Literature also indicates that mercury has a strong affinity to bind gold through a process known as amalgamation, where gold and mercury form an amalgam, a concept also utilized in gold mining (Donkor, Ghoveisi and Bonzongo 2024). Leveraging this, I selected mercury for my biofiltration assessment. This aligns with the global quest for sustainable mercury management in the environment (detection and removal). In this study, these biofilters were compared to an industrial filter (PierceTM Centrifuge Column, Thermo-Scientific, with a polyethylene filter and 30 µM pore size), with ordinary mycelia serving as the control. Results showed that Cef-AuNPs and Cit-AuNPs were effective under both nitrogen conditions, particularly with glutamine as the nitrogen source (Figure 4.10). Glc-AuNPs and other mycelia groups performed better in glutamine as the nitrogen source, while NaBH$_4$-AuNPs showed superior performance with nitrate as the nitrogen source, suggesting that mycelia surface properties may influence filtration effectiveness. Notably, when glutamine was the nitrogen source, all groups, including ordinary mycelia, achieved significant mercury reduction, with levels dropping from 5 ppb with up to 90% removal rate in some groups, demonstrating the system's suitability for mercury filtration (Figure 4.10). These findings highlight the eco-friendly potential of fungi in addressing heavy metal pollution and the importance of applied mycology intersecting with nanotechnology. It also showcases the tuneability of mycelia with different constituents (food sources or bioactive materials) and how this promotes their use in certain applications.

According to a chemical fact sheet published by the World Health Organization (WHO, 2011), the organization postulated the possibility of achieving mercury removal from raw, not-so-contaminated water down to 1 ppb using methods such as coagulation/sedimentation/filtration, Powdered Activated Carbon (PAC), and ion exchange. In the UK, previous methods reported in literature achieved mercury removal efficiencies of up to 52.2% during primary treatment and 29.5% during secondary treatment (Hargreaves, et al. 2016). This new system, however, offers significant improvements, especially in removing mercury from low-level contaminated

waters. In addition, my experiment has proven that glutamine treatment in the formation of AuNPs-Mycelia composite can accomplish this under laboratory conditions. This also fits into the regulatory requirements in countries with more stringent MAC for mercury (e.g., the United Kingdom and Canada), where the level as stated in the water regulation policy is 1 ppb (Health Canada 1979, The United Kingdom Government 2016).
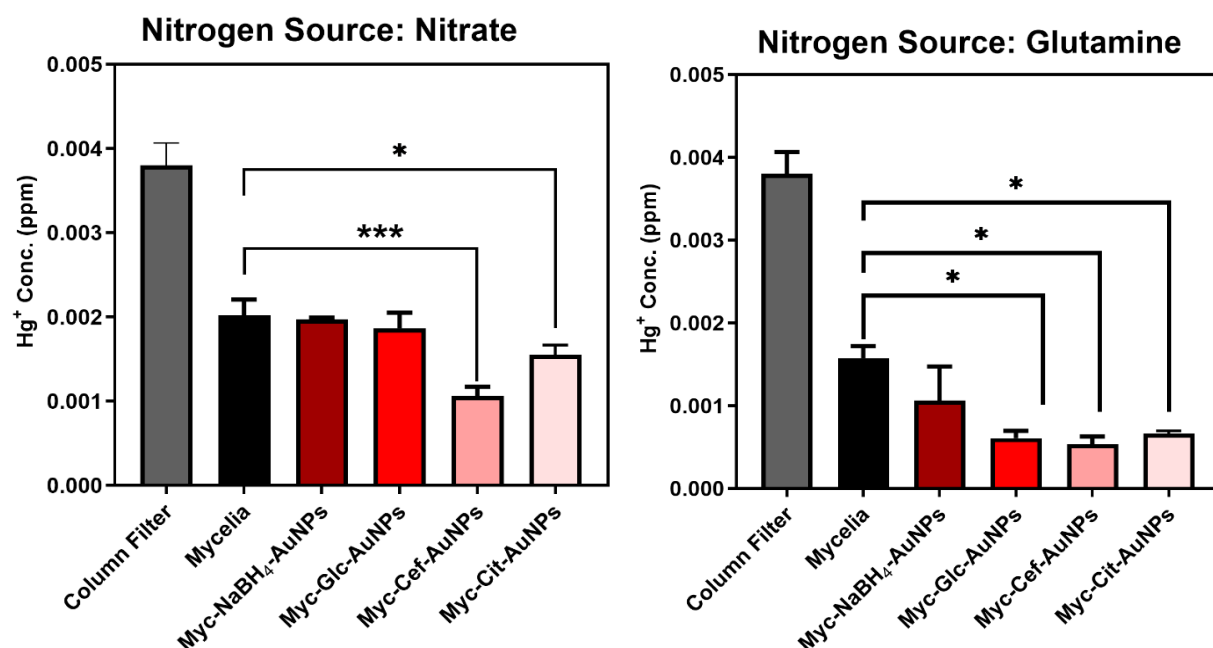
Figure 4.10: Quantitative comparison of the Hg^{2+} removed by *A. niger* mycelia at 30 µg/ mL when either nitrate or glutamine was used as a nitrogen source. The level of significance; * ($p \leq 0.05$), ** ($p \leq 0.01$), and *** ($P \leq 0.001$). The starting level of mercury is 5 ppb.

4.3.8.2. Reusability of the Composite in Mercury Filtration

Initial experiment results shown in Figure 410 demonstrated the effectiveness of certain AuNPs-fungal composite filters in mercury filtration, leading to their selection for further reusability screening. Results from five runs, presented in Figures 4.11A (glutamine) and 4.11B (nitrate), showed that mercury concentration in the initial test samples significantly dropped below 2 ppb (indicated by the green line), the United States Environmental Protection Agency's Maximum Allowable Concentration (USEPA MAC) for mercury in wastewater, also adopted by the WHO in a 2017 report (WHO, 2017). For the AuNPs-mycelia composite filters formed with glutamine (Figures 4.11A), three groups (Glc-AuNPs, Cef-AuNPs, and Cit-AuNPs) were selected based on the results described above. These groups effectively removed mercury over five consecutive runs, with ordinary mycelia also demonstrating some mercury removal, suggesting a complementary effect between AuNPs and mycelia. Compared to the WHO MAC,

the glutamine-treated AuNPs composites reduced mercury to levels even half the MAC over repeated use, demonstrating their efficiency and reusability. For composites formed with nitrate, only Cit-AuNPs and Cef-AuNPs were selected. Unlike the glutamine-treated composites, these showed varying responses over five runs. The Cef-AuNPs-mycelia biofilter became more efficient over time, with significant differences observed after the fifth run, while Cit-AuNPs showed improvement from the second run, maintaining this over subsequent runs. Compared to the WHO MAC, the Cef-AuNPs-mycelia composite proved to be an efficient biofilter, with both nitrate groups reducing mercury to the MAC over repeated use. From both groups treated with either nitrate or glutamine, it can be inferred that mycelia composites can serve as novel filtration systems for reducing low mercury concentrations in wastewater to levels below the WHO MAC (indicated by the green line). The differing behaviours of the composites under the two nitrogen sources suggest that other factors may influence effective filtration or interaction with mercury. The principal suspects are surface-free energy and the degree of wettability.
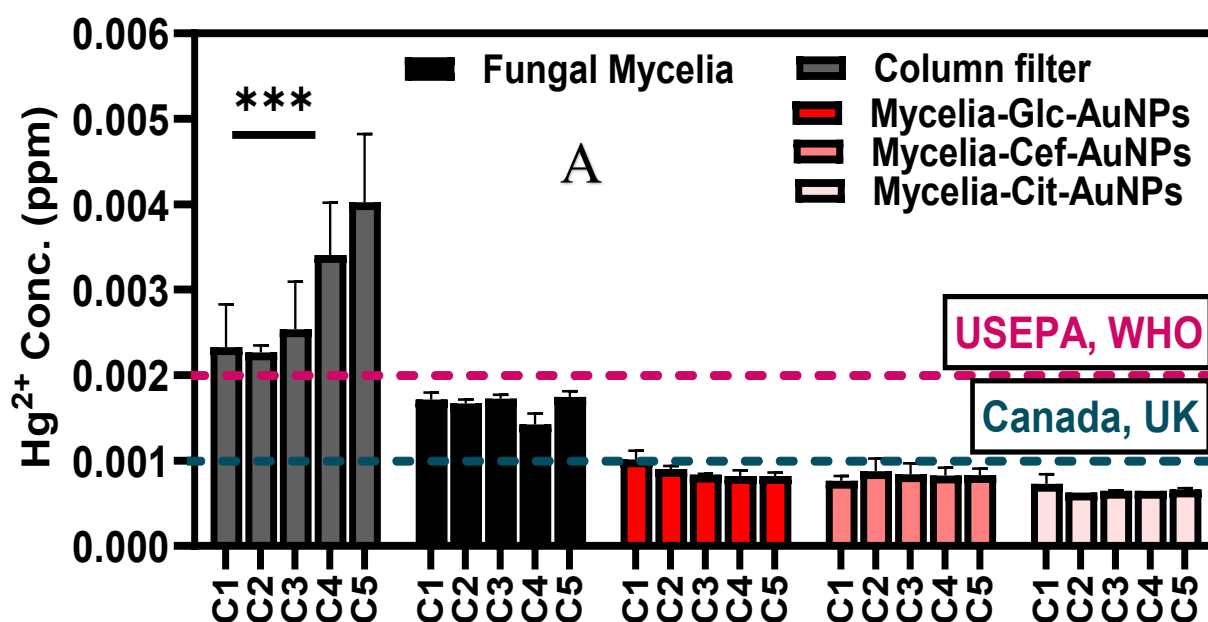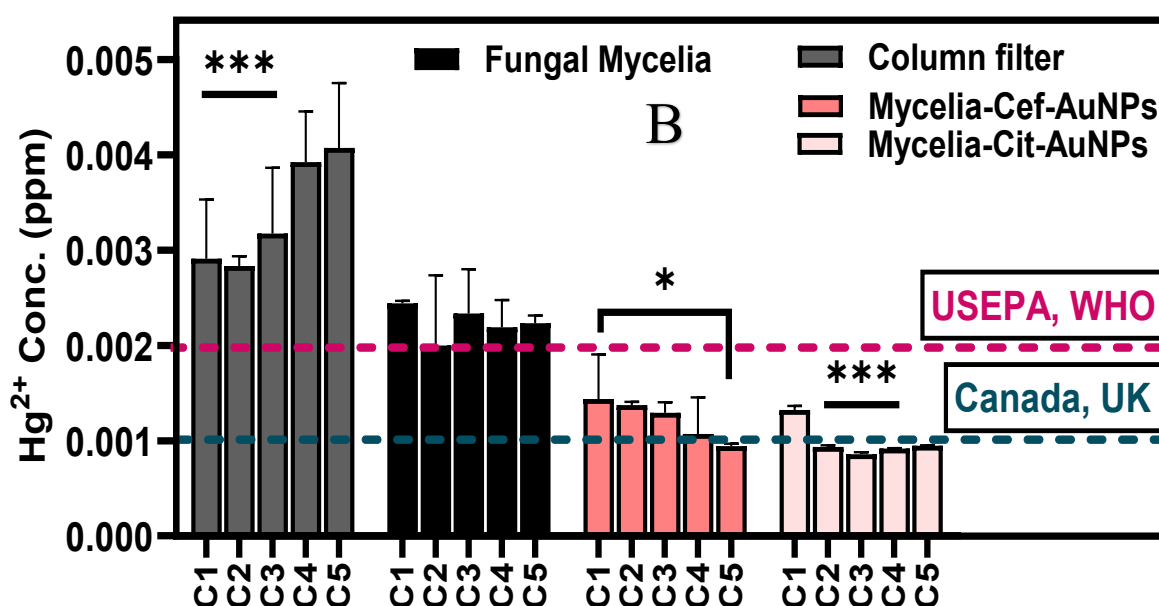
Figure 4.11: Mercury filtration using AuNPs-mycelia composites over five washes when the nitrogen source was (A) glutamine and (B) nitrate. The starting level of mercury is 5 ppb.

4.3.8.3. Recycling Mercury from AuNPs-Mycelia Composite

Recycling is a key concept in sustainable material use, and I tested the possibility of recycling mercury trapped in the AuNPs-mycelia composite using a pH adjustment to 8.0 for desorption. Progressive increases in mercury concentration were observed over five washes, depending on whether the composites were formed with glutamine or nitrate. Results, presented in Figures 4.12A and 4.12B, showed that mercury desorption from glutamine-treated composites was progressive but not significantly different over five washes. Cef-AuNPs and Cit-AuNPs groups showed a steady increase in mercury desorption, while Glc-AuNPs exhibited high initial mercury concentration, which reduced significantly in the second wash, followed by progressive desorption. This suggests that Glc-AuNPs may have mercury ions not firmly bound to the mycelia, relying on ion-ion interactions for filtration. For nitrate-treated composites, significant differences were observed over five washes, especially in Cit-AuNPs-mycelia. Cef-AuNPs-mycelia showed similar desorption patterns to Glc-AuNPs from glutamine treatments, possibly due to thorough distribution without clusters (Figure 4.7). Cef-AuNPs' non-homogeneous size might interfere with mercury release by offering different surface areas for binding. Generally, glutamine as a nitrogen source offers more potential for effective composite biofilters for mercury bioremediation. However, less than 10% of the mercury was removed over five washes, indicating the need for an alternative desorption system instead of ddH2O at

pH 8.0. The differing responses in ordinary mycelia suggest varying surface properties across the two different nitrogen sources, necessitating further exploration of their surface chemistries.
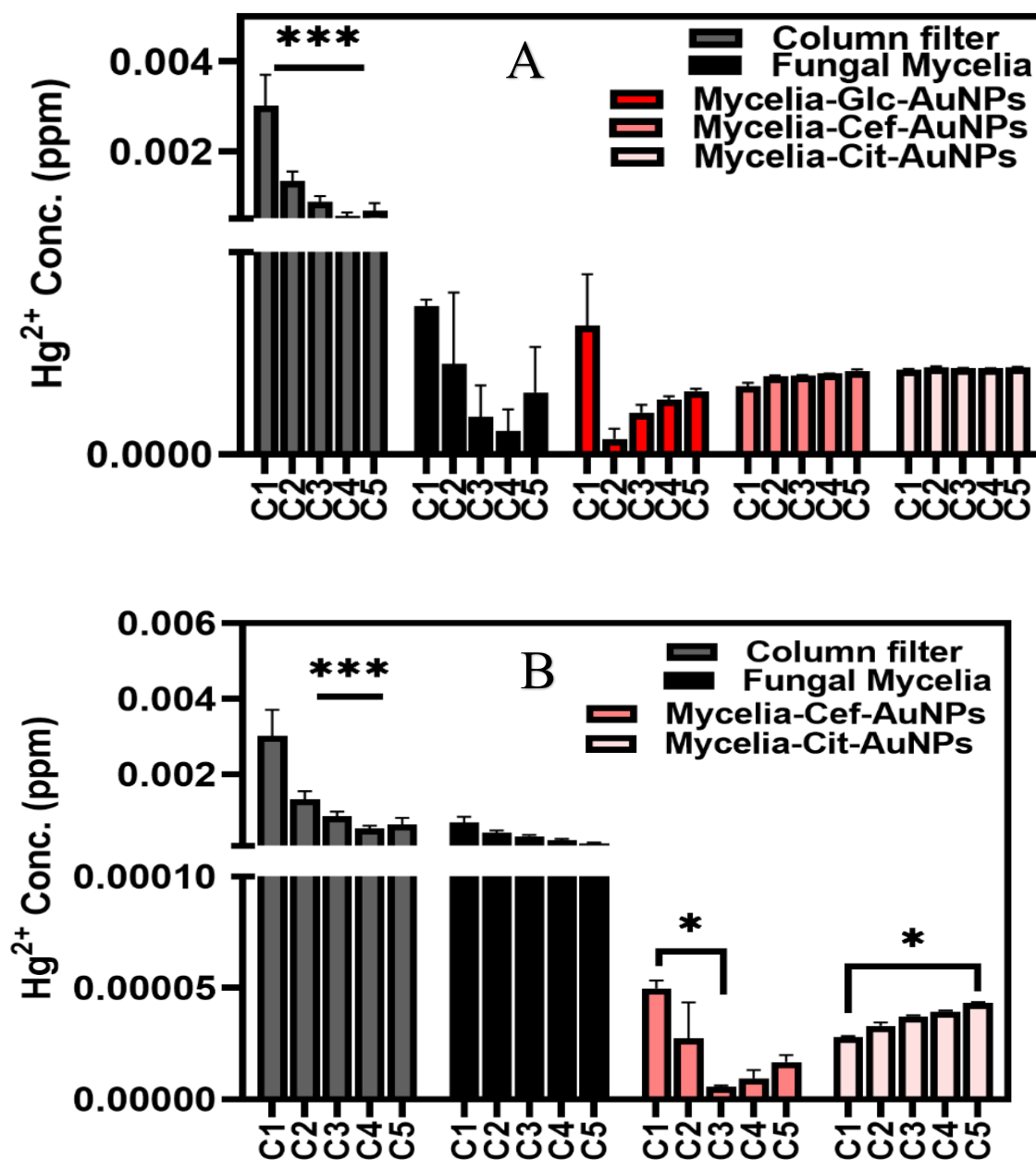
Figure 4.12: Mercury desorption from AuNPs-mycelia composites over five washes when the nitrogen source was (A) glutamine and (B) nitrate. The starting level of mercury is 5 ppb.

4.3.8.4. Surface Properties and Wettability of Mycelia and Implications for Filtration Efficiency

I evaluated the surface properties of the mycelia to determine if differences in wettability or surface-free energy could offer insight into the filtration efficiency when the fungus was grown with either glutamine or nitrate as the nitrogen source. This evaluation was conducted on both sides of the mycelia, and the results are presented in Figure 4.13 below. From Figure 4.13A, which shows the contact angle in water, the growth face (GF) of the mycelia was slightly hydrophobic and less wettable under both nitrogen source conditions. However, the media face (MF) for both conditions was very wettable, with the glutamine inclusion showing better wettability in water. Diiodomethane easily wets the growth face of the mycelia grown with glutamine, indicating that the surface has more non-polar groups compared to those grown with nitrate (Figure 4.13C). For the media face, diiodomethane ran through both groups, indicating moderate surface energy and ease of wetting (Figure 4.13C). While this result does not provide enough information to make definitive conclusions about the effects of surface chemistry, the expression of more surface-free energy on the surface of the glutamine-treated mycelia could have led to improved surface interactions. It also indicates a better environment for AuNP assembly and mercury removal.
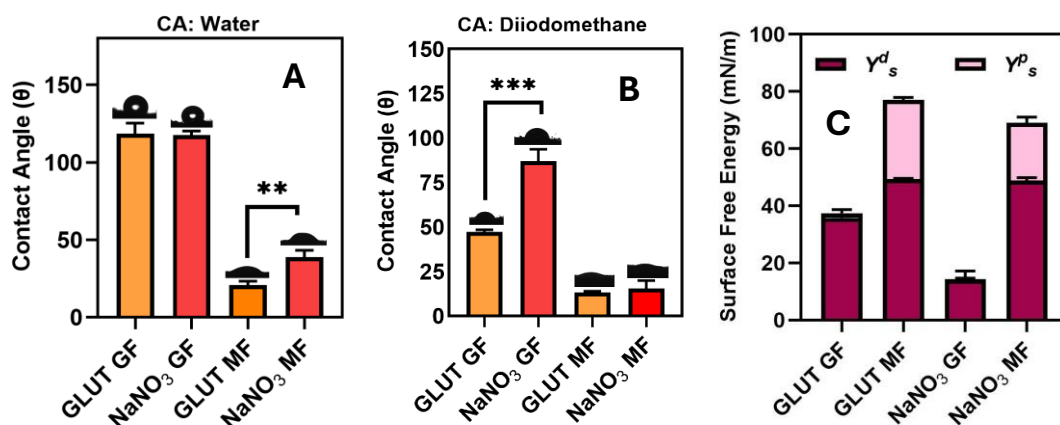
Figure 4.13: Evaluation of the surface properties of mycelia grown with either glutamine or nitrate as the nitrogen source. (A) contact angle in water; (B) contact angle in diiodomethane (C) surface free energy for both polar and non-polar groups

4.4. Experimental Challenges and Solutions Relevant to this Chapter

The formation of AuNPs-mycelial composites reported in this chapter presented several challenges due to the biomimetic nature of the process and the need to replicate a natural phenomenon on a laboratory scale. However, these changes also presented learning

opportunities both in method improvement and learning. The prominent challenges and their solutions are as follows:

1. **Materials Interaction with the Electron Beam of SEM**: As a biological sample, the mycelia could not withstand very high accelerating voltages (20kV) or probe currents (15 mAh) for imaging at high magnifications (above 70,000x). This led to the burning of samples, necessitating images to be taken at lower magnifications. To manage this, the accelerating voltage and probe current were reduced, samples were realigned, and stigmation was checked.

2. **Charge Effects**: The AuNPs assembled on the mycelia surface had their respective surface charges (reported as zeta potentials in Chapter 3). Particularly for composites formed from citrate AuNPs, charging effects caused the sample to drift on the stage. To address this, a thin layer of copper tape was used to form an electron bridge on the SEM stub holding the sample, which helped with electron distribution and reduced drifting.

3. **Interference with EDX Mapping**: The challenges initially affected the elemental mapping of the sample by SEM/EDX from the preliminary evaluation. Since EDX maps focus on a specific area within the samples and must remain stable until scanning is completed, drifting or charging could compromise result quality. To address this, EDX maps for Au were obtained in both spot and map scanning modes at higher and lower magnifications, yielding consistent and high-quality results in the main experiments.

4.5. Methodological Challenges in Identifying Mycelial Components Binding to AuNPs for Composite Biofilter Formation

I conducted an experiment to identify the specific component of the mycelia that binds to AuNPs to form a composite biofilter for each group, but the current methods were unsuccessful. The experiment involved multiple stages: fixation in osmium tetroxide, embedding in 3% low-gelling agarose, en-bloc staining with 1% uranyl acetate, multistep dehydration with increasing alcohol concentrations (50%, 70%, 90%, 100%), infiltration with a propylene oxide-resin mixture and 100% resin, sectioning of TEM samples into 500 nm slices collected onto APES-coated glass slides, staining with toluidine blue in methanol, washing with 90% ethanol, and viewing with an upright microscope, then TEM imaging. The goal was to obtain TEM images of the slices clearly showing the components of the mycelia that binds AuNPs in each group. However, after two attempts, the resin formed was not strong enough for microtome sectioning. With ten samples each for the nitrate and glutamine groups, repeating the experiment was unrealistic within the time frame for the doctoral research as new samples needed to be grown.

Despite these challenges, this experiment is intriguing as it connects material and environmental science with biochemistry.

4.6. Biofiltration with *A. niger* for Mercury Removal: Limitations and Scope

This novel study was conducted exclusively on *A. niger*, and its findings may not apply to other strains. Additionally, the biofiltration systems were tested solely for mercury bioremediation, and their effectiveness for other heavy metals or pollutants is beyond the scope of this research. I have documented the effects of varying nitrogen sources (nitrate and glutamine) on the yield and efficiency of the biofilter under laboratory conditions. However, these results may differ in non-laboratory environments or when other nutrient sources (e.g., carbon) are altered.

4.7. Conclusion

This study has successfully demonstrated the potential of *A. niger* mycelia functionalized with gold nanoparticles (AuNPs) as a sustainable and reusable biofilter for mercury bioremediation. By leveraging the unique properties of AuNPs and the inherent capabilities of *A. niger*, a composite material was developed that not only detects mercury but effectively removes it from aqueous solutions to concentrations below the World Health Organization's (WHO) maximum allowable limit. Key findings include the significant influence of nanoparticle concentration, nitrogen source, and growth duration on the deposition of AuNPs on *A. niger* mycelia, with glutamine enhancing mycelial yield and facilitating higher AuNP deposition, whereas nitrate favored specific AuNPs' functionalization efficiency. The exposure to AuNPs elicited varied physiological changes in *A. niger*, notably increased sporulation, particularly with nitrate as the nitrogen source, contributing to the effective integration of nanoparticles. The biofilters created from these composites exhibited exceptional mercury removal efficiency, outperforming conventional industrial filters, and the system's reusability and potential for mercury recovery underscore its eco-friendly and cost-effective attributes. Differences in surface free energy and wettability, as determined by nitrogen sources, were shown to influence filtration efficiency, providing insights into optimizing the composite's performance. This research underscores the innovative integration of fungal materials and nanotechnology for environmental applications, bridging gaps in mercury remediation and advancing sustainable practices.

CHAPTER 5

5.0. Correlating The Effect of 'Food' Source (Carbon) on the Mechanical Properties and Wettability of Fungal Mycelia

In this chapter, I investigated how different sugars and varying sugar concentrations affect the mechanical properties and surface wettability of five fungal strains (*Aspergillus niger*, *Botrytis cinerea*, *Rhizopus oryzae*, *Trametes versicolor*, and *Schizophyllum commune*). My findings reveal distinct sugar preferences in *R. oryzae* and demonstrate the impact of sugar concentration on mycelial characteristics and surface wettability across the fungal groups. Fungal mycelia are a suitable alternative to animal or petrochemical-derived materials with a broad range of sustainable applications, from bioremediation to biomaterials (Amobonye et al., 2023). Understanding how different carbon sources influence mycelial growth and properties is essential for optimizing their use. In the first experiment with *R. oryzae*, I focused on monosaccharides (glucose, fructose, galactose, and xylose), sugar alcohol (xylitol), and disaccharides (maltose and sucrose) as potential carbon sources. Minimal medium (MM) and potato dextrose broth (PDB) were employed as controls in the two-dimensional (2D) growth of the fungus. I observed a clear preference in *R. oryzae* for specific sugar types as carbon sources, as evidenced by mycelial growth and yield. Except for minimal media (MM), galactose, and sucrose treatments, all other groups produced sufficient mycelia for mechanical testing. Interestingly, these mechanical properties were independent of whether the test carbohydrates were monomeric or disaccharides. Notably, the 30 mM glucose-mycelia consistently exhibited favourable mechanical properties, including thickness, strength, elongation potential, and stiffness. In the second experiment, I included all five fungal strains which were either grown in PDB, MM, or MM with sugar as a carbon source at values from the literature reported to be optimum for a particular species (the concentration of sugar was also doubled). To ensure comparable structural and mechanical outcomes, I conducted this experiment using mycelia grown in both solid and liquid media under identical conditions. Notably, minimal media lacking sugars were unsuitable for mycelial growth, thus no results for mechanical testing or tensiometry are presented. When glucose or sucrose serves as the carbon source (for *A. niger*, *B. cinerea*, and *R. oryzae*), elevating the sugar concentration in minimal media from 60 mM to 120 mM significantly affects specific mechanical parameters and surface wettability for fungi grown in both liquid and solid media. Mycelia grown in 120 mM sugar concentration exhibited substantial thickness, impacting several measurable

parameters. Rapid synthesis of chitin in the cell wall due to sugar treatment accounts for this. In contrast, when *T. versicolor* and *S. commune* were cultivated in 30 mM and 60 mM fructose (in MM), fructose did not favour mycelial growth, resulting in poor mycelia development. Interestingly, mycelia which were grown in PDB displayed both qualitative and quantitative yield, characterized by increased thickness and pronounced hydrophobicity. Also, mycelial wettability increased as fructose concentration decreased, emphasizing the importance of sustained nutrient availability and the production of mycelial components that contribute to hydrophobicity. In addition, increasing fructose concentration had an impact on certain mechanical parameters. This study points to the significance of considering different carbon sources and concentrations in shaping mycelial structure and tunability. Furthermore, it establishes the relevance of this experimental approach for directing fungal growth toward desired mechanical and wettability properties.

Key Words: Fungal mycelia, Wettability, Hydrophobicity, Surface energy, Stiffness, Elasticity, rigidity, elongation potentials.

5.1. Introduction

Fungi comprise thousands of strains across different species and complexities, they represent the second-largest eukaryotic group of living organisms on earth (Raja et al., 2017). Amongst this class, there are broad diversities in their structural and biological properties, and this is the basis for their selection for different applications, especially in biomaterials or mycelia-based engineering (Naranjo-Ortiz & Gabaldón, 2020). Fungi have different microstructural arrangements to which their hyphae filaments conform to form mycelia (Islam et al., 2017), this arrangement (hyphae morphogenesis) into dense mycelia networks also depends on the degree of branching, branching patterns, and the organization of filaments (Lin et al., 2015). These characteristics play a huge role in the mycelia properties and choice of their selection for different applications (Lin et al., 2015). Studies have shown that these structural and functional properties can be tuned by altering certain external factors which alters their natural biochemistry and physical properties (Haneef et al., 2017). For example, in a study by (Tacer-Caba et al., 2020), the author established that varying the humidity conditions *Richoderma asperellum* and *Agaricus bisporus* grown on rapeseeds alters the stiffness of their mycelia. This shows the influence of environmental factors on the manipulation of mycelia properties. *In another study* (Schoder et al., 2024), established how environmental and nutritional conditions affected both the growth rate and the final mycelia outcomes of three fast-growing strains *Ganoderma lucidum*, *Pleurotus ostreatus*, and *T. versicolor*. Other factors such as temperature,

pH, and carbon and nitrogen sources have been shown by researchers to also influence the properties of fungal mycelia such as biosynthesis of compounds, metabolic process and external secretions (Achimón et al., 2022; Lazarević et al., 2016). While scientists have documented these over the years, correlating multiple properties of fungal mycelia under a test condition gives better understanding of the impacts of such a tuning process. This is a more robust approach that does not threaten fungal response experiments in isolation, and it provides researchers and industry professionals with an enhanced understanding of the valuable insights that can be gained from detailed fungal morphometrics. In this study, I correlated the effects of types and variations of concentrations of carbohydrates, to the mechanical properties and surface wettability of five strains of fungi (*A. niger*, *B. cinerea*, *R. oryzae*, *T. versicolor, and S. commune*), both in liquid and solid media. I also developed a new approach that is suitable for the removal of thin mycelia from a solid agar support, without damage to the integrity of the mycelia. My goal for this study was primarily to establish the intersection between carbohydrate types or concentration on the mechanical parameters and surface chemistry of the mycelia of selected strains. The concentration utilized in this study was derived by extrapolation from a separate ongoing investigation in which optimal fungal growth was observed. Subsequently, I selected best concretion of growth for each fungus and also doubled this concentration to facilitate a comparative analysis of the effects. This chapter addresses Objective 5 by investigating how carbohydrate type and concentration influence the mechanical and surface properties of five fungal strains.

5.2. Materials and Methods

5.2.1. Materials

Potato dextrose broth (P6685), agar (05040), Na_2HPO_4 (7558-79-4), Na_2SO_4 (7757-82-6), $(NH_4)_2C_4H_4O_6$ (3164-29-2), D-(+)-maltose monohydrate (6363-53-7), D-(+)-glucose (50-99-7), D-(−)-fructose (57-48-7), KH_2PO_4 (7778-77-0), $MgSO_4·7H_2O$ (10034-99-8), PBS-phosphate buffered saline (P4417), urea (57-13-6), D-(+)-xylose (58-86-6), $NaNO_3$ (7631-99-4), sucrose (57-50-1), Na_2SO_3 (7757-83-7), $FeCl_3 · 6H_2O$ (10025-77-1), KCl (P9333) and agarase from *Pseudomonas atlantica* (≥5,000 units/mg protein)- 37288-57-6; were sourced from Sigma Aldrich-Merck Life Science UK Limited, The Old Brickyard, New Rd Gillingham, Dorset SP8 4XT. $ZnSO_4·7H_2O$ (7446-20-0) and $MgCl_2·6H_2O$ (7791-18-6) were sourced from BDH Chemicals LTD, Broom Road, Poole, BH12 4NN United Kingdom, and $FeSO_4·7H_2O$ (11472178) was procured from Fisher Scientific, Leicestershire, LE11 5RG. All reagents were of analytical grade and used as per manufacturer recommendations.

5.2.2. Methods

The fungi strains that were studied are *R. oryzae* indexed NTUCC (Unknown strain), *S. commune, T. versicolor* indexed, *B. cinerae* indexed, and *A. niger* (ATCC 1015). Aside from *A. niger* (ATCC 1015), provided by collaborator Dr. Matthias Brock of Nottingham University, the remaining samples were sourced from the Nottingham Trent University Culture Collection (NTUCC).

5.2.2.1. Effect of Selected Carbon Sources on the Mechanical Properties of *R. oryzae*

To test for the effects of different concentrations of selected monosaccharides and disaccharides on the mechanical properties of *R. oryzae*, the fungus was grown in 200 mL Pyrex conical flasks. Each flask contained 100mL of either glucose (30 mM), fructose (30 mM), xylose (150 mM), galactose (20 mM), maltose (50 mM), sucrose (30 mM) and xylitol (150 mM). The sugars were prepared in minimal media that is specific for *R. oryzae*, and the content of the MM (salt mix and nitrogen source) is presented as MM4 (Table 5.5) in the appendix. The fungus was also grown in MM4 (without sugars), and PDB as controls. The fungal growth lasted for 10 days at 25 $^\circ$C (Labnet international 211DS Shaking Incubator, Appleton Woods Ltd., Birmingham, UK). The sample preparation and the mechanical test procedure are as per the description in the section below.

5.2.2.2 Impact of Carbon Sources on Fungal Mycelia Properties and Wettability

For the second experiment, the five fungal strains were each grown in 200mL flasks on potato dextrose broth (PDB), Specific Minimal Media (MM), and sugar-supplemented minimal media at two different concentrations (Appendix table 5.1). The fungi were grown for 15 days (except *R. oryzae* which was grown for 7 days) after which the mycelia were recovered from the growth media and washed 5 times with 200 mL ddH$_2$O. *B. cinerae* is pH sensitive and was grown at pH 4.5. Before freeze-drying (BT4KZLdryer-VirTis), the mycelia were frozen at -45 $^\circ$C in a conventional freezer (TEFCOLD SE-45 Series) for 1 h and subsequently freeze-dried for 3 days (condenser -70 $^\circ$C, Ambient 37.2 $^\circ$C, Vacuum 52mT). To compare the results, I conducted a separate replication of the experiment using solid media. I added 2% agar to the nutrient media (25 mL) and grew the fungi on polystyrene Petri plates. Each group had 3 biological and 3 technical repeats. All the media used in this study were sterilized before use (Crystal – MP25, Rodwell Scientific, UK), and all incubations were done in a Labnet international 211DS Shaking Incubator, Appleton Woods Ltd., Birmingham, UK. Each fungus was grown at its optimum condition and varied nutrients (in liquid and solid substrates). These conditions

are summarized in Table 5.1 in the appendix. Detailed information about the minimal media composition used for each strain is described in Table 5.2-5.5 in the Appendix.

5.2.2.3. Agar Digestion from Solid Substrate Before Analysis

Three Different methods were employed to remove the agar that is bound to the mycelia on solid substrates, the most suitable method was then adopted to generate a clean mycelium before mechanical and surface wettability tests. The presence of agar was monitored via FTIR (Thermo Scientific NICOLET iS50 FT-IR, with a DTGS detector and a KBr Split-filter.), Physical damages on mycelia were also noted.

Method A: Flash Heating Method

In a water bath (Nickel Electro^{TM} Clifton^{TM} Stainless Steel Digital DuoBath^{TM}), the Petri dish on which the fungal mycelia have grown was placed in hot water (100 ^{o}C) for 10 min (flash heating). The lid of the water bath was then opened to avoid condensation of water on the mycelia. The melted agar was washed and then washed 3* with 600mL ddH$_2$O before freezing and drying as described above.

Method B: Manual-Assisted Method

The agar on the mycelia was manually removed using a pair of fine tweezers (Dumont) and a sterile scalpel and dropped on a foil. 20mL of Phosphate buffer (PBS) was poured into a Petri dish and heated to 85 ^{o}C using a water bath. The mycelia were then transferred into the heated PBS and left for 15 min for the agar to melt. The PBS and melted agar were then washed off as described above for method 1.

Method C: Agar Removal Via Hydrolysis with Agarase

This method is as to method B but involves the use of an enzyme for agar digestion. Following manual removal of agar with a scalpel, the unremoved agar was treated with different concentrations of agarase (0.5 U/ mL, 1 U/ mL, 5 U/ mL) and incubated at 43 °C for 23 h while constantly rotating at 21 RPM in a Labnet international 211DS Shaking Incubator. The resulting mycelia was then washed with washed 3* with 600 mL ddH$_2$O. The agarase was prepared as per the manufacturer's protocol.

5.2.4 Effect of Carbon Sources on the Chitin Profile of Selected Fungal Strains

The dried mycelia of *A. niger*, *B. cinerea*, and *R. oryzae* were blended into a fine mass using a laboratory mortar and pestle. For each strain, 0.04 g of the mycelia was suspended in 4mL of 2M NaOH and heated at 90°C for 2 h while stirring (Stuart Digital Water Bath 15 L, SWB15D). The resulting chitin residue was collected, thoroughly washed to neutrality with ddH$_2$O in an Eppendorf tube, and then dried, quantified, and characterized by FTIR. This experiment was performed in triplicates for the three groups in each strain (Senthilkumar et al., 2021).
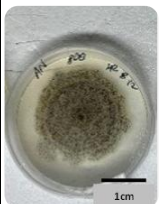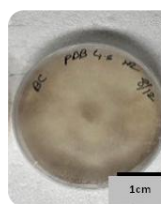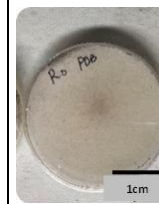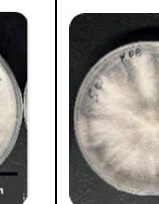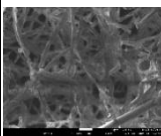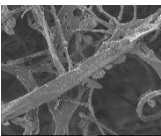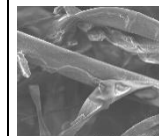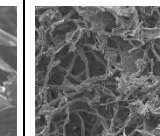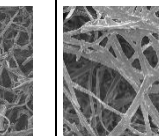
5.2.5 Analysis

For each group, experiments were performed in triplicate (both technical and biological), and the mean values with standard deviation from data analysis are reported in plots. One-way or two-way analysis of variance (ANOVA) was carried out to determine the significant differences among different treatment factors and their levels, and Tukey's Post hoc test was conducted for multiple comparisons amongst the means across different groups ($P < 0.05$). GraphPad Prism 10.0 under a laboratory licence was used for analysis. For all data analysed the level of significance is * ($p \leq 0.05$), ** ($p \leq 0.01$), and *** ($P \leq 0.001$).

5.3. Results and Discussion

The characteristics and identification of the selected fungal strains are summarized below.

Table 5.1: Summary of Fungal Characteristics, Hazard Groups, Morphological Characterization, and Representative Image of Fungal Growth on PDB.

Fungal	*A. niger*	*B. cinerea*	*R. oryzae*	*T. versicolor*	*S. commune*
Physical appearance (Scale bar: 1 cm)					
Hazard group	Cat.1	Cat.1	Cat.1	Cat.1	Cat.1
SEM of mycelia. (Scale bar: 10 μm)					

5.3.1. Effect of Different Sugars on the Mechanical Properties of *R. oryzae*

In Figure 5.1, I present a typical result illustrating the impact of different sugars on the mechanical properties of *R. oryzae* after 10 days of growth. Notably, *R. oryzae* exhibited a clear sugar preference, as evidenced by the quality of fungal growth and mycelial yield across the test groups (Figure 5.1). As a member of the Mucorales order, *R. oryzae* is favoured in material science due to its unique morphology. Specifically, growth in Potato Dextrose Broth (PDB, 24 g/L) resulted in the thickest mycelia, characterized by high endurance and elongation potential. However, this group was comparatively less flexible, possibly due to its denser structure. Xylose and xylitol (150 mM in 100 mL MM) yielded mycelia with similar thickness but maintained flexibility, except for xylitol. While the specific research context may vary slightly, this observation aligns with previous studies regarding the efficient utilization of xylose and xylitol by *R. oryzae* (Maas et al., 2008). The mycelia from the hexose monosaccharide groups exhibited distinct mechanical properties due to the varying preferences of each sugar as a carbon source. Notably, in this experiment, the concentration of maltose (50 mM) exceeded that of other hexose monosaccharides (30 mM for fructose and glucose). Despite this, the mycelium from glucose exhibited greater thickness, while mycelia grown in the presence of fructose demonstrated enhanced durability. All three groups displayed similar stiffness, yet maltose (50 mM) yielded the most elastic mycelia among the hexose groups. These results suggest that mycelia from the glucose and fructose groups at 30 mM exhibited an average of the tested mechanical properties, prompting further investigation into the specific roles played by these sugars in mycelia morphometrics. Interestingly, the groups cultured in ordinary minimal media (MM), galactose (20 mM), and sucrose (30 mM) did not exhibit significant growth suitable for mechanical testing. The absence of sufficient nutrients, particularly carbon sources, in minimal media may explain the limited germination and growth of mycelia (Kim & Kim, 2017). This emphasizes the critical role of nutrient availability for fungal germination. In the case of galactose, its low concentration might have hindered high-quality mycelial growth. Previous studies have indicated that galactose is not an optimal carbon source for fungi (Battaglia et al., 2011; Chroumpi et al., 2022). Specifically, Battaglia et al., 2011 demonstrated that *R. oryzae's* inability to metabolize galactose significantly was attributed to the lack of essential xylanolytic enzymes. These findings suggest that *R. oryzae's* sugar metabolism pattern is influenced by its genetic evolution. The selection of sugars utilized in this study is informed by prior research demonstrating their significant effects on fungal growth (Brannon, 1923; Hamad et al., 2014; Hao & Barker, 2022).
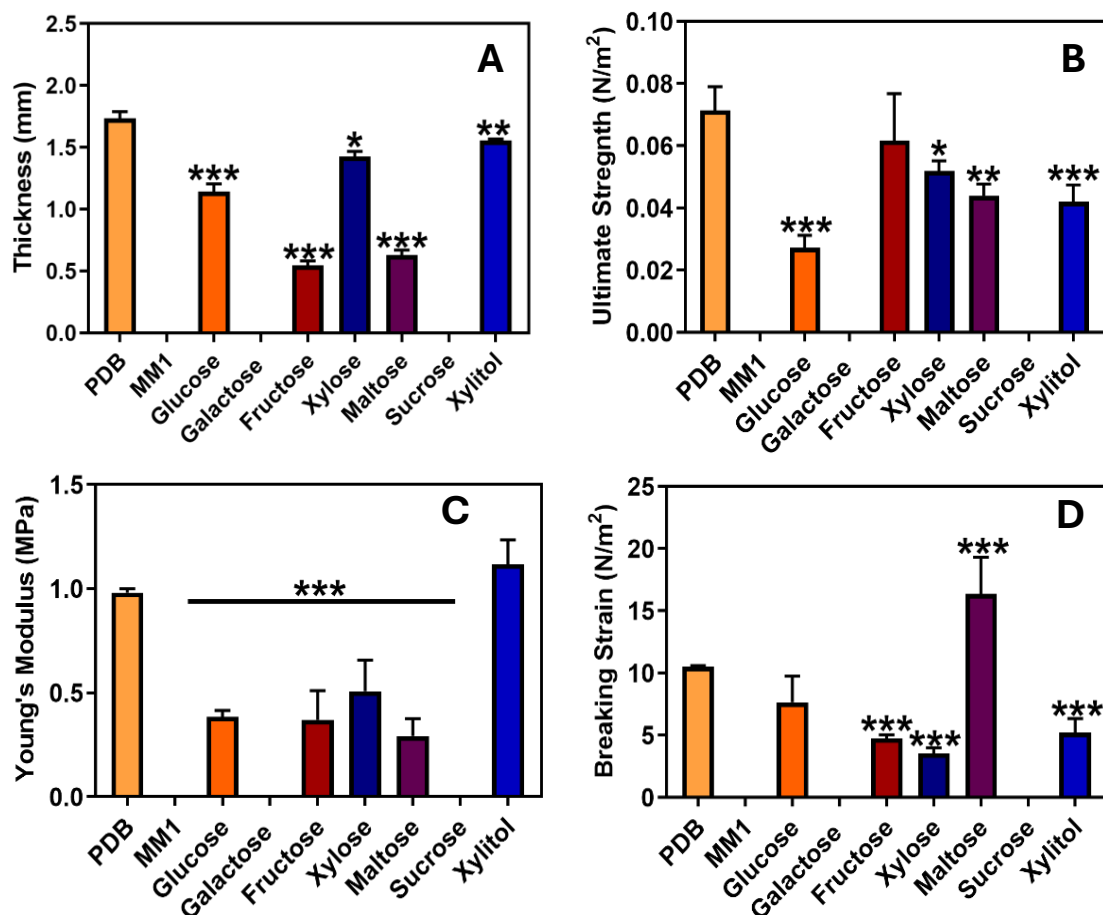
Figure 5.1: The mechanical properties the mycelia of *R. oryzae* under various carbohydrate carbon sources (A), thickness (B), ultimate strength (C), breaking strain and (D), Young's modulus. The level of significance is * ($p \leq 0.05$), ** ($p \leq 0.01$), and *** ($P \leq 0.001$).

5.3.2. Agar Digestion from the Solid Substrate Before Analysis

Before mechanical analysis, I tried several approaches to remove the agar bound to the mycelia from the solid substrate, aiming to ensure the mycelia remained intact without damage that could significantly impact mechanical outcomes. The agar remnant in each method was monitored by FTIR characterization, with a focus on the presence or absence of peaks that are unique to the agar. The FTIR plot is presented in Figure 5.2. The peaks at 930 cm^{-1}, 890 cm^{-1}, and 769 cm^{-1} for agar-agar correspond to the C-O of 3,6-anhydrogalactose, C1-H deformation vibration of beta-mannuronic units, and the skeletal bending of the beta-galactose ring, respectively (Thombare et al., 2023). The enzymatic process with 1 and 5 U/ mL of the enzyme was successful in digesting the agar, completely removing it from the mycelia. Additionally, scraping the agar with a spatula and heating it for 20 min at 85 °C in PBS also resulted in mycelia showing no agar peaks. I found that melting the agar covered by mycelia at 100 °C

was a fast method, but it left traces of agar stuck to the mycelia even after washing. Considering enzyme costs and my goal to use cost-effective methods, I opted for heating at 85 °C in PBS for 20 min. Interestingly, *R. oryzae* treated with 60 mM and 120 mM of glucose in Minimal media showed very reduced adhesion to the agar, allowing easy removal with a spatula without heating. This process is documented in a video available in the appendix.
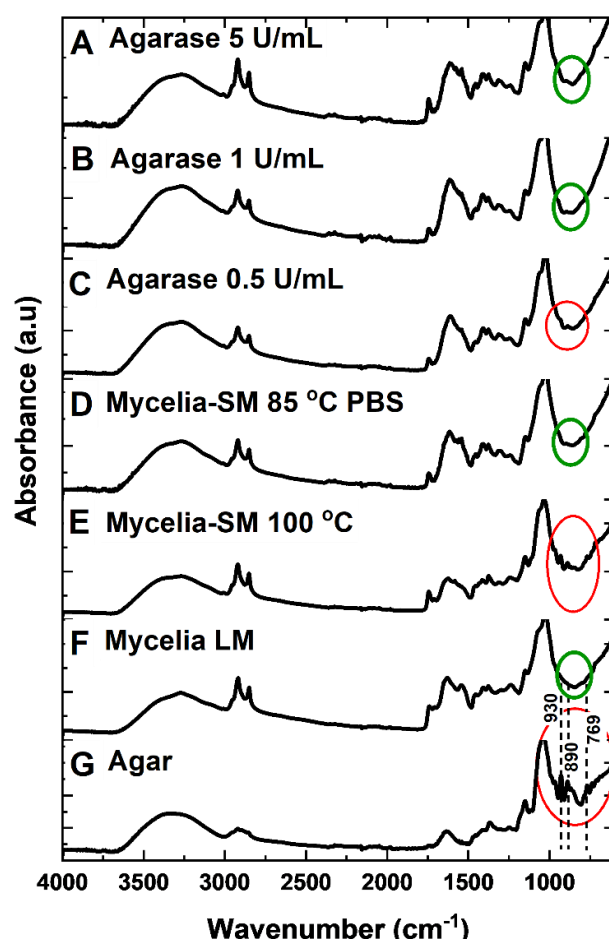
Figure 5.2: FTIR spectra indicating the presence or absence of agar on the mycelia after treatment under different conditions. SM: denotes Solid media; LM: denotes Liquid media. Green ring indicates no agar peaks while the red ring indicates agar peaks present.

5.3.3. Effect of Glucose Concentrations on Mechanical Properties and Surface Wettability of *A. niger* in Liquid and Solid Media

I investigated the mechanical properties and surface wettability of *A. niger* mycelia in response to varying glucose concentrations. The selection of glucose was informed by its observed effects on fungal growth in a separate experiment, as well as corroborated by earlier studies that demonstrate the selective growth of *A. niger* on various carbon sources. My results demonstrate significant effects on mycelial width, stiffness, elongation potential, flexibility,

and surface wettability. These are presented in Figures 5.3A and 5.3B below. *A. niger* is a filamentous fungus commonly known for its rapid sporulation, economic and health importance, melanin pigment, and as a pathogen in wounds and fruit rots (Munhuweyi et al., 2016). I aimed to understand how glucose concentration influences its growth and properties. At 120 mM glucose, mycelial width significantly increased from 0.72 ± 0.09 mm (at 60 mM) to approximately 1.28 ± 0.28 mm in liquid media. Similar observations were recorded in solid media, where mycelial width increased from 0.28 ± 0.01 mm (at 60 mM) to 0.33 ± 0.02 mm (at 120 mM). The mycelia at 60 mM were a fragile sheath that physically broke when over-folded, but this did not impact its ability to bear loads or potential for elongation in liquid media, but it does in solid media. Except for 60 mM-mycelia, the mycelia from other groups were quite hydrophobic (Contact angle >120°), and the representative surface free energy (SFE) for the non-polar component was above 80% of total SFE indicating hydrophobicity. In solid media, the SFE energy for the polar component was more conspicuous, and the mycelia were quite wettable with a contact angle below 70° across all groups. The observed differences in surface wettability between solid and liquid cultures warrant further investigation. However, these current findings contribute to my understanding of *A. niger* behaviour in response to nutrient availability (glucose).
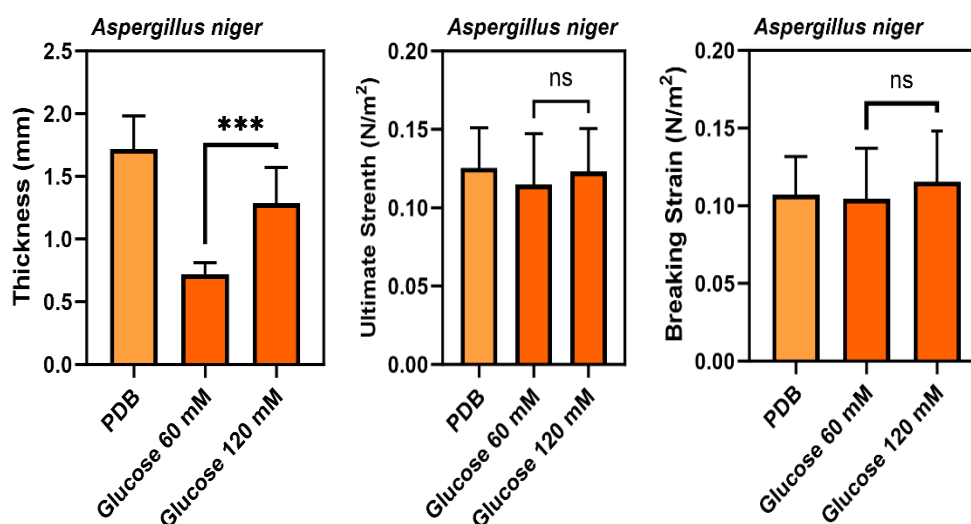
Figure 5.3A: The mechanical properties of the mycelia of *A. niger* in liquid media under varying glucose concentrations (A), thickness (B), ultimate strength (C), breaking strain (D), Young's modulus (E), contact angle in water and (F) surface free energy of the polar and non-polar component of the mycelia. The level of significance is * ($p \leq 0.05$), ** ($p \leq 0.01$), and *** ($P \leq 0.001$).

Figure 5.3B: The mechanical properties of the mycelia of *A. niger* in solid media under varying glucose concentrations (A), thickness (B), ultimate strength (C), breaking strain (D), Young's modulus (E), contact angle in Water and (F), surface free energy of the polar and non-polar component of the mycelia. The level of significance is * ($p \leq 0.05$), ** ($p \leq 0.01$), and *** ($P \leq 0.001$).

5.3.4. Effect of Glucose Concentrations on Mechanical Properties and Surface Wettability of *R. oryzae* in Liquid and Solid Media

I investigated the mechanical properties and surface wettability of *R. oryzae* mycelia in response to varying glucose concentrations. Research has indicated that Mucorales fungi exhibit varying sensitivity, and material yields to glucose concentrations compared to other strains (Brannon, 1923). However, the morphological response to variations of this specific sugar has not been reported. Understanding these dynamics will enable us to more effectively harness the potential of the fungus. My results demonstrate significant effects on mycelial width, stiffness, elongation potential, flexibility, and surface wettability, and this is presented in Figures 5.4A and 5.4B below. *R. oryzae*, belongs to the order Mucorales, it is a filamentous saprophytic fungus, and is very popular for its economic implication in mucormycosis (Tavvabi-Kashani et al., 2024). I explored how glucose concentration influences its growth and properties, and the results are presented as Figure 5.4 below. At 120 mM glucose, mycelial width increased significantly from 0.96 ± 0.09 mm (60 mM) to approximately $1.97 \pm 0.15.0$ mm in liquid media. Similar observations were recorded in solid media, where mycelia width increased from 0.067 ± 0.0081 mm (60 mM) to 0.49 ± 0.06 mm (120 mM). Surprisingly, mycelia from 120 mM glucose were more flexible than those from 60 mM, despite being the thickest among groups. However, their endurance decreased significantly, possibly due to less tightly packed mycelia. For the surface wettability, *R. oryzae* mycelia exhibited low contact angles (generally less 80º), indicating poor hydrophobicity. The interactive surface energy of polar components exceeded that of nonpolar components in both liquid and solid media, suggesting a wettable surface. Notably, the PDB-mycelia group in liquid media showed non-polar component surface energy exceeding 80% of the total surface energy. My findings highlight the critical relationship between glucose concentration and *R. oryzae* mycelial properties, with implications for its potential applications.

Figure 5.4A: The mechanical properties of the mycelia of *R. oryzae* in liquid media under varying glucose concentrations (A), thickness (B), ultimate strength (C), breaking strain (D), Young's modulus (E), contact angle in Water and (F), surface free energy of the polar and non-polar component of the mycelia. The level of significance is * (p ≤ 0.05), ** (p ≤ 0.01), and *** (P ≤ 0.001).

Figure 5.4B: The mechanical properties of the mycelia of *R. oryzae* in solid media under varying glucose concentrations (A), Thickness (B), Ultimate strength (C), Breaking strain (D), Young's modulus (E), Contact angle in Water and (F), Surface Free energy of the polar and non-polar component of the mycelia. The level of significance is * (p ≤ 0.05), ** (p ≤ 0.01), and *** (P ≤ 0.001).

5.3.5. Effect of Sucrose Concentrations on Mechanical Properties and Surface Wettability of *B. cinerea* in Liquid and Solid Media

I investigated the mechanical properties and surface wettability of *B. cinerea* mycelia in response to varying sucrose concentrations. My results reveal significant effects on mycelial width, stiffness, and elongation potential, presented in Figures 5.5A and 5.5B below. *B. cinerea*, a common fungal pathogen exhibits remarkable environmental adaptability, therefore I explored how sucrose concentration influences its growth and mechanical properties. The choice of sucrose for *B. cinerea* was based on previous studies. (Brannon, 1923) reported in their review that *B. cinerea* is sensitive to variations in carbohydrate concentration. A more advanced study (Vercesi et al., 1997) later determined these variations' morphological impact on branching and hyphae tips' growth rate, showing significant effects. This knowledge is vital for understanding fruit invasion by *B. cinerea* and the progression of colonization patterns. In this study, there was a remarkable impact on mycelia width. In liquid media, mycelial width increased from 1.19 ± 0.22 mm (at 60 mM) to 3.80 ± 0.39 mm (at 120 mM), representing a 233.3 % increase, while 57.14 % increase was also recorded in solid media (0.75 ± 0.05 mm to 1.06 ± 0.03 mm). The mycelia of *B. cinerea* became stiffer, with a decrease in elongation potential (approximately 0.2 N/m² in solid media and 0.035 N/m² in liquid media). The strength also significantly decreased with increasing sugar concentration, but this is only recorded in solid media. As for the surface wettability, the polar component expression increased, as evidenced by a low contact angle ($\theta < 100°$) and surface free energy (SFE) > 50% of the total SFE mN/m. Notably, the growth medium (solid vs. liquid) influenced wettability, particularly in the PDB group. The PDB-grown mycelia were hydrophobic (contact angle > 120°), while the non-polar component surface free energy exceeded 90% of the TSFE. The solid substrate mycelia showed greater expression of polar groups (contact angle < 50°), and thus very wettable across the treatment and control groups. The exact phenomenon for this is yet unknown but a study has shown that it is not due to the production of hydrophobins (Mosbach et al., 2011).
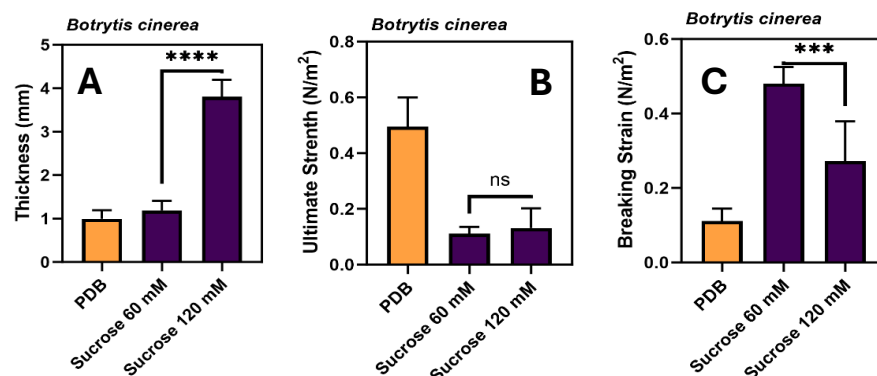
Figure 5.5A: The mechanical properties of the mycelia of *B. cinerae* in liquid media under varying sucrose concentration (A), thickness (B), ultimate strength (C), breaking strain (D), Young's modulus (E), contact angle in water and (F), surface free energy of the polar and non-polar component of the mycelia. The level of significance is * ($p \leq 0.05$), ** ($p \leq 0.01$), and *** ($P \leq 0.001$).
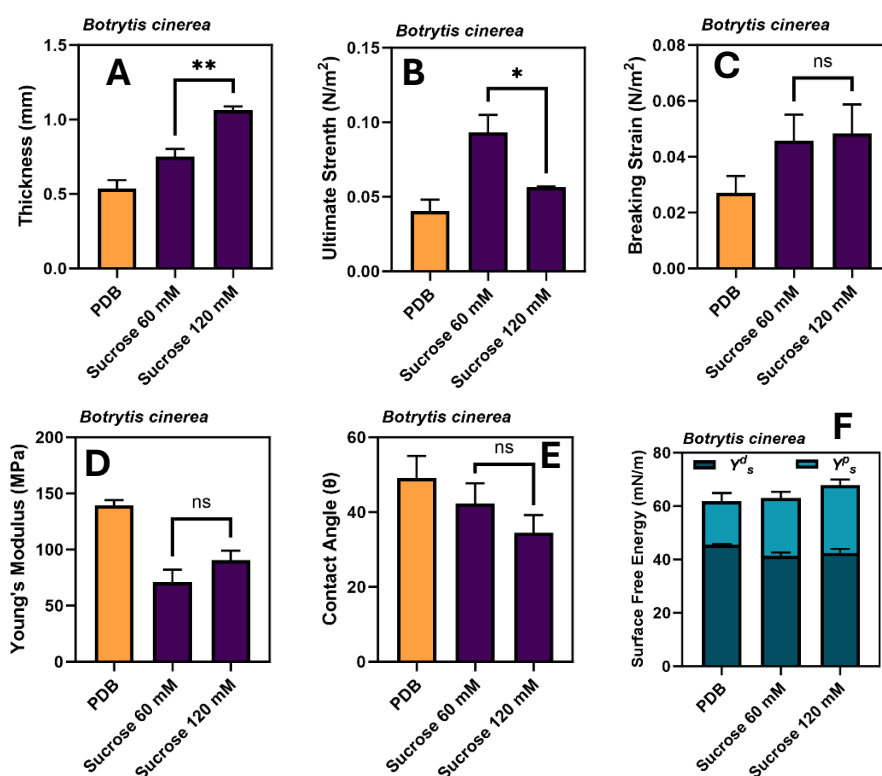
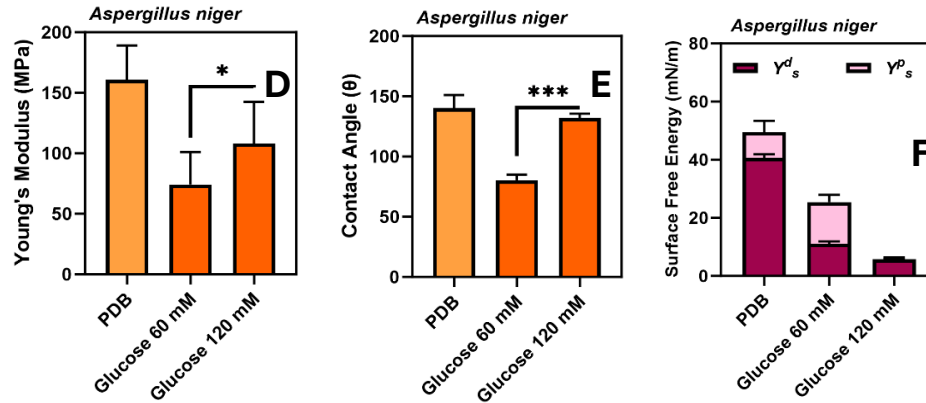Figure 5.5B: The mechanical properties of the mycelia of *B. cinerea* in solid media under varying glucose concentration (A) thickness (B) ultimate strength (C) breaking strain (D), Young's modulus (E) contact angle in water and (F) surface free energy of the polar and non-polar component of the mycelia. The level of significance; is * ($p \leq 0.05$), ** ($p \leq 0.01$), and *** ($P \leq 0.001$).
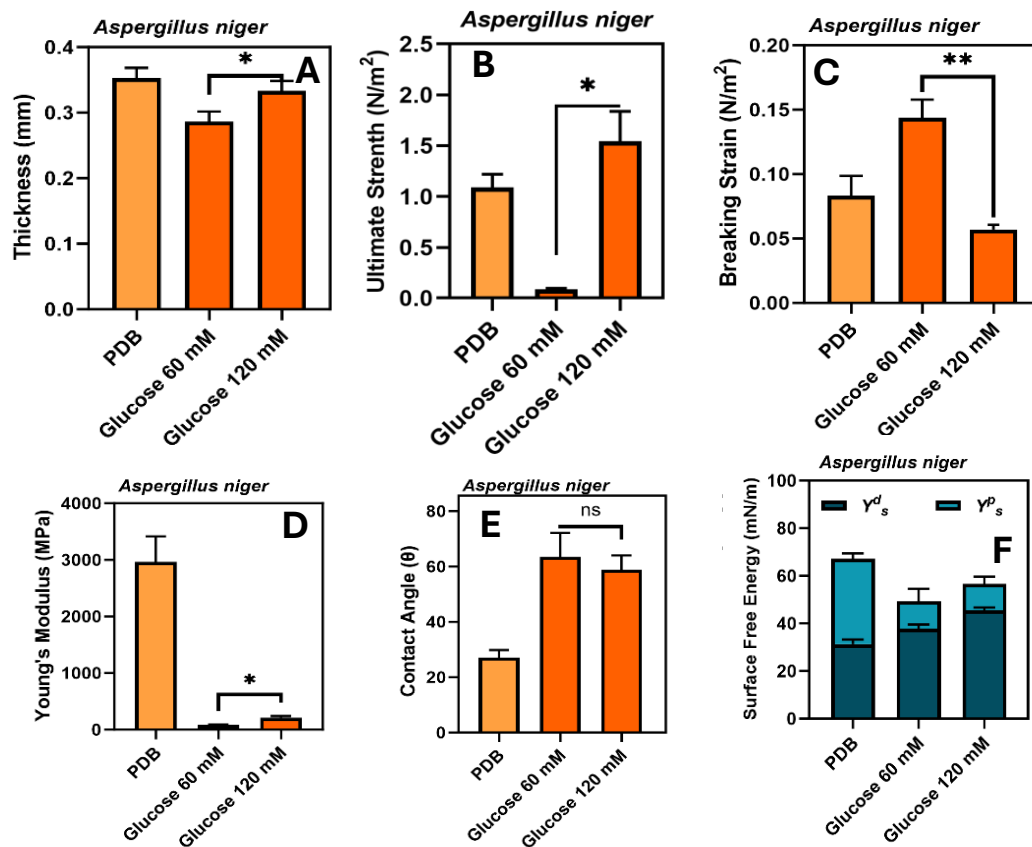
5.3.6. Effect of Fructose Concentrations on Mechanical Properties and Surface Wettability of *T. versicolor* in Liquid and Solid Media

I investigated the mechanical properties and surface wettability of *T. versicolor* mycelia in response to varying fructose concentrations. I selected fructose based on findings from a prior study that demonstrated its ability to reduce the total sugars present in the cell wall of *T. versicolor* (Pessoni et al., 2015). Understanding the mechanical dynamics of this phenomenon is essential due to the significant role of the fungus in various applications. My results reveal significant effects on mycelia width, stiffness, and elongation potential. The surface wettability was not impacted. These results are presented in Figures 5.6A and 5.6B below. *T.* versicolor is a polyporus (multicolor) fungus of the phylum Basidiomycota, this fungal has been used over the years in many sustainable applications because of its ability to bio-transform substrates (especially *lignocellulosic wastes*) owing to its metabolic prowess (Tišma et al., 2021). Therefore, I explored how fructose concentration influences its growth and mechanical properties. In liquid media, mycelial width increased from 0.17 ± 0.03 mm (30 mM) to 0.27 ± 0.0057 mm (60 mM), and from 0.025 ± 0.0057 mm (30 mM) to 0.061 mm ± 0.01 (60 mM) in solid media. This represents 38.4% and 104 % respectively. Even though this is not enough to make deductions on fructose suitability as a carbon source for *T. versicolor*, corresponding data from the PDB-mycelia groups where the mycelia width was 0.71 ± 0.091mm (SM) and 0.20 ± 0.03 mm (LM) respectively could be a pointer to this. However, a study by (Nguyen et al., 2021), has shown that fructose could be highly suitable for quality mycelia from *T. versicolor*, but at high concentrations of up to 15 g/L (83.26 mM). In my study, the increase in mycelia thickness impacted mechanical parameters. At 60 mM, the mycelia have better elongation potential in both solid and liquid media, but the ability to retain load (ultimate strength) only differed in liquid media. Generally, the mycelia were not very flexible, and the level of flexibility was significantly reduced with increasing fructose concentration. Except for the PDB-mycelia group in solid media (contact angle >100º) which has SFE for non-polar component > 90%, the mycelia from the fructose groups have a high proportion of surface free polar component and thus are very wettable.

Figure 5.6A: The mechanical properties of the mycelia of *T. versicolor* in liquid media under varying fructose concentration (A), thickness (B), ultimate strength (C), breaking strain (D), Young's modulus (E), contact angle in water and (F), surface free energy of the polar and non-polar component of the mycelia. The level of significance is * ($p \leq 0.05$), ** ($p \leq 0.01$), and *** ($P \leq 0.001$).
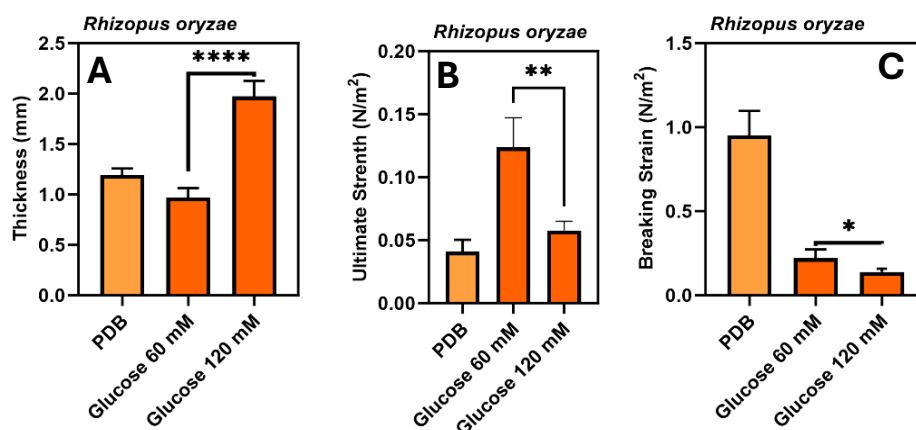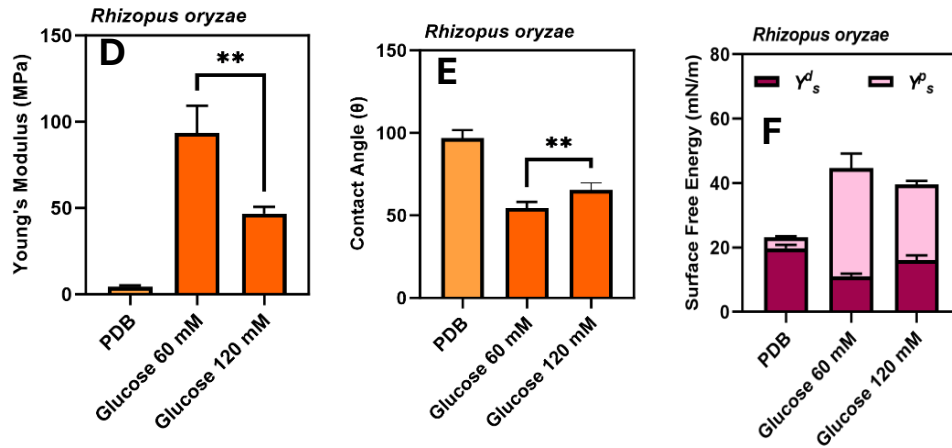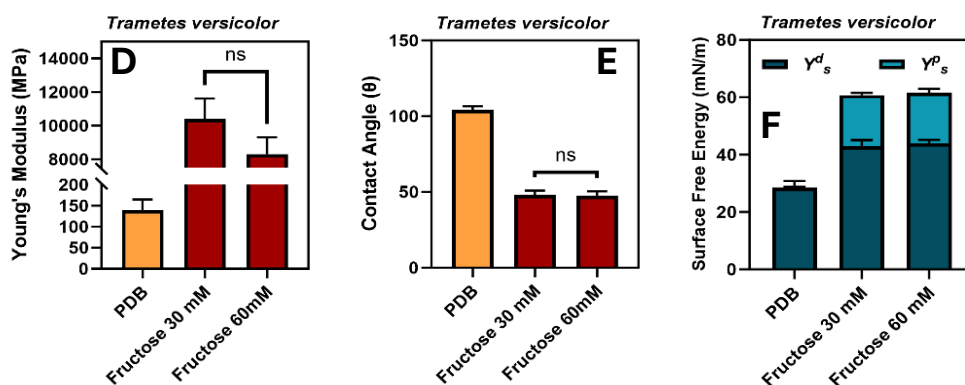
Figure 5.6B: The mechanical properties of the mycelia of *T. versicolor* in solid media under varying fructose concentration (A), thickness (B), ultimate strength (C), breaking strain (D), Young's modulus (E), contact angle in water and (F), surface free energy of the polar and non-polar component of the mycelia. The level of significance is * ($p \leq 0.05$), ** ($p \leq 0.01$), and *** ($P \leq 0.001$).
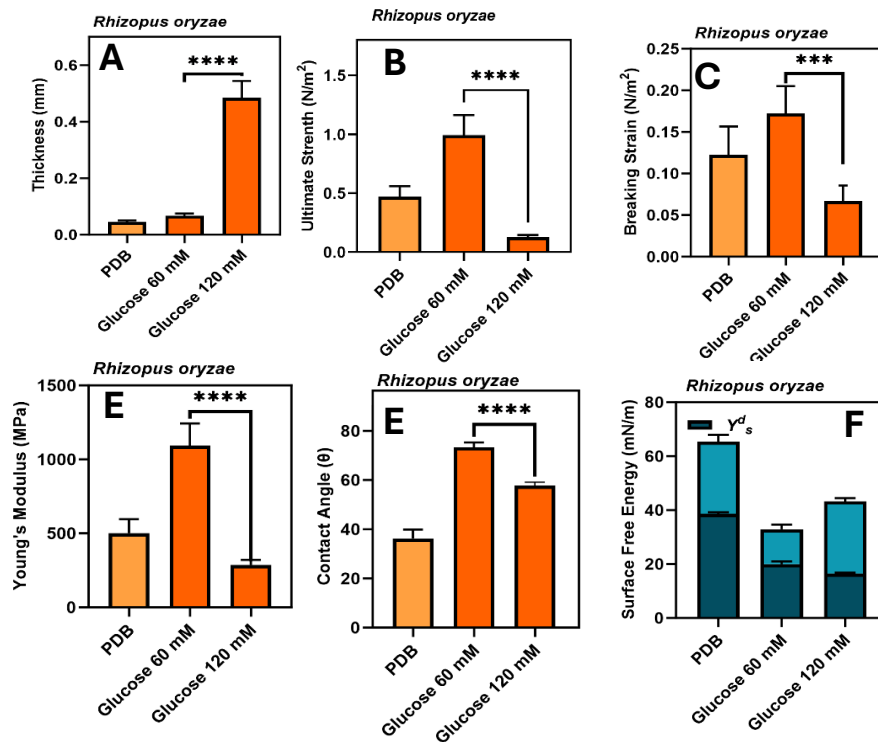
5.3.7. Effect of Fructose Concentrations on Mechanical Properties and Surface Wettability of *S. commune* in Liquid and Solid Media

I investigated the mechanical properties and surface wettability of *S. commune* mycelia in response to varying fructose concentrations. The nutritional dynamics of *S. commune* and their impact on the morphological properties of this fungus have not been extensively researched (Abd Razak et al., 2024). Given the shared similarities with *T. versicolor* (both being mushrooms), I opted to examine the effects of fructose, as it is also comparable in *S. commune*. My results reveal significant effects on hyphal width, stiffness, elongation potential and surface wettability but only for growth in liquid media. These results are presented in Figures 5.7A and 5.7B below. *S. commune* is an edible agaric mushroom, it is known for its remarkable ability to secrete a wide array of hydrolytic enzymes, including xylanases and endoglucanases, which are expressed across a diverse range of substrates (Tovar-Herrera et al., 2018). It shares similarities with *T. versicolor* in its ability to degrade lignocellulosic substrates (Tovar-Herrera et al., 2018). Therefore, I explored how fructose concentration influences its growth and mechanical properties. Like the results from *T. versicolor*, the growth of *S. communes* with fructose as a carbon source under the condition of this experiment comparable to PDB-mycelia were not favourable. For instance, the mycelia thickness was 4.21 ± 0.12 mm and 0.07 ± 0.01 mm respectively for PDB hyphae in liquid and solid media. The fructose groups compare to the PDB-mycelia on solid media with average 0.067 ± 0.01 mm and 0.063 ± 0.006 mm, but the width was just 0.395 ± 0.04 mm (30mM) and 1.47 ± 0.07 mm (60mM) respectively in liquid

media. Generally, the difference in thickness has no impact on the mycelia strength either at 30 mM or 60 mM, but the potential for elongation of 60 mM was significantly increased for mycelia but with reduced flexibility. There was no difference across all mechanical parameters tested for samples grown on solid media. Notably, increasing the sugar concentration significantly increased the hydrophobicity of the mycelia (contact angle >100°), and the non-polar component was also >90% of the total surface free energy indicating hydrophobicity. On solid media, the mycelia across groups were quite wettable with a contact angle < 80°.
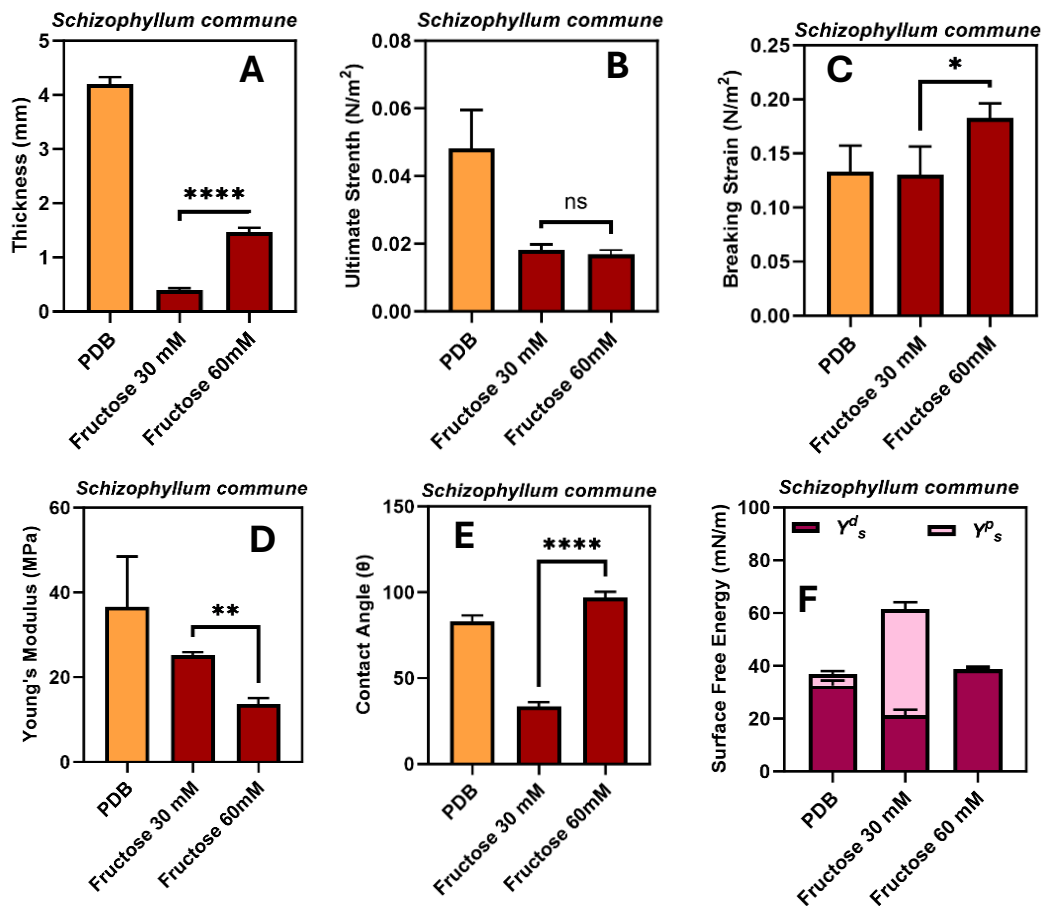
Figure 5.7A: The mechanical properties of the mycelia of *S. commune* in liquid media under varying fructose concentration (A), thickness (B), ultimate strength (C), breaking strain (D), Young's modulus (E), contact angle in water and (F), surface free energy of the polar and non-polar component of the mycelia. The level of significance is * ($p \leq 0.05$), ** ($p \leq 0.01$), and *** ($P \leq 0.001$).
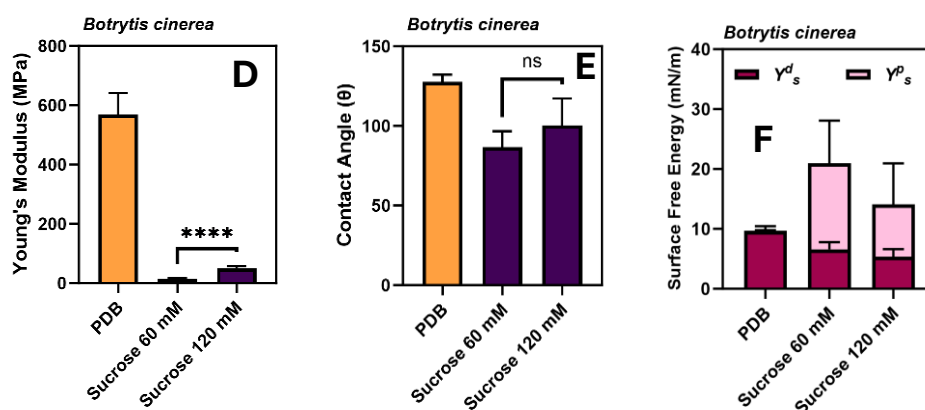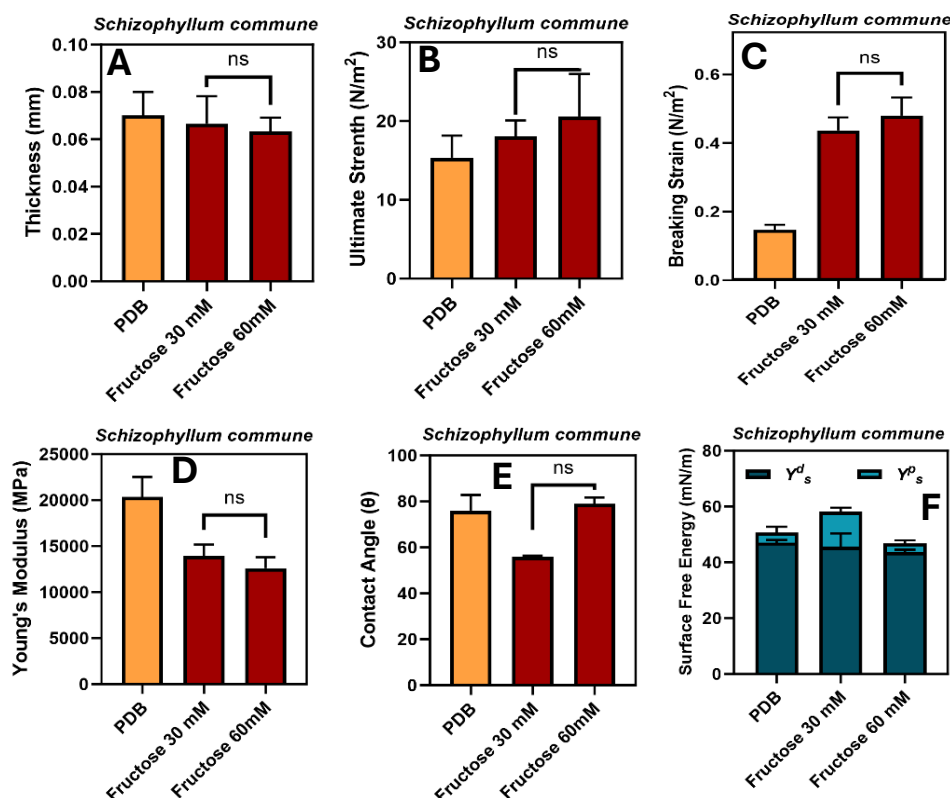
Figure 5.7B: The mechanical properties of the mycelia of *S. commune* in solid media under varying fructose concentration (A), thickness (B), ultimate strength (C), breaking strain (D), Young's modulus (E), contact angle in water and (F), surface free energy of the polar and non-polar component of the mycelia. The level of significance is * ($p \leq 0.05$), ** ($p \leq 0.01$), and *** ($P \leq 0.001$).

5.3.8. Structural Modifications Due to Food Sources Assessed via Chitin Quantification

Three fungal strains from this experiment that showed significant changes in their mycelial thickness due to increasing sugar concentrations are *R. oryzae*, *A. niger*, and *B. cinerea*. These strains were selected for further cell wall characterization to determine how the sugar altered their polymeric components, with chitin as the target polymer. Except for *B. cinerea* (treated with sucrose), the results indicated a significant increase in the chitin profile with increasing sugar (glucose) concentration for *R. oryzae* and *A. niger*, correlating with the observed mycelial thickness in liquid media (Figures 5.8A and 5.8B). For *B. cinerea*, the chitin profile did not differ across groups (figure 5.8 C). Previous studies (Cantu et al., 2009) showed that after 9 days of growth, chitin constitutes barely 8% of the cell wall of *B. cinerea*, suggesting that the thickness could be due to other polymers or biomolecular constituents like proteins, neutral sugars, and uronic acids (Cantu et al., 2009). This hypothesis is supported by well-documented findings from previous studies, where the fungus *B. cinerea*, through its sucrose synthase,

breaks down sucrose into fructose and UDP-glucose, thus triggering the reinforcement of the cell wall with callose and lignin (Lacrampe et al., 2021). it can be hypothesized that the cell wall reinforcement leading to thicker mycelia mat may be due to polymers other than chitin. For confirmation, the chitin from each group was characterized via infrared spectroscopy, and these results are presented alongside the corresponding chitin profile data in Figures 5.7A–5.7C. All characteristic chitin bands were observed across all groups: peaks around 3400–3305 cm^{-1} correspond to OH- stretching, the acetyl (CH_2OH) band around 2800–2910 cm^{-1}, the peak around 1650 cm^{-1} is assigned to the amide I band (C=O stretching), 1550–1560 cm^{-1} to the amide II band (N-H bending and C-N stretching), 1374–1417 cm^{-1} to CH bending vibration, 1130–1160 cm^{-1} to the C-O-C bridge in the chitin structure, and 830–900 cm^{-1} to the β-glycosidic linkages between sugar units (Wu et al., 2005).
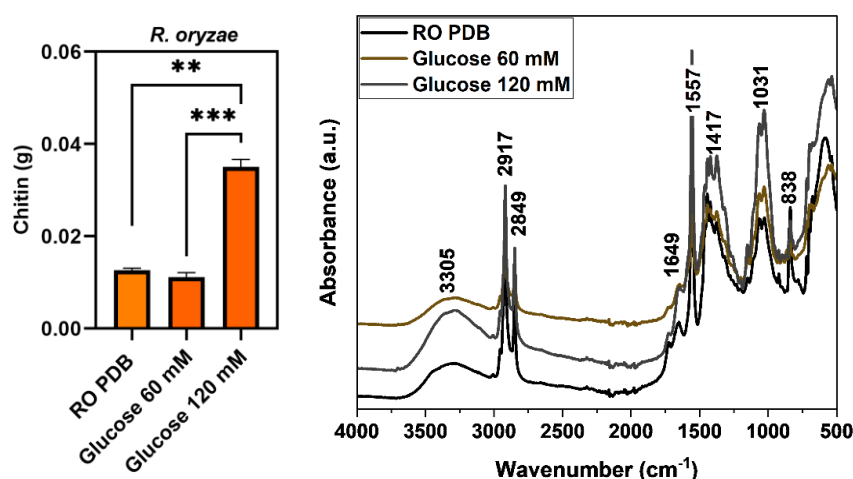
Figure 5.8A: Chitin yield from the mycelia of *R. oryzae* and corresponding infrared spectroscopy. The level of significance is * ($p \leq 0.05$), ** ($p \leq 0.01$), and *** ($P \leq 0.001$).
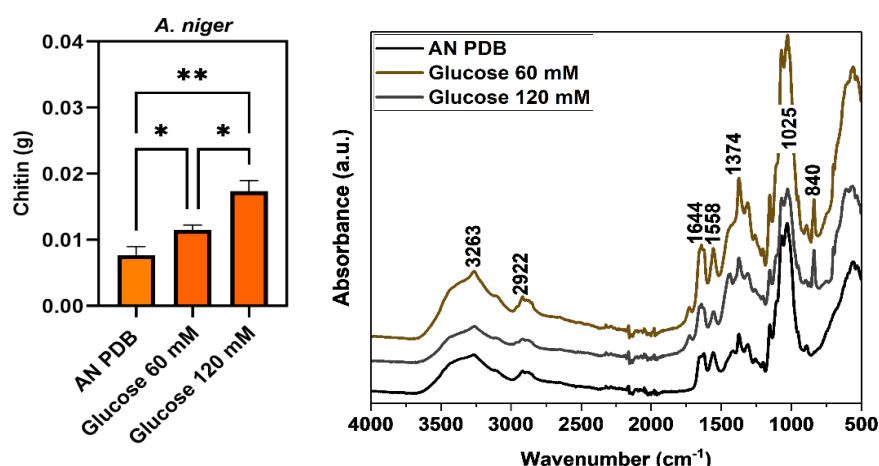
Figure 5.8B: Chitin yield from the mycelia of *A. niger* and corresponding infrared spectroscopy. The level of significance is * ($p \leq 0.05$), ** ($p \leq 0.01$), and *** ($P \leq 0.001$).
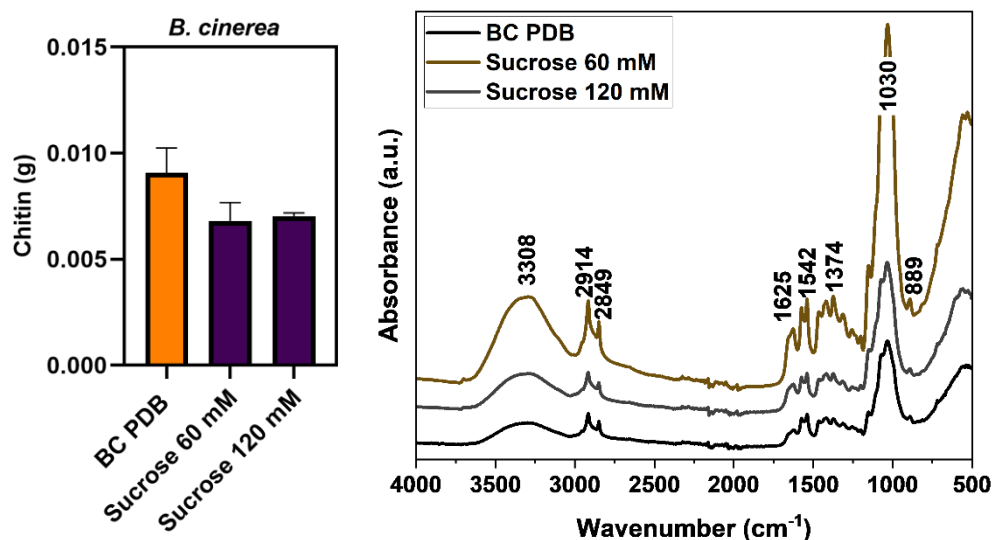
Figure 5.8C: Chitin yield from the mycelia of *B. cinerea* and corresponding infrared spectroscopy. The level of significance is * (p ≤ 0.05), ** (p ≤ 0.01), and *** (P ≤ 0.001).

5.4. Conclusions

In my study, I consistently observed that increasing glucose or sucrose concentrations led to thicker mycelia mat across various fungal groups. This finding aligns with (Antinori et al., 2020)'s documentation of increased *Ganoderma lucidum* mycelium thickness. The underlying biochemistry may explain this phenomenon. Specifically, fungi exhibit a higher uptake of glucose and sucrose compared to fructose. This increased availability of monosaccharides or disaccharides contributes to cell wall formation, especially since many cell wall biomolecules are glucose-based polymers (e.g., chitin) (Iiolligan & Jennings, 1972). Additionally, the differences in growth response between glucose and fructose raise some questions about monosaccharide chemistry. In general, fructose and glucose share similar chemical structures and can undergo isomerization in weak alkaline solutions. However, research by (Lilly & Barnett, 1953) revealed an alternative form of selectivity among sugars that aligns closely with my findings. Initially, both fructose and glucose supported the growth of *R. oryzae*, but subsequent experiments indicated that fructose might not be the optimal choice for certain strains (such as *T. versicolor* and *S. commune*), particularly at low concentrations. In the study by (Lilly & Barnett, 1953), the reduced growth of certain fungi on fructose, as compared to glucose, may have arisen from the distinctive structure of fructose or other contributing factors. The authors also noted that autoclaving tends to darken fructose more than glucose, implying that fructose undergoes more significant alterations during this sterilization process than the aldose sugars. Furthermore, the author's preliminary experiments suggest the possibility of the

formation of inhibitory substances when fructose is autoclaved alongside other medium constituents. In my study, I observed significant colour alteration in the media from groups treated with fructose (Appendix, Table 5.6. Interestingly, this phenomenon was not observed for glucose or sucrose, the latter being a fructose and glucose disaccharide. This suggests two things, the first being that sucrose is not broken-down during autoclaving, allowing the fructose component to remain available in its original form for fungal use. The second is that fructose is more susceptible and there is a need for characterization after the autoclaving process. Notably, the group treated with sucrose (*B. cinerea*) exhibited excellent mycelial thickness. In solid media, PDB-mycelia exhibit remarkable hydrophobicity across most groups. However, the hydrophobic nature of *S. commune* mycelia due to increasing sugar concentration is an intriguing finding. Notably, this phenomenon occurred only in liquid media and specifically in one of the two fungi treated with fructose. According to the literature, *S. commune* produces hydrophobins, molecules that allow the fungus to thrive outside aqueous environments and confer hydrophobic properties to the fungal surface (Wang et al., 2005). While there isn't a direct link between fructose and hydrophobin synthesis in fungi, my study revealed a significant reduction in aerial growth in liquid media (Appendix, Table 5.6) when fructose was used. Hydrophobins, as reported in the literature, play a crucial role in fungal growth and development by forming a layer at interfaces, reducing surface tension, and promoting the formation of aerial mycelial hyphae (Lopatukhin et al., 2024). This observation suggests that hydrophobins could potentially explain the observed effect. However, the relationship between increasing fructose concentrations and this phenomenon still requires further investigation.

CHAPTER 6

6.0 Engineering Multifunctional Biodegradable Scaffolds from *M. rouxii* and *R. oryzae*: Surface non-wettability, Thermostability, and UV-Radiation Protection.

In this chapter, I evaluated the suitability of mycelia-based materials from two mucorales species (*M. rouxii* and *R. oryzae*) for novel applications, including surface non-wettability, thermostability, and UV-radiation protection. I identified challenges related to the compatibility of current methods with the mycelia and proposed solutions. Ultimately, my results demonstrated the potential for use of these materials. From chapter two (methods development), I reported that useable materials could be generated from *M. rouxii* and *R. oryzae*, and that these could also yield varying physical and mechanical properties under different drying processes (either air dry, oven dry, convectional freeze then freeze dry or cryogenic freeze then freeze dry), the pattern of which could also significantly differ between the two strains. Despite being members of the same family, these two fungal strains have structural differences, hence their choice for comparative assessment in these areas of applications. Beyond the mechanical characterisation of this material, I have now advanced my study towards innovative applications. In this study, I focused on developing titania (TiO_2) NPs modified mycelia (from *M. rouxii* and *R. oryzae*) as biodegradable, multifunctional scaffolds (hydrophobic surface, thermostability, and UV-radiation protection). I recorded successful functionalization of mycelia with TiO_2 NPs (deposited on dried mycelia), confirmed through SEM/EDX analysis. These nanoparticles altered the surface properties, impacting the surface free energies and increasing the hydrophobicity of the mycelia as recorded via contact angle measurements and tensiometry. The growth face (GF) of the mycelia, where sporangiophores emerge, exhibited tighter packing and greater nanoparticle incorporation compared to the face in contact with the growth media (MF). Although the chemistry as assessed by FTIR was similar on both sides, SEM revealed distinct microstructural arrangements at both surfaces. This difference likely influenced the distribution of TiO_2 nanoparticles during composite formation. Doping with TiO_2 NPs improved the thermal stability of the mycelia, delaying degradation of the organic matrix by almost 100 °C. The ultraviolet protection factor (UPF) values also significantly increased with the presence of titania NPs, making the mycelia more effective at blocking harmful UV-A and UV-B radiation. Complementary experiments with exemplar strains on UV-radiation protection yielded higher UV-radiation protection factors, indicating their suitability for this aspect of the study, and addressed the shortcomings that were reported with the initial

fabrication method. This study lends credence to the mucorales family as a potential source for innovative materials engineering. It also provides valuable insights into mycelial behaviour and their potential applications as multifunctional biodegradable scaffolds.

Keywords: Mycelia-based materials, Mucorales, surface non-wettability, thermostability, UV-radiation protection, titania (TiO_2 NPs), biodegradable scaffolds, and nanoparticle functionalization.

6.1. Introduction

There is a growing global demand for sustainable materials that are biodegradable, readily available, and environmentally friendly (Raghunathan et al., 2024). Mycelia-based materials have emerged as a promising solution to meet this demand with their unique physicochemical and mechanical properties (Sharma et al., 2024). Their unique properties and eco-friendly nature make them ideal candidates for various applications, filling a crucial gap in the market for sustainable materials (Sharma et al., 2024). They possess physicochemical properties allowing for tuneability with different functional groups and bioactive materials (Antinori et al., 2020). When combined with nanostructures, they form bioactive scaffolds or composites that can be used for a wide range of environmental and biomedical applications not limited to environmental pollutant management (Wang et al., 2024). This highlights how the nature, and chemistry of mycelial networks could be utilized in solving some of the evolving challenges of the world such as smart packaging and UV radiation protection. Globally, there has been increasing global warming due to the continuous degradation of the ozone layer (Vazquez Santiago et al., 2024). The UV-radiation that reaches the earth does so with increasing penetration power posing health risks, this underscores the need for sun protective materials (Bais et al., 2018). Ultraviolet-visible (UV) light blocking as a safety measure is increasingly common amongst different populations because the UV radiation if unchecked can inflict damage to the biological systems (Rabiei et al., 2022) including increases in the prevalence of cancers. UV protective materials offer different levels of protection against UV radiation, and this depends on their Ultraviolet Protection factor (UPF) (Rabiei et al., 2022). Similarly, there is a growing trend in sustainable practices within the smart materials industry aimed at enhancing current methods. Hydrophobic materials with low surface wettability and thermal stability can be utilized as biodegradable packaging for food or stored products. This approach helps reduce the risk of contamination from waterborne pathogens and or thermo-risks, offering a safer and more eco-friendly solution for packaging needs (Frota et al., 2022). Compared to fungi from the orders agaricales (e.g., *Agaricus bisporus* and *Pleurotus ostreatus*), polyporales

(*Ganoderma lucidum*), and schizophyllales (*S. commune*), the mycelia of fungi from the order mucorales have been less extensively utilized for generating mycelium-based materials, despite their excellent food-to-mycelium conversion ratio (Shin et al., 2025; Whabi et al., 2024). This underutilization could be due to a lack of in-depth information on the mycelial morphometrics for mucorales, or the most suitable application channels for these materials. In this study, I explore two strains from the order mucorales with innovative material designs and a translational outlook. By combining fungal mycelia with bioactive materials such as TiO_2 nanoparticles (NPs), I aim to create novel, multifunctional, and highly biodegradable matrices/scaffolds. My study further characterizes mycelial materials from these strains, which I will then dope with TiO_2 NPs to develop a novel scaffold featuring hydrophobic surfaces, thermal stability, and UV radiation protection. This chapter addresses Objective 6 by characterizing *M. rouxii* and *R. oryzae* mycelia and developing Titania nanoparticle-modified composites for UV shielding, water repellence, and thermal stability.

6.2. Materials and Methods

6.2.1. Materials

Titanium (IV) isopropoxide (546-68-9), ethanol- (64-17-5), and diiodomethane (75-11-6) which were all sourced from Sigma-Aldrich LTD (The Old Brickyard, New Road, Gillingham, Dorset, SP8 4XT). All other reagents for fungal growth are as reported in the *Rhizopus* in chapter five. Titanium tetrachloride ($TiCl_4$) was initially considered for use; however, concerns about hazardous by-products like HCl led to its replacement with titanium (IV) isopropoxide to promote sustainability.

6.2.2. Method

6.2.2.1. Growth Conditions and Preparation of *M. rouxii and R. oryzae*

The growth conditions for the two fungal strains in PDB are the same as in Chapter 2 for *M. rouxii* and *R. oryzae*. However, instead of drying under four different conditions, I adopted the convectional freezing (TEFCOLD SE-45 Series) followed by freeze-drying (BT4KZL dryer-VirTis) method. This choice was based on the excellent overall average mechanical results from the experiment (e.g. strength, thickness, etc.), which showed that sample preparation via this method produced an excellent material suitable for use in composite formation.

6.2.2.2. Physicochemical Characterization of Fungal Mycelia

The fungal mycelia were further characterized by the following methods: Yield (dry weight), Colour and texture (physical observation), Optical properties (reflectance UV-Vis; JASCO solid UV spectrophotometer (V-670), morphology and structural orientation (SEM; JSM-7100F LV FEG-SEM).

6.2.2.3. Deposition of TiO$_2$ NPs on the Mycelia of *M. rouxii* and *R. oryzae*

The sol-gel hydrolysis method was used in the deposition of TiO$_2$ NPs on the fungal mycelial, but this was done in situ following the method described by (Shaheen et al., 2019), with some modifications (because of the biological nature of mycelia). Briefly, two solutions were formed, Solution A: 10 mL titanium (IV) isopropoxide (TTIP) was added in 10 mL dry ethanol and stirred for 5 min. Solution B: to 30 mL dry ethanol 3.5 mL deionized water was added and stirred for 15 min. The mycelia were infiltrated in solution B in a 500 mL beaker for 5 min to allow for proper penetration, then solution A was added to solution B dropwise via a dropping funnel slowly with continuous stirring. This continued for either 20, 40, or 60 min, to establish the best condition for the formation of well-distributed NPs on the mycelia. The formed composite was thoroughly washed thrice in 10mL DDH$_2$O to remove the excess non-binding NPs and 3X in 50% ethanol. Then it was dried at 90°C for 1 hr, after which it was removed and stored in a dried container to allow for condensation and particle growth at 25 °C on a Teflon sheet in a Petri plate. After this, the wash process was repeated, and the mycelia dried at 90 °C for 30 min.

6.2.2.4. Characterization of Mycelia and TiO$_2$ Modified Mycelial Composite of *M. rouxii* and *R. oryzae.*

The biomolecular composition was assessed using FTIR Spectroscopy. Surface characteristics were examined through Scanning Electron Microscopy (SEM), revealing the morphological structure of both ordinary mycelia and mycelia modified with TiO$_2$ nanoparticles. Elemental mapping was performed using Energy-Dispersive X-ray Spectroscopy (EDX) during composite formation, and crystallinity was determined via powder X-ray Diffraction (Rigaku Ultima IV X-Ray Diffractometer). Chapter 2 contains information on how to measure the mechanical properties of mycelia, including thickness, strength, rigidity, and flexibility.

6.2.2.5. Thermal Stability Evaluation

The heat response of both ordinary mycelia and mycelia modified with TiO$_2$ was assessed using thermogravimetric analysis (TGA). The TGA/DSC 3+ instrument from Mettler-Toledo

International Inc. was employed, with samples heated in air at a rate of 10°C/ min over the temperature range of 30°C to 900°C.

6.2.2.6. Evaluation of Surface Chemistry (Wettability and Surface Energy)

Contact angles were measured on both sides of the mycelia (either growth face or media face) using an Attention Theta Lite Tensiometer connected to a Navitar Zoom 6000® Lens System with a magnification range of 0.09-393X. The measurements were taken via the OneAttension software. Contact angles were obtained by dropping 4 µL of double deionized water or diiodomethane (polar and non-polar fluids, respectively) at various points on the mycelia surface, with each measurement repeated three times. The experimental procedure followed the description provided by (Huang et al., 2019). Surface free energies were subsequently calculated using the Fowkes & Extended Fowkes Model (Fowkes, 1964).

6.2.2.7. Ultraviolet (UV) Radiation Protection Evaluation

The level of UV-radiation protection of the dried mycelia was determined in a JASCO solid UV-VIS spectrophotometer (V-670) in transmittance mode. The mycelia were fine-cut to fit the sample holder before mounting, direct transmission of UV radiation through the mycelia was then measured between 200 - 400 nm with 20 nm NIR bandwidth, 2nm UV-Vis bandwidth, and at a scanning speed of 500 nm/ min. The UPF (Ultraviolet Protection Factor), UV-A (315-400 nm) protection factor, and UV-B (280-315 nm) protection factor were determined according to the AS/NZ 4399:1996 standard, using the equation below. For each sample, three replicated measurements were conducted, and the average value was reported (Rabiei et al., 2022).

$$UPF = \frac{\sum_{290}^{400} E(\lambda) \cdot S(\lambda)}{\sum_{290}^{400} E(\lambda) \cdot S(\lambda) \cdot T(\lambda)} \times 100 \quad \ldots\ldots\ldots\ldots\ldots\text{Equation 6.1}$$

6.2.2.8. Data analysis

All the qualitative experiments were conducted in triplicate, and the mean values along with their standard deviations reported in plots or tables (for easy visualization). Depending on the data, I performed either one-way or two-way analysis of variance (ANOVA) to assess significant differences among various treatment factors and their levels. Subsequently, Tukey's Post hoc test was used for multiple comparisons of means across different groups (with a significance level of $P < 0.05$). I used either OriginPro Labs 2023 or GraphPad Prism 10.0 for statistical analysis, while graphical data were analyzed using ImageJ (ImageJ 1.53t w/Adiposoft 1.1) software.

6.3. Results and Discussion

6.3.1. Fungal Biomass

The characteristic properties of the mycelial biomass from *M. rouxii* and *R. oryzae* are presented in Table 6.1 below. Both fungi exhibited excellent growth in potato dextrose broth (PDB), reaching the exponential phase within 3-5 days of inoculation. The onset of sporangiophore production was recorded at the log-stationary interphase, occurring between 5-10 days. Healthy mycelia for characterization were harvested at 10 days and freeze-dried for use in the experiment (Figure 6.1A and 6.1B). The microstructural characterization of *M. rouxii* and *R. oryzae via* SEM is presented below in Figure 6.1C and D, respectively. *R. oryzae* displays a highly branching, interconnecting mycelial network, while *M. rouxii* shows interconnecting, over-layering hyphae. The diameter of 100 hypha for each fungus was measured, with *M. rouxii* averaging 11.3 (±2.23) µm and *R. oryzae* averaging 5.9 (±1.58) µm. Compared to *M. rouxii*, *R. oryzae* yielded more mycelia for each circle of growth, indicating a better nutrient-to-mycelia conversion ratio. Compared to existing studies, average diameters of 1-30 µm have been reported for *M. rouxii* (Garcia et al., 2023), and 10-15 µm for *R. oryzae* (Marques et al., 2024). However, I take cognizance of the effect of growth conditions.

Table 6.1: A Summary of characteristics of Mucorales (*M. rouxii* and *R. oryzae*)

Fungal	Colour	Diameter of hyphae (µM)	Dry yield (g)
M. rouxii	Milky-faintly yellowish when fresh	11.3 (±2.23)	0.31 ± 0.01
R. oryzae	Milky when fresh	5.9 (±1.58)	0.54 ±0.03
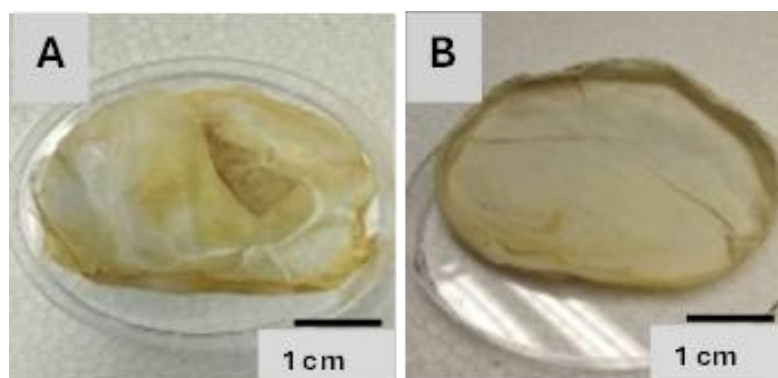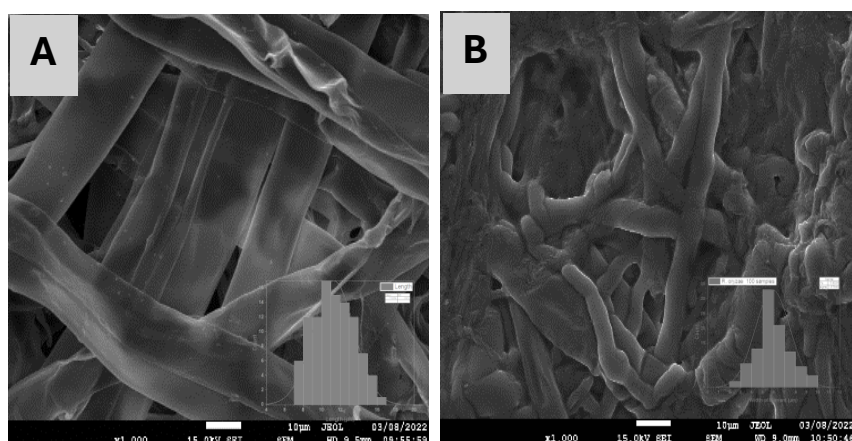
Figure 6.1: Representative scanning electron microscopy (SEM) images of the morphological structures of (A) *M. rouxii* and (B) *R. oryzae*. The insets show histograms of hyphal diameter based on 100 hyphal measurements. SEM images include a scale bar representing 10 μm.

6.3.2. Characterization of the Optical Behaviour of *M. rouxii* and *R. oryzae*

The optical characteristics depicting the absorption properties of the mycelia of *M. rouxii* and *R. oryzae* measured in the solid state are presented as Figure 6.2 below. The two faces, the nutrient-interacting face of the mycelia (labelled MF) and the face with active vertical growth (labelled GF), show distinct maximum absorption peaks within 200 – 600 nm. Both fungi have three absorption bands around 268 to 296 nm, a maximum peak at 339 nm, and another at 414 nm. Additionally, *M. rouxii* has two extra bands at 461 nm and 493 nm. The initial peaks between 200 and 415 nm are the same as the UV-Vis absorption band for standard melanin, suggesting that melanin could be the predominant pigment in the fungi (Mohite et al., 2017). This finding aligns with previous studies on the pigment dynamics of Mucorales (Lax et al., 2020). For *R. oryzae*, these absorption properties in the solid state correspond to those reported when its mycelia were extracted with different solvents (Narendrababu & Shishupala, 2017). The extra peaks for *M. rouxii* can be explained by data from previous studies, which indicate extended peaks of melanin in the visible light region, further confirming the hypothesis that the fungal pigment is likely to be predominantly melanin (Bagy et al., 2023). Beyond pigment confirmation, solid-state UV-Vis is more efficient for reproducibility in fungal characterization via spectroscopy methods, reducing the interference of extraction solvents. This method can also be used to monitor the aging process in mycelia or the degradation in quality (Frei, 1976). The presence of melanin in the mycelia of these strains suggests they could be suitable for use in UV radiation protection (Brenner & Hearing, 2008), prompting further studies.
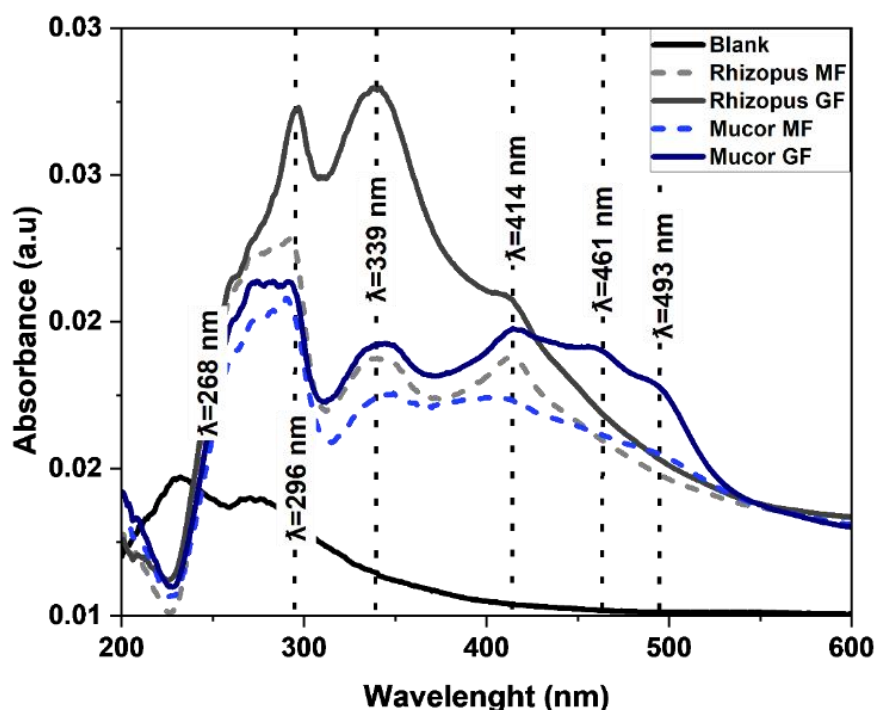
Figure 6.2: Optical Characteristics of *M. rouxii* and *R. oryzae* mycelia by diffuse reflectance UV-Vis.

6.3.3. Method Selection for TiO₂ Nanoparticle- modified Mycelia in *M. rouxii* and *R. oryzae*

Before I formed the multifunctional composite using TiO₂-NPs and fungal mycelia (either *M. rouxii* or *R. oryzae*), I evaluated several methods used in similar studies and identified their prospects and limitations. These are summarized in Table 6.2 below. This process was necessary because, at the time of the experiment, there were no existing methods outlining how fungal mycelia could be modified with TiO₂-NPs for use in biodegradable UV-radiation protection or as a hydrophobic surface. From the methods evaluated, the approach proposed by (Shaheen et al., 2019), appeared promising and was adopted for my study, but with modifications. Generally, apart from direct functionalization in growth media (a novel approach I used for AuNPs and *A. niger*, reported in Chapter 4), other methods previously used for TiO₂ NPs functionalization on cotton fibres or fabrics raised either suitability or environmental concerns. These concerns included the compatibility of the process with the nature and mechanics of the mycelia, and the use of harsh chemicals, which contrasts sharply with my environmental sustainability goals, or the applicability of the model to mycelia. I summarize these considerations in Table 6.2. I also dropped the direct functionalization model because the maximum concentration (2 % V/V) of TiO₂ NPs that both fungi could tolerate for

growth was not sufficient to deposit a significant amount of TiO$_2$ NPs on the mycelia, which can aid the intended area of application (see Figure 6.3 below).

Table 6.2: Evaluation of Methods and Their Limitations for Mycelial Functionalization

S/N	Method	Description	Challenges	Literature Reference and Area of Application
1.	In situ sol-gel Method Direct impregnation of starting materials before TiO$_2$ NP synthesis.	The titanium isopropoxide was impregnated into the cotton fabric and then used for in situ synthesis.	The sol-gel method used in textiles is quite promising, but the similarities to mycelium-based materials, particularly in the rigorous gel formation process, could be challenging.	(Shaheen et al., 2019) UV-Protection
2.	Introduction of the starting materials into TiO$_2$ NPs reaction medium for sol-gel coating in situ.	The fibre is cut 4 by 4 cm and immersed in the reaction medium while the hydrolysis and sol formation continue. This is then washed.	This method was used for fibre (fabrics). This is also a different class of biomaterial. Though promising, it involves a high concentration of NaOH (4.2M).	(Rabiei et al., 2022) UV-Protection
3.	Dipping or spraying of the mycelia (5 by 5) with already	The conventional sol-gel method of synthesis described by Velazquez could be used for sol formation. This could be sprayed	Concerns with purity (HCl as catalyst in Velázquez-Martínez et al., 2018).	(Velázquez-Martínez et al., 2018)

	synthesized sol in situ.	on mycelia or mycelia could be dipped. Formation of layers is also possible following Yang et al., 2018.	Progression to form gel	(Yang et al., 2018) Self-cleaning.
4.	Direct functionalization with sol-from growth medium	The sol is synthesized using any of 3 methods above and introduced to the growth medium for incorporation.	Yield may not be so suitable for application, except grown in big flask. Also requires prior synthesis of TiO_2-NPs	Not yet reported in Literature
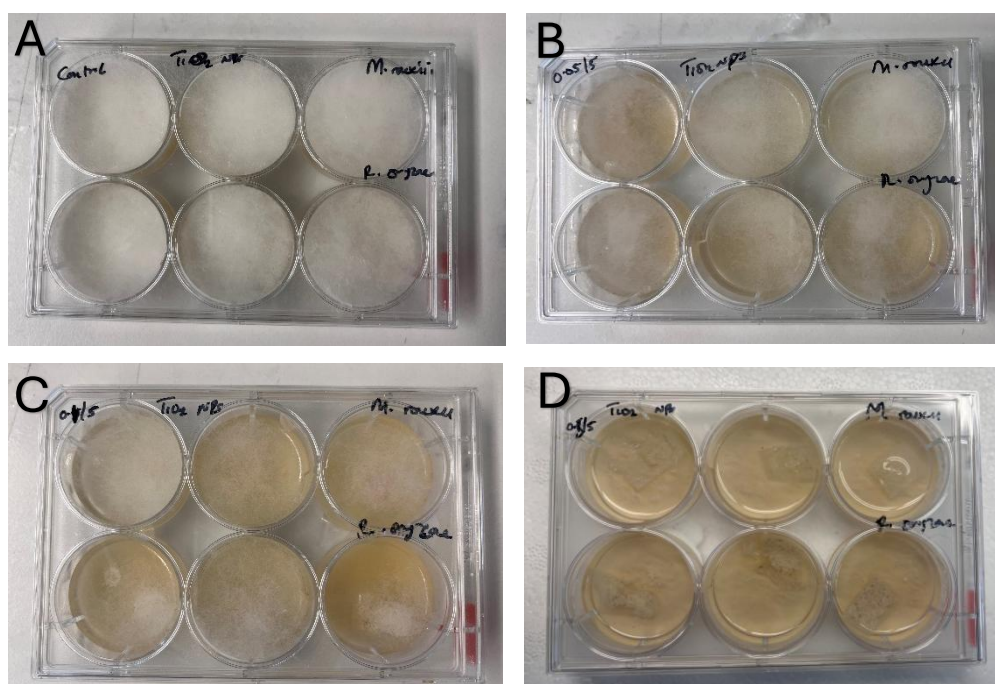
Figure 6.3: Maximum concentration of TiO_2 NPs tolerated by *M. rouxii* and *R. oryzae* for growth. The pots are for (a) control with no TiO_2 NPs, (b) fungal culture with 1%V/V of TiO_2 NPs (c) fungal culture with 2% V/V of TiO_2 NPs, and (d) fungal culture with 5% V/V of TiO_2 NPs.
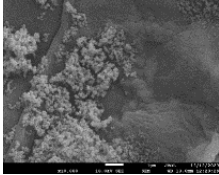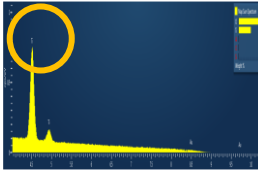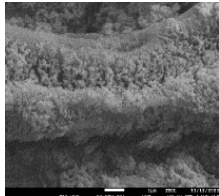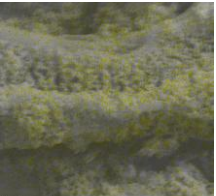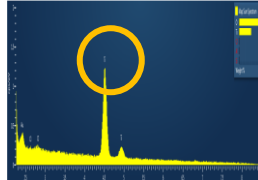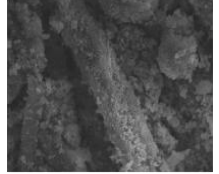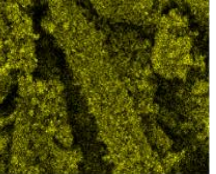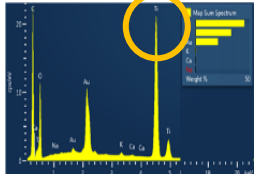
6.3.4. Preliminary Characterization of TiO$_2$-NPs Mycelia Composite to Determine Best Conditions for Further Experiments

Once the method for composite formation was selected, a preliminary investigation into its applicability for mycelium-based material was necessary to validate its usability. Therefore, composite materials were formed at different time points using this method to determine the best conditions for material formation. I assessed the level of functionalization and the distribution of NPs on the mycelia at various time points (20, 40, or 60 min). Preferences were also given to the ability to remove the mycelia from the NPs-Sol before thorough gel formation. The samples were thoroughly washed upon removal (3X in 10 mL water + 3X in 50% ethanol) to remove all non-binding organic or inorganic moieties. The moisture was dried at 90°C for 30 min and then left for condensation and particle growth for 10 h. The resulting sample was rewashed 3X in 10 mL 50% ethanol and dried again ready for microscopy characterization. Notably, the mycelia survived this improved method of composite formation with no visible tears under the conditions used for the formation of mycelia-TiO$_2$ NPs composite.

Table 6.3 shows photographic (taken with an iPhone 13 camera) and SEM images, illustrating the different conditions under which I initially functionalized the mycelia before SEM imaging. Within the first 20 min, deposition occurred, indicating that the onset of the process was quite fast, as also seen in the instant change of the solution's colour from colourless to turbid white during sol formation. By 40 min, all areas of the mycelia were already covered, denoted by the well-distributed appearance of the NPs confirmed by EDX. At 60 min, the NPs began forming agglomerated gels as seen under the microscope. Consequently, I selected the 40-min time point for further experiments. To determine the phase of the Titania, an X-ray diffractogram revealed that the TiO$_2$ NPs on the mycelia were amorphous.

Table 6.3: Photographic and SEM Images of TiO₂-NPs Functionalization on Mycelia at Different Time Points. Peaks with Circular Rings at Denote Titanium Peaks.
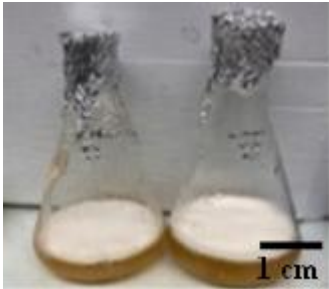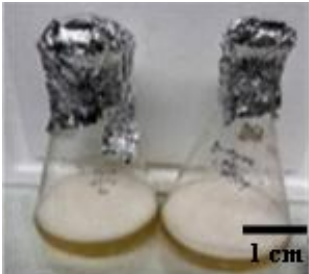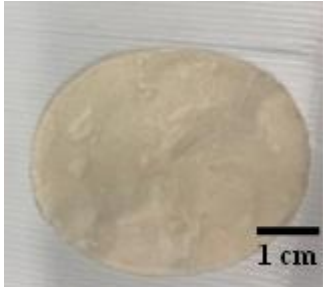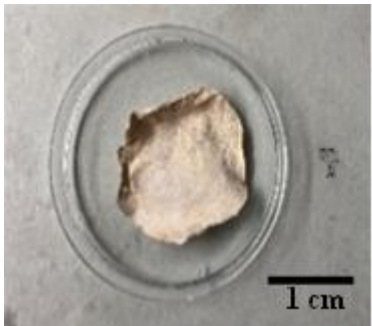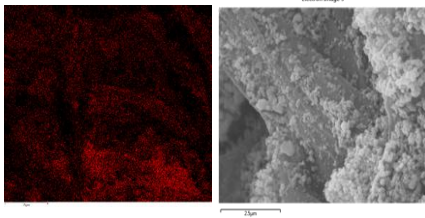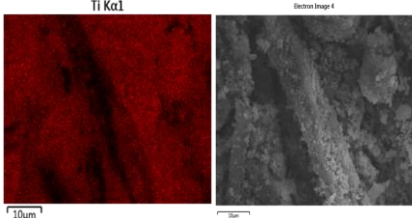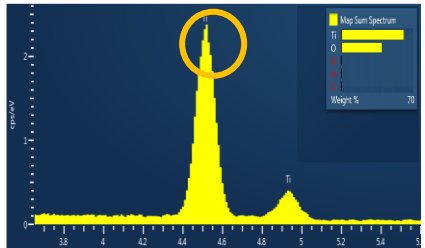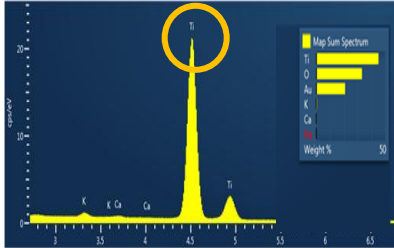
Note: Due to varying x-axis scales across EDX spectra, the Ti peak consistently appears at approximately 4.5–4.6 keV, corresponding to the Ti Kα emission line. Scale bar on SEM images represents 25µm.

Sample	Image	SEM/EDX	EDX Map
20 min			
40 min			
60 min			

6.3.5. Developing and Characterizing *M. rouxii* and *R. oryzae* Mycelia-TiO₂ NPs Composite

The choice of method and duration for the study was confirmed to be effective based on the results obtained from the formation and characterization of new composites. These results are presented in Table 6.4. The bulk mycelium from the Mucorales (Rows 1 and 2) resembled a membrane well-covered with TiO₂ NPs (Row 3). Scanning electron microscopy (SEM) characterization showed that the composites exhibited well-distributed TiO₂ NPs, as confirmed by energy-dispersive X-ray (EDX) mapping (Row 4). The clear titanium peaks, indicated by circular rings in the map, confirm the presence of TiO₂ NPs within the composite (Row 5). The formed materials were subsequently tested to assess the impact of the functionalization process in comparison to the original properties of the ordinary mycelium for both *M. rouxii* and *R. oryzae*.

Table 6.4: Representative Images and Characterization of Mycelia-TiO₂ NPs Composite. All images include a 1 cm scale bar; SEM/EDX images show 25 µm.

Fungal sample	*M. oryzae*	*M. rouxii*
Fungal culture		
Fungal mycelia before functionalization		
TiO₂ NPs-Mycelia Composite		
SEM/EDX		
EDX Map		

6.3.6. Mechanical Impact of TiO$_2$ NPs Functionalization on Mycelia of *M. rouxii* and *R. oryae*

I investigated changes in the mechanical properties of both *M. rouxii* and *R. oryzae* mycelia following doping with TiO$_2$ NPs. Notably, I observed significant effects on mycelial thickness, strength, elongation potential, and flexibility (Figure 6.4). Under the growth conditions (PDB-24g/L), *R. oryzae* exhibited thicker mycelia mat than *M. rouxii*, but it was more impacted by functionalization. Specifically, the thickness of *R. oryzae* mycelia decreased significantly, while their strength remained relatively unchanged (Figure 6.4A). This behaviour could be attributed to the highly interwoven hyphal in *R. oryzae*. In contrast, *M. rouxii* maintained its thickness but experienced a significant reduction in mycelial strength after functionalization (Figure 6.4B). However, both groups shared a common trend: the unmodified mycelia demonstrated better elongation potential and flexibility compared to their TiO$_2$ NPs-functionalized counterparts. This could be due to the interaction of the NPs and the individual hyphae making them stiffer after the completion of gelation. TiO$_2$ NPs are known for their high surface area, stability, and mechanical strength, which can enhance the structural properties of mycelial networks when incorporated (Ghareeb et al., 2024). The mechanical test on mycelial strips revealed that breakage occurred near the force application area, indicating a weak point due to stress concentration (Figure 6.4 E-F). However, this does not necessarily indicate non-uniformity in the distribution of the NPs on the mycelia.

,
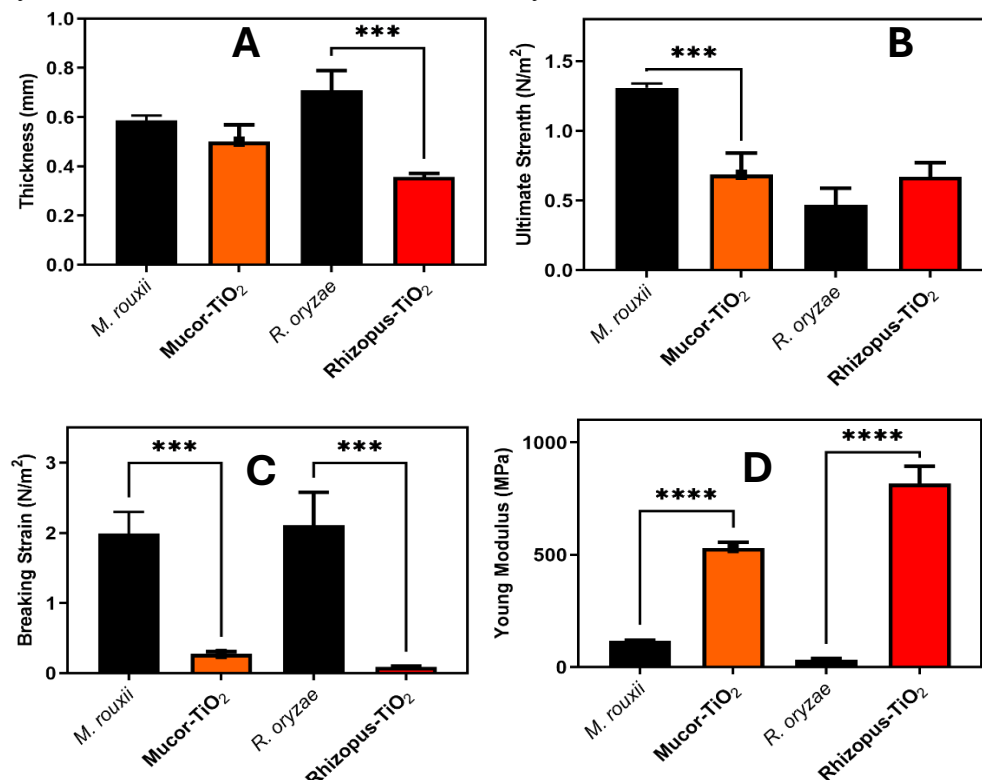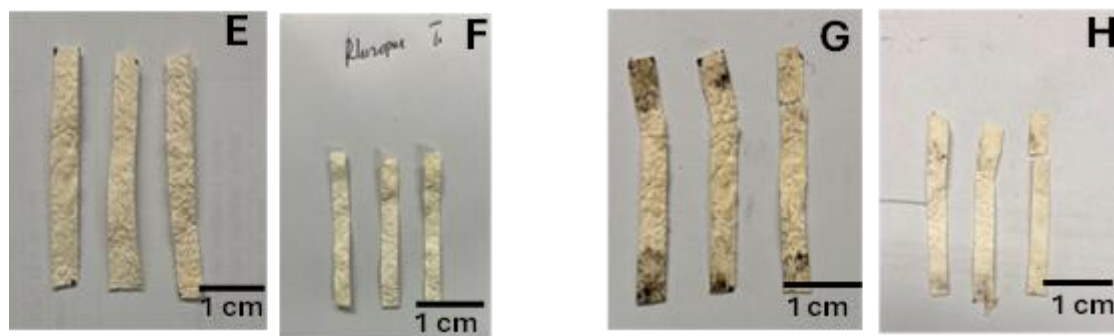
Figure 6.4 Comparison of mechanical properties between ordinary mycelia and TiO$_2$ NPs-modified mycelia of *M. rouxii* and *R. oryzae*. Panels (A) through (D) represent thickness, ultimate strength, breaking strain, and Young's modulus, respectively. Freshly cut mycelia strips for *M. rouxii* and *R. oryzae* are denoted as E and F, while their breaking patterns are labelled as G and H, respectively. All images include a scale bar representing 1 cm.

6.3.7. Surface Wettability Modification by TiO$_2$ NPs- Modified Mycelia of *M. rouxii* and *R. oryzae*

In this study, I explored changes in the surface properties of mycelia due to doping with TiO$_2$ NPs. I assessed surface-free energies and wettability on both sides of the mycelia. Specifically, I designated the side in contact with nutrient media as the media face (MF) and the side where active sporangiospore growth occurred as the growth face (GF). My observations show significant alterations in surface wettability (Figure 6.5). Generally, the ordinary mycelia exhibit high wettability, especially on the media face, with a contact angle for polar solvents (< 70°). However, doping the mycelia with TiO$_2$ NPs had a substantial impact. The surface contact angle for polar solvents (such as water) increased to over 130° (Figure 6.5A), while the contact angle for the non-polar solvent (diiodomethane) decreased (Figure 6.5B). In summary, the mycelia surface has become more hydrophobic and less wettable by water, while becoming more wettable by non-polar liquids like diiodomethane. This shift indicates the development of a hydrophobic surface which may be somewhat oleophilic (Broje & Keller, 2005). Additionally, the assessment of total surface free energy highlighted changes that contributed to altered wettability (Figure 6.5C and D). Notably, the non-polar component of the mycelia exhibited increased surface energy due to NP functionalization, whether at the media face or growth face. As a result, the overall wettability of the mycelia decreased. In summary, this work yielded a highly hydrophobic TiO$_2$ NPs-functionalized mycelia scaffold from *M. rouxii* and *R. oryzae.* Although this modification slightly affected mechanical properties compared to ordinary mycelia, it opens exciting possibilities for applications in various fields.
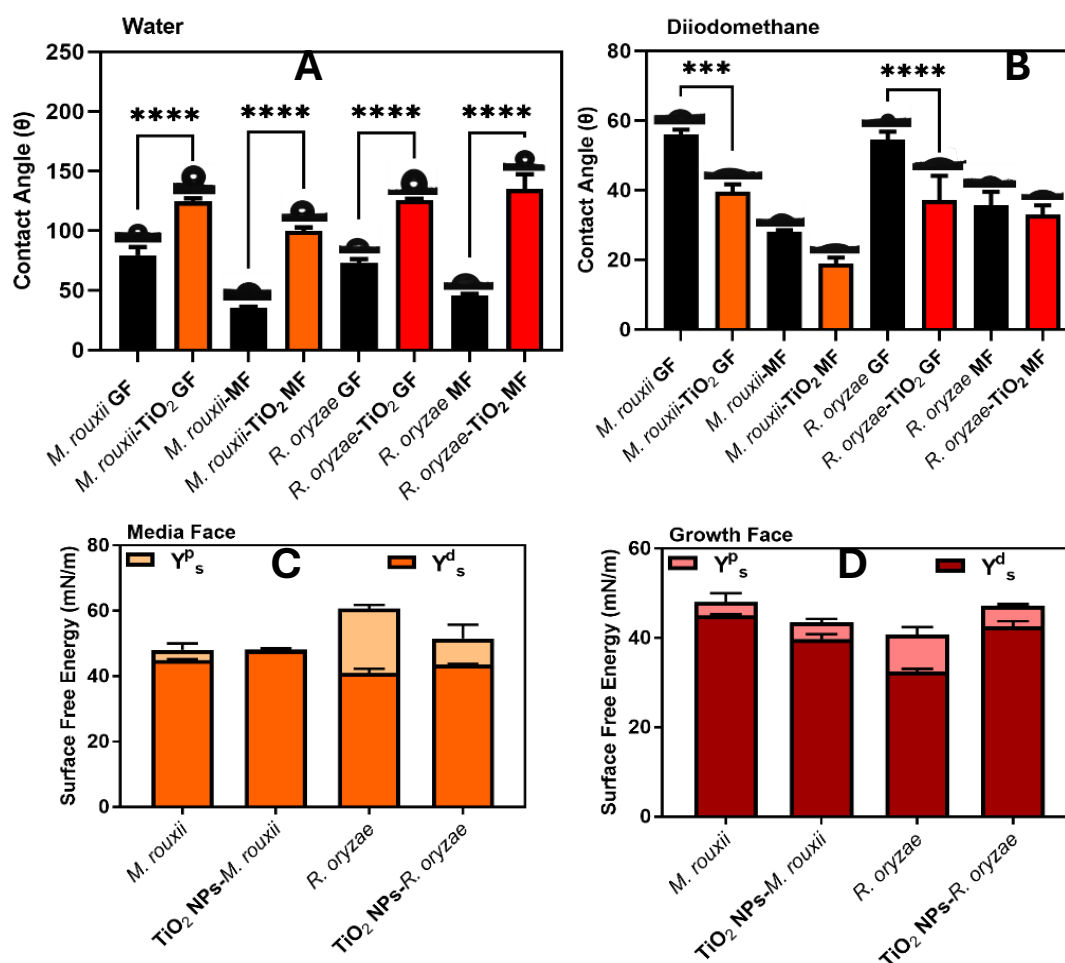
Figure 6.5: Surface Wettability Modification of Mycelia by TiO$_2$ NP Doping. (A) contact angle for water on modified mycelia (B) contact angle for diiodomethane on modified mycelia (C) changes in total surface free energy on the media face (MF) and growth face (GF), and (D) changes in total surface free energy on the growth face (GF)

6.3.8. Characterization of the Morphology and Chemical Composition at the Growth and Media Faces of Mycelia to Investigate Wettability Differences

My study aimed to determine whether the chemical composition or morphological structure contributed to the wettability differences between the growth and media faces of mycelia. Results from infrared (FTIR) analysis to determine if the biomolecular constituents vary, revealed no significant difference in chemical properties between the mycelia at the two faces (Figure 6.6A). However, further morphological characterization using scanning electron microscopy (SEM) at both low and high magnifications revealed an interesting pattern. The growth face of the mycelia appeared more tightly packed compared to the media face (Figure 6.6B). This phenomenon was observed in both fungi. Notably, the media face exhibited numerous empty, unoccupied areas within the mycelial network for both strains. Since mycelial

volume significantly influences surface wettability, I hypothesize that the media face may lack the same volume support as the growth face. This conforms to the explanation that the more tightly packed structure of the mycelia (growth face) likely results in a higher density of hyphae, reducing the surface area exposed to air and increasing wettability (Jarray et al., 2020). Additionally, I acknowledged that subtle variations in surface molecules or minor compounds, which might not be detected by FTIR, could impact wettability (Jothi Prakash & Prasanth, 2021). This comprehensive approach helps to explain the observed differences in wettability between the growth and media faces of mycelia.
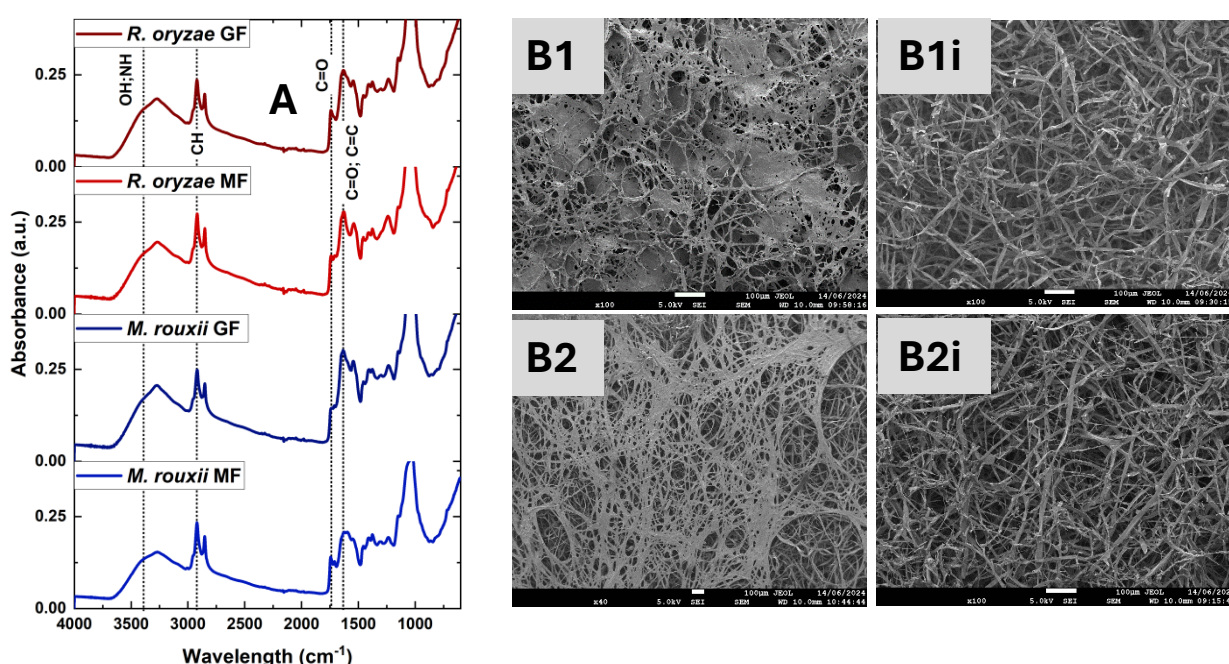
Figure 6.6: Chemical and morphological characterization of the growth face and media face of *M. rouxii* and *R. oryzae* mycelia. (A) FTIR, in panel B, (B1 and B1i) represent the growth face for *M. rouxii*, while B2 and B2i correspond to the growth face and media face for *R. oryzae*, respectively. All SEM images include a scale bar representing 100 μm.

6.3.9. Evaluation of thermal protection by TiO₂ NPs on the fungal composite via thermogravimetric analysis and FTIR

Thermogravimetric analysis (TGA) from RT to 900°C is a valuable technique for assessing material stability under increasing temperatures. I examined whether coating the mycelia of *M. rouxii* and *R. oryzae* with TiO_2 nanoparticles (NPs) would enhance their thermal stability. My results, shown in Figure 6.7 (A-D), indicate that the TiO_2-coated mycelia exhibited delayed

thermal degradation compared to the uncoated mycelia. Between RT and 120°C, both the uncoated and TiO$_2$ NPs-coated mycelia experienced significant weight loss, likely due to moisture evaporation. At around 220°C, the uncoated mycelia underwent substantial thermal degradation, attributed to the breakdown of a specific component, likely a major organic constituent. In contrast, the TiO$_2$ NPs-coated mycelia did not show this degradation until approximately 320°C, indicating nearly a 100°C delay. This delay suggests that the TiO$_2$ coating provides a protective effect, enhancing the thermal stability of the mycelia. Complete digestion of the uncoated mycelia occurred at around 600°C. However, at this temperature, only about 55% of the TiO$_2$-coated mycelia had degraded. The remaining undigested portion is likely the inorganic TiO$_2$ NPs, which have a digestion temperature above 900°C (Bekele et al., 2020). This significant difference in thermal stability highlights the effectiveness of TiO$_2$ NPs in protecting the mycelia from thermal degradation. Infrared (FTIR) spectroscopy analysis of the residue revealed the absence of peaks associated with mycelia, confirming that the organic components were completely burned (Figure 9(E and F). This result supports my hypothesis that TiO$_2$ coating could significantly enhance the thermal stability of the mycelia.
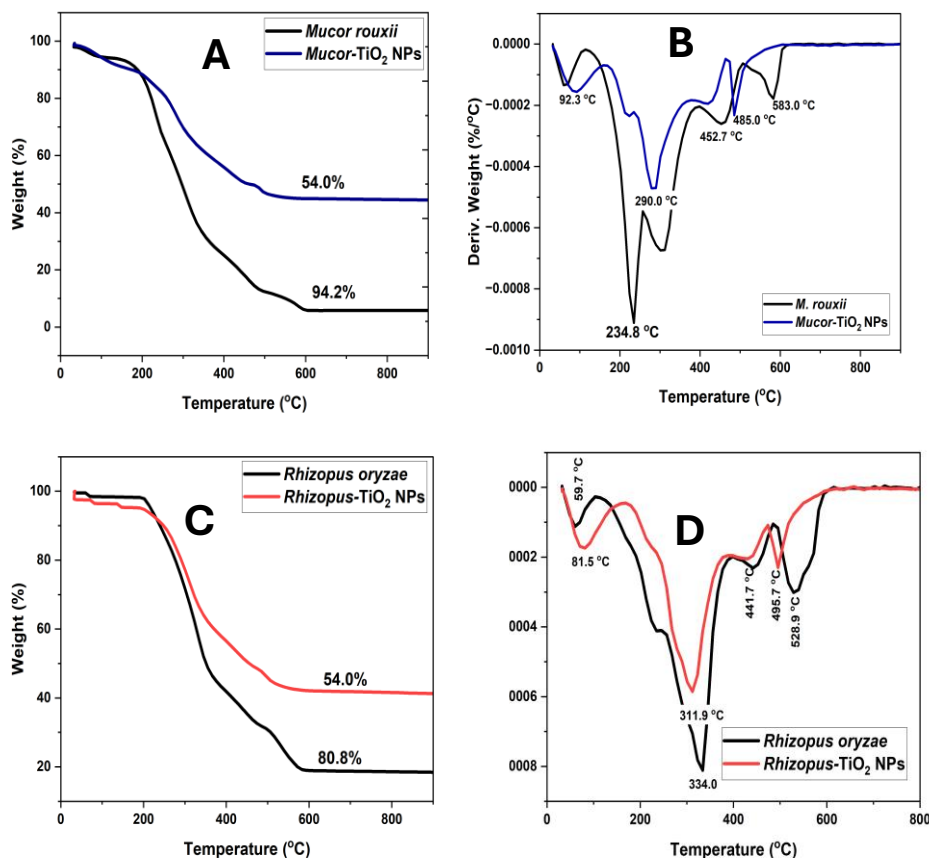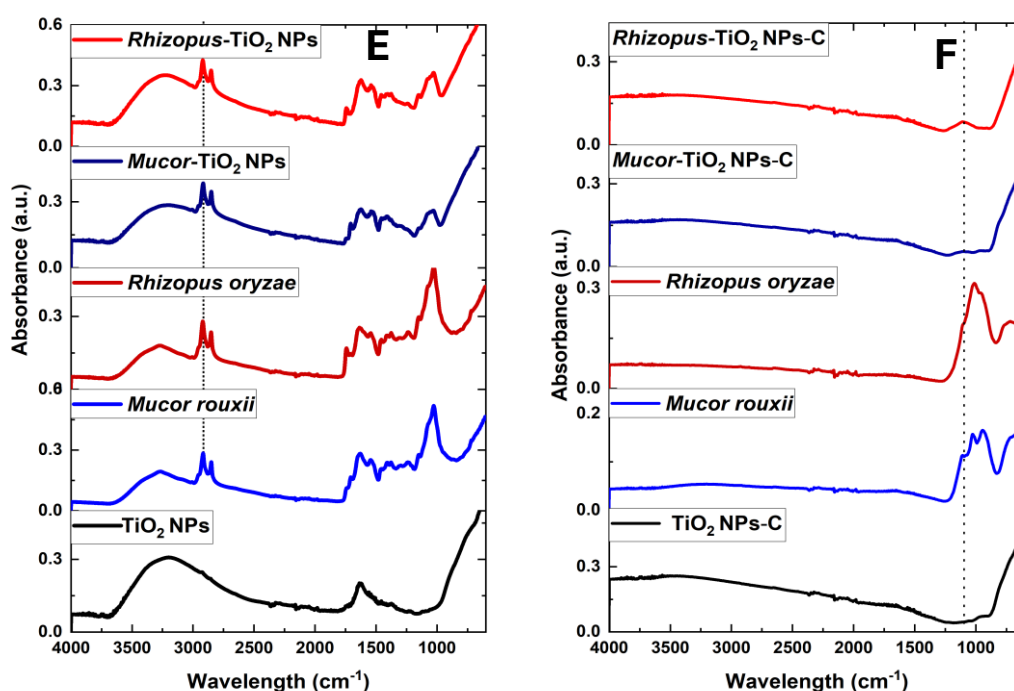
Figure 6.7: Heat response evaluated through thermogravimetric analysis and infrared (IR) characterization of fresh material and degraded samples. In Panel A and B, the thermogram and order of digestion are shown for *M. rouxii* respectively, while Panels C and D represent the same for *R. oryzae*. Panels E and F display the IR spectra of fresh mycelia and TiO_2 NPs-modified mycelia, along with their degraded forms after exposure to 900°C

6.3.10. Evaluation of UV Radiation protection of TiO_2 NPs - Modified mycelia composite

Measuring the amount of radiation absorbed or transmitted in the ultraviolet-visible light region can provide insights into the protective nature of material against UV-A (351-400 nm) and UV-B (280-315 nm) radiation. My experiment, guided by my previous findings on the morphology of both sides of the mycelia of *M. rouxii* and *R. oryzae*, primarily evaluated the growth face of ordinary mycelia and those modified with TiO_2 nanoparticles (NPs) for UV protection. My study indicated a progressive increase in Ultraviolet Protection Factor (UPF) values due to functionalization with TiO_2 NPs and this is presented in Table 6.5 below. The UPF values of the ordinary mycelia were calculated as 3.64 for *M. rouxii* and 2.12 for *R. oryzae*. However, with TiO_2 doping, these values increased to 6.20 and 4.49, respectively. Notably, only 17.02% (down from 26.30%) and 22.36% (down from 41.52%) of UV-B was transmitted through the TiO_2-coated *M. rouxii* and *R. oryzae*, respectively. According to Zhang et al., (2016), cotton fiber naturally has a UPF value of 6.0, with a UV-A transmission of 23.60% and a UV-B

transmission of 14.54%, resulting in a UPF value of around 6.0. After functionalization with TiO_2 NPs, the UPF value increased to between 30 and 50, though the complex chemicals used may not align with environmental acceptability. In another study by (Rabiei et al., 2022), a different method was employed, achieving a UPF value greater than 50 from less than 20 in ordinary fabric. This method when introduced resulted in a UPF increase to 6.20 in *M. rouxii* and 4.49 in *R. oryzae*. However, the high concentration of NaOH used led to the deacetylation of the mycelia, forming chitosan during the experiment. This was confirmed through FTIR spectroscopy of the resulting composite (Figure 6.8).
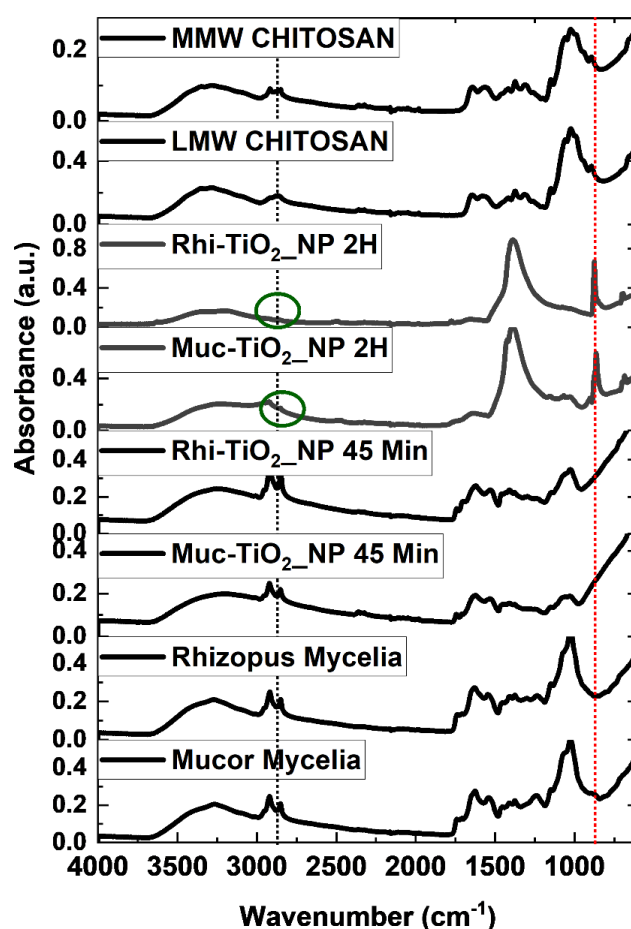
Figure 6.8: FTIR Spectroscopy indicating deacetylation resonances of fungal Mycelia: green rings highlight regions of interest for N–H and amide-related bands.

UV radiation is marked around 100 – 400 nm within the electromagnetic spectrum and is characterized by its short wavelength and higher energies which give high penetration power (Patil et al., 2021). The UV- R is divided into three distinct regions based on their effects on biological tissues, and these are UV- A (320 - 400 nm), UV-B (280 to 300 nm) and UV- C (100-280 nm) (Zayat et al., 2007). The proportion of the different UV-rays that reaches the

earth differs, but all have the sun as the primary source (Patil et al., 2021). UV-C has the highest energy, and it is also the most damaging, but it is completely absorbed by oxygen and ozone reducing its potential to cause earth damage, while almost 95 % of UVB is also absorbed by the ozone layer of the stratosphere but the remainder still reaches the earth (Black, 2014; Maverakis et al., 2010). The UV-A is almost unhindered and a significant percentage of it reaches the earth, but it has the least energy of the three. This proportion that reaches the earth synergistically combines with UV-B in many health, biomedical, and environmental situations like Cancer, DNA damage, food deterioration, and sunburn (Lucas et al., 2019; Nerín et al., 2006). My results show a significant reduction in the amount of transmitted UV radiation, making this a very promising outlook with few modifications needed to optimize the effect. My results show a significant reduction in the amount of transmitted UV radiation, suggesting a promising outlook for UV protection with further modifications.

Table 6.5: UV-Radiation Protection by Mycelia and TiO$_2$-Functionalized Mycelia

Sample	UV-A (%)	UV-B (%)	UPF Value	REF
Cotton fibre (before modification)	23.60	14.54	6.00	Zhang et al., (2016)
M. rouxii	32.27	26.30	3.64	
Mucor-TiO$_2$ Normal Method	46.68	17.02	5.16	
Mucor-TiO$_2$ Inclusion of NaOH-5 h	14.57	16.59	6.20	Rabiei et al., (2022).
R. oryzae	55.93	41.52	2.12	
Rhizopus-TiO$_2$ Normal Method	44.03	18.70	4.82	
Rhizopus-TiO$_2$ Inclusion of NaOH-5 h	23.29	22.36	4.49	

6.3.10.1. Technical Modifications to Extend the Depth of the Study

So far, although the method by (Rabiei et al., 2022) yielded better UPF values, it resulted in thinner mycelia films due to the nature of Mucorales, which have free chitosan in their mycelia or undergo chitin deacetylation when exposed to high concentrations of NaOH. To address this, I revisited my previous results. In Chapter 5, I developed mycelia with varying properties by altering the concentration of carbohydrates and carbon sources in some fungal strains. I have introduced selected groups with interesting mechanical properties (especially thickness) and natural melanin (Belozerskaya et al., 2017) for UV-radiation protection evaluation in this study. I chose and evaluated *A. niger* (PDB), *B. cinerea* (PDB), and *B. cinerea* (120 mM glucose). Initial results indicated that these fungi provided better UV radiation protection in their natural state compared to *M. rouxii* and *R. oryzae*. The results are summarized in Table 6.6. Further experiments involved doping their mycelia with TiO_2 NPs, which increased UPF values across the groups, with notable absorption of up to 80% of either UVA or UVB (Table 6.6). Due to sustainability concerns, I opted for the method by (Shaheen et al., 2019) for this study, despite (Rabiei et al., 2022) giving better initial results. From the experiments, I observed that nutrients played a role; *Botrytis* with 20 mM glucose in its media grew thicker but softer mycelia, allowing more interaction with the TiO_2 NPs during composite formation compared to *Botrytis* in PDB, which was crustier and had reduced interaction. With progressive experiments on the effects of nutrients and how they modify the mechanical properties of the mycelia, further breakthroughs are expected in future experiments.

Future experiments could focus on tuning the mycelia by modifying the carbon source to achieve better UPF values. Interestingly, with both *Aspergillus* and *Botrytis* being naturally melanin-pigmented fungi, future works could also evaluate the specific roles of pigments and the possibility of integrating lab-designed pigments or functional compounds to enhance this function.

Table 6.6: UV Radiation Protection and UPF Values of Selected Fungi

Sample	UV-A (%)	UV-B (%)	UPF Value	
B. cinerea (120 mM Glucose)	33.81	30.47	3.13	
B. cinerea PDB	24.84	24.07	3.95	
A.s niger PDB	14.61	16.57	6.10	

After Modification with TiO$_2$ NPs				
B. cinerea (120 mM Glucose)	19.50	17.30	5.88	
B. cinerea PDB	29.46	16.56	5.76	
A. niger PDB	17.30	10.70	6.41	

6.4. Conclusion

In this study, I explored the potential of mycelia-based materials from *M. rouxii* and *R. oryzae* for innovative applications, including surface non-wettability, thermostability, and UV-radiation protection. My findings demonstrated that these mycelia, when modified with titania (TiO$_2$) nanoparticles, exhibit significant improvements in these properties, making them suitable for multifunctional biodegradable scaffolds. I successfully functionalized the mycelia with TiO$_2$ nanoparticles, as confirmed through SEM/EDX analysis. This functionalization altered the surface properties, increasing hydrophobicity and enhancing thermal stability. The TiO$_2$- modified mycelia showed a delayed degradation of the organic matrix by nearly 100°C, indicating improved thermal resistance. Additionally, the UV protection factor (UPF) values significantly increased, making the mycelia more effective at blocking harmful UV-A and UV-B radiation. My study also highlighted the differences in the structural and surface properties of the growth face (GF) and media face (MF) of the mycelia. The GF exhibited tighter packing and greater nanoparticle incorporation, which influenced the distribution of TiO$_2$ nanoparticles and contributed to the observed enhancements in surface and thermal properties. The interdisciplinary nature of this research, combining mycology, materials science, and nanotechnology, underscores the potential of mycelia-based materials for sustainable and innovative applications. The successful development of TiO$_2$- modified mycelia scaffolds opens new avenues for their use in various fields, including environmental protection and biomedical engineering. This work provides valuable insights into the behaviour and potential applications of mycelia-based materials, paving the way for future research and development in this promising area. The findings contribute to the growing body of knowledge on sustainable materials and their role in addressing global challenges.

CHAPTER 7

7.0 Nutrient Sensing in Mucorales: Exploring Fungal Polymer, Glyconanoparticles via the Agar-Bridge Model

In this chapter, I explored the sensing of glyconanoparticles (with either glucose or chitosan surfaces) by mucorales fungi (*M. rouxii* and *R. oryzae*) and their role in self-control using a novel nutrient-sensing model, the agar-bridge model. My aim was to extend the application of mucorales beyond just bulk mycelia materials, by linking the use of biopolymer extracted from mucorales with fungal growth control at the fundamental levels. I synthesized carbohydrate-coated gold nanoparticles (AuNPs) and examined the chemical and biological impacts of glucose and chitosan surfaces on the growth and filament structures of *M. rouxii* and *R. oryzae*. In previous studies (Chapter 3), I reported on the synthesis and characterization of glucose-capped gold nanoparticles (AuNPs) as glyconanoparticles. In this chapter, I focus on the synthesis of glyconanoparticles from fungal-extracted chitosan using an improved method. However, both types of glyconanoparticles are used in this chapter for their application. The chitosan-surfaced nanoparticles exhibited fascinating physicochemical (TEM/EDX) and thermogravimetric behaviour (TGA), with sizes ranging from 30 to 40 nm and near-complete digestion of surface material around 600°C. Peaks corresponding to gold were recorded in their crystallinity study (XRD), confirming the formation and crystalline nature of AuNPs. I investigated whether these carbohydrate biomolecules retained biological functions beyond their chemical roles. Using the agar-bridge model, fungal mycelia initially grew within an inner agar core, then crossed a bridge containing the biomolecules in aqueous media to reach the outer agar area for continued growth. Hydrophilic dyes (Brilliant Blue and Cochenille Red) were used to understand diffusion across the agar, and between the agar areas which diffused within 4 h, providing insights into the behaviour and sensing potentials of glyconanoparticles. My observations revealed that glucose-capped AuNPs acted as a nutrient source for both *M. rouxii* and *R. oryzae*, while chitosan-capped AuNPs exhibited fungistatic properties, inhibiting fungal growth for approximately 12 h. From further analysis, the chitosan derived from *mucor* inhibited the growth of the two fungi for up to 72 h showing potential for fungicidal effects. Notably, the chitosan used was extracted from the deacetylation of chitin from each fungus. I conclude that the carbohydrates retained their biological properties to a reasonable extent despite being surface materials and that the agar-bridge model is an excellent and innovative

approach to characterize fungal sensitivity and response to nanoparticle surface materials within the same experimental setup.

Key Words: Glyconanoparticles; Mucorales; agar-bridge model; Mycelia biopolymer; AuNPs (Gold Nanoparticles); Glucose; Chitosan; Fungistatic.

7.1. Introduction

Fungi, such as Mucorales, can chemically detect environmental chemicals (nutrient-sensing) and respond in various ways, including changing growth direction, delaying growth via spore inactivation, or adopting dynamic growth patterns like heterogeneous branching of filaments (Meyer et al., 2021; Noman et al., 2022). As saprophytes, their survival largely depends on their environment, and they constantly sense their surroundings and make necessary structural or chemical changes (Meyer et al., 2021). Under controlled conditions, I can explore this trait either in biocontrol or in materials engineering. While previous studies focused on hyphal tips, directional changes, and chemical concentrations (Turrà et al., 2016), I focus on growth dynamics across obstacles (from glyconanoparticle stimuli) and how these changes affect fungal structure during growth. Additionally, fungi regulate the activities of other organisms by secreting secondary metabolites (Nguyen et al., 2023). By extracting fungal bio-actives and reintroducing them at higher concentrations, I can potentiate the self-control of the fungi using their own bio-active compounds. This study focuses on chitosan, a polysaccharide obtained from fungal biomass via chitin extraction and deacetylation. It also examines D-glucose, a common carbon source in fungal culture. I compare the biological activity of these compounds when used as capping materials on AuNPs and determine if they retain their activities, using a new nutrient-sensing model developed for this purpose.

Several models have been developed to study tropical behaviours in fungi, but modifications are often needed to suit different compounds and new measurement parameters. According to Schunke et al., (2020), traditional dish-based assays (Turrà et al., 2016) and microfluidic devices (Millet et al., 2019) have limitations in gradient consistency, reproducibility, and compatibility with filamentous fungi. Dish-based assays rely on manually created gradients, leading to variability, while microfluidic devices offer precise chemical control but are suited for single-cell organisms in liquid environments. The 3D-printed device by (Schunke et al., 2020) ensures standardized gradient formation, compatibility with solid matrices, and improved microscopy integration, making it reliable for investigating chemical sensitivity in filamentous fungi. Despite its advantages, the 3D-printed device has limitations. Bioactive

diffusion across wells can cause interference, making it unsuitable for evaluating unique compounds like nanoparticles with surface coatings. It may not determine whether molecules like carbohydrates retain their biological functions beyond their chemical roles. For materials engineering, fungal exposure to obstacles can force structural changes, but this system is limited in addressing such changes. By introducing the agar-bridge model, I can monitor in real time the chemical and biological effects of bioactives (such as glyconanoparticles) on fungi and explore how these effects change over different areas. I can also monitor structural changes and predict how biomolecules affect fungal structural changes at the fundamental level. The goal is to compare two types of glyconanoparticles capped with either glucose or chitosan (derived from the chitin of *M. rouxii* and *R. oryzae*) and determine if they retain their biological properties. Importantly, I also seek to understand what happens at the bridge and how this affects the pre-crossing, crossing, and post-crossing structure of the mycelia. This chapter addresses Objective 7 by comparing chitosan from shrimp and fungal origins in AuNP synthesis, and evaluating nutrient-sensing effects on fungal growth using glyconanoparticles in a novel agar bridge model.

7.2. Material and Methods

7.2.1. Materials

Gold (III) chloride trihydrate (HAuCl$_4$.3H$_2$O) (204390), 14 kDa cellulose dialysis tubing (D9527), low molecular weight chitosan-150-250 kDa (448869), medium molecular weight chitosan- 190-310 kDa (448877), were purchased from Sigma Aldrich (UK), and used as received. Acetic acid glacial (10384970), Brilliant Blue (E 133), and Cochenille Red (E 124) were purchased from Fisher Scientific UK Ltd. The glucose-capped AuNPs were synthesized and the details of all the properties are reported in Chapter 3. Information about growth media (agar) was also reported in Chapter 5.

7.2.2 Methods

7.2.2.1 Fungal Mycelia

The process for the cultivation and extraction of fungal materials and the mycelia characterization of the fungal mycelia used in this chapter is described in Chapter 6. The fungi are Mucorales (*M. rouxii* and *R. oryzae*).

7.2.2.2. Chitin Extraction and Conversion to Chitosan

Freshly harvested fungal mycelia deactivated at 120 °C in an autoclave (Crystal – MP25, Rodwell Scientific, UK) to halt production of extracellular products was washed 6 times with ddH$_2$O (100 g/600 ml). The deactivated mycelia were further freeze-dried at 223 K using a BT4KZL dryer (VirTis). Chitin extraction and conversion were done by adopting the two-step deproteinization and deacetylation process (Sivashankari & Prabaharan, 2017; Yuan et al., 2021) and subsequently characterized for physicochemical properties.

7.2.2.3. Optimization of Chitosan Gold Nanoparticles Synthesis, and Characterization

The synthesis and stabilization of chitosan gold nanoparticles (CHS-AuNPs) was achieved using four categories of chitosan. The low molecular weight chitosan (LMW-CHS) and middle molecular weight chitosan (MMW-CHS) are of crustacean origin (shrimp), and industrially sourced, while the *Mucor* chitosan (MUC-CHS) and *Rhizopus* chitosan (RHI-CHS) are from fungi, and lab extracted. CHS-AuNPs synthesis followed the procedure reported by Mohan et al, (2019) but with further optimization. Briefly, 1% acetic acid in a Pyrex 250 mL conical was heated and maintained at 90 °C in a water bath for 30 min to dissolve the chitosan completely at 0.25 %. Upon dissolution, 5 mL of 10 mM HAuCl$_4$.3H$_2$O was added while stirring continued. The absorbance of the synthesized CHS-AuNPs (monitored between 3-24 min at T3, T6, T9, T12, T15, T18, T21, T24, T27, and T30) complemented by hydrodynamic size evaluation (Zetasizer Nano-S Zen 600 (Malvern Instruments Ltd.) was used to determine the optimal conditions for synthesis.

7.2.2.4. Characterization of Chitosan Stabilized AuNPs (CHS-AuNPs)

Other than UV-Vis and dynamic light scattering which were done over different time points to monitor the best conditions at which the CHS-AuNPs can be synthesized, all of the other methods and conditions that were adopted for the physicochemical and morphological characterization of the Chitosan-AuNPs are the same as those reported in Chapter 3 for AuNPs with different surfaces.

7.2.2.5. The Formation of Agar Well, Fungal Inoculation and Glyco-AuNPs Treatment

The inner core of the agar, 0.2 cm thick and 1.0 cm in diameter, was bored with a 1.0 cm agar borer. The outer agar layer, 1.0 cm thick, surrounds the well, leaving a 0.25 cm empty bridge between the layers (Figure 7.1A). The agar was made from potato dextrose broth (24 g/L) containing 2% agar. A volume of 100 μL of either the test sample, glyconanoparticles, their respective surface material compounds, or controls was spotted in the space per sample.

Thermogravimetric analysis of the glyconanoparticles provided information about the amounts of chitosan or glucose on the AuNPs. This data was used to ensure equal concentrations of the carbohydrates as controls. Sample equilibration was tested via dye diffusion tests. To ensure the equal presence of surface materials, TGA analysis provided quantitative information about the surface materials on the AuNPs, which was then used for further calculations. Inoculation was done with 5 µL of the spore suspension of either *M. rouxii* or *R. oryzae* at a recorded concentration, and the fungal samples were incubated at 25 °C for 24 h before imaging on a thunder fluorescence microscope. The experiment was performed in triplicate.
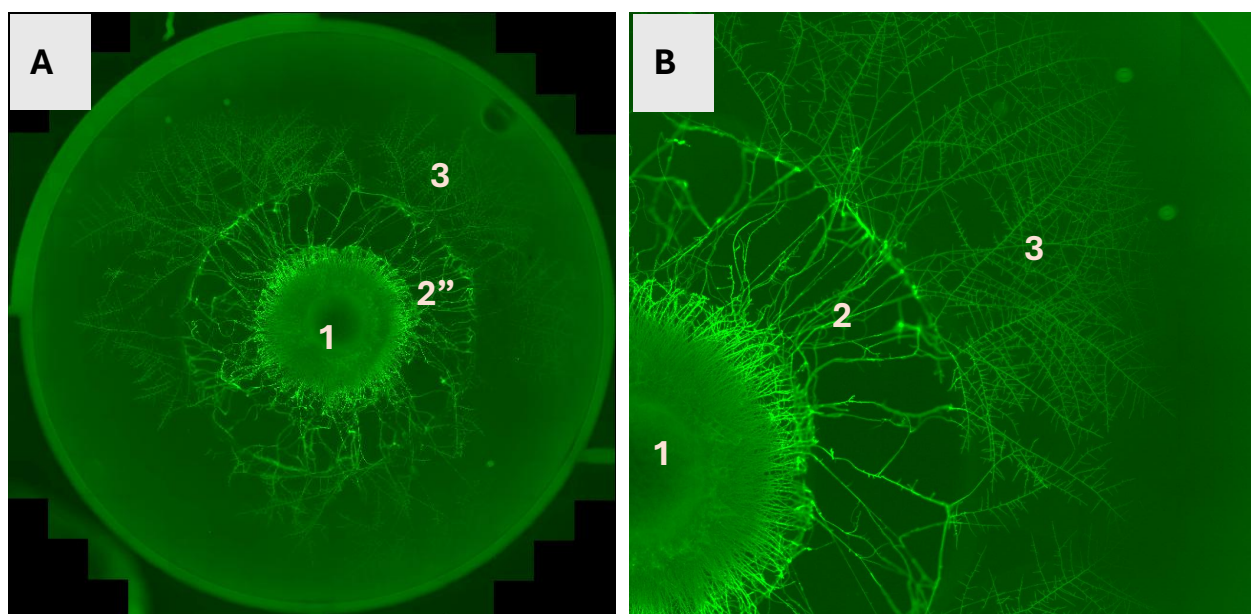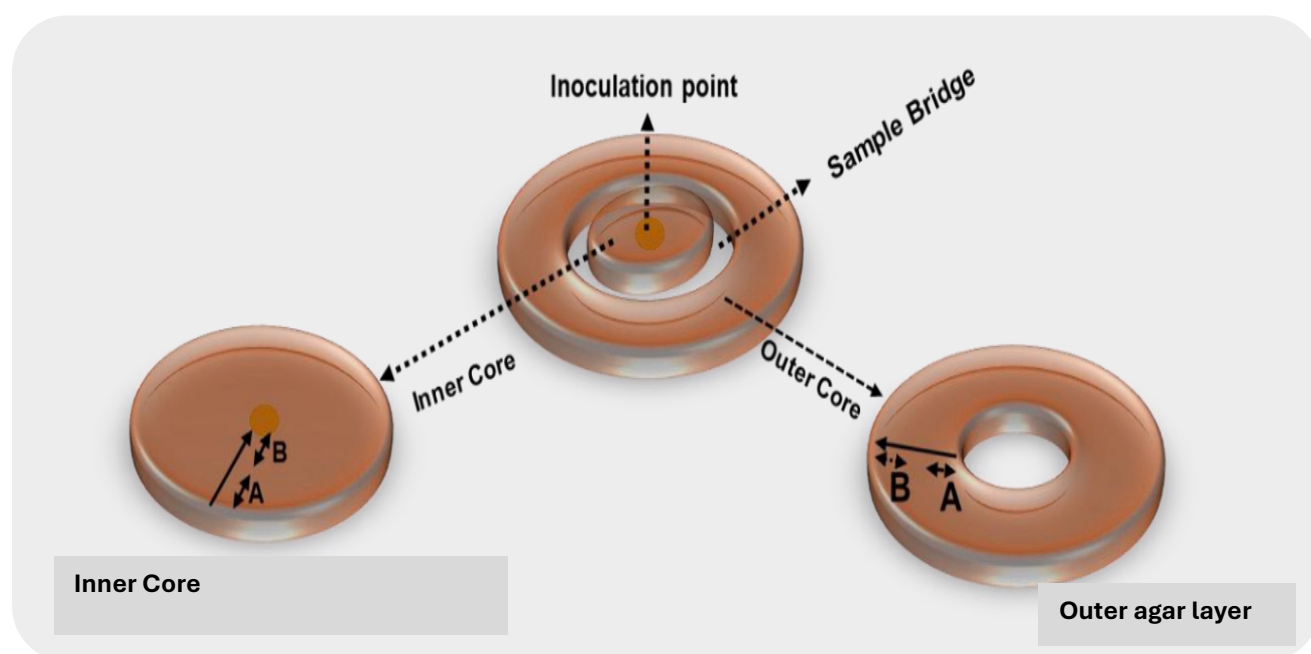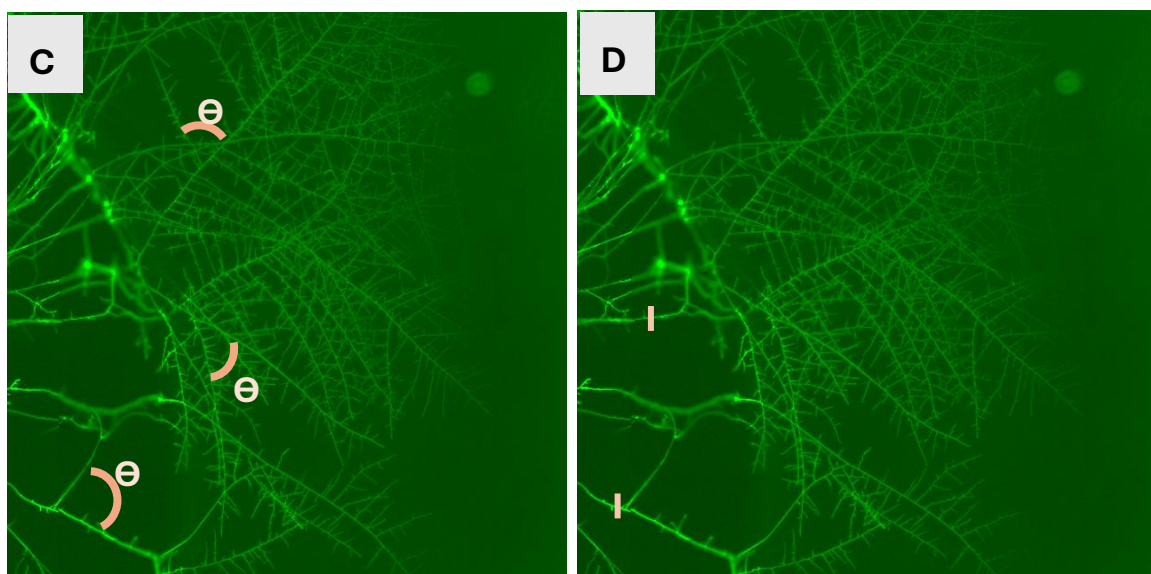
Figure 7.1: Agar-bridge model for assaying fungal growth alteration by glyconanoparticles. This Figure A represents three distinct areas: 1. inner core; 2. bridge; and 3. outer agar layer. Figure B is the amplified form of Figure A for label clarity. C shows the regions for measuring branching angles, and D indicates the areas for measuring hyphal diameter.

7.2.2.6. Dye Diffusion Assay to Determine the Rate of Diffusion Across the Agar.

The dye diffusion of two hydrophilic dyes (Cochenille Red and Brilliant Blue) was done at different time points 0, 15, 30, 45, 60, 90, 120, 150, 180, and 240 at a concentration of 100 μg/ mL, in DDH$_2$O. Images were taken after each point under stable conditions and the intensity of diffusion was measured using ImageJ (ImageJ 1.53t w/Adiposoft 1.1) software.

7.2.2.7. Fluorescence Imaging of Samples

Before imaging, 1mL of Calcofluor White dye (0.035 mg/ mL in 10% KOH) was spotted in each well. Finally, the samples were imaged using a fluorescent microscope (THUNDER fluorescence Imager -Live Cell & 3D Assay- from Leica) with an excitation wavelength of 380 nm and an emission wavelength of 475 nm. The images were taken in fluorescence mode monitoring growth in the three distinct areas (inner, bridge, and outer). From the images, approximately 20-100 filaments across the growth areas were measured, either in the inner agar core, the agar bridge, or the outer agar area, to determine hyphal diameter and branching angles, depending on the extent of growth. The growth area includes all filament growth areas from the point of inoculation.

7.2.2.8. Data Analysis
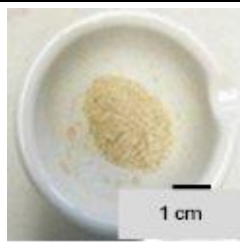
Except stated otherwise, the qualitative data generated in triplicate was analysed via analysis of Variance and presented in plots as mean ± standard deviation. For comparison, Tukey's Post hoc multiple comparison tests were performed to establish the possibility of significant differences in samples. Microscopy Images were processed using ImageJ (ImageJ 1.53t w/Adiposoft 1.1) software.

7.3. Results and Discussion

7.3.1. Optimizing Chitin Extraction and Conversion to Chitosan

In my study, I successfully extracted chitin (presented in Table 7.1 below) and highly deacetylated chitosan from the mycelia of *M. rouxii* and *R. oryzae*. I considered various extraction methods to optimize both yield and quality. Ospina et al. (2014) evaluated five different methods, finding that the highest chitin yield (using 1 M NaOH, 1:30 w/v, at 40°C for 2 h) had the least similarity to standard chitin, while the method with the best comparable properties (using NaOH 4 M, 1:20 w/v, at 100 °C for 3 h) resulted in a lower yield. This highlighted a trade-off between quantity and quality, with quality improving at higher temperatures. (Pochanavanich & Suntornsuk, 2002) demonstrated that chitin could be efficiently extracted from various fungi and yeast at 1 M NaOH (1:30 w/v) at 121°C for just 15 min in an autoclave, while (Yuan et al., 2021) achieved similar results at 121 °C for 30 min. These findings guided my approach, leading us to adopt higher-temperature methods for faster extraction. Consequently, I obtained chitin with good properties and successfully converted it to chitosan with a high degree of deacetylation (DDA), which is ~90%. This balance of efficient extraction and high-quality conversion was crucial for my study. DDA assessment followed the NMR protocol described by (Lavertu et al., 2003).

Table 7.1: Chitin Extraction Yields and Properties from Mycelia of *M. rouxii* and *R. oryzae*

Sample	% Yield Mycelia-Chitin	DDA (%)	Chitin	% by weight of Chitin-Chitosan
M. rouxii	12.56 ± 1.12	92.1		88.1
R. oryzae	10.25 ± 0.73	92.9		80.0
Shrimp Chitin (Industrially Sourced)	NA	71.0		NA

7.3.2. Characterization of chitin and chitosan

7.3.2.1. Morphology of Fungal Chitin and Chitosan

The microstructural geometry observed by Scanning Electron Microscopy (SEM) reveals the morphology of the chitins and highly deacetylated chitins (chitosan), as shown in Figure 7.2A. The chitins appear as well-packed materials with somewhat flat surfaces, as reported by (Erdoğmuş et al., 2023). Interestingly, after the deacetylation process, the deacetylated chitin appears less tightly packed, with clear spaces between the fibres. There are no distinct differences in the morphology of both chitin and deacetylated chitin for *M. rouxii* (Figure 7.2 1A) and *R. oryzae* (Figure 7.2 1B).
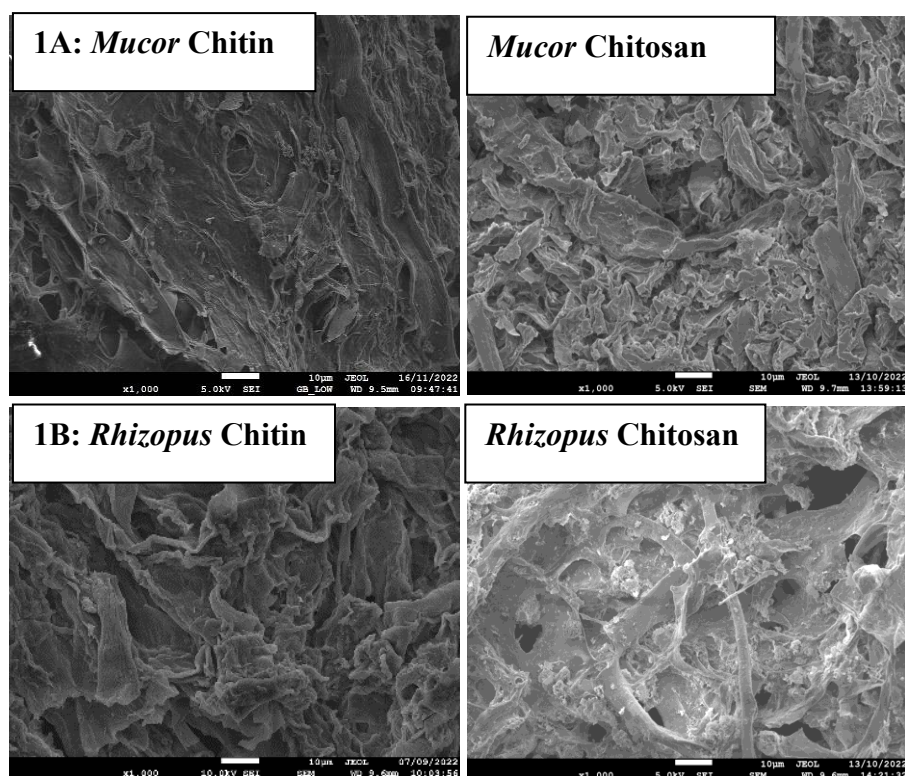
Figure 7.2A: Scanning electron microscope (SEM) images showing the morphology of chitins and highly deacetylated chitins (Chitosan) from (A) *M. rouxii* and (B) *R. oryzae*. SEM images include a scale bar representing 10 µm.

7.3.2.2. Characterization of Chitin by FTIR, XRD, and TGA

The characteristic chitin peaks for *R. oryzae*, *M. rouxii*, and standard chitin, denoting the functional groups, are revealed from the spectra resulting from FTIR analyses and presented in Figure 7.2B. Compared to the standard chitin, all characteristic peaks were recorded at their unique wavelengths between 4000-600 cm^{-1}. These correspond to OH stretching vibration at 3257 cm^{-1}, C–H sp³ vibration at 2920 cm^{-1}, C=O stretching of amide I at 1625 cm^{-1}, NH bending of amide II at 1560 cm^{-1}, CN stretching of amide III at 1375 cm^{-1}, and –C–O–C stretching vibration at 1026 cm^{-1} (Harmami et al., 2019; Triunfo et al., 2022). The nomenclature of the chitins (α, β, or γ) can be established using relevant distinctions from the FTIR spectra as guided by the literature. For example, (Kumirska et al., 2010) established a model for the application of spectroscopic techniques for the natural analysis of chitin and chitosan. According to the authors, the C=O stretching region between 1700-1500 cm^{-1}, representing an amide moiety, produces different peaks for α and β-chitins. The α-chitin is identified by a

unique amide band split, producing two characteristic peaks around 1660 cm⁻¹ and 1630 cm⁻¹, respectively. The cause of this occurrence has been explained by authors, linking it to either the influence of hydrogen bonding or the existence of the amide moiety in enol form (Focher et al., 1992; Jang et al., 2004). For β-chitins, a single peak is formed around 1630-1650 cm⁻¹ (Jang et al., 2004; Kumirska et al., 2010). Another interesting spectral difference between α and β-chitins is the band shift from around 890 cm⁻¹ in β-chitins to around 895 cm⁻¹ in α-chitins (Kumirska et al., 2010). Based on these descriptions, the standard chitins in this study all have a band split around the 1660 cm⁻¹ region. According to the descriptions of Jang et al., (2004) and Kumirska et al., (2010), it can be suggested that the chitins are of alpha (α) nomenclature.
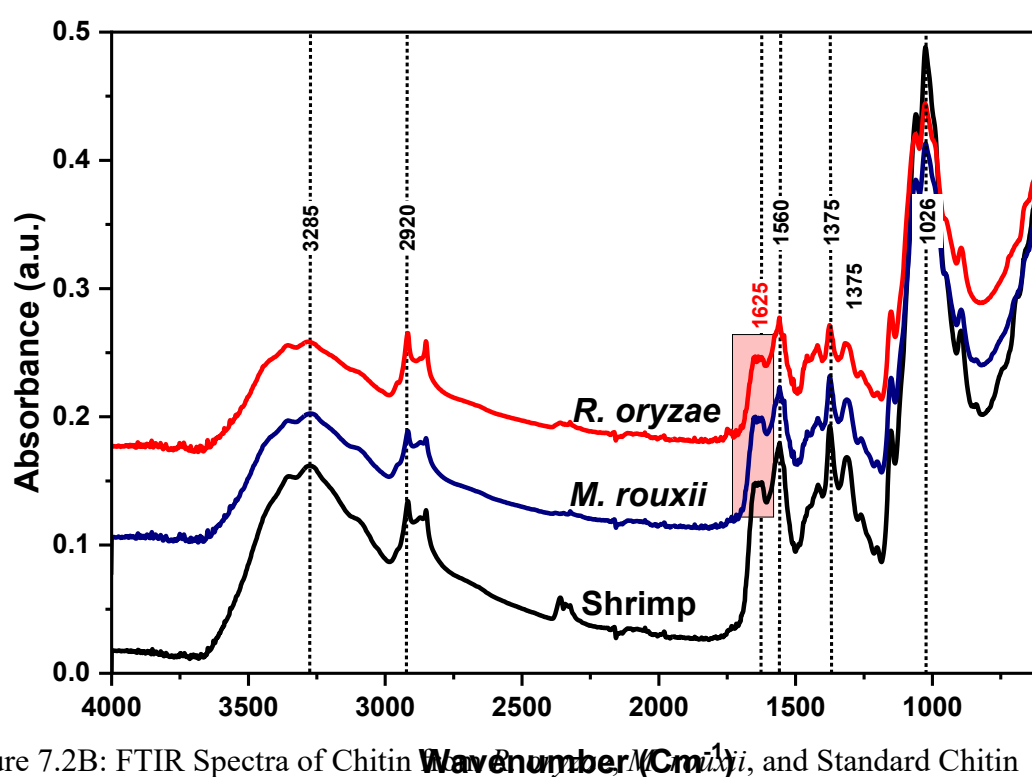
Figure 7.2B: FTIR Spectra of Chitin from Shrimp, R. oryzae, M. rouxii, and Standard Chitin

7.3.2.3. X-ray Diffraction (XRD) Analysis of Chitin

The X-ray diffraction patterns of chitin from shrimp, *R. oryzae*, and *M. rouxii* within the 5–80° 2θ region show distinct crystallinity features, Figure 7.2C. The shrimp chitin has well-defined peaks at 9.6°, 19.6°, 23.2°, and 39.1° (2θ), indicating high crystallinity typical of α-chitins (Kaya et al., 2014). Both fungal chitins are also crystalline, with *Rhizopus* chitin displaying broader peaks at 9.6°, 19.6°, and 26.3°, suggesting lower crystallinity characteristics of fungal chitins.
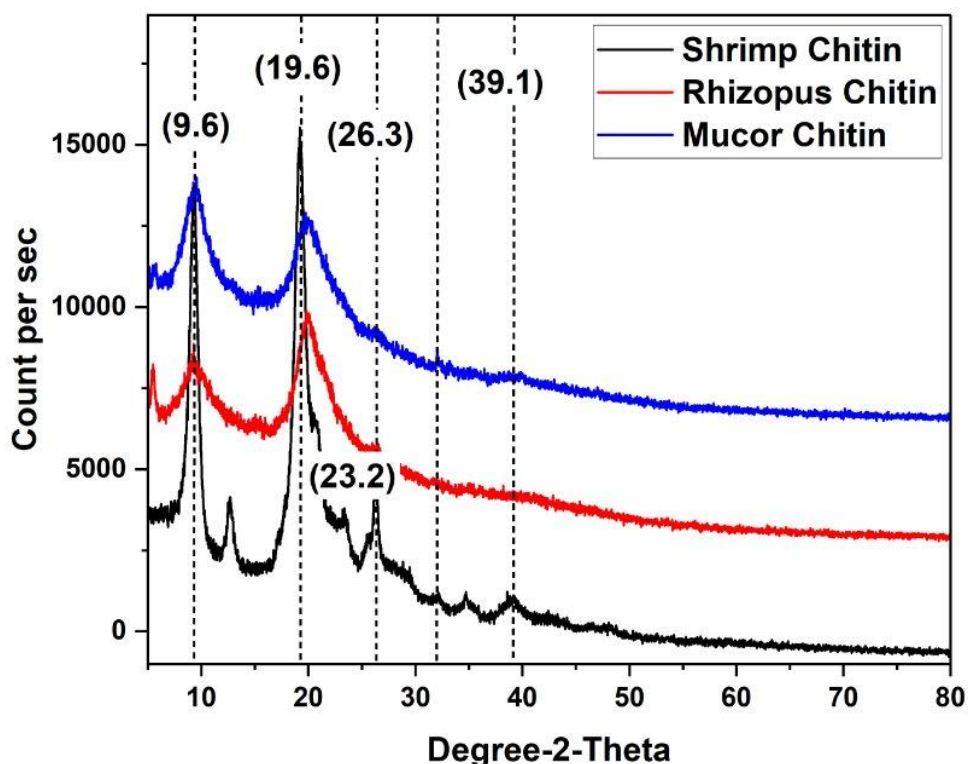
Figure 7.2C: X-ray diffractogram of chitin from *R. oryzae*, *M. rouxii,* and standard chitin

7.3.2.4. Thermogravimetric Analysis (TGA) of Chitins

The thermogravimetric analysis (TGA) of industrial chitin, *Rhizopus* chitin, and *Mucor* chitin reveals distinct thermal stability profiles within 0 – 900 °C. This is presented in Figure 7.2D. The initial weight loss observed below 70 - 100°C corresponds to the evaporation of residual moisture (Rai et al., 2010). The major degradation step occurs between 280°C and 340°C, indicating the thermal decomposition of the polysaccharide backbone (Girometta et al., 2019). Within this range, the industrial chitin exhibits a higher degradation temperature (340 °C), this suggests greater thermal stability due to its highly ordered crystalline structure as recorded from XRD analysis (Zeng et al., 2010). In contrast, *Rhizopus* and *Mucor* chitins degrade at slightly lower temperatures between 300–320°C), indicating lower crystallinity and weaker polymer interactions. The fungal chitins also display a broader degradation range, which may be attributed to structural heterogeneity and different acetylation patterns (Girometta et al., 2019).
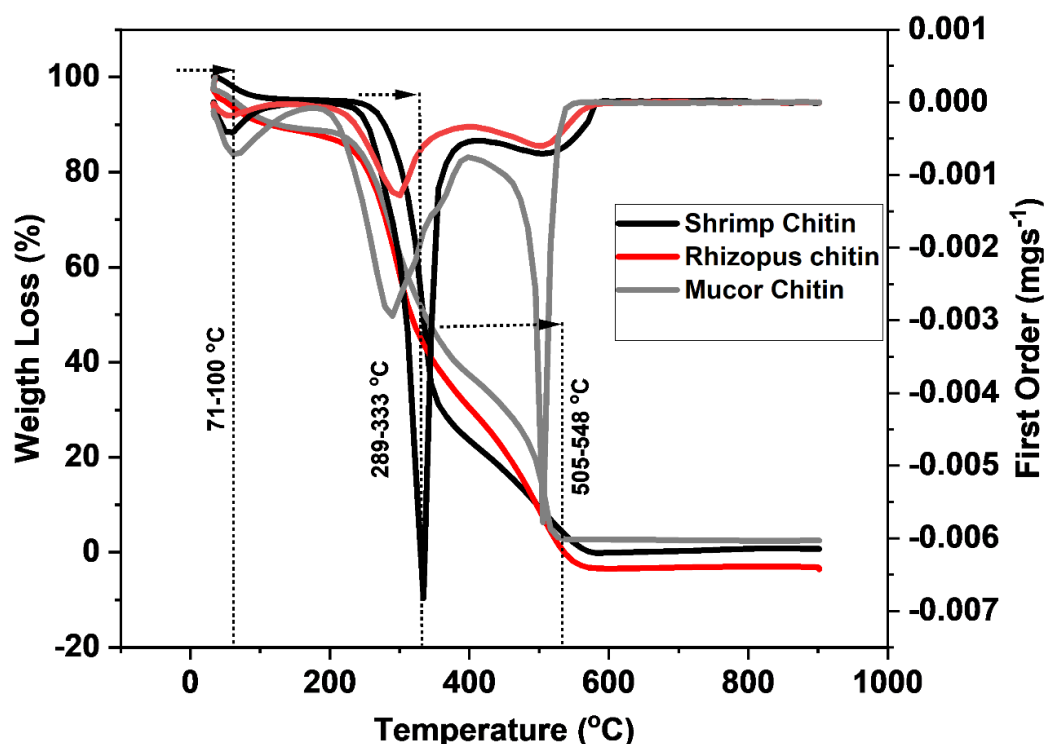
Figure 7.2D: Thermogravimetric Analysis (TGA) of Industrial, *Rhizopus*, and *Mucor* Chitins

7.3.3. Optimization of Synthesis Conditions for Chitosan-Stabilized Gold Nanoparticles

I conducted preliminary evaluations to determine the optimal conditions for synthesizing CHS-AuNPs, testing various time points for mixing/ reaction time between 3- and 30-min. UV-Vis spectroscopy was employed to monitor surface plasmon properties. The surface plasmon resonance (SPR) properties of the synthesized CHS-AuNPs, derived from low and middle molecular weight chitosan, showed maximum absorption peaks between 520-540 nm, characteristic of AuNPs (Huang & Yang, 2004; Mohan et al., 2019). These are illustrated in Figure (7.3A and B). A gradual shift in the SPR peak from λmax=540 nm at T3 to λmax=520 nm at T30 was observed, suggesting changes in the size or shape of the CHS-AuNPs over time (Huang and Yang, 2004). Chitosan from fungal or crustacean sources has been used as a reducing and stabilizing agent in AuNP synthesis, with various conditions yielding particles with different physicochemical and morphological properties (El-Naggar et al., 2022; Mohan et al., 2019; Mostafa et al., 2022). Factors influencing the outcomes of CHS-AuNP synthesis include chitosan concentration (Huang & Yang, 2004), synthesis duration (Kalaivani et al., 2020), and temperature. Literature suggests that more stable CHS-AuNPs with homogeneous distribution properties can be synthesized at 0.25% chitosan concentration. However, I demonstrated that optimal synthesis conditions for low and middle-molecular weight chitosan

exceed 15 min at 90°C. This finding is valuable for exploring fungal-derived chitosan, which is more industrially viable, cost-effective, and sustainable. In my study, I observed improving SPR peak properties up to 27 min under conditions like those adopted by (Mohan et al., 2019). However, traces of aggregation, monitored by DLS, were observed at T30 for MMW_CHS_AuNPs, guiding the synthesis of fungal-CHS-AuNPs at T27, which exhibited comparable SPR properties to those of low and middle molecular weight chitosan (Figure 7.3 C). All the CHS-AuNPs have cybercritics brick red colour (Figure 7.3 D) and a single band (λ_{max}) around 520 nm within the 300 – 800 nm region which is a confirmation of the synthesis of CHS-AuNPs (Huang and Yang, 2004).
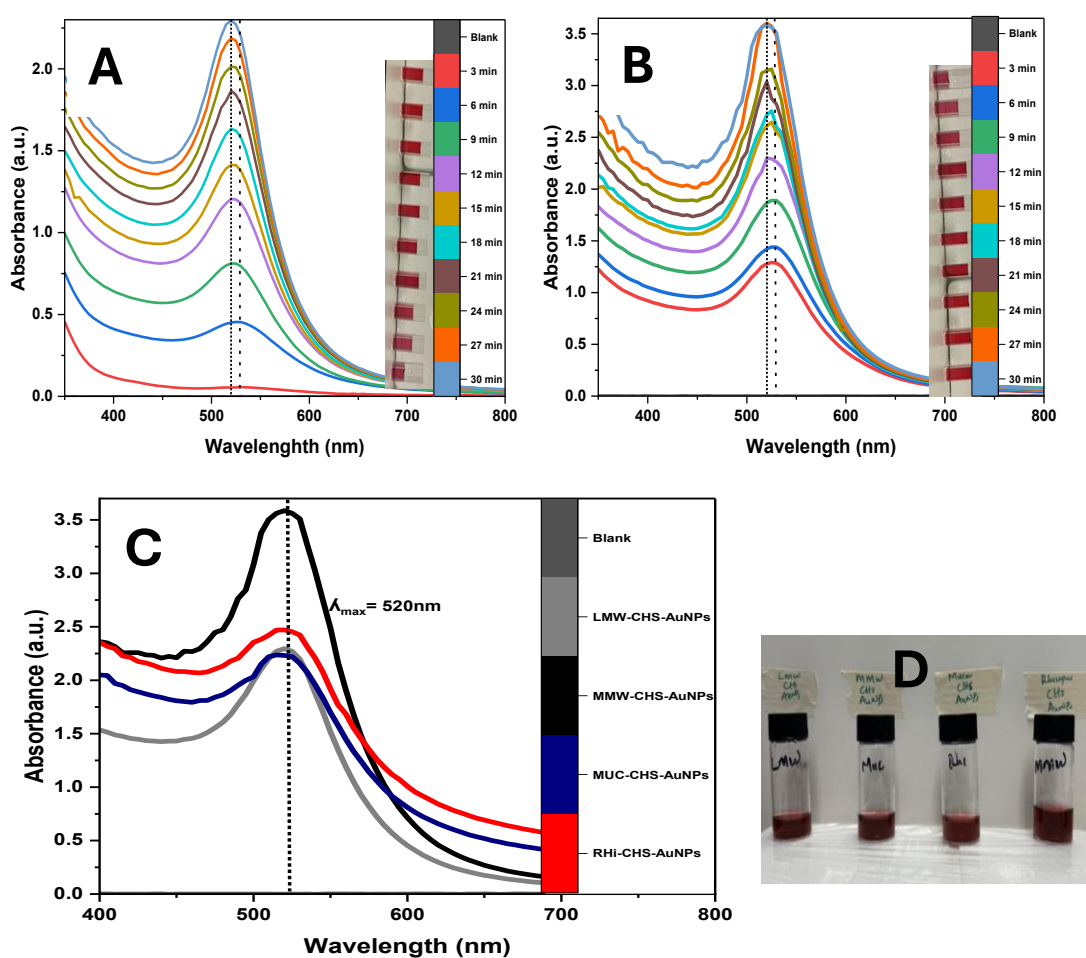
Figure 7.3: Ultraviolet-visible light spectra showing the surface plasmon resonance peaks of (A) LMM-CHS-AuNPs (T1-T30); (B) MMW-CHS-AuNPs (T1-T30); (C) fungal and standard CHS-AuNPs; and (D) a representative image of the chitosan AuNPs from standard and fungal chitins.

7.3.3.1. Hydrodynamic Size and Stability of Chitosan-Stabilized Gold Nanoparticles

The hydrodynamic size and zeta potentials of the synthesized CHS-AuNPs, evaluated through DLS, are presented in Table 7.2. The fungal chitosan-mediated nanoparticles, whether from *Mucor* or *Rhizopus*, have comparable hydrodynamic sizes (by number) to those synthesized from industrial chitosan. Generally, the size distribution was recorded around 30.0 – 35.0 nm, with surface charges ranging from 44.0 to 47.0 mV. High surface charges are good predictors of nanoparticle stability, and the overall positive charge is believed to be due to the free amino groups of the chitosan coat (Sharma et al., 2019). The CHS-AuNPs are also uniformly distributed, marked by very low polydispersity indices (0.1 - 0.3).

Table 7.2: Hydrodynamic Size and Zeta Potentials of CHS-AuNPs Evaluated by DLS

Sample	Hydrodynamic Size (nm)	Surface Zeta potentials (mV)	Electrophoretic mobility (μmcm/Vs)	Conductivity (mS/cm)
LMW-Chs-AuNPs	34.34 ± 10.03	44.40 ± 4.76	3.54	0.91
MMW-Chs-AuNPs	36.10 ± 11.53	45.10 ± 4.34	3.77	0.82
Mucor-Chs-AuNPs	33.09 ± 5.10	40.41 ± 5.55	3.41	1.14
Rhi-W-Chs-AuNPs	35.75 ± 12.87	46.43 ± 4.59	3.70	1.06

7.3.3.2. NMR Analysis of Chitosan Samples

The NMR spectra presented in Figure 7.4 compare different chitosan samples, including medium molecular weight (MMW-CHS), low molecular weight (LMW-CHS), Rhizopus-derived (Rhi-CHS) chitosan, and a deacetylated *Mucor* sample (Muc-CHS). The spectral differences observed among these samples align with their respective degrees of deacetylation (DDA), as detailed in Table 7.3. The MMW and LMW laboratory standards exhibit similar spectral profiles, consistent with their comparable DDA values of 73.35% and 73.53%, respectively. The presence of strong signals in regions associated with residual acetyl groups suggests that these samples retain a significant proportion of n-acetylglucosamine units (Akpan et al., 2020). In contrast, the *Rhizopus*-derived chitosan (Rhi-CHS) exhibits sharper and more

distinct peaks, which may indicate a higher degree of structural order or differences in the polymer composition (Hirai et al., 1991). This observation corresponds with its higher DDA of 95.54%, as increased deacetylation typically results in reduced spectral complexity due to the prevalence of glucosamine units. The deacetylated *Mucor* sample demonstrates the highest DDA (98.04%), indicative of extensive acetyl group removal (Akpan et al., 2020). This high level of deacetylation is likely reflected in the NMR spectrum through diminished acetyl-related peaks, signifying a polymer structure predominantly composed of glucosamine units (Akpan et al., 2020). The Degree of Deacetylation (DDA) was determined by analysing the integrals of the NMR peaks corresponding to the proton H1 of the deacetylated monomer (H1-D) and the three protons of the acetyl group (H-Ac) following (Lavertu et al., 2003).
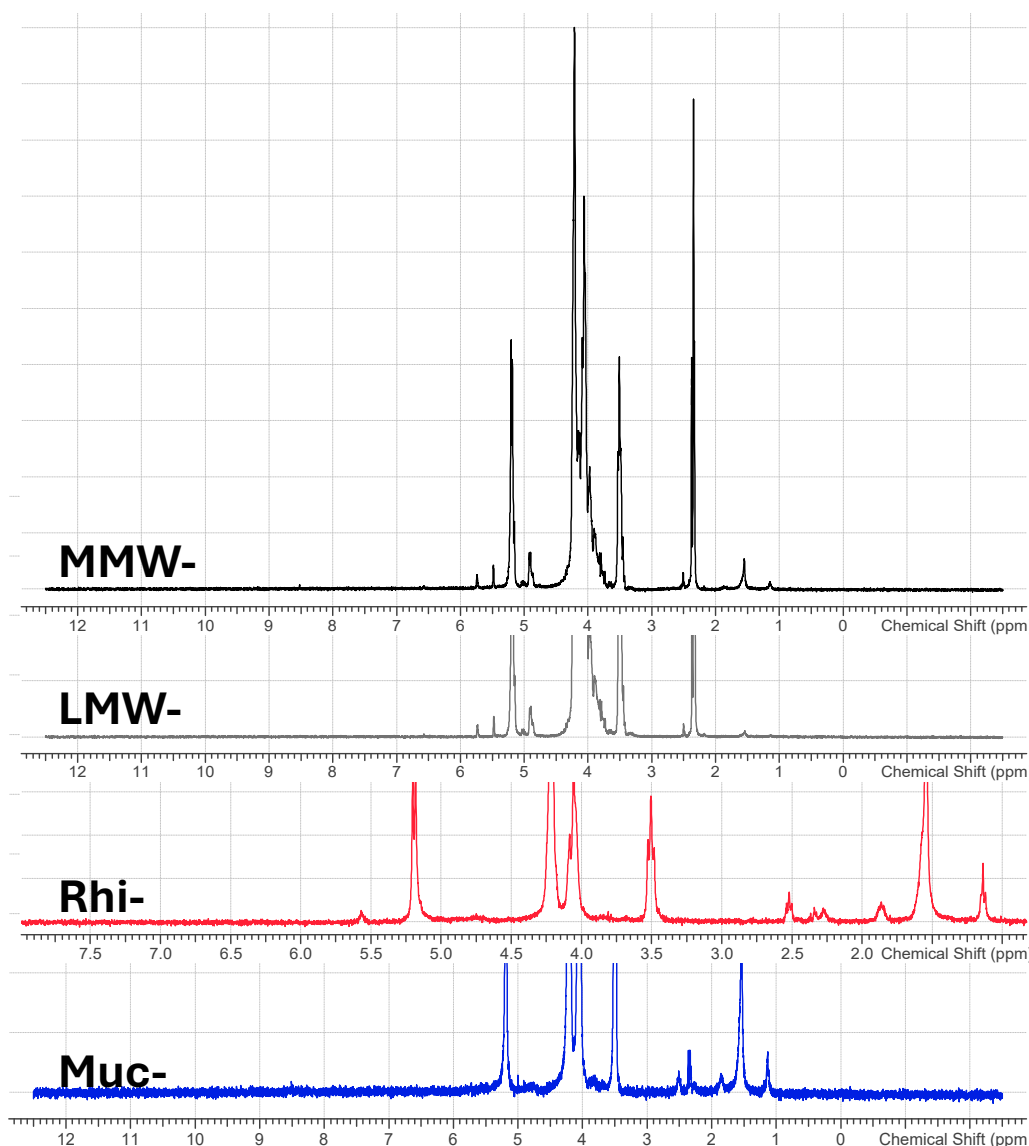
Figure 7.4: ^{1}H-Nuclear magnetic resonance spectra of chitosan from different sources.

Table 7.3: Degree of Acetylation of Different Chitosan from NMR Analysis

Sample Description	Condition of Deacetylation	HID	Hac	DDA (%)
Deacetylated *Mucor*	Autoclave 2M/121 °C/20 min	1	0.06	98.04
Deacetylated *Rhizopus*	Autoclave 2M/121 °C/20 min	1	0.14	95.54
MMW Lab Standard		1	1.09	73.35
LMW Lab Standard		1	1.08	73.54

- HID: This stands for the integral of the proton signal from deacetylated units specifically, the H-2 proton of the glucosamine residue (the free amine form).
- Hac: This is the integral of the proton signal from acetylated units specifically, the methyl protons (-CH$_3$) of the N-acetyl group in N-acetylglucosamine.

7.3.3.3. FTIR Characterization of Pure Chitosan and Synthesized CHS-AuNPs.

The characterization of the pure chitosan groups (Figure 7.5A) and the synthesized CHS-AuNPs (Figure 7.5B) by FTIR showed band vibrations denoting the functional groups and their corresponding peaks. For the pure chitosan (SI), distinct peaks were recorded at 3357, 3290, 2917, 2362, 1640, 1584, 1373, and 1031 cm^{-1}. The broadband with two peaks at 3357 and 3920 cm^{-1} were assigned to O-H and N-H vibrations, while 2917 cm^{-1} corresponds to C-H stretching. The band at 1649 cm^{-1} was linked to the C=O (carbonyl; amide I) bonds of the O=CNHR, and 1584 cm^{-1} represents the N-H (amide II, NH$_2$) band (Mohan et al., 2019). The bands at 1373 and 1031 cm^{-1} correspond to N-H bending and C-O groups, respectively, as previously reported (Kalaivani et al., 2020; Mohan et al., 2019). Comparatively, the CHS-AuNPs showed similar FTIR band vibrations with some differences. For example, while the C-N band at 3357 cm^{-1} appeared indistinct on the CHS-AuNPs, the C=O vibration at 1584 cm^{-1} showed a much stronger vibration compared to the ordinary chitosan.
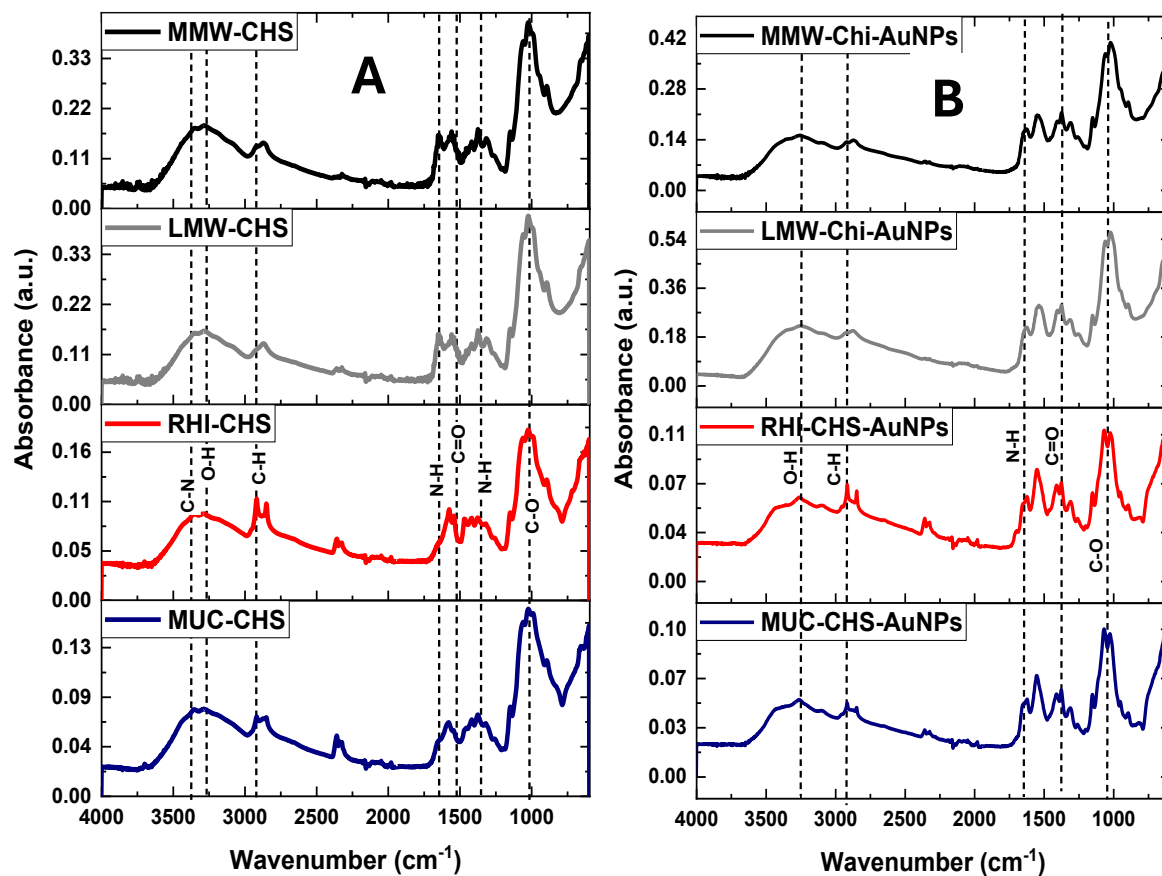
Figure 7.5: FTIR Spectra of (A) pure chitosan and, (B) synthesized CHS-AuNPs.

7.3.3.4. TEM and EDX Analysis of Synthesized Chitosan-AuNPs

The morphological structure and size of the synthesized chitosan AuNPs are presented as TEM images in Figure 7.6 A-D. The TEM images show that the gold nanostructures exist as unagglomerated spherical particles with slight variations in size distribution. The AuNPs synthesized from industrially sourced chitosan (Low and middle molecular weight) are comparable in size to those synthesized from fungi-extracted chitosan (*M. rouxii*) and (*R. oryzae*). The LMW-CHS-AuNPs (Figure 7.6A) averaged 12.51 (± 3.58) nm in diameter, while 13.62 (± 3.47) nm, 14.53 (± 3.45) nm, and 9.58 (± 1.65) nm correspond to the size of the MMW-CHS-AuNPs (Figure 7.6B), Muc-CHS-AuNPs (Figure 7.6C), and Rhi-CHS-AuNPs (Figure 7.XD), respectively. Complementary EDX analysis for each group of the AuNPs (Figure 7.6E and 7.6F) showed well-defined absorption bands peculiar for gold (2.2 keV) and elemental components of chitosan, especially carbon (C) and oxygen (O), confirming the presence of chitosan on the synthesized AuNPs. This observation was not found in the blank sample, which is the ordinary grid without the AuNPs.

174
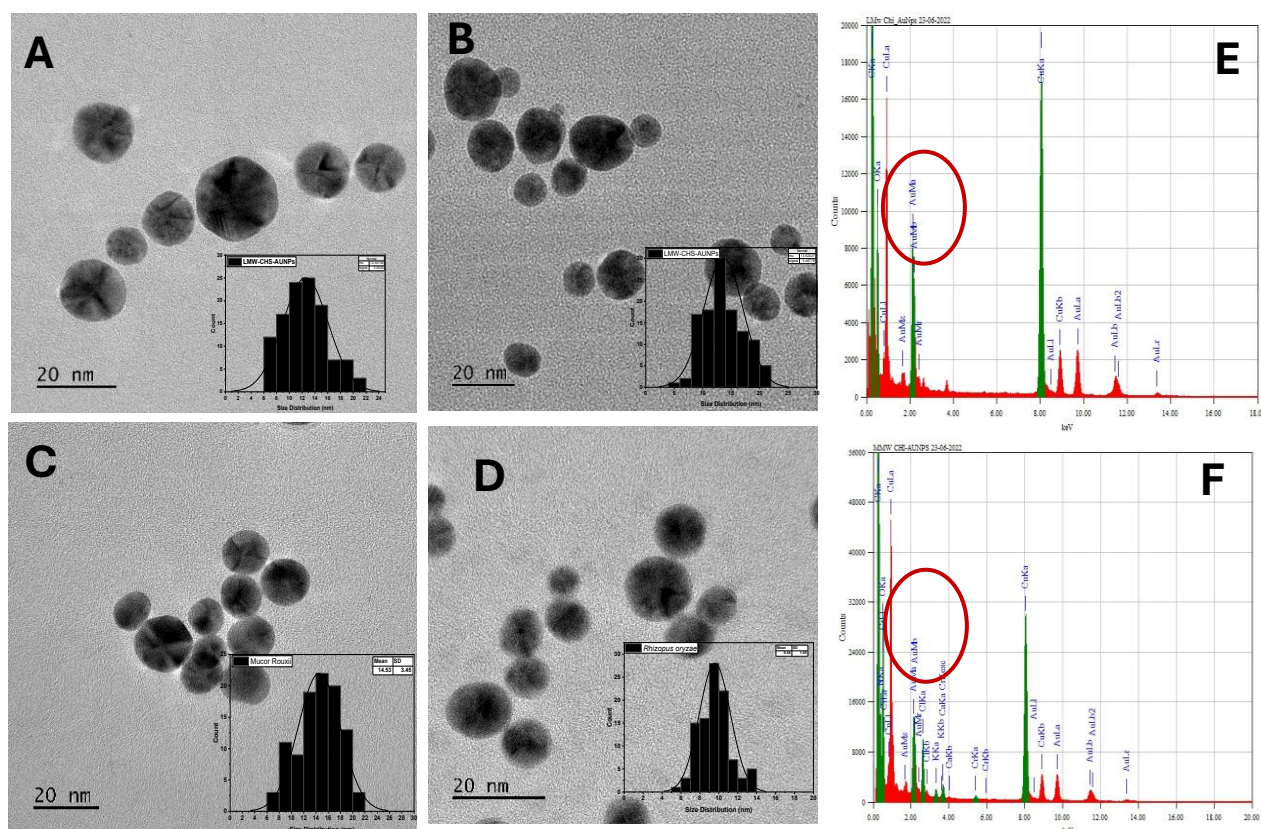
Figure 7.6: Transmission electron micrographs of (A) LMW-CHS-AuNPs; (B) MMW-CHS-AuNPs; (C) Muc-CHS-AuNPs; (D) Rhi-CHS-AuNPs (E) Rep. EDX spectra of AuNPs from industrially sourced chitosan; (F) Rep. EDX spectra of AuNPs from fungal sourced chitosan.

7.3.3.5. X-Ray Diffraction Analysis of Chitosan and CHS-AuNPs

The powder X-ray diffraction crystallography (XRD) diffractogram provides detailed information about the crystallinity properties, phase behaviour, and unit cell dimensions of ordinary chitosan and the synthesized CHS-AuNPs. This is presented in Figure 7.7A and 7.7B, respectively. Compared to ordinary chitosan, which has characteristic 2θ peaks around 8.0-9.0°, 13.1°, and 19-20° depending on the source, all the synthesized CHS-AuNPs have additional characteristic diffraction peaks unique to the face-cantered cubic (FCC) structure of AuNPs (JCPDS 04-0784) around 38.4°, 44.4°, 64.6°, and 77.9°, corresponding to H, K, L values (111), (200), (220), and (311) (Hashem et al., 2022). The highest intensity peak (111) was used to determine the crystallite domain size for the synthesized particles, and this is presented in Table 7.A below. Comparing the crystallite domain size to the particle size obtained from TEM, it can be suggested that the synthesized AuNPs comprise single-crystal domains. Comparatively, the hydrodynamic size of the AuNPs from DLS is higher than the particle size from TEM or

175

the crystallite domain size from pXRD. This phenomenon has been explained to be due to the presence of water molecules around the synthesized AuNPs (Gittings & Saville, 1998). The presence of chitosan as a coating on the synthesized gold nanoparticles, as revealed by FTIR and pXRD, allows for utilization in several applications. From chitosan chemistry, it has been reported that it could provide sufficient steric hindrance suitable for both stability and functionalization of the AuNPs (Sugunan et al., 2005). This phenomenon allows for the utilization of the amine functional groups of chitosan, which has been proven in heavy metal sensing in water (Sugunan et al., 2005).
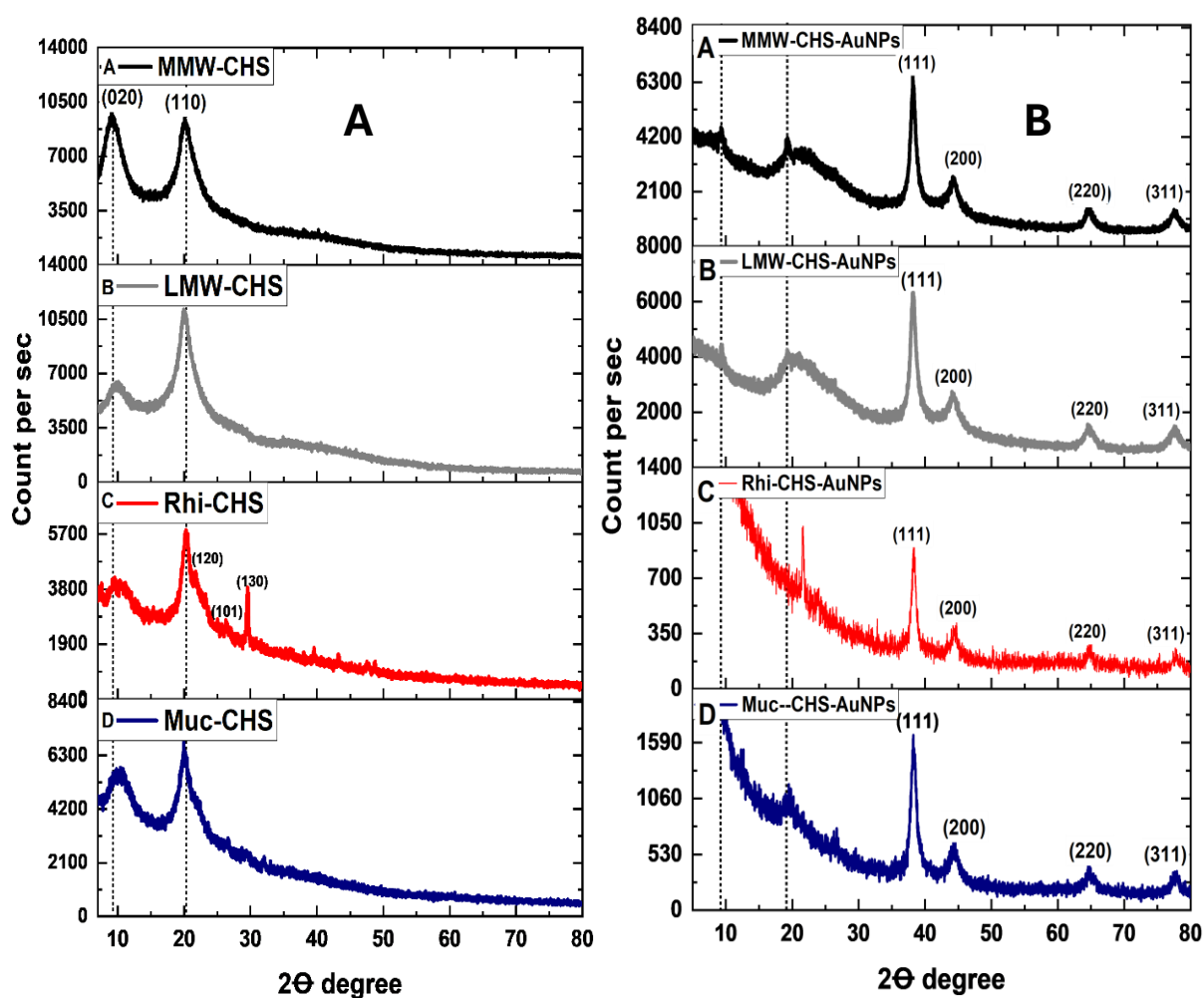
Figure 7.7: XRD Diffractograms of (A) ordinary chitosan and, (B) synthesized CHS-AuNPs.

Table 7.4: Crystallite Domain Size of Synthesized CHS-AuNPs

Sample	2Thetha	D-spacing	FWHM	crystallite domain size (nm)
Muc-CHS-AuNPs	38.28776	2.34888	0.9301	9.04
Rhi-CHS-AuNPs	38.26649	2.35014	0.7646	10.99
LMW-CHS-AuNPs	38.16695	2.35604	1.0241	8.22
MMW-CHS-AuNPs	38.13312	2.35805	1.0656	7.88

7.4. Dye Diffusion Assay to Monitor Diffusion Across Agar-Bridge Well

To determine the time a hydrophilic substance is likely to diffuse through the agar bridge, as a measure of the conditions to be set for the glyconanoparticles, I assayed the diffusion of two hydrophilic dyes (Brilliant Blue and Cochenille Red) to predict the potential diffusion patterns of the glyconanoparticles. This experiment was conducted in two distinct areas of the agar bridge. The starting point was either towards the inner core or the outer agar layer around the well, which is the edge of the well where the dye was spotted. For the internal core (Figure 7.8A), the intensity of the dye was measured from the edge of the well, where the agar diffuses inward (part A), and the midpoint of the core, where the agar diffuses (part B), to determine the arrival of the dyes. A similar experiment was carried out on the outer agar layer surrounding the agar bridge (where samples are spotted) (Figure 7.8B). Measurements were taken from the point of diffusion in the bridge (part A) to the point of outward diffusion within the outer agar layer. My results indicated that for both dyes, the midpoint of the agar core (point of inoculation) could be reached within just four h (Figure 7.8). The same observation was made for the outside edge of the agar after the bridge. All areas were completely saturated by agar diffusion within four h. This indicates that polar groups on the AuNPs can completely diffuse within four h.
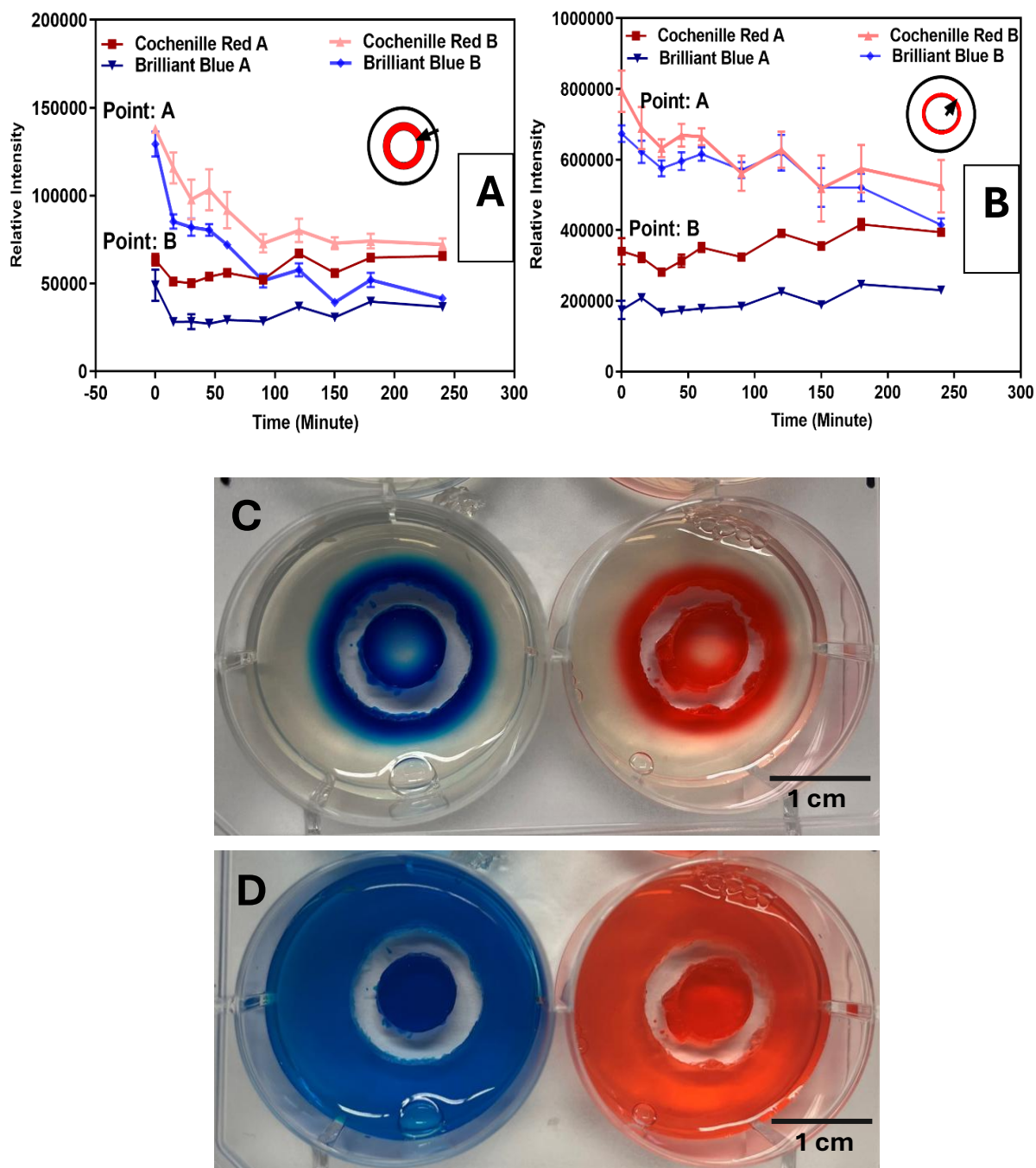
Figure 7.8: The diffusion pattern of Brilliant Blue and Cochenille Red dyes into (A) the inner agar core and (B) the outer agar core. Pictures in (C) and (D) are representative images showing the rate of diffusion at 30 min and 4 h, respectively.

7.5. Glyconanoparticles and the Agar-Bridge Model

7.5.1. Assessment of Fungal Growth Behaviour and Hyphal Diameter Alterations

The fluorescence images of *M. rouxii* and *R. oryzae* in the agar-bridge model show that fungal behaviour varies under different conditions, making this method suitable for assessing the impact of surface materials of glyconanoparticles on fungal filament growth and tuning. In the results presented (Figure 7.9 A-D), I, B, and O denote the inner agar core (area of initial growth), the bridge (empty well where NP samples and controls were spotted), and the outer agar layer (another area of agar after the bridge), respectively. Figures 7.10 A-G are also the plates showing the fluorescence image for each group. For the experiments, three parameters were measured: changes in hyphal diameter across the three areas, branching angles of the fungal filaments across the three areas, and total growth area. Representative illustrations of these are presented in Figure 7.1. For the hyphal diameter (Figure 7.9 A), there was no unique pattern for hyphal diameters across the groups. However, significant differences were observed in the hyphal diameter of *M. rouxii* when PDB or glucose AuNPs were administered, with the hyphal diameter being thinner in the region designated as the outer agar layer. Notably, this is the area where the hyphal filaments actively grow (Steinberg, 2007).
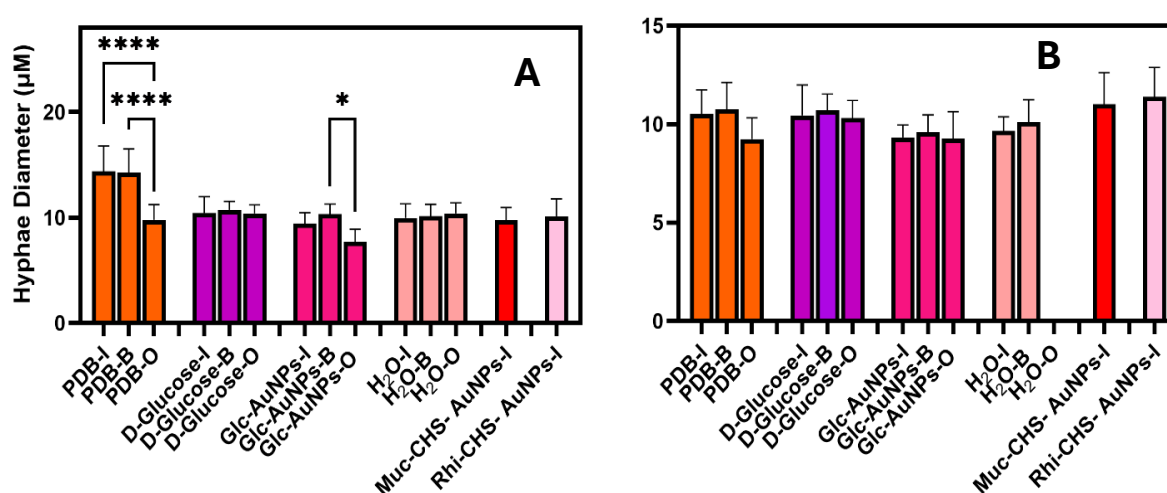
Figure 7.9A: Plots of hyphal diameter for (a) *M. rouxii* and (b) *R. oryzae* within the inner core, bridge, and outer agar layer of an agar-bridge nutrient-sensing model. Asterisks denote the level of significance (* $P \leq 0.05$, ** $P \leq 0.01$, *** $P \leq 0.001$, **** $P \leq 0.0001$).

7.5.2. Assessment of Fungal Growth Behaviour and Branching Angle.

When I assayed for differences in branching angle due to different treatments, I generally observed that functionalization with AuNPs increases the branching angle, especially within the internal core compared to the non-functionalized counterparts, suggesting that the presence of gold nanoparticles affects the structural conformation or branching behaviour. In addition, progressive branching of hyphae filaments was observed as the fungi crossed from the inner core, over the bridge, to the outer agar layer (Figure 7.9B). This branching was significant for glucose and glucose-capped gold nanoparticles in both *M. rouxii* and *R. oryzae*, and the PDB group in *R. oryzae*. Growth inhibition effects prevented results for the chitosan groups. Results for the fungi-mediated chitosan gold nanoparticles were only available for branching within the inner core due to limited growth. For these conditions, fungal growth was initiated only after 12 h of inoculation. The results for branching angle also show a reverse trend to those of hyphal diameter, where more hyphal thickness in the core correlates to less branching and reduced thickness in the outer agar area to more branching angle.
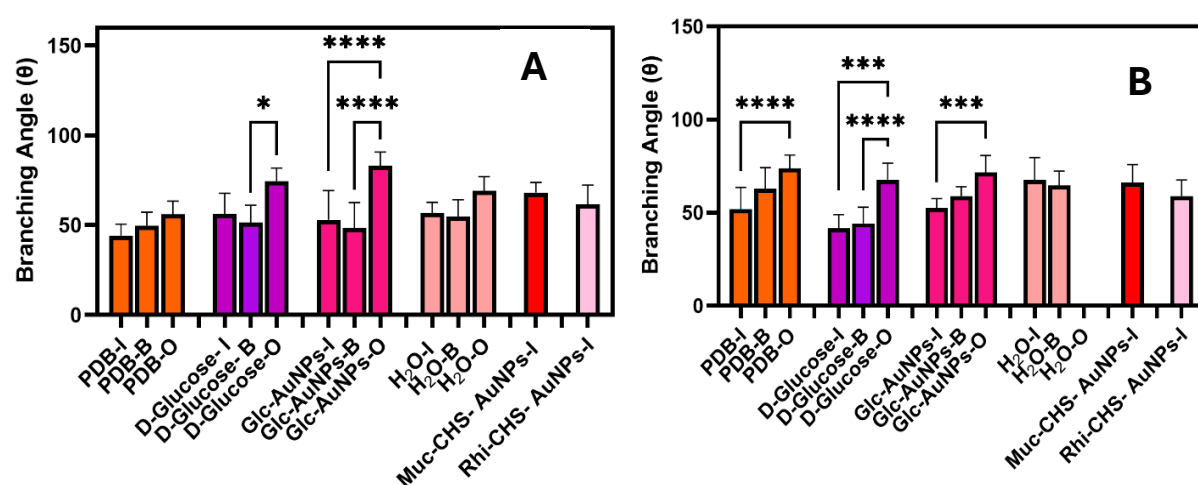
Figure 7.9B: Plots of branching angle for (a) *M. rouxii* and (b) *R. oryzae* within the **i**nner core, **b**ridge, and **o**uter agar layer of an agar bridge nutrient-sensing model. Asterisks denote the level of significance (* $P \leq 0.05$, ** $P \leq 0.01$, *** $P \leq 0.001$, **** $P \leq 0.0001$).

7.5.3. Assessment of Fungal Growth Behaviour and Growth Area.

I assessed the effects of different treatments on the growth areas to determine how the various groups affect the extent of growth. The results are presented in Figure 7.9C. The results show that D-glucose and Glc-AuNPs significantly enhance growth compared to PDB, indicating that glucose, especially when functionalized on gold nanoparticles, promotes greater growth, possibly through enhanced nutrient uptake (Suvarna et al., 2017). In contrast, Muc-CHS-AuNPs and Rhi-CHS-AuNPs drastically reduce growth, suggesting inhibitory effects likely due to the antimicrobial properties of chitosan derivatives (Ke et al., 2021). The minimal growth observed with H_2O confirms its role as a negative control. These findings highlight the dual role of glyconanoparticles in either enhancing or inhibiting growth depending on their functionalization, offering insights into potential applications in nutrient delivery, antimicrobial treatments, or for tuning in materials engineering.
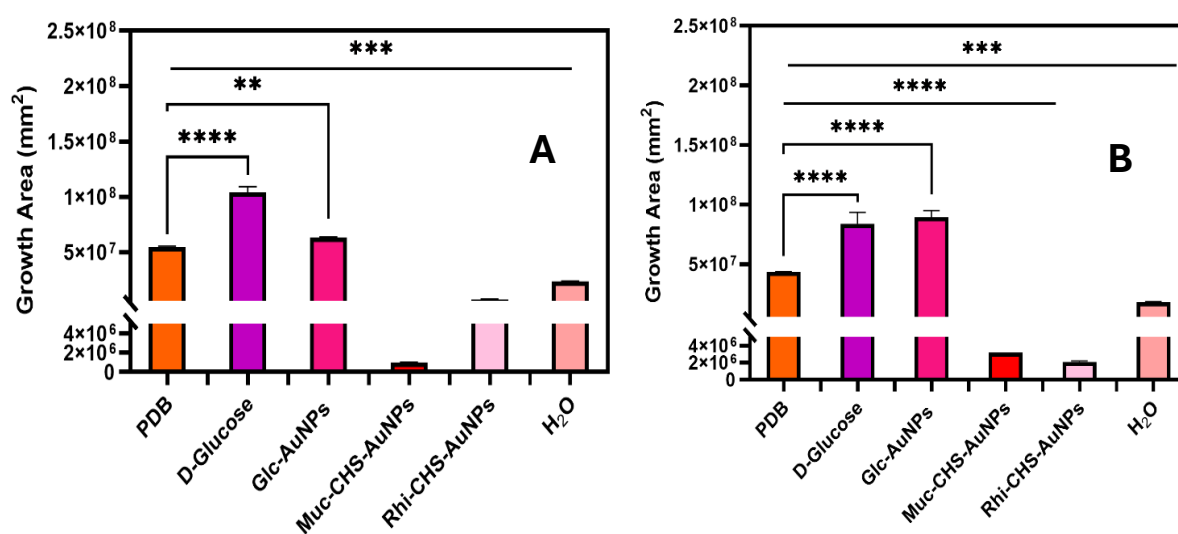
Figure 7.9C: Plots of growth area for (a) *M. rouxii* and (b) *R. oryzae* within the **i**nner core, **b**ridge, and **o**uter agar layer of an agar-bridge nutrient-sensing model. Asterisks denote the level of significance (* $P \leq 0.05$, ** $P \leq 0.01$, *** $P \leq 0.001$, **** $P \leq 0.0001$).

7.5.4. Assessment of Fungal Growth Behaviour and Self-Control.

Following the trend of the results, I also evaluated the possibility of self-control in the two fungal strains, and I recorded interesting findings. This is presented in Figure 7.9D. The results demonstrate that chitosan nanoparticles (CHS-AuNPs) derived from each fungal strain

effectively inhibit the growth of their respective source strains, indicating a form of self-control. Specifically, MCHS-AuNPs and RCHS-AuNPs significantly reduce growth compared to their glucose and Glc-AuNP counterparts. This suggests that the chitosan functionalization retains bioactivity that selectively inhibits the parent strain, possibly due to species-specific antimicrobial properties or autoregulation (Hazen & Cutler, 1979). The lack of growth inhibition in other strains confirms this targeted effect. These findings highlight a unique self-regulatory mechanism, offering potential applications in fungal growth control and antifungal strategies tailored to specific fungal species.
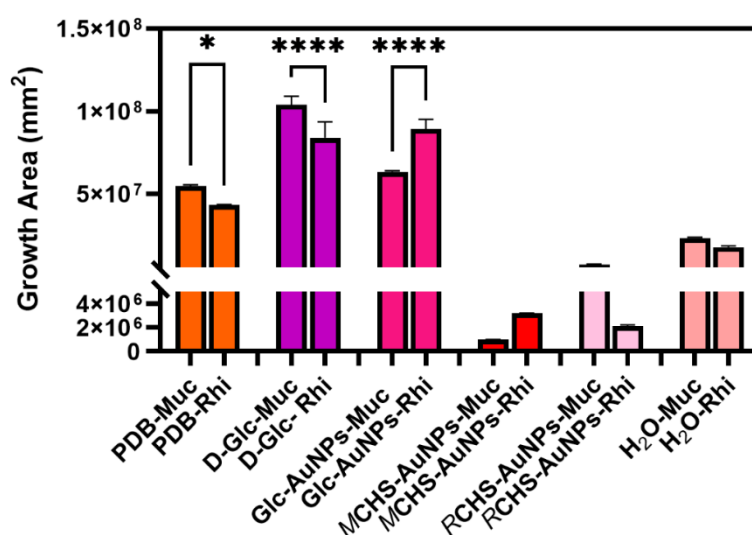
Figure 7.9D: Plots of growth comparison in *M. rouxii* and *R. oryzae* showing self-control. Asterisks denote the level of significance (* P ≤ 0.05, ** P ≤ 0.01, *** P ≤ 0.001, **** P ≤ 0.0001).

7.5.4. Growth Plates Indicating the Pattern of Growth under The Different Treatments
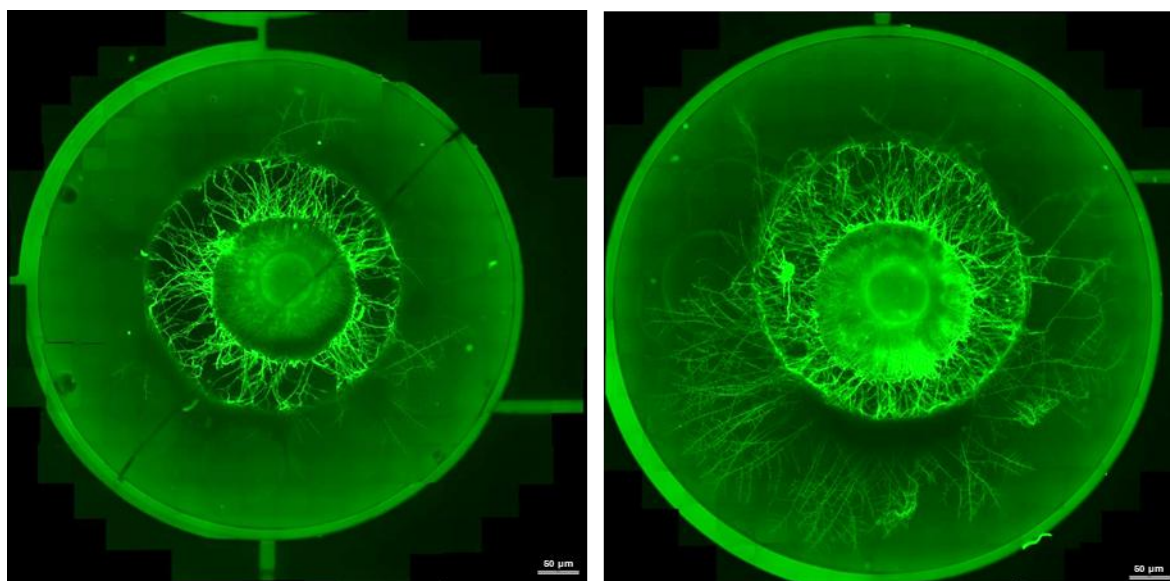
Figure 7.10 A: 24-h fluorescence image showing the growth of *M. rouxii* and *R. oryzae* under normal growth conditions in PDB. All images include a scale bar representing 50 µm.
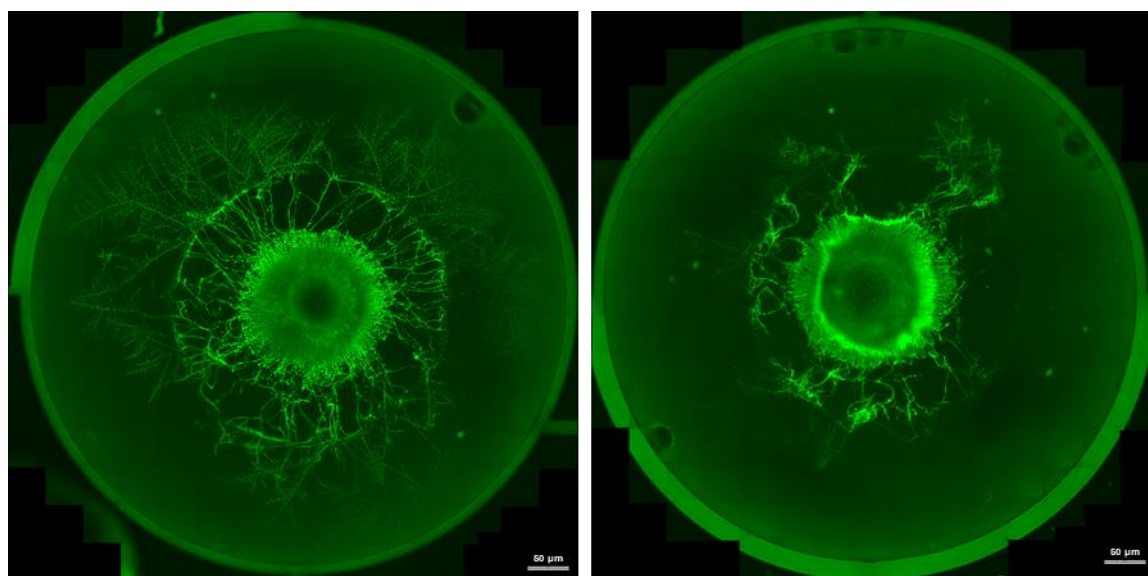
Figure 7.10 B: 24-h fluorescence image of *M. rouxii* and *R. oryzae* with D-glucose added to the well. All images include a scale bar representing 50 µm.
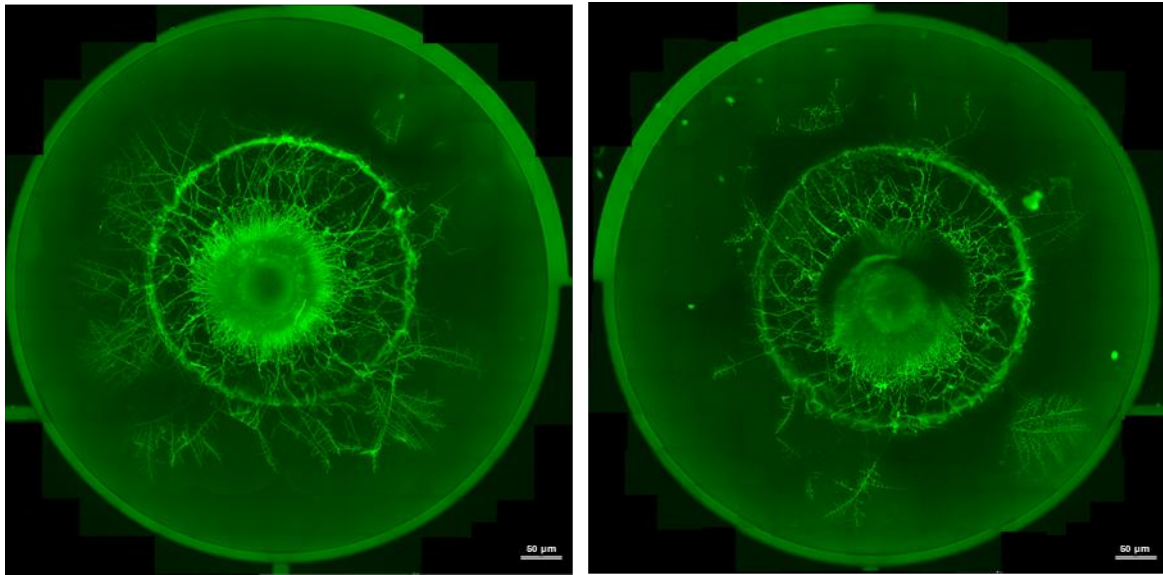
Figure 7.10 C: 24-h fluorescence image of *M. rouxii* and *R. oryzae* with glucose-capped AuNPs added to the well. All images include a scale bar representing 50 µm.
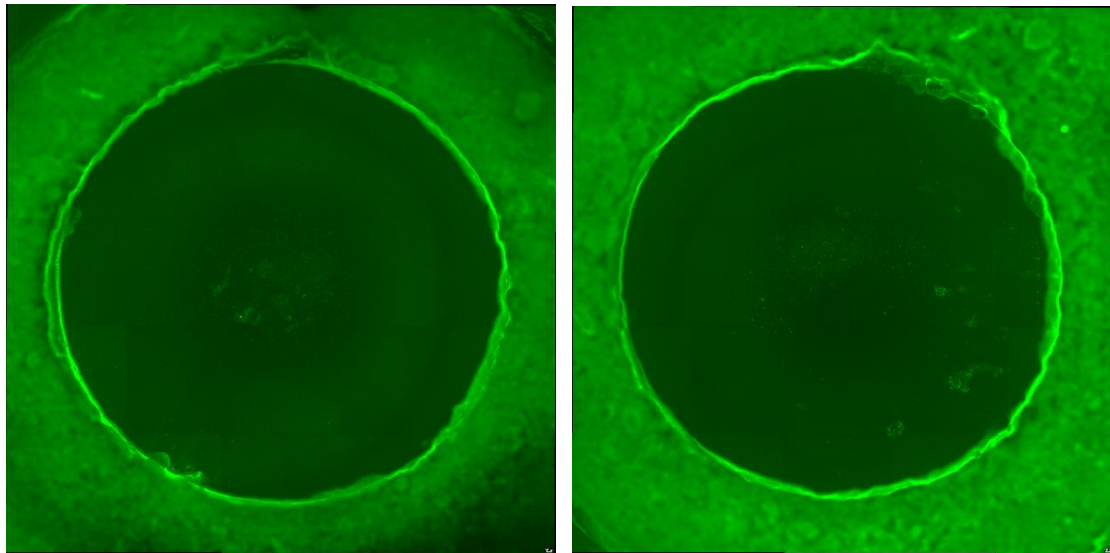
Figure 7.10 D: 24-h fluorescence image of *M. rouxii* and *R. oryzae* with chitosan from *Mucor* added to the well. Since there was no growth, only the inner ager core was captured to show the non-germinating spores. All images include a scale bar representing 100 µm.
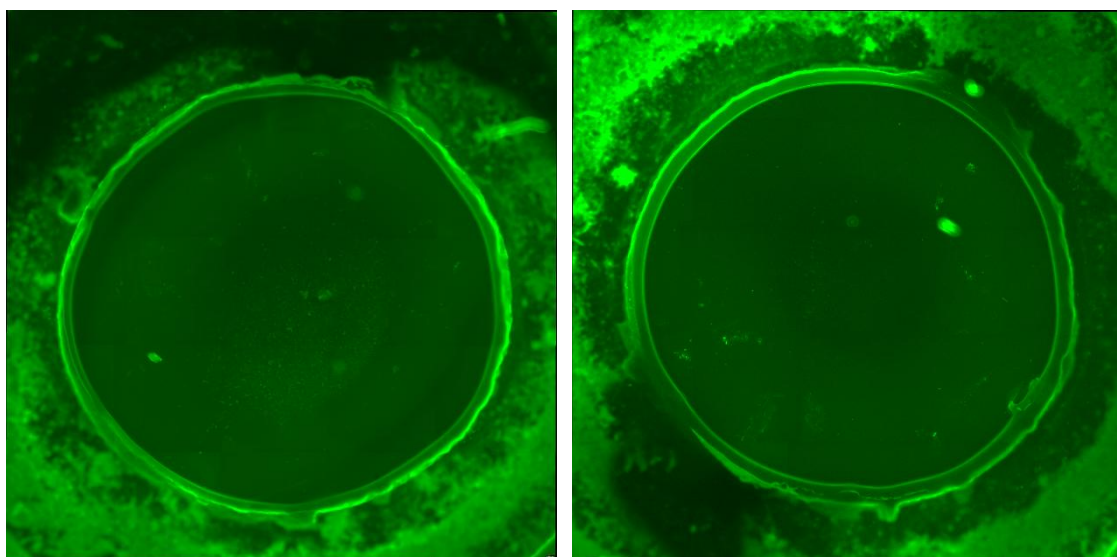
Figure 7.10 E: 24-h fluorescence image of *M. rouxii* and *R. oryzae* with chitosan from *Rhizopus* added to the well. Since there was no growth, only the inner ager core was captured to show the non-germinating spores. All images include a scale bar representing 100 μm.
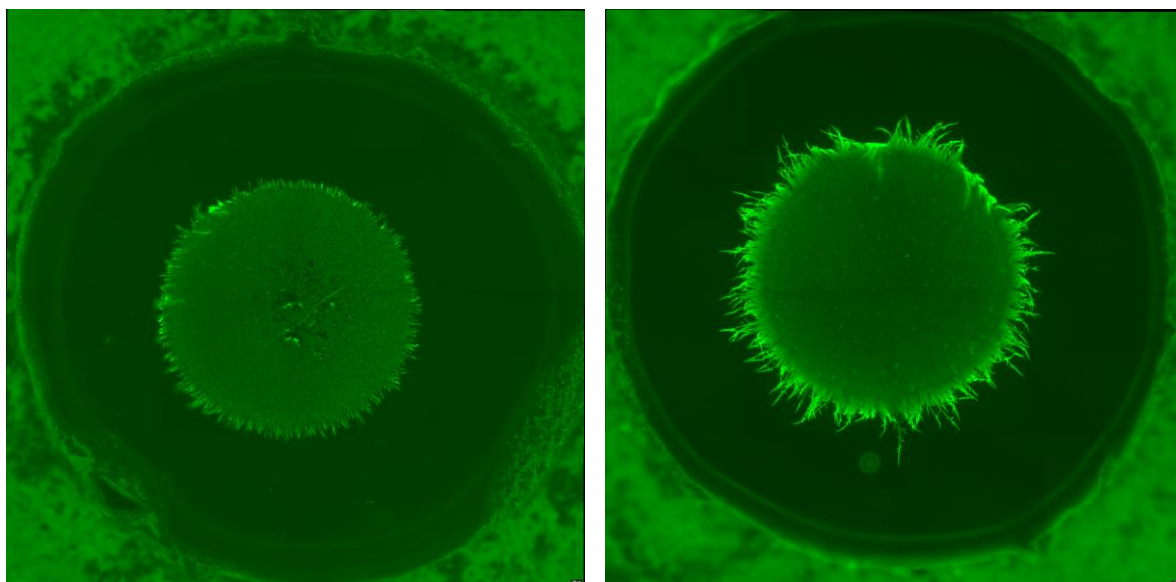
Figure 7.10 F: 24-h fluorescence image of *M. rouxii* and *R. oryzae* with chitosan-AuNPs synthesized using *Mucor* chitosan. Since there was limited growth, only the inner ager core was captured to show the non-germinating spores. All images include a scale bar representing 100 μm.
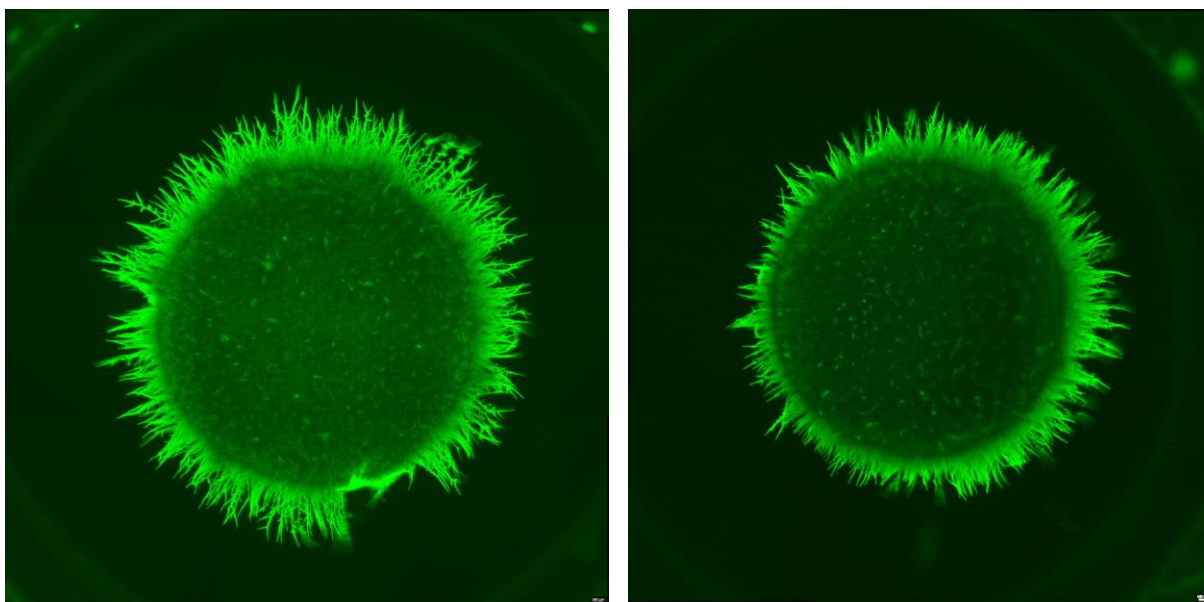
Figure 7.10 G: 24-h fluorescence image of *M. rouxii* and *R. oryzae* with chitosan-AuNPs synthesized using *Rhizopus* chitosan. Since there was limited growth, only the inner ager core was captured to show the non-germinating spores. All images include a scale bar representing 100 µm.
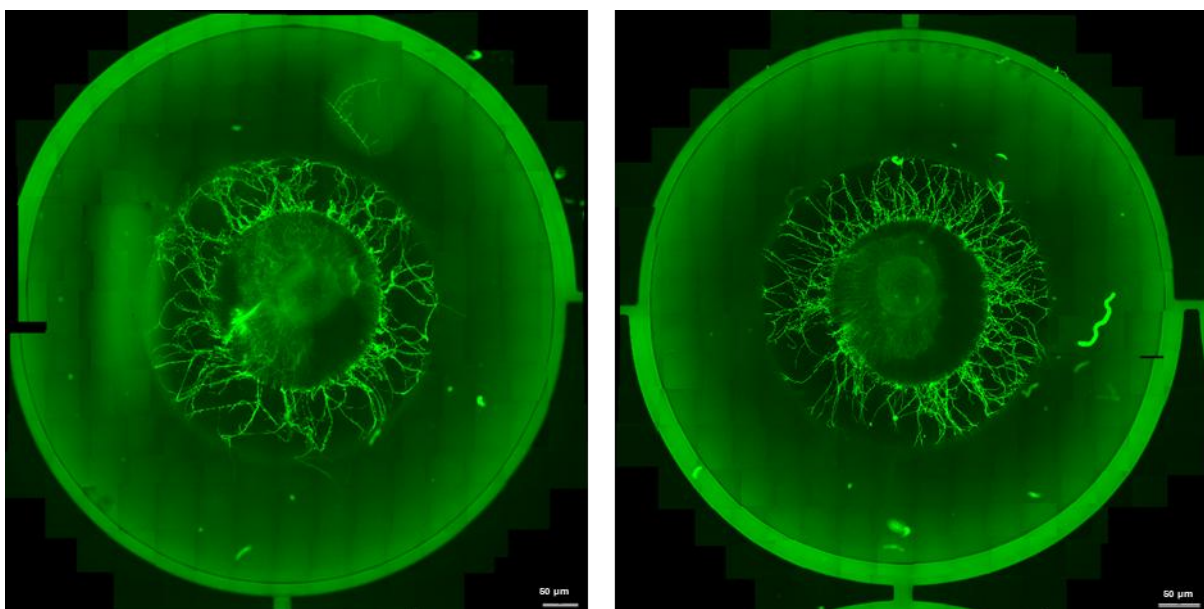
Figure 7.10 H: 24-h fluorescence image of *M. rouxii* and *R. oryzae* with ordinary DDH$_2$O added to the well. All images include a scale bar representing 50 µm.

7.6. Effects of Growth Duration (72 h) on Chitosan and Chitosan AuNPs Effects

Following the observation of growth patterns, I decided to specifically check if the chitosan exhibited fungistatic (inhibiting growth) or fungicidal (killing fungi) effects (Abo El-Ela et al., 2024). Since there was no growth within the initial 24 h, I extended the experiment to 72 h under similar conditions. After 72 h, there was no growth in the groups treated with chitosan from *M. roxuii*, while the spores in the groups treated with chitosan from *R. oryzae* had germinated. From IR characterization (Figure 7.5), I know that both chitosans from the mycelia have alpha nomenclature and NMR shows that they have a similar degree of deacetylation of about 93% in both groups (Figure 7.4). However, NMR also indicates the possibility of structural differences, which might explain the differences in the results. *R. oryzae* seems to have greater structural heterogeneity which could have contributed to differences in molecular weight.

Since the growth in the chitosan AuNPs groups was delayed by up to 12 h, I extended the experiment for chitosan gold nanoparticles to 72 h. I recorded an increase in growth in both groups, with interesting outcomes. For both groups of chitosan-AuNPs, the fungi started sporulating within 3 days, which could be due to the AuNPs inducing stress on the fungi. Ordinarily, the onset of sporulation is usually at the lag phase of growth, above 10 days. Another interesting observation is that self-control was consistent in the fungi, with *Rhizopus* showing more susceptibility to its own material, whether chitosan or chitosan AuNPs, compared to *M. rouxii*. I hypothesize that this could be a natural control mechanism for self-regulation in the fungi.
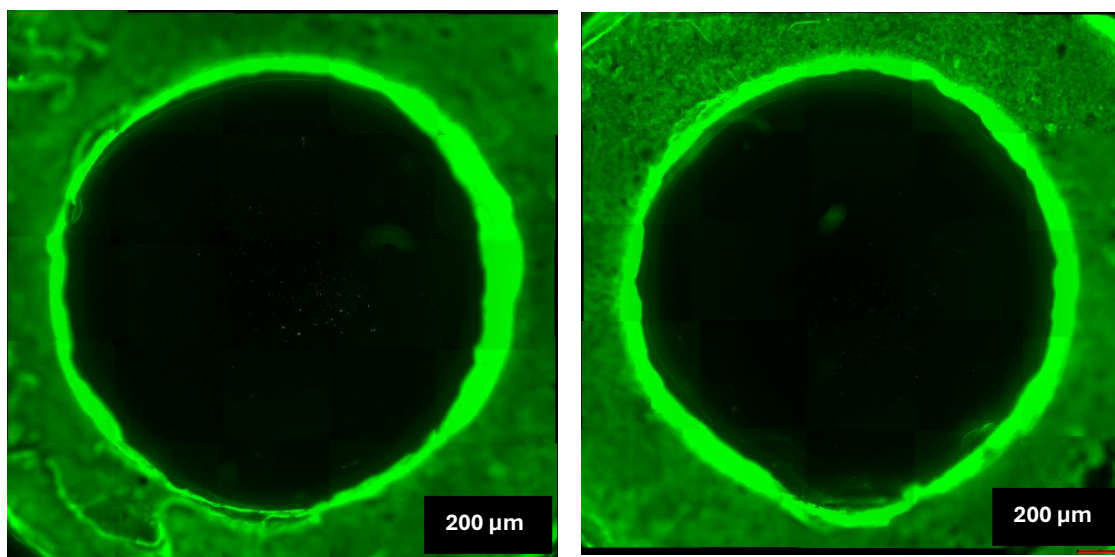
Figure 7.11A: 72-h fluorescence image of *M. rouxii* and *R. oryzae* with chitosan from *Mucor*. Since there was no growth, only the inner ager core was captured to show the non-germinating spores.
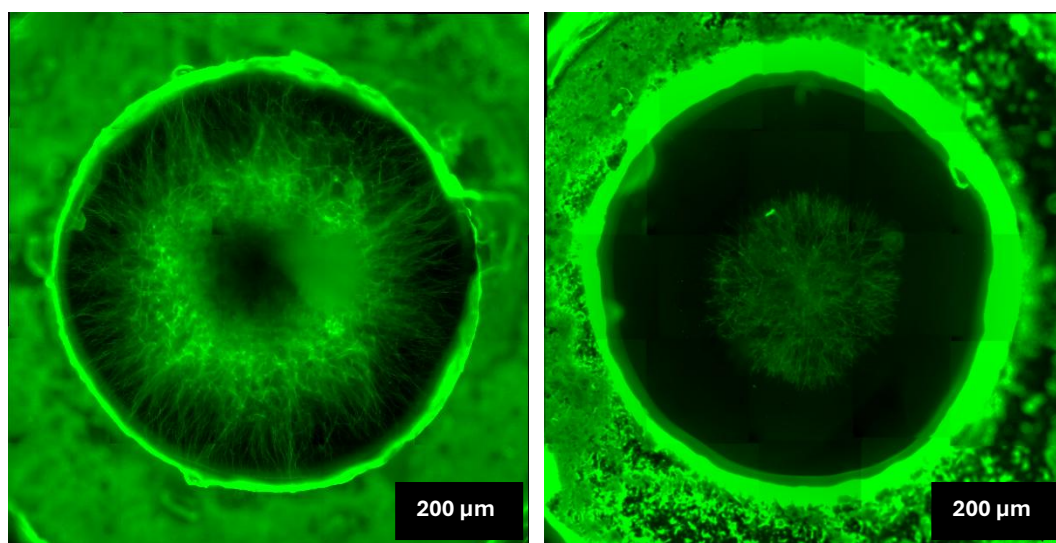
Figure 7.11B: 72-h fluorescence image of *M. rouxii* and *R. oryzae* with chitosan from *Rhizopus*. Due to limited growth, largely only the inner ager core was captured
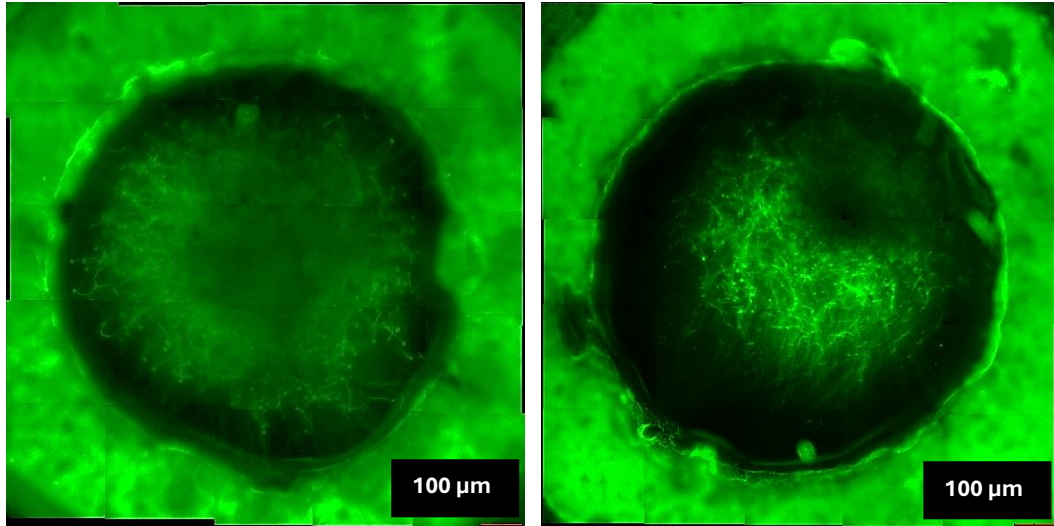
Figure 7.11C: 72-h fluorescence image of *M. rouxii* and *R. oryzae* with chitosan-AuNPs synthesized using *Mucor* chitosan. Due to limited growth, only the inner ager core was captured.
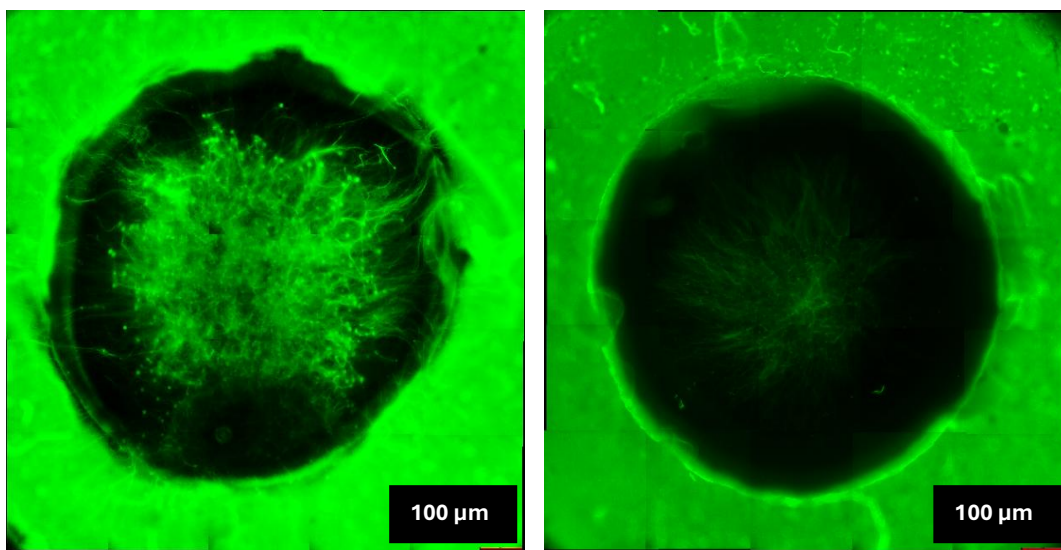
Figure 7.11D: 72-h fluorescence image of *M. rouxii* and *R. oryzae* with chitosan-AuNPs synthesized using *Rhizopus* chitosan. Due to limited growth, only the inner ager core was captured.

The limited growth observed might be due to the interaction between the chitosan-AuNPs and the fungal cells, which potentially hinders their proliferation (Hashem et al., 2022). This indicates that chitosan possesses antimicrobial properties that can influence fungal growth.

7.7. Conclusion

This study demonstrates the potential of glyconanoparticles with different surfaces to influence fungal growth dynamics, particularly in Mucorales species (*M. rouxii* and *R. oryzae*). Using the agar-bridge model, the nutrient-sensing responses of these fungi to glucose- and chitosan-capped gold nanoparticles (AuNPs) investigated showed interesting outcomes. Glucose-functionalized AuNPs promote fungal growth as a nutrient source, while chitosan-capped AuNPs exhibit fungistatic properties, inhibiting fungal proliferation for about 24 h. This indicates that carbohydrate-coated nanomaterials retain their biological activities despite surface functionalization. I also discovered the possibility of a natural self-control system in the fungi using their own chitosan. The agar-bridge model effectively assesses fungal nutrient-sensing and structural adaptation, providing a controlled system for real-time observation of fungal responses. The study also confirms that fungal-derived chitosan differs structurally from industrial chitosan (derived from crustaceans), influencing its functional behaviour in nanoparticle synthesis and application. Future studies should consider environmental factors and more broader parameters. The model's application in engineering materials with different properties can be explored further. This study highlights the role of glyconanoparticles in modulating fungal growth, with potential applications in antifungal strategies and bioengineering, integrating fungal biology with nanotechnology for innovative biomaterial development and fungal control strategies.

General Discussion and Recommendations

This research explores the innovative use of fungi in developing next-generation materials for environmental and biomedical applications, leveraging knowledge in physics, microbiology, chemistry, engineering, and nanotechnology. Functionalizing fungi with nanoparticles through biomimetic and in-situ approaches created composite microstructures for applications including heavy metal bioremediation, UV-radiation protection, non-wettable surfaces, and thermally stable scaffolds. The results presented show successful modification of the fungal surface with a choice of bioactive materials, and that fungal composites have innovative applications in modern-day environmental and biomedical solutions. The impact of carbohydrate identity on the mechanical and surface properties of fungal materials was thoroughly investigated and I learned that to get myco-materials with desired properties such as stiffness, thickness, flexibility, load retention potentials, strength, and surface non-wettability, I can tune them at the fundamental level via nutrient variation.

The results of this study are noteworthy and demonstrate the potential of fungi-based materials as sustainable alternatives to conventional materials, aligning with the global emphasis established in the Sustainable Development Goals (SDGs). A significant advancement in eco-friendly material synthesis is highlighted by the natural biomimetic process that allows for the self-deposition of gold nanoparticles without the use of extraneous chemicals. The composite system developed from *A. niger* and gold nanoparticles (AuNPs) for mercury removal is reusable for at least five cycles while consistently reducing concentrations to levels below the international minimum acceptable standard of 2 parts per billion (ppb) during each cycle. This research reveals that nature can yield impactful solutions, and by harnessing these natural processes and mimicking them, highly innovative outcomes can be achieved that benefit both human society and the broader ecosystem. I have moved beyond traditional surface functionalization methods, which typically depend on chemical coupling agents, with respect given to these foundational works (Li, et al. 2003, Das, Shome and Guha 2012, Mukherjee, et al. 2001). I have also moved beyond hypothetical guesses as to the feasibility of natural functionalization that does not require artificial agents (Bohu, et al. 2019). I introduced novelty in materials design and application. The focus of the current study is on the engineering of highly eco-friendly composites in which fungi inherently facilitate the coupling process without external intervention. Not only has this material been generated through natural means, but I have also demonstrated its initial application in bioremediation and established its potential for reusability. Moreover, I have demonstrated that the phenomenon observed in

Australia (Bohu et al., 2019) where fungi naturally bioaccumulate gold can be replicated at the laboratory scale and that this is also possible by employing fungal strains other than *F. oxysporum.* Despite exploring a range of parameters, including concentration, nitrogen sources, and timeframes, this study indicates that further research is warranted to develop further innovative designs in the future. I recommend conducting a similar study using various carbohydrate sources, as the influence of carbohydrates on mycelial mechanics may yield significant insights (Schoder, et al. 2024, Haneef, et al. 2017). Furthermore, I advocate for the introduction of additional strains and the investigation of new classes of heavy metals, or nanoparticles with their own distinct properties. It is also important to consider the concentrations of nanoparticles carefully and to explore potential applications that extend beyond bioremediation.

The functionalization of fungal mycelia with gold nanoparticles (AuNPs) and titanium dioxide nanoparticles (TiO_2 NPs) has underscored the potential of fungi to serve as the basis for multifunctional composites. Before this investigation, there had been no documented instance of directly functionalizing Mucorales (*M. rouxii* and *R. oryzae*) or any other fungal strain with TiO_2 NPs specifically to create a multifunctional scaffold that offers UV radiation blocking, a non-wettable surface, and thermal stability. This study enhanced existing methodologies for other biomaterials (Shaheen, Salem and Zaghloul 2019, Rabiei, et al. 2022, Velázquez-Martínez, et al. 2018, Yang, et al. 2018), adapting them for application with mycelia. By introducing mycelia into this domain, I demonstrated its significant potential as a biomaterial, particularly for advanced applications. When TiO_2 NPs are employed for surface modification of mycelia to create composites, the resulting materials exhibit noteworthy properties, such as effective UV radiation blocking, enhanced surface wettability, and improved thermal stability. Nonetheless, it is essential to acknowledge that this process entails certain trade-offs, notably alterations in the mechanical properties of the mycelia (usually giving materials with poorer properties). Furthermore, the differing morphological characteristics observed on opposite sides of the same mycelium appear to influence the overall outcomes. This is a pointer to the possibility of future design as Janus membranes (Cavalcante and Szekely, 2023). In this current study, I advanced methodologies and identified specific limitations inherent in the application of these techniques to fungal mycelia, representing a substantial step forward for future research endeavours. To further this investigation, it would be prudent to explore fungal materials with a variety of mechanical and optical properties, including the integration of pigment considerations. The extensive diversity of available fungal strains presents significant

opportunities for innovation in this specialized field. Moreover, there exists potential for the introduction of a new class of nanomaterials. The experiments conducted were carried out under controlled laboratory conditions, with immediate analysis of samples based on the selected methodologies. Assessments of long-term durability, biodegradability, and environmental impact should be executed under real-world conditions to ascertain the viability of large-scale applications.

This study investigated the effects of various types and concentrations of carbohydrates on the mechanical and wettability properties of fungal mycelia. I employed five distinct fungal strains: *A. niger, B. cinerea, R. oryzae, S. commune,* and *T.versicolor*. The research demonstrates that it is feasible to modify the properties of fungal mycelium directly through variations in nutrient composition, rather than relying on external bioactive compounds for surface adherence. This approach exemplifies an "inside-out" modification strategy, whereby alterations at a fundamental level due to nutrient variations are reflected in the bulk properties of the mycelia. The findings indicate that different fungal strains exhibit unique preferences for carbon sources, which significantly affect their growth, strength, elongation, stiffness, surface energy, and hydrophobicity in certain ways. Notably, my results reveal that achieving near superhydrophobicity (with a contact angle of 150°) through mere adjustments in nutrient concentrations represents an effective and sustainable method for engineering environmentally friendly materials. Certain strains, such as *R. oryzae, A. niger, and B. cinerea*, produced materials that were two to three times thicker than average under similar conditions. In the future, these insights will facilitate the customization of mycelial properties, thereby enabling targeted applications across varied industries. In contrast to existing literature (Schoder, et al. 2024, Jo, et al. 2009, Schritt, Vidi and Pleissner 2021), this study broadens the range of carbohydrates utilized, modifies their concentrations, incorporates multiple strains, and thoroughly characterizes the resultant materials. Intracellular modifications due to nutrient variation led to physical and biological alterations that were subsequently characterized in the bulk mycelia. Experiments conducted on both solid and liquid media were aimed at determining how the nature of nutrient availability influences the observed outcomes. It was recorded that this affects growth rate and material quantity. Generally, the trends identified in my results for this work provide a foundation for the introduction of new strains or further optimization of existing ones, thereby unlocking the potential for enhanced applications. For instance, I discussed the engineering of materials with titanium dioxide nanoparticles for multifunctional scaffolds, now I suggest that pre-modification with nutrients could yield

improved results in forming multifunctional scaffolds. I recommend that future studies build upon the "inside-out" modification approach by investigating the implications of these sugars at the fundamental level. This includes exploring their impact on omics and genetic properties, as well as their effects on biochemistry, such as cell wall carbohydrate properties and microstructural filament characteristics. Furthermore, the introduction of a wider variety of fungal strains and exploration of interactions with nanoparticles or peptides presents opportunities for the development of advanced multifunctional materials. While I have not proposed specific applications for this class of material, future research should also focus on analysing the effects of environmental conditions, scalability, and sustainability for industrial applications. Promising avenues for exploration may include testing real-world applications, such as coatings and filtration systems, UV-shielding, experimenting with multi-nutrient combinations for hybrid properties, studying long-term material behaviour under varying conditions, and investigating biomedical applications like tissue engineering scaffolds or biocompatible systems. Ultimately, these efforts could facilitate the advancement of tailored and sustainable material innovations.

This study presents innovative methodologies for engaging with fungi and characterizing fungal materials. Notably, I introduce advanced techniques for spatial mapping of mycelial homogeneity and analyse the effects of various drying conditions on material properties. While prior literature has indicated that a mycelium may not be a homogeneous structure, the extent of this inhomogeneity has not been fully characterized. My investigation has successfully characterized the mechanical dynamics associated with mycelial inhomogeneity in two mucorales (*M. rouxii* and *R. oryzae*). Specifically, I discovered that distinct regions within a single mycelium can demonstrate differing mechanical properties over a defined growth period. Furthermore, my assessment of four different drying processes indicates that the chosen method significantly impacts mechanical properties such as strength, flexibility, and thickness. For example, both air-drying and oven-drying resulted in increased stiffness but decreased flexibility, whereas cryogenic freezing led to physical tearing of the material. These findings emphasize the critical need to optimize processing methods to achieve consistent material properties. Given the increasing investment in nature-based materials across various economic sectors, this research provides valuable insights for selecting specific material characteristics for diverse applications. It also serves as a crucial reminder for professionals in the field of biomaterials regarding the importance of understanding the spatial characteristics of the materials being developed, ensuring compliance with ISO standards for material development.

The investigation into the nutrient-sensing model utilizing glyconanoparticles represents an innovative methodology that has yielded valuable insights into the biological interactions between nanoparticles and fungi. The introduction of the Agar-Bridge Model as a novel nutrient-sensing system provides a unique framework for understanding nutrient-sensing mechanisms and the self-regulation of fungal growth with glyconanoparticles, thereby enabling further research into bio-sensing. From literature, the most recent techniques employed for analogous assessments in fungi have primarily consisted of two-dimensional and three-dimensional sensing systems (Schunke, Pöggeler and Nordzieke 2020, Turrà, et al. 2016, Millet, et al. 2019). However, these approaches do not facilitate the necessary dynamism to examine how fungi respond to various bioactive elements under special conditions, such as the introduction of obstacles or differing growth layers. The Agar-Bridge Model allows for the incorporation of obstacles along growth pathways, thus enabling researchers to investigate fungal responses and changes in growth patterns. This study presents, for the first time, evidence of how glyconanoparticles induce structural changes in Mucorales across two layers of agar separated by a bridge. There were significant differences in the branching behaviour of the fungi, which were observed along with documentation of ongoing self-regulatory mechanisms. This new methodology is not only relevant for materials development but also holds potential applications in antifungal strategies and growth monitoring systems. It is recommended to implement this system on larger platforms, such as Petri dishes, over extended periods (exceeding five days) to facilitate the generation of bulk mycelium, the properties of which may be examined in unique ways. The current study utilized two classes of glyconanoparticles (capped with either glucose or chitosan), and future investigations may incorporate additional classes of bioactive substances, minerals, or biomolecular constituents. Additionally, non-diffusing materials may also be introduced to explore the possibility of functionalizing fungal materials as they traverse the bridge.

In general, this research connects material science and applied mycology by showcasing the potential of fungi-based composites to tackle real-world challenges such as heavy metal contamination, UV protection, and environmental sustainability. By employing biomimetic synthesis and in-situ functionalization techniques, the study advances green chemistry and the development of sustainable materials.

General Conclusion

This doctoral thesis presents research contributions from over three years of study. The work advances the fields of fungal materials and applied mycology by introducing new methods and sustainable, multifunctional bio-composites. The innovative approaches to nanoparticle functionalization and the strategic use of carbohydrates to modify mechanical properties have led to the development of eco-friendly materials with various applications, this includes environmental monitoring which is currently prioritized on a global scale. Furthermore, the integration of biomimetic processes and in-situ functionalization techniques has opened new pathways for green synthesis and composite engineering. The research has effectively demonstrated the potential of fungi-based materials in heavy metal bioremediation, UV protection, and environmental sustainability, supporting the Sustainable Development Goals (SDGs) related to health, clean water, climate action, and responsible consumption (SDGs 3,6, 12 and 13). These findings pave the way for the next generation of sustainable materials that combine functionality and translational potential with environmental and biomedical responsibility. Most importantly, this work contributes to the broader scientific community by providing novel methodologies for characterizing fungal materials, manipulating their growth, and understanding the interactions between nanoparticles and fungi. It emphasizes the significance of multidisciplinary approaches in advancing materials science, biotechnology, and environmental engineering. Based on the findings of this doctoral study, I can make general recommendations. To address trends in material inhomogeneity, future studies should replicate experiments with additional fungal strains while also examining morphology, surface chemistry, and molecular properties, using advanced cultivation techniques like controlled environmental chambers to minimize spatial variations within mycelial networks. Building on my composite formation efforts with *A. niger, B. cinerea, M. rouxii,* and *R. oryzae*, researchers should explore other fungal strains and nanoparticle combinations to enhance the functional diversity of fungi-based composites. Additionally, assessing long-term durability, biodegradability, and environmental impact under real-world conditions is essential to evaluate the feasibility of large-scale applications. Further exploration of the nutrient-sensing model is recommended to understand nanoparticle-fungi interactions at the molecular level, enabling advanced applications in bio-sensing and environmental monitoring. Optimizing carbohydrate concentrations and types could improve targeted mechanical and surface properties, significantly increasing the versatility of fungal composites. Finally, building on the foundational knowledge established, scalable production methods should be developed in

collaboration with industrial partners to commercialize fungi-based bio-composites, with future insights leveraging machine learning to design fungal materials by linking bulk properties to fundamental changes, paving the way for sustainable material science and environmental innovation.

List of References

Abd Razak, D. L., Abd Ghani, A., Lazim, M. I. M., Khulidin, K. A., Shahidi, F., & Ismail, A. (2024). *Schizophyllum commune* (Fries) mushroom: A review on its nutritional components, antioxidative, and anti-inflammatory properties. *Current Opinion in Food Science, 56*, 101129.

Abdur Rahman, M., Haque, S., Athikesavan, M. M., & Kamaludeen, M. B. (2023). A review of environmental friendly green composites: production methods, current progresses, and challenges. *Environmental Science and Pollution Research, 30*(7), 16905–16929.

Abo El-Ela, F. I., Hassan, W. H., Amer, A. M., & El-Dek, S. I. (2024). Antifungal activity of chitosan polymeric nanoparticles and correlation with their pH against *Mucor circinelloides* causing mucormycosis, along with Penicillium notatum and *Aspergillus species*. *Current Microbiology, 81*(1), 47.

Abo Elsoud, M. M., & El Kady, E. M. (2019). Current trends in fungal biosynthesis of chitin and chitosan. *Bulletin of the National Research Centre, 43*(1), 1–12.

Achimón, F., Brito, V. D., Pizzolitto, R. P., & Zygadlo, J. A. (2022). Effect of carbon sources on the production of volatile organic compounds by Fusarium verticillioides. *Journal of Fungi, 8*(2), 158.

Akash, M. S. H., Rehman, K., Akash, M. S. H., & Rehman, K. (2020). Ultraviolet-visible (UV-VIS) spectroscopy. *Essentials of Pharmaceutical Analysis, *, 29–56.

Akpan, E. I., Gbenebor, O. P., Adeosun, S. O., & Cletus, O. (2020). Chapter 5 - Solubility, degree of acetylation, and distribution of acetyl groups in chitosan. In S. Gopi, S. Thomas & A. Pius (Eds.), *Handbook of Chitin and Chitosan* (pp. 131–164). Elsevier. 10.1016/B978-0-12-817970-3.00005-5

Alemu, D., Tafesse, M., & Mondal, A. K. (2022). Mycelium-based composite: The future sustainable biomaterial. *International Journal of Biomaterials, 2022*(1), 8401528.

Alengebawy, A., Abdelkhalek, S. T., Qureshi, S. R., & Wang, M. (2021a). Heavy metals and pesticides toxicity in agricultural soil and plants: Ecological risks and human health implications. *Toxics, 9*(3), 42.

Al-Hakkani, M. F. (2019). Guideline of inductively coupled plasma mass spectrometry "ICP–MS": Fundamentals, practices, determination of the limits, quality control, and method validation parameters. *SN Applied Sciences, 1*(7), 791.

Alves, A. K., & Alves, K. (2022). *Environmental applications of nanomaterials*. Springer.

Amer, E. A. A. A., Meyad, E. M. A., Meyad, A. M., & Mohsin, A. (2024). The impact of natural resources on environmental degradation: a review of ecological footprint and CO2 emissions as indicators. *Frontiers in Environmental Science, 12*, 1368125.

American Chemical Society, Tyner, T., & Francis, J. (2016). *ACS Reagent Chemicals: Specifications and Procedures for Reagents and Standard-Grade Reference Materials*. ACS Publications.

Andrievski, R. A. (2014). Review of thermal stability of nanomaterials. *Journal of Materials Science, 49*, 1449–1460.

Antinori, M. E., Ceseracciu, L., Mancini, G., Heredia-Guerrero, J. A., & Athanassiou, A. (2020). Fine-tuning of physicochemical properties and growth dynamics of mycelium-based materials. *ACS Applied Bio Materials, 3*(2), 1044–1051.

Bagy, M. M., Nafady, N. A., Hassan, E. A., & Reyad, M. S. (2023). Isolation and characterization of pigment producing fungi. *Assiut University Journal of Multidisciplinary Scientific Research, 52*(1), 152–176.

Bais, A. F., Lucas, R. M., Bornman, J. F., Williamson, C. E., Sulzberger, B., Austin, A. T., Wilson, S. R., Andrady, A. L., Bernhard, G., & McKenzie, R. L. (2018). Environmental effects of ozone depletion, UV radiation and interactions with climate change: UNEP Environmental Effects Assessment Panel, update 2017. *Photochemical & Photobiological Sciences, 17*(2), 127–179.

Bandara, S., Du, H., Carson, L., Bradford, D., & Kommalapati, R. (2020). Agricultural and biomedical applications of chitosan-based nanomaterials. *Nanomaterials, 10*(10), 1903.

Barhoum, A., & Luisa García-Betancourt, M. (2018). Chapter 10 - Physicochemical characterization of nanomaterials: size, morphology, optical, magnetic, and electrical properties. In A. Barhoum, & A. S. H. Makhlouf (Eds.), *Emerging Applications of Nanoparticles and Architecture Nanostructures* (pp. 279–304). Elsevier. 10.1016/B978-0-323-51254-1.00010-5

Battaglia, E., Benoit, I., van den Brink, J., Wiebenga, A., Coutinho, P. M., Henrissat, B., & de Vries, R. P. (2011). Carbohydrate-active enzymes from the zygomycete fungus *Rhizopus*

oryzae: a highly specialized approach to carbohydrate degradation depicted at genome level. *BMC Genomics, 12*, 1–12.

Bayer, E., & McIntyre, G. (2016). No title. *Method for Producing Grown Materials and Products made Thereby,*

Beauchemin, D. (2017). Inductively Coupled Plasma Mass Spectrometry Methods. In J. C. Lindon, G. E. Tranter & D. W. Koppenaal (Eds.), *Encyclopedia of Spectroscopy and Spectrometry (Third Edition)* (pp. 236–245). Academic Press. 10.1016/B978-0-12-409547-2.11222-3

Bekele, E. T., Gonfa, B. A., Zelekew, O. A., Belay, H. H., & Sabir, F. K. (2020). Synthesis of titanium oxide nanoparticles using root extract of Kniphofia foliosa as a template, characterization, and its application on drug resistance bacteria. *Journal of Nanomaterials, 2020*(1), 2817037.

Belozerskaya, T. A., Gessler, N. N., & Aver'yanov, A. A. (2017). Melanin pigments of fungi. *Fungal Metabolites, 8*, 263–291.

Berthomieu, C., & Hienerwadel, R. (2009). Fourier transform infrared (FTIR) spectroscopy. *Photosynthesis Research, 101*, 157–170.

Bhattacharjee, S. (2016). DLS and zeta potential – What they are and what they are not? *Journal of Controlled Release, 235*, 337–351. 10.1016/j.jconrel.2016.06.017

Bhattacharya, R., Patra, C. R., Earl, A., Wang, S., Katarya, A., Lu, L., Kizhakkedathu, J. N., Yaszemski, M. J., Greipp, P. R., & Mukhopadhyay, D. (2007). Attaching folic acid on gold nanoparticles using noncovalent interaction via different polyethylene glycol backbones and targeting of cancer cells. *Nanomedicine: Nanotechnology, Biology and Medicine, 3*(3), 224–238.

Birdsong, B. K., Capezza, A. J., Nejati, M., Bjurström, A., Li, Y., Jiménez-Quero, A., & Olsson, R. T. (2025). Silicon oxide nanofibers using fungi mycelium as template material/from water purification to space insulation. *RSC Applied Interfaces, 2*(1), 210–219.

Biswas, M. C., Jony, B., Nandy, P. K., Chowdhury, R. A., Halder, S., Kumar, D., Ramakrishna, S., Hassan, M., Ahsan, M. A., & Hoque, M. E. (2022). Recent advancement of biopolymers and their potential biomedical applications. *Journal of Polymers and the Environment, *, 1–24.

Black, A. T. (2014). Ultraviolet B.

Bohu, T., Anand, R., Noble, R., Lintern, M., Kaksonen, A. H., Mei, Y., Cheng, K. Y., Deng, X., Veder, J., & Bunce, M. (2019). Evidence for fungi and gold redox interaction under Earth surface conditions. *Nature Communications, 10*(1), 2290.

Boitor, R. A., Tódor, I. S., Leopold, L. F., & Leopold, N. (2015). Room temperature synthesis of highly monodisperse and Sers-active glucose-reduced gold nanoparticles. *Journal of Applied Spectroscopy, 82*, 415–419.

Bolaños, K., Kogan, M. J., & Araya, E. (2019). Capping gold nanoparticles with albumin to improve their biomedical properties. *International Journal of Nanomedicine, *, 6387–6406.

Boruah, J. S., Devi, C., Hazarika, U., Reddy, P. V. B., Chowdhury, D., Barthakur, M., & Kalita, P. (2021). Green synthesis of gold nanoparticles using an antiepileptic plant extract: in vitro biological and photo-catalytic activities. *RSC Advances, 11*(45), 28029–28041.

Botha, A., & Botes, A. (2014). *Mucor*. In C. A. Batt, & M. L. Tortorello (Eds.), *Encyclopedia of Food Microbiology (Second Edition)* (pp. 834–840). Academic Press. 10.1016/B978-0-12-384730-0.00228-7

Bouhedja, W., Sockalingum, G. D., Pina, P., Allouch, P., Bloy, C., Labia, R., Millot, J. M., & Manfait, M. (1997). ATR-FTIR spectroscopic investigation of E. coli transconjugants β-lactams-resistance phenotype. *FEBS Letters, 412*(1), 39–42.

Braissant, O., Astasov-Frauenhoffer, M., Waltimo, T., & Bonkat, G. (2020). A review of methods to determine viability, vitality, and metabolic rates in microbiology. *Frontiers in Microbiology, 11*, 547458.

Brannon, J. M. (1923). Influence of glucose and fructose on growth of fungi. *Botanical Gazette, 76*(3), 257–273.

Brenner, M., & Hearing, V. J. (2008). The protective role of melanin against UV damage in human skin. *Photochemistry and Photobiology, 84*(3), 539–549.

Broje, V. A., & Keller, A. A. (2005). A method to characterize materials to be used on oleophilic skimmers. Paper presented at the *International Oil Spill Conference, , 2005*(1) 837–840.

Brust, M., Walker, M., Bethell, D., Schiffrin, D. J., & Whyman, R. (1994). Synthesis of thiol-derivatised gold nanoparticles in a two-phase liquid–liquid system. *Journal of the Chemical Society, Chemical Communications, *(7), 801–802.

Brydson, R., Brown, A., Hodges, C., Abellan, P., & Hondow, N. (2015). Microscopy of nanoparticulate dispersions. *Journal of Microscopy, 260*(3), 238–247.

Buzmakov, S. A., & Khotyanovskaya, Y. V. (2020). Degradation and pollution of lands under the influence of oil resources exploitation. *Applied Geochemistry, 113*, 104443.

Cadet, F., Pérez-Guaita, D., Garrigues, S., & de la Guardia, M. (2006). Quantitative analysis, infrared. *Encyclopedia of Analytical Chemistry: Applications, Theory and Instrumentation, ,* 1–49.

Cantu, D., Carl Greve, L., Labavitch, J. M., & Powell, A. L. T. (2009). Characterization of the cell wall of the ubiquitous plant pathogen *Botrytis cinerea*. *Mycological Research, 113*(12), 1396–1403. 10.1016/j.mycres.2009.09.006

Carnovale, C., Bryant, G., Shukla, R., & Bansal, V. (2019). Identifying trends in gold nanoparticle toxicity and uptake: size, shape, capping ligand, and biological corona. *ACS Omega, 4*(1), 242–256.

Castillo, N. A., Valdez, A. L., & Fariña, J. I. (2015). Microbial production of scleroglucan and downstream processing. *Frontiers in Microbiology, 6*, 1106.

Cavalcante, J., & Szekely, G. (2023). Surface engineering of a superamphiphilic, self-growing fibrous Janus membrane prepared from mycelium. *Journal of Materials Chemistry A, 11*(45), 24598–24607.

Challa, S. (2019). Mucormycosis: Pathogenesis and pathology. *Current Fungal Infection Reports, 13*, 11–20.

Chaouay, J., Bentiss, F., Zbair, M., Belattmania, Z., Sabour, B., Lamonier, J., Duquesne, S., & Jama, C. (2024). Study of mercury adsorption using biochars derived from the invasive brown seaweed "Sargassum muticum" as a low-cost and ecofriendly adsorbent in the aqueous phase. *International Journal of Environmental Science and Technology, ,* 1–14.

Chen, L., Dudek, A., Lee, Y., & Chang, C. (2007). Adsorption of carboxylate-modified gold nanoparticles on an octadecylamine monolayer at the air/liquid interface. *Langmuir, 23*(6), 3123–3127.

Chen, Q., Pei, Y., Tang, K., & Albu-Kaya, M. G. (2023). Structure, extraction, processing, and applications of collagen as an ideal component for biomaterials-a review. *Collagen and Leather, 5*(1), 20.

Cheng, G., & Hight Walker, A. R. (2010). Transmission electron microscopy characterization of colloidal copper nanoparticles and their chemical reactivity. *Analytical and Bioanalytical Chemistry, 396*, 1057–1069.

Chrissafis, K., & Bikiaris, D. (2011). Can nanoparticles really enhance thermal stability of polymers? Part I: An overview on thermal decomposition of addition polymers. *Thermochimica Acta, 523*(1-2), 1–24.

Chroumpi, T., Martínez-Reyes, N., Kun, R. S., Peng, M., Lipzen, A., Ng, V., Tejomurthula, S., Zhang, Y., Grigoriev, I. V., & Mäkelä, M. R. (2022). Detailed analysis of the D-galactose catabolic pathways in *Aspergillus niger* reveals complexity at both metabolic and regulatory level. *Fungal Genetics and Biology, 159*, 103670.

Coradeghini, R., Gioria, S., García, C. P., Nativo, P., Franchini, F., Gilliland, D., Ponti, J., & Rossi, F. (2013). Size-dependent toxicity and cell interaction mechanisms of gold nanoparticles on mouse fibroblasts. *Toxicology Letters, 217*(3), 205–216.

Cutrupi, F., Osinska, A. D., Rahmatika, I., Afolayan, J. S., Vystavna, Y., Mahjoub, O., Cifuentes, J. I., Pezzutto, D., & Muziasari, W. (2024). Towards monitoring the invisible threat: a global approach for tackling AMR in water resources and environment. *Frontiers in Water, 6*, 1362701.

Dadachova, E., & Casadevall, A. (2008). Ionizing radiation: how fungi cope, adapt, and exploit with the help of melanin. *Current opinion in microbiology*, *11*(6), 525-531.

Daéid, N. N. (2005). Forensic sciences: systematic drug identification. *Encyclopedia of analytical science* (pp. 471–480). Elsevier.

Danaei, M., Dehghankhold, M., Ataei, S., Hasanzadeh Davarani, F., Javanmard, R., Dokhani, A., Khorasani, S., & Mozafari, M. R. (2018). Impact of particle size and polydispersity index on the clinical applications of lipidic nanocarrier systems. *Pharmaceutics, 10*(2), 57.

Danish, U. R., & Khan, S. (2019). Determinants of the ecological footprint: role of renewable energy, natural resources, and urbanization. Sustain Cities Soc 54: 101996.

Das, S. K., Shome, I., & Guha, A. K. (2012). Surface functionalization of *A. versicolor* mycelia: in situ fabrication of cadmium sulphide nanoparticles and removal of cadmium ions from aqueous solution. *RSC Advances, 2*(7), 3000–3007.

Da Silva, M. C., Leal, R. D. C. A., Da Silva, H. N., & Fook, M. V. L. (2020). Biodegradable suture threads as controlled drug delivery systems. *Materials Research Innovations*.

Dave, V., Sharma, P., Kuila, A., & Sahay, S. S. (2024). Revolutionizing environmental sustainability: exploring the transformative potential of nanocomposites/nanomaterials from recycled waste. *Environmental Science and Pollution Research, 31*(29), 41621–41623.

de Araujo Scharnberg, A. R., & Ravanello, F. (2022). Wastewater Treatment Using Nanomaterials. *Environmental Applications of Nanomaterials, ,* 17–31.

de Haan, K., Ballard, Z. S., Rivenson, Y., Wu, Y., & Ozcan, A. (2019). Resolution enhancement in scanning electron microscopy using deep learning. *Scientific Reports, 9*(1), 12050.

De Souza, C. D., Nogueira, B. R., & Rostelato, M. E. C. (2019). Review of the methodologies used in the synthesis gold nanoparticles by chemical reduction. *Journal of Alloys and Compounds, 798*, 714–740.

Debye, P., & Scherrer, P. (1917). Interference on inordinate orientated particles in x-ray light. III. *Physikalische Zeitschrift, 18*, 291–301.

Devi, Y. M., Basha, V. S., & Sailaja, G. (2020). *Formulation, Characterization and Comparison of Cefixime, Cefaclor and Cefdinir Microspheres*https://doi.org/10.21276/ijpbs.2020.10.2.30

Distler, D. (2001). Polymer dispersions. *Encyclopedia of Materials: Science and Technology, ,* 7272–7275.

Donkor, A. K., Ghoveisi, H., & Bonzongo, J. J. (2024). Use of metallic mercury in artisanal gold mining by amalgamation: a review of temporal and spatial trends and environmental pollution. *Minerals, 14*(6), 555.

Eaton, P., Quaresma, P., Soares, C., Neves, C., de Almeida, M. P., Pereira, E., & West, P. (2017). A direct comparison of experimental methods to measure dimensions of synthetic nanoparticles. *Ultramicroscopy, 182*, 179–190. 10.1016/j.ultramic.2017.07.001

Edo, G. I., Ndudi, W., Makia, R. S., Ainyanbhor, I. E., Yousif, E., Gaaz, T. S., ... & Umar, H. (2024). Beta-glucan: An overview in biological activities, derivatives, properties, modifications and current advancements in food, health and industrial applications. *Process Biochemistry*, *147*, 347-370.

Eid, K. A., Salem, H. F., Zikry, A. A., El-Sayed, A. F., & Sharaf, M. A. (2011). Antifungal effects of colloidally stabilized gold nanoparticles: screening by microplate assay. *Nature, 2*(9)

El-Naggar, N. E., Saber, W. I., Zweil, A. M., & Bashir, S. I. (2022). An innovative green synthesis approach of chitosan nanoparticles and their inhibitory activity against phytopathogenic *Botrytis cinerea* on strawberry leaves. *Scientific Reports, 12*(1), 3515.

Elsacker, E., De Laet, L., & Peeters, E. (2022). Functional grading of mycelium materials with inorganic particles: The effect of nanoclay on the biological, chemical and mechanical properties. *Biomimetics, 7*(2), 57.

Elsalih, M. (2021). No title. *Probabilistic Risk Assessment of Offshore Blowouts,*

Erdoğmuş, S. F., Altıntaş, Ö E., & Çelik, S. (2023). Production of fungal chitosan and fabrication of fungal chitosan/polycaprolactone electrospun nanofibers for tissue engineering. *Microscopy Research and Technique, 86*(10), 1309–1321.

Exbrayat, J. -. (2016). Microscopy: Light Microscopy and Histochemical Methods. In B. Caballero, P. M. Finglas & F. Toldrá (Eds.), *Encyclopedia of Food and Health* (pp. 715–723). Academic Press. 10.1016/B978-0-12-384947-2.00460-8

Faghihzadeh, F., Anaya, N. M., Schifman, L. A., & Oyanedel-Craver, V. (2016). Fourier transform infrared spectroscopy to assess molecular-level changes in microorganisms exposed to nanoparticles. *Nanotechnology for Environmental Engineering, 1*, 1–16.

Falih, K. T., Mohd Razali, S. F., Abdul Maulud, K. N., Abd Rahman, N., Abba, S. I., & Yaseen, Z. M. (2024). Assessment of petroleum contamination in soil, water, and atmosphere: a comprehensive review. *International Journal of Environmental Science and Technology, 21*(13), 8803–8832.

Farajollah, R., Nikje, M. M. A., Saadat, E., & Dorkoosh, F. A. (2021). Star-hyperbranched waterborne polyurethane based on D-glucose-poly (ε-caprolactone) core as a biomaterial candidate. *European Polymer Journal, 147*, 110318.

Focher, B., Naggi, A., Torri, G., Cosani, A., & Terbojevich, M. (1992). Structural differences between chitin polymorphs and their precipitates from solutions—evidence from CP-MAS 13C-NMR, FT-IR and FT-Raman spectroscopy. *Carbohydrate Polymers, 17*(2), 97–102.

Fowkes, F. M. (1964a). Attractive forces at interfaces. *Industrial & Engineering Chemistry, 56*(12), 40–52.

Frei, R. W. (1976). Diffuse reflectance spectroscopy; applications, standards, and calibration (with special reference to chromatography). *Journal of Research of the National Bureau of Standards.Section A, Physics and Chemistry, 80*(4), 551.

Frens, G. (1973). Controlled nucleation for the regulation of the particle size in monodisperse gold suspensions. *Nature Physical Science, 241*(105), 20–22.

Frota, M. M., Mattos, A. L. A., Miranda, K. W. E., Cheng, H. N., Biswas, A., & Bastos, M. d. S. R. (2022). Superhydrophobic systems in food science and technology: Concepts, trends, challenges, and technological innovations. *Applied Food Research, 2*(2), 100213.

Gadd, G. M. (Ed.). (2001). *Fungi in bioremediation* (No. 23). Cambridge University Press.

Gao, J., Wang, Y., & Hao, H. (2012). Investigations on dehydration processes of trisodium citrate hydrates. *Frontiers of Chemical Science and Engineering, 6*, 276–281.

Garcia, A., Smith, C. P., & Lee, S. C. (2023). Dimorphism and pathogenesis in *Mucor* species. *Evolution of Fungi and Fungal-Like Organisms* (pp. 93–101). Springer.

Gelardi, D. L., Li, C., & Parikh, S. J. (2019). An emerging environmental concern: Biochar-induced dust emissions and their potentially toxic properties. *Science of the Total Environment, 678*, 813–820.

Geraldes, A. N., Rosero, W. A., Rostelato, M. E. C., & Sarkis, J. E. (2024). Calculation of the Budget of Uncertainty on Measurements Size Nanoparticles Using Dynamic Light Scattering. *Journal of the Brazilian Chemical Society, 35*(8), e–20240039.

Ghareeb, A., Fouda, A., Kishk, R. M., & El Kazzaz, W. M. (2024). Unlocking the potential of titanium dioxide nanoparticles: an insight into green synthesis, optimizations, characterizations, and multifunctional applications. *Microbial Cell Factories, 23*(1), 341.

Giersig, M., & Mulvaney, P. (1993). Preparation of ordered colloid monolayers by electrophoretic deposition. *Langmuir, 9*(12), 3408–3413.

Gil, M., Núñez, J. L., Palafox, M. A., & Iza, N. (2001). FTIR study of five complex β-lactam molecules. *Biopolymers: Original Research on Biomolecules, 62*(5), 278–294.

Gimeno, M. C. (2008). The chemistry of gold. *Modern Supramolecular Gold Chemistry, 1*, 1.

Girometta, C., Picco, A. M., Baiguera, R. M., Dondi, D., Babbini, S., Cartabia, M., Pellegrini, M., & Savino, E. (2019). Physico-mechanical and thermodynamic properties of mycelium-based biocomposites: A review. *Sustainability, 11*(1), 281.

Gittings, M. R., & Saville, D. A. (1998). The determination of hydrodynamic size and zeta potential from electrophoretic mobility and light scattering measurements. *Colloids and Surfaces A: Physicochemical and Engineering Aspects, 141*(1), 111–117. 10.1016/S0927-7757(98)00207-6

Goci, M. C., Leudjo Taka, A., Martin, L., & Klink, M. J. (2023). Chitosan-based polymer nanocomposites for environmental remediation of mercury pollution. *Polymers, 15*(3), 482.

Gohel, N. M., Raghunandan, B. L., Patel, N. B., Parmar, H. V., & Raval, D. B. (2022). Role of fungal biocontrol agents for sustainable agriculture. *Fungal diversity, ecology and control management* (pp. 577–606). Springer.

Golding, C. G., Lamboo, L. L., Beniac, D. R., & Booth, T. F. (2016). The scanning electron microscope in microbiology and diagnosis of infectious disease. *Scientific Reports, 6*(1), 1–8.

Gomes, J., Batra, J., Chopda, V. R., Kathiresan, P., & Rathore, A. S. (2018). Chapter 25 - Monitoring and Control of Bioethanol Production From Lignocellulosic Biomass. In T. Bhaskar, A. Pandey, S. V. Mohan, D. Lee & S. K. Khanal (Eds.), *Waste Biorefinery* (pp. 727–749). Elsevier. 10.1016/B978-0-444-63992-9.00025-2

Gore, A. H., & Prajapat, A. L. (2022). Biopolymer nanocomposites for sustainable UV protective packaging. *Frontiers in Materials, 9*, 855727.

Gore, C. T., Omwoma, S., Chen, W., & Song, Y. (2016). Interweaved LDH/PAN nanocomposite films: Application in the design of effective hexavalent chromium adsorption technology. *Chemical Engineering Journal, 284*, 794–801.

Gow, N. A., & Lenardon, M. D. (2023). Architecture of the dynamic fungal cell wall. *Nature Reviews Microbiology*, *21*(4), 248-259.Gulfam, R., & Chen, Y. (2022). Recent growth of wettability gradient surfaces: A review. *Research,*

Gow, N. A. (2025). Fungal cell wall biogenesis: structural complexity, regulation and inhibition. *Fungal Genetics and Biology*, 103991.

Guo, B., Finne-Wistrand, A., & Albertsson, A. (2010). Enhanced electrical conductivity by macromolecular architecture: hyperbranched electroactive and degradable block copolymers based on poly (ε-caprolactone) and aniline pentamer. *Macromolecules, 43*(10), 4472–4480.

Gutti, B., Aji, M. M., & Magaji, G. (2012). Environmental impact of natural resources exploitation in Nigeria and the way forward. *Journal of Applied Technology in Environmental Sanitation, 2*(2), 95–102.

Hamad, H., Alma, M., Ismael, H., & Göçeri, A. (2014). The effect of some sugars on the growth of *Aspergillus niger*. *KSÜ Doğa Bilimleri Dergisi, 17*(4), 7–11.

Hameed, I. H., Hamza, L. F., & Kamal, S. A. (2015). Analysis of bioactive chemical compounds of *Aspergillus niger* by using gas chromatography-mass spectrometry and fourier-transform infrared spectroscopy. *Journal of Pharmacognosy and Phytotherapy, 7*(8), 132–163.

Haneef, M., Ceseracciu, L., Canale, C., Bayer, I. S., Heredia-Guerrero, J. A., & Athanassiou, A. (2017). Advanced materials from fungal mycelium: fabrication and tuning of physical properties. *Scientific Reports, 7*(1), 41292.

Hao, G., & Barker, G. C. (2022). Fatty acid secretion by the white-rot fungus, *Trametes versicolor*. *Journal of Industrial Microbiology and Biotechnology, 49*(1), kuab083.

Hargreaves, A. J., Vale, P., Whelan, J., Constantino, C., Dotro, G., & Cartmell, E. (2016). Mercury and antimony in wastewater: fate and treatment. *Water, Air, & Soil Pollution, 227*, 1–17.

Harmami, H., Ulfin, I., Sakinah, A. H., & Ni'mah, Y. L. (2019). Water-soluble chitosan from shrimp and mussel shells as corrosion inhibitor on tinplate in 2% NaCl. *Malaysian Journal of Fundamental and Applied Sciences, 15*(2), 212–217.

Hashem, A. H., Shehabeldine, A. M., Ali, O. M., & Salem, S. S. (2022). Synthesis of chitosan-based gold nanoparticles: Antimicrobial and wound-healing activities. *Polymers, 14*(11), 2293.

Hayer, K., Stratford, M., & Archer, D. B. (2014). Germination of *Aspergillus niger* conidia is triggered by nitrogen compounds related to L-amino acids. *Applied and Environmental Microbiology, 80*(19), 6046–6053.

Hazen, K. C., & Cutler, J. E. (1979). Autoregulation of germ tube formation by Candida albicans. *Infection and Immunity, 24*(3), 661–666.

He, Z., Yin, H., Chang, C., Wang, G., & Liang, X. (2020). Interfacing DNA with gold nanoparticles for heavy metal detection. *Biosensors, 10*(11), 167.

Health Canada. (1979). *Guidelines for Canadian Drinking Water Quality: Guideline Technical Document – Mercury.* .Health Canada. https://www.canada.ca/en/health-canada/services/publications/healthy-living/guidelines-canadian-drinking-water-quality-guideline-technical-document-mercury.html

Henry, C. A., Singh, T. B., & Oyedotun, T. D. T. (2023). The Environmental Risks Posed by the Oil and Gas Development and Its Potential Impacts on Mangrove Ecosystems and the Coastal Community's Well-Being. *Journal of Geoscience and Environment Protection, 11*(5), 17–46.

Hirai, A., Odani, H., & Nakajima, A. (1991). Determination of degree of deacetylation of chitosan by 1 H NMR spectroscopy. *Polymer Bulletin, 26*, 87–94.

Hodgkinson, P., & Emsley, L. (2000). Numerical simulation of solid-state NMR experiments. *Progress in Nuclear Magnetic Resonance Spectroscopy, 36*(3), 201–239. 10.1016/S0079-6565(99)00019-9

Hoffmann, K., Pawłowska, J., Walther, G., Wrzosek, M., De Hoog, G. S., Benny, G. L., Kirk, P. M., & Voigt, K. (2013). The family structure of the Mucorales: a synoptic revision based on comprehensive multigene-genealogies. *Persoonia-Molecular Phylogeny and Evolution of Fungi, 30*(1), 57–76.

Holder, C. F., & Schaak, R. E. (2019). Tutorial on powder X-ray diffraction for characterizing nanoscale materials. *Acs Nano, 13*(7), 7359–7365.

Holgate, J. H., & Webb, J. (2003). MICROSCOPY | Light Microscopy and Histochemical Methods. In B. Caballero (Ed.), *Encyclopedia of Food Sciences and Nutrition (Second Edition)* (pp. 3917–3922). Academic Press. 10.1016/B0-12-227055-X/00778-1

Holt, G. A., Mcintyre, G., Flagg, D., Bayer, E., Wanjura, J. D., & Pelletier, M. G. (2012). Fungal mycelium and cotton plant materials in the manufacture of biodegradable molded packaging material: Evaluation study of select blends of cotton byproducts. *Journal of Biobased Materials and Bioenergy, 6*(4), 431–439.

Huang, H., & Yang, X. (2004). Synthesis of chitosan-stabilized gold nanoparticles in the absence/presence of tripolyphosphate. *Biomacromolecules, 5*(6), 2340–2346.

Huang, T., Chen, C., Li, D., & Ek, M. (2019). Hydrophobic and antibacterial textile fibres prepared by covalently attaching betulin to cellulose. *Cellulose, 26*, 665–677.

Hutchings, G. J., Brust, M., & Schmidbaur, H. (2008). Gold—an introductory perspective. *Chemical Society Reviews, 37*(9), 1759–1765.

Ijadpanahsaravi, M., Punt, M., Wösten, H. A., & Teertstra, W. R. (2021). Minimal nutrient requirements for induction of germination of *Aspergillus niger* conidia. *Fungal Biology, 125*(3), 231–238.

Iiolligan, P. M., & Jennings, D. H. (1972). carbohydrate metabolism in the fungus dendryphiella salina: ii. the influence of different carbon and nitrogen sources on the accumulation of mannitol and arabitol. *New Phytologist, 71*(4), 583–594.

Islam, M. R., Tudryn, G., Bucinell, R., Schadler, L., & Picu, R. C. (2017). Morphology and mechanics of fungal mycelium. *Scientific Reports, 7*(1), 13070.

Italia, H., Patel, I., & Shah, J. (2016). Experimental study of bacterial self-healing effect on concrete: a review. *Journal of Civil Engineering and Environmental Technology, 3*(1), 78–81.

Jang, M., Kong, B., Jeong, Y., Lee, C. H., & Nah, J. (2004). Physicochemical characterization of α-chitin, β-chitin, and γ-chitin separated from natural resources. *Journal of Polymer Science Part A: Polymer Chemistry, 42*(14), 3423–3432.

Jarray, A., Wijshoff, H., Luiken, J. A., & den Otter, W. K. (2020). Systematic approach for wettability prediction using molecular dynamics simulations. *Soft Matter, 16*(17), 4299–4310.

Jiang, L., Walczyk, D., McIntyre, G., Bucinell, R., & Tudryn, G. (2017). Manufacturing of biocomposite sandwich structures using mycelium-bound cores and preforms. *Journal of Manufacturing Processes, 28*, 50–59. 10.1016/j.jmapro.2017.04.029

Jing, A. J., Zhang, A., & Wu, Z. (2002). Chapter 11 - Thermal analysis of polymer fibers. *Handbook of Thermal Analysis and Calorimetry, 3*, 409–490. 10.1016/S1573-4374(02)80014-0

Jing, Y. D., He, Z. L., & Yang, X. E. (2007). Effects of pH, organic acids, and competitive cations on mercury desorption in soils. *Chemosphere, 69*(10), 1662–1669.

Jo, W., Cho, Y., Cho, D., Park, S., Yoo, Y., & Seok, S. (2009). Culture conditions for the mycelial growth of Ganoderma applanatum. *Mycobiology, 37*(2), 94–102.

Johnson, R. L., & Schmidt-Rohr, K. (2014). Quantitative solid-state 13C NMR with signal enhancement by multiple cross polarization. *Journal of Magnetic Resonance, 239*, 44–49. 10.1016/j.jmr.2013.11.009

Jones, M., Bhat, T., Kandare, E., Thomas, A., Joseph, P., Dekiwadia, C., Yuen, R., John, S., Ma, J., & Wang, C. (2018). Thermal degradation and fire properties of fungal mycelium and mycelium-biomass composite materials. *Scientific Reports, 8*(1), 17583.

Jothi Prakash, C. G., & Prasanth, R. (2021). Approaches to design a surface with tunable wettability: a review on surface properties. *Journal of Materials Science, 56*, 108–135.

Joy, F., Devasia, J., Nizam, A., Lakshmaiah, V. V., & Krishna, S. B. N. (2023). Fungi-templated silver nanoparticle composite: synthesis, characterization, and its applications. *Applied Sciences, 13*(4), 2158.

Kalaivani, R., Maruthupandy, M., Muneeswaran, T., Singh, M., Sureshkumar, S., Anand, M., Ramakritinan, C. M., Quero, F., & Kumaraguru, A. K. (2020). Chitosan mediated gold nanoparticles against pathogenic bacteria, fungal strains and MCF-7 cancer cells. *International Journal of Biological Macromolecules, 146*, 560–568.

Karimi, S., Moshaii, A., & Nikkhah, M. (2019). Controlled synthesis of colloidal monodisperse gold nanoparticles in a wide range of sizes; investigating the effect of reducing agent. *Materials Research Express, 6*(11), 1150f2.

Kawamoto, T., & Ryu, I. (2014). Radical reactions of borohydrides. *Organic & Biomolecular Chemistry, 12*(48), 9733–9742.

Kaya, M., Baran, T., Mentes, A., Asaroglu, M., Sezen, G., & Tozak, K. O. (2014). Extraction and characterization of α-chitin and chitosan from six different aquatic invertebrates. *Food Biophysics, 9*, 145–157.

Ke, C., Deng, F., Chuang, C., & Lin, C. (2021). Antimicrobial actions and applications of chitosan. *Polymers, 13*(6), 904.

Keller, S., Macheleidt, J., Scherlach, K., Schmaler-Ripcke, J., Jacobsen, I. D., Heinekamp, T., & Brakhage, A. A. (2011). Pyomelanin formation in *Aspergillus fumigatus* requires HmgX and the transcriptional activator HmgR but is dispensable for virulence. *PLoS One, 6*(10), e26604.

Kendall, M., Hodges, N. J., Whitwell, H., Tyrrell, J., & Cangul, H. (2015). Nanoparticle growth and surface chemistry changes in cell-conditioned culture medium. *Philosophical Transactions of the Royal Society B: Biological Sciences, 370*(1661), 20140100.

Kim, K., Leem, Y., Kim, K., Kim, K., & Choi, H. T. (2002). Transformation of the medicinal basidiomycete *Trametes versicolor* to hygromycin B resistance by restriction enzyme mediated integration. *FEMS Microbiology Letters, 209*(2), 273–276.

Kim, H. J., Wang, W., Mallapragada, S. K., & Vaknin, D. (2021). The effects of temperature on the assembly of gold nanoparticle by interpolymer complexation. *The Journal of Physical Chemistry Letters, 12*(5), 1461–1467.

Kim, J., & Kim, K. H. (2017). Effects of minimal media vs. complex media on the metabolite profiles of Escherichia coli and Saccharomyces cerevisiae. *Process Biochemistry, 57*, 64–71.

Kim, T. H., Park, S. H., Lee, S., Bharadwaj, A. S., Lee, Y. S., Yoo, C. G., & Kim, T. H. (2023). A review of biomass-derived UV-shielding materials for bio-composites. *Energies, 16*(5), 2231.

Koch, S. M., Freidank-Pohl, C., Siontas, O., Cortesao, M., Mota, A., Runzheimer, K., Jung, S., Rebrosova, K., Siler, M., & Moeller, R. (2023). *Aspergillus niger* as a cell factory for the production of pyomelanin, a molecule with UV-C radiation shielding activity. *Frontiers in Microbiology, 14*, 1233740.

Koga, D., Kusumi, S., Shibata, M., & Watanabe, T. (2021). Applications of scanning electron microscopy using secondary and backscattered electron signals in neural structure. *Frontiers in Neuroanatomy, 15*, 759804.

Konwarh, R., Palanisamy, S. B., & Jogi, P. K. (2020). A mini review on prospects and challenges of harnessing fungi for concrete-crack healing. *Material Science Research India, 17*(2), 117–128.

Koshani, R., Jafari, S. M., & van de Ven, T. G. M. (2020). Going deep inside bioactive-loaded nanocarriers through Nuclear Magnetic Resonance (NMR) spectroscopy. *Trends in Food Science & Technology, 101*, 198–212. 10.1016/j.tifs.2020.05.010

Krijgsheld, P., Bleichrodt, R. v., Van Veluw, G. J., Wang, F., Müller, W. H., Dijksterhuis, J., & Wösten, H. (2013). Development in *Aspergillus*. *Studies in Mycology, 74*(1), 1–29.

Kumar, A., Das, N., Satija, N. K., Mandrah, K., Roy, S. K., & Rayavarapu, R. G. (2019). A novel approach towards synthesis and characterization of non-cytotoxic gold nanoparticles using taurine as capping agent. *Nanomaterials, 10*(1), 45.

Kumar, B., Smita, K., & Flores, L. C. (2017). Plant mediated detoxification of mercury and lead. *Arabian Journal of Chemistry, 10*, S2335–S2342.

Kumari, S., & Kishor, R. (2020). Chitin and chitosan: origin, properties, and applications. *Handbook of chitin and chitosan* (pp. 1–33). Elsevier.

Kumirska, J., Czerwicka, M., Kaczyński, Z., Bychowska, A., Brzozowski, K., Thöming, J., & Stepnowski, P. (2010). Application of spectroscopic methods for structural analysis of chitin and chitosan. *Marine Drugs, 8*(5), 1567–1636.

Kundu, J., Kim, D., Chae, I. G., Lee, J. K., Lee, S., Jeong, C., & Chun, K. (2018). Silicon dioxide nanoparticles induce COX-2 expression through activation of STAT3 signaling pathway in HaCaT cells. *Toxicology in Vitro, 52*, 235–242. 10.1016/j.tiv.2018.06.008

Kwon, K., Lee, K. Y., Lee, Y. W., Kim, M., Heo, J., Ahn, S. J., & Han, S. W. (2007). Controlled synthesis of icosahedral gold nanoparticles and their surface-enhanced Raman scattering property. *The Journal of Physical Chemistry C, 111*(3), 1161–1165.

Kwon, Y., Cho, S., Kwon, J., Hwang, M., Hwang, H., Kang, Y. J., Lee, H., Kim, J., & Kim, W. K. (2022). Anti-atopic dermatitis effects of Parasenecio auriculatus via simultaneous inhibition of multiple inflammatory pathways. *BMB Reports, 55*(6), 275.

Lacrampe, N., Lopez-Lauri, F., Lugan, R., Colombié, S., Olivares, J., Nicot, P. C., & Lecompte, F. (2021). Regulation of sugar metabolism genes in the nitrogen-dependent susceptibility of tomato stems to *Botrytis cinerea*. *Annals of Botany, 127*(1), 143–154.

Lang, N. J., Liu, B., & Liu, J. (2014). Characterization of glucose oxidation by gold nanoparticles using nanoceria. *Journal of Colloid and Interface Science, 428*, 78–83.

Lavertu, M., Xia, Z., Serreqi, A. N., Berrada, M., Rodrigues, A., Wang, D., Buschmann, M. D., & Gupta, A. (2003). A validated 1H NMR method for the determination of the degree of deacetylation of chitosan. *Journal of Pharmaceutical and Biomedical Analysis, 32*(6), 1149–1158. 10.1016/S0731-7085(03)00155-9

Lax, C., Pérez-Arques, C., Navarro-Mendoza, M. I., Cánovas-Márquez, J. T., Tahiri, G., Pérez-Ruiz, J. A., Osorio-Concepción, M., Murcia-Flores, L., Navarro, E., & Garre, V. (2020). Genes, pathways, and mechanisms involved in the virulence of mucorales. *Genes, 11*(3), 317.

Laycock, A., Clark, N. J., Clough, R., Smith, R., & Handy, R. D. (2022). Determination of metallic nanoparticles in biological samples by single particle ICP-MS: A systematic review from sample collection to analysis. *Environmental Science: Nano, 9*(2), 420–453.

Lazarević, J., Stojičić, D., & Keča, N. (2016). Effects of temperature, pH and carbon and nitrogen sources on growth of in vitro cultures of ectomycorrhizal isolates from Pinus heldreichii forest. *Forest Systems, 25*(1), e048.

Leem, Y., Kim, S., Ross, I. K., & Choi, H. T. (1999). Transformation and laccase mutant isolation in Coprinus congregatus by restriction enzyme-mediated integration. *FEMS Microbiology Letters, 172*(1), 35–40.

Levy, G. C., & Craik, D. J. (1981). Recent developments in nuclear magnetic resonance spectroscopy. *Science, 214*(4518), 291–299.

Li, K., Jia, J., Wu, N., & Xu, Q. (2022). Recent advances in the construction of biocomposites based on fungal mycelia. *Frontiers in Bioengineering and Biotechnology, 10*, 1067869.

Li, X., Wan, C., Tao, T., Chai, H., Huang, Q., Chai, Y., & Wu, Y. (2024). An overview of the development status and applications of cellulose-based functional materials. *Cellulose, 31*(1), 61–99.

Li, Z., Chung, S. W., Nam, J. M., Ginger, D. S., & Mirkin, C. A. (2003). Living templates for the hierarchical assembly of gold nanoparticles. *Angewandte Chemie-International Edition, 42*(20), 2306–2309.

Lilly, V. G., & Barnett, H. L. (1953). *The utilization of sugars by fungi*. West Virginia University Agricultural Experiment Station.

Lin, X., Alspaugh, J. A., Liu, H., & Harris, S. (2015). Fungal morphogenesis. *Cold Spring Harbor Perspectives in Medicine, 5*(2), a019679.

Liu, J., Qin, G., Raveendran, P., & Ikushima, Y. (2006). Facile "green" synthesis, characterization, and catalytic function of β-D-glucose-stabilized Au nanocrystals. *Chemistry–A European Journal, 12*(8), 2131–2138.

Liu, S., Wang, H., & Yang, J. (2024). Influence of preparation methods and nanomaterials on hydrophobicity and anti-icing performance of nanoparticle/epoxy coatings. *Polymers, 16*(3), 364.

Liu, X., Zhang, J., & Zhu, K. Y. (2019). Chitin in arthropods: biosynthesis, modification, and metabolism. *Targeting Chitin-Containing Organisms, ,* 169–207.

Lopatukhin, E. V., Ihalainen, Y. A., Markelova, N. N., Kuvarina, A. E., & Sadykova, V. S. (2024). Fungal hydrophobins: biosynthesis, properties, and possibilities of application in biotechnology. *Applied Biochemistry and Microbiology, 60*(3), 372–382.

Lopez-Moya, F., Suarez-Fernandez, M., & Lopez-Llorca, L. V. (2019). Molecular mechanisms of chitosan interactions with fungi and plants. *International Journal of Molecular Sciences, 20*(2), 332.

Lou, T., Chen, L., Zhang, C., Kang, Q., You, H., Shen, D., & Chen, L. (2012). A simple and sensitive colorimetric method for detection of mercury ions based on anti-aggregation of gold nanoparticles. *Analytical Methods, 4*(2), 488–491.

Lu, P., Huang, S., Chen, Y., Chiueh, L., & Shih, D. Y. (2015). Analysis of titanium dioxide and zinc oxide nanoparticles in cosmetics. *Journal of Food and Drug Analysis, 23*(3), 587–594.

Lu, P., Li, H., Chang, H., Wu, N., & Hung, C. (2017). Gold nanoparticles induce cell death and suppress migration of melanoma cells. *Journal of Nanoparticle Research, 19*, 1–12.

Lucas, R. M., Yazar, S., Young, A. R., Norval, M., De Gruijl, F. R., Takizawa, Y., Rhodes, L. E., Sinclair, C. A., & Neale, R. E. (2019). Human health in relation to exposure to solar ultraviolet radiation under changing stratospheric ozone and climate. *Photochemical & Photobiological Sciences, 18*(3), 641–680.

Luo, J., Chen, X., Crump, J., Zhou, H., Davies, D. G., Zhou, G., Zhang, N., & Jin, C. (2018). Interactions of fungi with concrete: Significant importance for bio-based self-healing concrete. *Construction and Building Materials, 164*, 275–285.

Lv, S., Liang, S., Zuo, J., Zhang, S., Wang, J., & Wei, D. (2023). Lignin-based anti-UV functional materials: recent advances in preparation and application. *Iranian Polymer Journal, 32*(11), 1477–1497.

Ma, S., Lei, T., Meng, J., Liang, X., & Guan, D. (2023). Global oil refining's contribution to greenhouse gas emissions from 2000 to 2021. *The Innovation, 4*(1)

Machi, K., Ono, Y., & Iwahashi, H. (2024). Citrate, a TCA cycle metabolite, plays a role as a hydroxyl radical scavenger in vitro. *Journal of Photochemistry and Photobiology A: Chemistry, 454*, 115691.

Malatesta, M. (2021). Transmission electron microscopy as a powerful tool to investigate the interaction of nanoparticles with subcellular structures. *International Journal of Molecular Sciences, 22*(23), 12789.

Malik, A. K., & Kumar, R. (2016). Spectroscopy: Types.

Malm, A. V., & Corbett, J. C. (2019a). Improved dynamic light scattering using an adaptive and statistically driven time resolved treatment of correlation data. *Scientific Reports, 9*(1), 13519.

Malm, A. V., & Corbett, J. C. (2019b). Improved dynamic light scattering using an adaptive and statistically driven time resolved treatment of correlation data. *Scientific Reports, 9*(1), 13519.

Manan, S., Ullah, M. W., Ul-Islam, M., Atta, O. M., & Yang, G. (2021). Synthesis and applications of fungal mycelium-based advanced functional materials. *Journal of Bioresources and Bioproducts, 6*(1), 1–10.

Marcilla, A., Gómez-Siurana, A., Beltrán, M., Martínez-Castellanos, I., Blasco, I., & Berenguer, D. (2018). TGA-FTIR study of the pyrolysis of sodium citrate and its effect on the pyrolysis of tobacco and tobacco/SBA-15 mixtures under N2 and air atmospheres. *Journal of the Science of Food and Agriculture, 98*(15), 5916–5931.

Marie, E., & Torbjörn, W. (2007). 4 - Surface Analytical Techniques Applied to Cleaning Processes. In I. Johansson, & P. Somasundaran (Eds.), *Handbook for Cleaning/Decontamination of Surfaces* (pp. 747–789). Elsevier Science B.V. 10.1016/B978-044451664-0/50023-1

Marques, M. J. d. A. M., Alves, F., Sousa, M., Guimarães, F. E. G., & Kurachi, C. (2024). Morphological aspects and the effectiveness of photodynamic inactivation against *Rhizopus oryzae* in different life cycles. *Photochemical & Photobiological Sciences, 23*(7), 1323–1339.

Maverakis, E., Miyamura, Y., Bowen, M. P., Correa, G., Ono, Y., & Goodarzi, H. (2010). Light, including ultraviolet. *Journal of Autoimmunity, 34*(3), J247–J257.

Max, J., & Chapados, C. (2004). Infrared spectroscopy of aqueous carboxylic acids: comparison between different acids and their salts. *The Journal of Physical Chemistry A, 108*(16), 3324–3337.

Mazarakioti, E. C., Zotos, A., Thomatou, A., Kontogeorgos, A., Patakas, A., & Ladavos, A. (2022). Inductively coupled plasma-mass spectrometry (ICP-MS), a useful tool in authenticity of agricultural products' and foods' origin. *Foods, 11*(22), 3705.

Menon, R. R., Luo, J., Chen, X., Zhou, H., Liu, Z., Zhou, G., Zhang, N., & Jin, C. (2019). Screening of fungi for potential application of self-healing concrete. *Scientific Reports, 9*(1), 2075.

Meyer, V.Connecting materials sciences with fungal biology: a sea of possibilities. Fungal Biol Biotechnol. 2022; 9: 1–4.

Meyer, V., Cairns, T., Barthel, L., King, R., Kunz, P., Schmideder, S., Müller, H., Briesen, H., Dinius, A., & Krull, R. (2021). Understanding and controlling filamentous growth of fungal cell factories: novel tools and opportunities for targeted morphology engineering. *Fungal Biology and Biotechnology, 8*(1), 8.

Millet, L. J., Aufrecht, J., Labbé, J., Uehling, J., Vilgalys, R., Estes, M. L., Miquel Guennoc, C., Deveau, A., Olsson, S., & Bonito, G. (2019). Increasing access to microfluidics for studying fungi and other branched biological structures. *Fungal Biology and Biotechnology, 6*, 1–14.

Mohamed, M. A., Jaafar, J., Ismail, A. F., Othman, M., & Rahman, M. A. (2017). Fourier transform infrared (FTIR) spectroscopy. *Membrane characterization* (pp. 3–29). Elsevier.

Mohan, C. O., Gunasekaran, S., & Ravishankar, C. N. (2019). Chitosan-capped gold nanoparticles for indicating temperature abuse in frozen stored products. *Npj Science of Food, 3*(1), 2.

Mohite, P., Kumar, A. R., & Zinjarde, S. (2017). Relationship between salt tolerance and nanoparticle synthesis by Williopsis saturnus NCIM 3298. *World Journal of Microbiology and Biotechnology, 33*, 1–11.

Money, N. P. (2024). Molds, Mushrooms, and Medicines: Our Lifelong Relationship with Fungi.

Moore, T. L., Rodriguez-Lorenzo, L., Hirsch, V., Balog, S., Urban, D., Jud, C., Rothen-Rutishauser, B., Lattuada, M., & Petri-Fink, A. (2015). Nanoparticle colloidal stability in cell

culture media and impact on cellular interactions. *Chemical Society Reviews, 44*(17), 6287–6305.

Mosbach, A., Leroch, M., Mendgen, K. W., & Hahn, M. (2011). Lack of evidence for a role of hydrophobins in conferring surface hydrophobicity to conidia and hyphae of *Botrytis cinerea*. *BMC Microbiology, 11*, 1–14.

Moseson, D. E., Jordan, M. A., Shah, D. D., Corum, I. D., Alvarenga Jr., B. R., & Taylor, L. S. (2020). Application and limitations of thermogravimetric analysis to delineate the hot melt extrusion chemical stability processing window. *International Journal of Pharmaceutics, 590*, 119916. 10.1016/j.ijpharm.2020.119916

Mostafa, E. M., Abdelgawad, M. A., Musa, A., Alotaibi, N. H., Elkomy, M. H., Ghoneim, M. M., Badawy, M. S. E., Taha, M. N., Hassan, H. M., & Hamed, A. A. (2022). Chitosan silver and gold nanoparticle formation using endophytic fungi as powerful antimicrobial and anti-biofilm potentialities. *Antibiotics, 11*(5), 668.

Mourdikoudis, S., Pallares, R. M., & Thanh, N. T. (2018). Characterization techniques for nanoparticles: comparison and complementarity upon studying nanoparticle properties. *Nanoscale, 10*(27), 12871–12934.

Mukherjee, P., Ahmad, A., Mandal, D., Senapati, S., Sainkar, S. R., Khan, M. I., Ramani, R., Parischa, R., Ajayakumar, P. V., & Alam, M. (2001). Bioreduction of AuCl4-ions by the fungus, Verticillium sp. and surface trapping of the gold nanoparticles formed. *Angewandte Chemie-International Edition, 40*(19), 3585–3588.

Munhuweyi, K., Lennox, C. L., Meitz-Hopkins, J. C., Caleb, O. J., & Opara, U. L. (2016). Major diseases of pomegranate (Punica granatum L.), their causes and management—A review. *Scientia Horticulturae, 211*, 126–139.

Murthy, S. K. (2007). Nanoparticles in modern medicine: state of the art and future challenges. *International Journal of Nanomedicine, 2*(2), 129–141.

Nanda, B. P., Rani, P., Paul, P., Aman, Ganti, S. S., & Bhatia, R. (2024). Recent trends and impact of localized surface plasmon resonance (LSPR) and surface-enhanced Raman spectroscopy (SERS) in modern analysis. *Journal of Pharmaceutical Analysis, 14*(11), 100959. 10.1016/j.jpha.2024.02.013

Naranjo-Ortiz, M. A., & Gabaldón, T. (2020). Fungal evolution: cellular, genomic and metabolic complexity. *Biological Reviews, 95*(5), 1198–1232.

Narendrababu, B. N., & Shishupala, S. (2017). Spectrophotometric detection of pigments from *Aspergillus* and *Penicillium* isolates. *J.Appl.Biol.Biotechnol, 5*, 53–58.

National Centers for Environmental Information. (2025). *NOAA National Centers for Environmental Information, Monthly Global Climate Report for January 2025.* .The United Kingdom Government. https://www.ncei.noaa.gov/access/metadata/landing-page/bin/iso?id=gov.noaa.ncdc:C00672 https://www.ncei.noaa.gov/access/monitoring/monthly-report/global/202501

Nayak, N. C., & Shin, K. (2006). Synthesis of L-phenylalanine stabilized gold nanoparticles and their thermal stability. *Journal of Nanoscience and Nanotechnology, 6*(11), 3512–3516.

Nerín, C., Tovar, L., Djenane, D., Camo, J., Salafranca, J., Beltrán, J. A., & Roncalés, P. (2006). Stabilization of beef meat by a new active packaging containing natural antioxidants. *Journal of Agricultural and Food Chemistry, 54*(20), 7840–7846.

Nguyen, B. T. T., Le, V. V., Nguyen, H. T. T., Nguyen, L. T., Tran, T. T. T., & Ngo, N. X. (2021). Nutritional requirements for the enhanced mycelial growth and yield performance of Trametes versicolor. *Journal of Applied Biology and Biotechnology*, *9*(1), 1-7.

Nguyen, T. A. N., Higa, T., Shiina, A., Utami, Y. D., & Hiruma, K. (2023). Exploring the roles of fungal-derived secondary metabolites in plant-fungal interactions. *Physiological and Molecular Plant Pathology, 125*, 102021. 10.1016/j.pmpp.2023.102021

Nisbet, M. C., Maibach, E., & Leiserowitz, A. (2011). Framing peak petroleum as a public health problem: Audience research and participatory engagement in the United States. *American Journal of Public Health, 101*(9), 1620–1626.

Niżnik, Ł, Noga, M., Kobylarz, D., Frydrych, A., Krośniak, A., Kapka-Skrzypczak, L., & Jurowski, K. (2024). Gold nanoparticles (AuNPs)—Toxicity, safety and green synthesis: A critical review. *International Journal of Molecular Sciences, 25*(7), 4057.

Noman, E., Al-Gheethi, A., Saphira Radin Mohamed, R. M., Talip, B., Othman, N., Hossain, S., Vo, D. N., & Alduais, N. (2022). Inactivation of fungal spores from clinical environment by silver bio-nanoparticles; optimization, artificial neural network model and mechanism. *Environmental Research, 204*, 111926. 10.1016/j.envres.2021.111926

Novodvorska, M., Hayer, K., Pullan, S. T., Wilson, R., Blythe, M. J., Stam, H., Stratford, M., & Archer, D. B. (2013). Transcriptional landscape of Aspergillus niger at breaking of conidial dormancy revealed by RNA-sequencing. *BMC Genomics, 14*, 1–18.

Omidi, M., Fatehinya, A., Farahani, M., Akbari, Z., Shahmoradi, S., Yazdian, F., Tahriri, M., Moharamzadeh, K., Tayebi, L., & Vashaee, D. (2017). 7 - Characterization of biomaterials. In L. Tayebi, & K. Moharamzadeh (Eds.), *Biomaterials for Oral and Dental Tissue Engineering* (pp. 97–115). Woodhead Publishing. 10.1016/B978-0-08-100961-1.00007-4

Ong, J. L., Appleford, M. R., & Mani, G. (2014). *Introduction to biomaterials: basic theory with engineering applications*. Cambridge university press.

Öztürk, K., Kaplan, M., & Çalış, S. (2024). Effects of nanoparticle size, shape, and zeta potential on drug delivery. *International Journal of Pharmaceutics, *, 124799.

Padhi, S., & Behera, A. (2022). Biosynthesis of silver nanoparticles: Synthesis, mechanism, and characterization. *Agri-Waste and Microbes for Production of Sustainable Nanomaterials* (pp. 397–440). Elsevier.

Parameshwaran, R., Sarı, A., Jalaiah, N., & Karunakaran, R. (2018). Chapter 13 - Applications of Thermal Analysis to the Study of Phase-Change Materials. *Handbook of Thermal Analysis and Calorimetry, 6*, 519–572. 10.1016/B978-0-444-64062-8.00005-X

Pardhiya, S., Priyadarshini, E., & Rajamani, P. (2020). In vitro antioxidant activity of synthesized BSA conjugated manganese dioxide nanoparticles. *SN Applied Sciences, 2*, 1–12.

Parida, V. K., Sikarwar, D., Majumder, A., & Gupta, A. K. (2022). An assessment of hospital wastewater and biomedical waste generation, existing legislations, risk assessment, treatment processes, and scenario during COVID-19. *Journal of Environmental Management, 308*, 114609.

Park, J., & Shumaker-Parry, J. S. (2014). Structural study of citrate layers on gold nanoparticles: role of intermolecular interactions in stabilizing nanoparticles. *Journal of the American Chemical Society, 136*(5), 1907–1921.

Passos, M. L., & Saraiva, M. L. M. (2019). Detection in UV-visible spectrophotometry: Detectors, detection systems, and detection strategies. *Measurement, 135*, 896–904.

Patil, A. S., Nille, O. S., Kolekar, G. B., Sohn, D., & Gore, A. H. (2021). UV-shielding biopolymer@ nanocomposites for sustainable packaging applications. *Sustainable Packaging,* , 177–202.

Patrulea, V., Ostafe, V., Borchard, G., & Jordan, O. (2015). Chitosan as a starting material for wound healing applications. *European Journal of Pharmaceutics and Biopharmaceutics, 97*, 417–426.

Penaloza, D. (2017). The role of biobased building materials in the climate impacts of construction. *Doctoral, School of Architecture and the Built Environment, Department of Civil and Architectural Engineering, Division of Building Materials, KTH Royal Institute of Technology,*

Perillo, B., Di Donato, M., Pezone, A., Di Zazzo, E., Giovannelli, P., Galasso, G., Castoria, G., & Migliaccio, A. (2020). ROS in cancer therapy: the bright side of the moon. *Experimental & Molecular Medicine, 52*(2), 192–203.

Pessoni, R. A., Tersarotto, C. C., Mateus, C. A., Zerlin, J. K., Simões, K., de Cássia L. Figueiredo-Ribeiro, R., & Braga, M. R. (2015). Fructose affecting morphology and inducing β-fructofuranosidases in Penicillium janczewskii. *SpringerPlus, 4*, 1–11.

Pestov, A., Nazirov, A., Modin, E., Mironenko, A., & Bratskaya, S. (2015). Mechanism of Au(III) reduction by chitosan: Comprehensive study with 13C and 1H NMR analysis of chitosan degradation products. *Carbohydrate Polymers, 117*, 70–77. 10.1016/j.carbpol.2014.09.030

Philip, D. (2010). Rapid green synthesis of spherical gold nanoparticles using Mangifera indica leaf. *Spectrochimica Acta Part A: Molecular and Biomolecular Spectroscopy, 77*(4), 807–810.

Pochanavanich, P., & Suntornsuk, W. (2002). Fungal chitosan production and its characterization. *Letters in Applied Microbiology, 35*(1), 17–21.

Pochapski, D. J., Carvalho dos Santos, C., Leite, G. W., Pulcinelli, S. H., & Santilli, C. V. (2021). Zeta potential and colloidal stability predictions for inorganic nanoparticle dispersions: Effects of experimental conditions and electrokinetic models on the interpretation of results. *Langmuir, 37*(45), 13379–13389.

Pulido-Chadid, K., Virtanen, E., & Geldmann, J. (2023). How effective are protected areas for reducing threats to biodiversity? A systematic review protocol. *Environmental Evidence, 12*(1), 18.

Pykett, I. L., Newhouse, J. H., Buonanno, F. S., Brady, T. J., Goldman, M. R., Kistler, J. P., & Pohost, G. M. (1982). Principles of nuclear magnetic resonance imaging. *Radiology, 143*(1), 157–168.

Quetzeri-Santiago, M. A., Castrejón-Pita, J. R., & Castrejón-Pita, A. A. (2020). On the analysis of the contact angle for impacting droplets using a polynomial fitting approach. *Experiments in Fluids, 61*, 1–13.

Rabiei, H., Farhang Dehghan, S., Montazer, M., Khaloo, S. S., & Koozekonan, A. G. (2022). UV protection properties of workwear fabrics coated with TiO2 nanoparticles. *Frontiers in Public Health, 10*, 929095.

Raghunathan, R., Nelluri, P., Rajendran, D., Pandiselvam, R., Thulasiraman, V., Sahoo, S. K., Pillai, S., Jerome, R. E., & Kothakota, A. (2024). Biodegradable products from renewable sources: impact on replacing single-use plastic for protecting the environment. *International Journal of Environmental Science and Technology, ,* 1–28.

Rai, A., Prabhune, A., & Perry, C. C. (2010). Antibiotic mediated synthesis of gold nanoparticles with potent antimicrobial activity and their application in antimicrobial coatings. *Journal of Materials Chemistry, 20*(32), 6789–6798.

Raja, H. A., Miller, A. N., Pearce, C. J., & Oberlies, N. H. (2017). Fungal identification using molecular tools: a primer for the natural products research community. *Journal of Natural Products, 80*(3), 756–770.

Raja, P. B., Munusamy, K. R., Perumal, V., & Ibrahim, M. N. M. (2022). 5 - Characterization of nanomaterial used in nanobioremediation. In H. M. N. Iqbal, M. Bilal & T. A. Nguyen (Eds.), *Nano-Bioremediation : Fundamentals and Applications* (pp. 57–83). Elsevier. 10.1016/B978-0-12-823962-9.00037-4

Rami, J. M., Patel, C. D., Patel, C. M., & Patel, M. V. (2021). Thermogravimetric analysis (TGA) of some synthesized metal oxide nanoparticles. *Materials Today: Proceedings, 43*, 655–659. 10.1016/j.matpr.2020.12.554

Rashdan, W., & Ashour, A. (2023). Mycelium-based materials: An alternative for sustainable interior design. Paper presented at the *Ideas, , 7*(1) 44–61.

Raval, N., Maheshwari, R., Kalyane, D., Youngren-Ortiz, S. R., Chougule, M. B., & Tekade, R. K. (2019). Chapter 10 - Importance of Physicochemical Characterization of Nanoparticles in Pharmaceutical Product Development. In R. K. Tekade (Ed.), *Basic Fundamentals of Drug Delivery* (pp. 369–400). Academic Press. 10.1016/B978-0-12-817909-3.00010-8

Renaudin, G., Gomes, S., Hagemann, H., Keller, L., & Yvon, K. (2004). Structural and spectroscopic studies on the alkali borohydrides MBH4 (M= Na, K, Rb, Cs). *Journal of Alloys and Compounds, 375*(1-2), 98–106.

Reyes, C., Fivaz, E., Sajó, Z., Schneider, A., Siqueira, G., Ribera, J., Poulin, A., Schwarze, F. W., & Nyström, G. (2024). 3D printed cellulose-based fungal battery. *ACS Sustainable Chemistry & Engineering, 12*(43), 16001–16011.

Ribeiro, H., Mucha, A. P., Almeida, C. M. R., & Bordalo, A. A. (2013). Bacterial community response to petroleum contamination and nutrient addition in sediments from a temperate salt marsh. *Science of the Total Environment, 458*, 568–576.

Riquelme, M., Aguirre, J., Bartnicki-García, S., Braus, G. H., Feldbrügge, M., Fleig, U., Hansberg, W., Herrera-Estrella, A., Kämper, J., & Kück, U. (2018). Fungal morphogenesis, from the polarized growth of hyphae to complex reproduction and infection structures. *Microbiology and Molecular Biology Reviews, 82*(2), 10.1128/mmbr. 00068–17.

Riseh, R. S., Vazvani, M. G., & Kennedy, J. F. (2023). The application of chitosan as a carrier for fertilizer: A review. *International Journal of Biological Macromolecules, 252*, 126483.

Roy, A., Sharma, A., Yadav, S., Jule, L. T., & Krishnaraj, R. (2021). Nanomaterials for remediation of environmental pollutants. *Bioinorganic Chemistry and Applications, 2021*(1), 1764647.

Saha, B., Saha, A., Das, P., Kakati, A., Banerjee, A., & Chattopadhyay, P. (2024). A comprehensive review of ultraviolet radiation and functionally modified textile fabric with special emphasis on UV protection. *Heliyon,*

Saldan, I., Dobrovetska, O., Sus, L., Makota, O., Pereviznyk, O., Kuntyi, O., & Reshetnyak, O. (2018). Electrochemical synthesis and properties of gold nanomaterials. *Journal of Solid State Electrochemistry, 22*, 637–656.

Sampath Kumar, T. S. (2013). Chapter 2 - Physical and Chemical Characterization of Biomaterials. In A. Bandyopadhyay, & S. Bose (Eds.), *Characterization of Biomaterials* (pp. 11–47). Academic Press. 10.1016/B978-0-12-415800-9.00002-4

Sánchez-Machado, D. I., López-Cervantes, J., Correa-Murrieta, M. A., Sánchez-Duarte, R. G., Cruz-Flores, P., & de la Mora-López, G. S. (2019). Chitosan. *Nonvitamin and nonmineral nutritional supplements* (pp. 485–493). Elsevier.

Sani, A., Cao, C., & Cui, D. (2021). Toxicity of gold nanoparticles (AuNPs): A review. *Biochemistry and Biophysics Reports, 26*, 100991.

Sarma, G. K., Sen Gupta, S., & Bhattacharyya, K. G. (2019). Nanomaterials as versatile adsorbents for heavy metal ions in water: a review. *Environmental Science and Pollution Research, 26*, 6245–6278.

Scherrer, P. (1918). Determination of the size and internal structure of colloidal particles using X-rays. *Nachr.Ges.Wiss.Göttingen, 2*, 98–100.

Schoder, K. A., Krümpel, J., Müller, J., & Lemmer, A. (2024). Effects of Environmental and Nutritional Conditions on Mycelium Growth of Three Basidiomycota. *Mycobiology, 52*(2), 124–134.

Schritt, H., Vidi, S., & Pleissner, D. (2021). Spent mushroom substrate and sawdust to produce mycelium-based thermal insulation composites. *Journal of Cleaner Production, 313*, 127910. 10.1016/j.jclepro.2021.127910

Schunke, C., Pöggeler, S., & Nordzieke, D. E. (2020). A 3D printed device for easy and reliable quantification of fungal chemotropic growth. *Frontiers in Microbiology, 11*, 584525.

Scimeca, M., Bischetti, S., Lamsira, H. K., Bonfiglio, R., & Bonanno, E. (2018). Energy Dispersive X-ray (EDX) microanalysis: A powerful tool in biomedical research and diagnosis. *European Journal of Histochemistry: EJH, 62*(1)

Schumacher, J., de Larrinoa, I. F., & Tudzynski, B. (2008). Calcineurin-responsive zinc finger transcription factor CRZ1 of *Botrytis cinerea* is required for growth, development, and full virulence on bean plants. *Eukaryotic Cell, 7*(4), 584–601.

Senthilkumar, M., Amaresan, N., Sankaranarayanan, A., Senthilkumar, M., Amaresan, N., & Sankaranarayanan, A. (2021). No title. *Extraction of Fungal Chitinase Enzyme,*

Shaheen, T. I., Salem, S. S., & Zaghloul, S. (2019). A new facile strategy for multifunctional textiles development through in situ deposition of SiO2/TiO2 nanosols hybrid. *Industrial & Engineering Chemistry Research, 58*(44), 20203–20212.

Shankar, M. P., Hamza, A., Khalad, A., Shanthi, G., Kuppireddy, S., & Kumar, D. S. (2024). Engineering mushroom mycelium for a greener built environment: Advancements in mycelium-based biocomposites and bioleather. *Food Bioscience*, 105577.

Sharma, M., Verma, S., Chauhan, G., Arya, M., & Kumari, A. (2024). Mycelium-based biocomposites: synthesis and applications. *Environmental Sustainability, 7*(3), 265–278.

Sharma, R., Raghav, R., Priyanka, K., Rishi, P., Sharma, S., Srivastava, S., & Verma, I. (2019). Exploiting chitosan and gold nanoparticles for antimycobacterial activity of in silico identified antimicrobial motif of human neutrophil peptide-1. *Scientific Reports, 9*(1), 7866.

Sharma, R., Jafari, S. M., & Sharma, S. (2020). Antimicrobial bio-nanocomposites and their potential applications in food packaging. *Food Control, 112*, 107086.

Sharma, S., & Bhattacharya, A. (2017). Drinking water contamination and treatment techniques. *Applied Water Science, 7*(3), 1043–1067.

Shin, H., Ro, H., Kawauchi, M., & Honda, Y. (2025). Review on mushroom mycelium-based products and their production process: from upstream to downstream. *Bioresources and Bioprocessing, 12*(1), 1–21.

Silva, L. I., Perez-Gramatges, A., Larrude, D. G., Almeida, J. M., Aucelio, R. Q., & da Silva, A. R. (2021). Gold nanoparticles produced using NaBH4 in absence and in the presence of one-tail or two-tail cationic surfactants: Characteristics and optical responses induced by aminoglycosides. *Colloids and Surfaces A: Physicochemical and Engineering Aspects, 614*, 126174.

Simpson, A. J., Simpson, M. J., & Soong, R. (2012). No title. *Nuclear Magnetic Resonance Spectroscopy and its Key Role in Environmental Research,*

Singh, A. K. (2016). Chapter 4 - Experimental Methodologies for the Characterization of Nanoparticles. In A. K. Singh (Ed.), *Engineered Nanoparticles* (pp. 125–170). Academic Press. 10.1016/B978-0-12-801406-6.00004-2

Singh, M. K., & Singh, A. (2022). Chapter 14 - Nuclear magnetic resonance spectroscopy. In M. K. Singh, & A. Singh (Eds.), *Characterization of Polymers and Fibres* (pp. 321–339). Woodhead Publishing. 10.1016/B978-0-12-823986-5.00011-7

Sivaprasad, S., Byju, S. K., Prajith, C., Shaju, J., & Rejeesh, C. R. (2021). Development of a novel mycelium bio-composite material to substitute for polystyrene in packaging applications. *Materials Today: Proceedings, 47*, 5038–5044.

Sivashankari, P. R., & Prabaharan, M. (2017). Deacetylation modification techniques of chitin and chitosan. *Chitosan Based Biomaterials Volume 1* (pp. 117–133). Elsevier.

Soldado, A., Barrio, L. C., Díaz-Gonzalez, M., de la Escosura-Muñiz, A., & Costa-Fernandez, J. M. (2022). Chapter One - Advances in quantum dots as diagnostic tools. *Advances in Clinical Chemistry, 107*, 1–40. 10.1016/bs.acc.2021.07.001

Speight, J. G. (2020). Chapter 12 - Petrochemicals. In J. G. Speight (Ed.), *Handbook of Industrial Hydrocarbon Processes (Second Edition)* (pp. 511–552). Gulf Professional Publishing. 10.1016/B978-0-12-809923-0.00012-6

Steinberg, G. (2007). Hyphal growth: a tale of motors, lipids, and the Spitzenkorper. *Eukaryotic Cell, 6*(3), 351–360.

Stetefeld, J., McKenna, S. A., & Patel, T. R. (2016). Dynamic light scattering: a practical guide and applications in biomedical sciences. *Biophysical Reviews, 8*, 409–427.

Su, Y., Qi, Y., & Cai, L. (2012). Induction of sporulation in plant pathogenic fungi. *Mycology, 3*(3), 195–200.

Sugunan, A., Thanachayanont, C., Dutta, J., & Hilborn, J. G. (2005). Heavy-metal ion sensors using chitosan-capped gold nanoparticles. *Science and Technology of Advanced Materials, 6*(3-4), 335.

Sun, W. (2024). Fungal mycelia: From innovative materials to promising products: Insights and challenges. *Biointerphases, 19*(1)

Suryanarayanan, T. S., & Azevedo, J. L. (2023). From forest to plantation: a brief history of the rubber tree. *Indian Journal of History of Science, 58*(1), 74–78.

Suvarna, S., Das, U., Kc, S., Mishra, S., Sudarshan, M., Saha, K. D., Dey, S., Chakraborty, A., & Narayana, Y. (2017). Synthesis of a novel glucose capped gold nanoparticle as a better theranostic candidate. *PloS One, 12*(6), e0178202.

Sydor, M., Cofta, G., Doczekalska, B., & Bonenberg, A. (2022). Fungi in mycelium-based composites: usage and recommendations. *Materials, 15*(18), 6283.

Sylvestre, J., Kabashin, A. V., Sacher, E., Meunier, M., & Luong, J. H. (2004). Stabilization and size control of gold nanoparticles during laser ablation in aqueous cyclodextrins. *Journal of the American Chemical Society, 126*(23), 7176–7177.

Tacer-Caba, Z., Varis, J. J., Lankinen, P., & Mikkonen, K. S. (2020). Comparison of novel fungal mycelia strains and sustainable growth substrates to produce humidity-resistant biocomposites. *Materials & Design, 192*, 108728.

Tavvabi-Kashani, N., Hasanpour, M., Rahimi, V. B., Vahdati-Mashhadian, N., & Askari, V. R. (2024). Pharmacodynamic, pharmacokinetic, toxicity, and recent advances in Eugenol's potential benefits against natural and chemical noxious agents: A mechanistic review. *Toxicon, 238*, 107607.

The United Kingdom Government. (2016). *The Water Supply (Water Quality) Regulations 2016.* .The United Kingdom Government. https://www.legislation.gov.uk/uksi/2016/614/contents

Thombare, N., Mahto, A., Singh, D., Chowdhury, A. R., & Ansari, M. F. (2023). Comparative FTIR characterization of various natural gums: a criterion for their identification. *Journal of Polymers and the Environment, 31*(8), 3372–3380.

Tišma, M., Žnidaršič-Plazl, P., Šelo, G., Tolj, I., Šperanda, M., Bucić-Kojić, A., & Planinić, M. (2021). *Trametes versicolor* in lignocellulose-based bioeconomy: State of the art, challenges and opportunities. *Bioresource Technology, 330*, 124997.

Tissue, B. M. (2002). Ultraviolet and visible absorption spectroscopy. *Characterization of Materials,*

Titus, D., James Jebaseelan Samuel, E., & Roopan, S. M. (2019). Chapter 12 - Nanoparticle characterization techniques. In A. K. Shukla, & S. Iravani (Eds.), *Green Synthesis, Characterization and Applications of Nanoparticles* (pp. 303–319). Elsevier. 10.1016/B978-0-08-102579-6.00012-5

Tlotleng, N., Vetten, M. A., Keter, F. K., Skepu, A., Tshikhudo, R., & Gulumian, M. (2016). Cytotoxicity, intracellular localization and exocytosis of citrate capped and PEG functionalized gold nanoparticles in human hepatocyte and kidney cells. *Cell Biology and Toxicology, 32*, 305–321.

Tomaszewska, E., Soliwoda, K., Kadziola, K., Tkacz-Szczesna, B., Celichowski, G., Cichomski, M., Szmaja, W., & Grobelny, J. (2013). Detection limits of Dls and Uv-Vis spectroscopy in characterization of polydisperse nanoparticles colloids. *Journal of Nanomaterials, 2013*(1), 313081.

Tovar-Herrera, O. E., Martha-Paz, A. M., Pérez-LLano, Y., Aranda, E., Tacoronte-Morales, J. E., Pedroso-Cabrera, M. T., Arévalo-Niño, K., Folch-Mallol, J. L., & Batista-García, R. A. (2018). *Schizophyllum commune*: An unexploited source for lignocellulose degrading enzymes. *MicrobiologyOpen, 7*(3), e00637.

Tranter, G. E. (2017). FTIR spectroscopy of aqueous solutions.

Triunfo, M., Tafi, E., Guarnieri, A., Salvia, R., Scieuzo, C., Hahn, T., Zibek, S., Gagliardini, A., Panariello, L., & Coltelli, M. B. (2022). Characterization of chitin and chitosan derived from Hermetia illucens, a further step in a circular economy process. *Scientific Reports, 12*(1), 6613.

Turkevich, J., Stevenson, P. C., & Hillier, J. (1953). The formation of colloidal gold. *The Journal of Physical Chemistry, 57*(7), 670–673.

Turkevich, J., Stevenson, P. C., & Hillier, J. (1951). A study of the nucleation and growth processes in the synthesis of colloidal gold. *Discussions of the Faraday Society, 11*, 55–75.

Turrà, D., Nordzieke, D., Vitale, S., El Ghalid, M., & Di Pietro, A. (2016). Hyphal chemotropism in fungal pathogenicity. *Seminars in Cell & Developmental Biology, 57*, 69–75. 10.1016/j.semcdb.2016.04.020

Van Wylick, A., Monclaro, A. V., Elsacker, E., Vandelook, S., Rahier, H., De Laet, L., Cannella, D., & Peeters, E. (2021). A review on the potential of filamentous fungi for microbial self-healing of concrete. *Fungal Biology and Biotechnology, 8*(1), 16.

Vazquez Santiago, J., Hata, H., Martinez-Noriega, E. J., & Inoue, K. (2024). Ozone trends and their sensitivity in global megacities under the warming climate. *Nature Communications, 15*(1), 10236.

Vechia, I. C. D., Steiner, B. T., Freitas, M. L., dos Santos Pedroso Fidelis, G., Galvani, N. C., Ronchi, J. M., Possato, J. C., Fagundes, M. Í, Rigo, F. K., & Feuser, P. E. (2020). Comparative cytotoxic effect of citrate-capped gold nanoparticles with different sizes on noncancerous and cancerous cell lines. *Journal of Nanoparticle Research, 22*, 1–11.

Velázquez-Martínez, S., Silva-Martínez, S., Pineda-Arellano, C. A., Jiménez-González, A., Salgado-Tránsito, I., Morales-Pérez, A. A., & Peña-Cruz, M. I. (2018). Modified sol-gel/hydrothermal method for the synthesis of microsized TiO2 and iron-doped TiO2, its characterization and solar photocatalytic activity for an azo dye degradation. *Journal of Photochemistry and Photobiology A: Chemistry, 359*, 93–101. 10.1016/j.jphotochem.2018.04.002

Velgosova, O., Varga, P., Ivánová, D., Lisnichuk, M., & Hudá, M. (2024). Effect of Storage Conditions on the Stability of Colloidal Silver Solutions Prepared by Biological and Chemical Methods. *Metals, 14*(5), 513.

Vercesi, A., Locci, R., & Prosser, J. I. (1997). Growth kinetics of *Botrytis cinerea* on organic acids and sugars in relation to colonization of grape berries. *Mycological Research, 101*(2), 139–142.

Vikrant, K., & Kim, K. (2019). Nanomaterials for the adsorptive treatment of Hg (II) ions from water. *Chemical Engineering Journal, 358*, 264–282.

Vincent, J. B. (2016). Chromium: Properties and Determination. In B. Caballero, P. M. Finglas & F. Toldrá (Eds.), *Encyclopedia of Food and Health* (pp. 114–118). Academic Press. 10.1016/B978-0-12-384947-2.00161-6

Wang, F., Zhang, L., Zhou, J., Rengel, Z., George, T. S., & Feng, G. (2022). Exploring the secrets of hyphosphere of arbuscular mycorrhizal fungi: processes and ecological functions. *Plant and Soil*, *481*(1), 1-22.

Wang, H., Tao, J., Wu, Z., Weiland, K., Wang, Z., Masania, K., & Wang, B. (2024). Fabrication of living entangled network composites enabled by mycelium. *Advanced Science, 11*(24), 2309370.

Wang, L., Ma, W., Xu, L., Chen, W., Zhu, Y., Xu, C., & Kotov, N. A. (2010). Nanoparticle-based environmental sensors. *Materials Science and Engineering: R: Reports, 70*(3-6), 265–274.

Wang, X., Shi, F., Wösten, H., Hektor, H., Poolman, B., & Robillard, G. T. (2005). The SC3 hydrophobin self-assembles into a membrane with distinct mass transfer properties. *Biophysical Journal, 88*(5), 3434–3443.

Wani, M. Y., Malik, M. A., Wani, M. Y., & Malik, M. A. (2021). Chemistry of Gold. *Gold and its Complexes in Anticancer Chemotherapy,* , 69–79.

Wawata, I. G., & Fabiyi, O. A. (2024). Sustainable application of nanomaterials in the removal of heavy metals from water. *Sustainable Nanomaterials: Synthesis and Environmental Applications* (pp. 21–44). Springer.

Whabi, V., Yu, B., & Xu, J. (2024). From nature to design: tailoring pure Mycelial materials for the needs of tomorrow. *Journal of Fungi, 10*(3), 183.

Wilschefski, S. C., & Baxter, M. R. (2019). Inductively coupled plasma mass spectrometry: introduction to analytical aspects. *The Clinical Biochemist Reviews, 40*(3), 115.

World Health Organization. (2011). Guidelines for drinking-water quality. *WHO Chronicle, 38*(4), 104–108.

World Health Organization. (2017). *Mercury in Drinking-water Background document for development of WHO Guidelines for Drinking-water Quality.* . https://www.who.int/docs/default-source/wash-documents/wash-chemicals/mercury-background-document.pdf?sfvrsn=9b117325_4

Wu, T., Zivanovic, S., Draughon, F. A., Conway, W. S., & Sams, C. E. (2005). Physicochemical properties and bioactivity of fungal chitin and chitosan. *Journal of Agricultural and Food Chemistry, 53*(10), 3888–3894.

Wu, N., Zhang, J., Ou, W., Chen, Y., Wang, R., Li, K., ... & Huang, H. (2021). Transcriptome analysis of Rhizopus oryzae seed pellet formation using triethanolamine. *Biotechnology for Biofuels*, *14*(1), 230.

Wunderlich, B. (2001). Thermal Analysis. In K. H. J. Buschow, R. W. Cahn, M. C. Flemings, B. Ilschner, E. J. Kramer, S. Mahajan & P. Veyssière (Eds.), *Encyclopedia of Materials: Science and Technology* (pp. 9134–9141). Elsevier. 10.1016/B0-08-043152-6/01648-X

Xiang, J. (2018). Foutier Transform Infrared Spectroscopy Instrumentation and Integration with Thermogravimetry.

Xu, L., Wu, X., & Zhu, J. (2008). Green preparation and catalytic application of Pd nanoparticles. *Nanotechnology, 19*(30), 305603.

Yan, D., Li, Y., Liu, Y., Li, N., Zhang, X., & Yan, C. (2021). Antimicrobial properties of chitosan and chitosan derivatives in the treatment of enteric infections. *Molecules, 26*(23), 7136.

Yang, H., Hou, J., Chen, V., & Xu, Z. (2016). Janus membranes: exploring duality for advanced separation. *Angewandte Chemie International Edition, 55*(43), 13398–13407.

Yang, J., Li, H., Chen, Z., He, A., Zhong, Q., & Xu, Z. (2019). Janus membranes with controllable asymmetric configurations for highly efficient separation of oil-in-water emulsions. *Journal of Materials Chemistry A, 7*(13), 7907–7917.

Yang, M., Liu, W., Jiang, C., He, S., Xie, Y., & Wang, Z. (2018). Fabrication of superhydrophobic cotton fabric with fluorinated TiO2 sol by a green and one-step sol-gel process. *Carbohydrate Polymers, 197*, 75–82. 10.1016/j.carbpol.2018.05.075

Yannopoulos, J. C. (2012). *The extractive metallurgy of gold*. Springer Science & Business Media.

Yu, R., Li, M., Wang, Y., Bai, X., Chen, J., Li, X., Wang, H., & Zhang, H. (2021). Chemical investigation of a co-culture of *Aspergillus fumigatus* D and Fusarium oxysporum R1. *Rec.Nat.Prod, 15*, 130–135.

Yuan, Y., Li, H., Leite, W., Zhang, Q., Bonnesen, P. V., Labbé, J. L., Weiss, K. L., Pingali, S. V., Hong, K., & Urban, V. S. (2021). Biosynthesis and characterization of deuterated chitosan in filamentous fungus and yeast. *Carbohydrate Polymers, 257*, 117637.

Zare, Y. (2016). Study of nanoparticles aggregation/agglomeration in polymer particulate nanocomposites by mechanical properties. *Composites Part A: Applied Science and Manufacturing, 84*, 158–164. 10.1016/j.compositesa.2016.01.020

Zayat, M., Garcia-Parejo, P., & Levy, D. (2007). Preventing UV-light damage of light sensitive materials using a highly protective UV-absorbing coating. *Chemical Society Reviews, 36*(8), 1270–1281.

Zaynab, M., Al-Yahyai, R., Ameen, A., Sharif, Y., Ali, L., Fatima, M., Khan, K. A., & Li, S. (2022). Health and environmental effects of heavy metals. *Journal of King Saud University-Science, 34*(1), 101653.

Zeng, M., Gao, H., Wu, Y., Fan, L., & Li, A. (2010). Preparation and characterization of nanocomposite films from chitin whisker and waterborne poly (ester-urethane) with or without ultra-sonification treatment. *Journal of Macromolecular Science, Part A: Pure and Applied Chemistry, 47*(8), 867–876.

Zhang, D., Wang, L., Qian, H., & Li, X. (2016). Superhydrophobic surfaces for corrosion protection: a review of recent progresses and future directions. *Journal of Coatings Technology and Research, 13*, 11–29.

Zhang, H., Huang, Y., Wang, C., Wang, L., & Shao, J. (2016). Properties of anti-UV-finished cotton fabrics cured by blue light irradiation. *Fibers and Polymers, 17*, 396–401.

Zulkifli, S. N., Rahim, H. A., & Lau, W. (2018). Detection of contaminants in water supply: A review on state-of-the-art monitoring technologies and their applications. *Sensors and Actuators B: Chemical, 255*, 2657–2689.

<h1 style="text-align: center;">Special Contributions and Achievements</h1>

This gives an overview of contributions, awards, and honours during the PhD program. These achievements highlight my dedication to advancing research in my field and my commitment to academic excellence. Additionally, my efforts in promoting social development and sustainability have been acknowledged, reflecting my commitment to creating a positive impact beyond academia.

HONOURS AND AWARDS

1. **The British Mycological Society- Eunice Jones Postgraduate Fund (£1000). 2024**
   Conference Grant for participation in the International Mycology Conference (IMC12), Maastricht Netherlands.

2. **Howard Eggins Early Career Mycologist Award (£50).   2023**
   Best Talk (2nd Prize), 2023 British Mycological Society General Conference, Newcastle

3. **The Kofi Annan Foundation Changemaker Award (CHF 3000).   2022**
   A special award recognizing highly impactful young changemakers around the world

JOURNAL PUBLICATIONS

A. *Academic publications*

1. **Afolayan, J. S.,** Sadaf, A., & Perry, C. C. (2024). Developing gold nanoparticle mycelial composites: Effect of nanoparticle surface functionality on *Aspergillus niger* viability and cell wall biochemistry. *Current Research in Biotechnology*, 7, 100185. https://doi.org/10.1016/j.crbiot.2024.100185.

2. **Afolayan, J. S**., Varney, A. M., Thomas, J. C., McLean, S., & Perry, C. C. (2024). A rapid microwave approach for 'one-pot' synthesis of antibiotic conjugated silver nanoparticles with antimicrobial activity against multi-drug-resistant bacterial pathogens. *Colloids and Surfaces B: Biointerfaces*, 114280. https://doi.org/10.1016/j.colsurfb.2024.114280

B. **Governance and policy publications**

1. Cutrupi, F., Osinska, A. D., Rahmatika, I., **Afolayan, J. S.,** Vystavna, Y., Mahjoub, O., ... & Muziasari, W. (2024). Towards monitoring the invisible threat: a global approach for tackling AMR in water resources and environment. *Frontiers in Water*, 6, 1362701. https://doi.org/10.3389/frwa.2024.1362701

2. Hill, R., Pickford, R., Abdelmalak, E., **Afolayan, S.,** Brittain, M., Nadeem, L., Stock, C. and Stolz, R. (2023). Mapping the Health and Wellbeing Across the Firefighting Career and Assessing the Current Demands. Nottingham: Nottingham Trent University. Available here

CONFERENCE PRESENTATIONS (ORAL AND POSTER)

1. **Afolayan JS., Perry CC. (2024). "**Sustainable Solutions for Heavy Metal Filtration and Surface Wettability: Harnessing Nanomaterials and Fungal Structures to generate functional composites". Poster Presentation: Midlands Inorganic Discussions, Nottingham Trent University, 2024.

2. **Afolayan JS., Perry CC. (2024). "**Sustainable Solutions for Heavy Metal Filtration and Surface Wettability: Harnessing Nanomaterials and Fungal Structures to generate functional composites". Poster Presentation: 12th International Mycological Society Conference, Maastricht Netherlands (IMC 12).

3. **Afolayan JS., Perry CC. (2023). "Engineering functional fungal materials with bioactive nanoparticles; a natural interaction process for fabricating reusable heavy metal scavenger in waste-water purification".** Oral Presentation: British Mycology Conference; Fungal Interactions, Newcastle, United Kingdom.

4. **Afolayan JS., Perry CC. (2023). Nottingham Trent University** School of Science and Technology Research (STAR) Conference 2023. Oral Presentation: Directional Growth Control of *Aspergillus niger* and *Botrytis cinerea* using Bioactive Gold Nanoparticles.

5. **Afolayan JS**, Djalia U (2023). Hybridization of water response; a new paradigm in modeling water sustainability in Africa. Oral Presentation (virtual): The Radboud Conference on Earth System Governance; Bridging science and society for sustainability transformations, *(2023)*.

6. **Afolayan JS., Perry CC. (2023). "Engineering functional fungal materials using bioactive nanoparticles". Oral presentation:** Nottingham Trent University Post Graduate Interdisciplinary Research Conference, N**ottingham United Kingdom.**

7. **Afolayan JS., Perry CC. (2022). "Engineering functional fungal materials using bioactive nanoparticles". Oral presentation:** Novel functionalization with gold nanomaterials, for chemotropic, antibacterial, and photothermal applications, Nottingham, United Kingdom.

8. **Afolayan JS. (2022).** Modelling Intergenerational Dialogue and Capacity Development for Young Water Professionals (YWPs) and Entrepreneurs (YWEs) in

Africa; A Sustainable approach. In: [Conference proceedings of the 21st African Water Association (AfWA) Congress & Exhibition and the 7th International Faecal Sludge Management, held on 19th- 23rd February 2023, Abidjan Côte d'Ivoire.](#)

PROFESSIONAL TRAINING, WORKSHOPS AND CERTIFICATIONS

1. **Associate Fellow of the Higher Education Academy (AFHEA) 2025**
   Education Qualification for teaching and supporting learning in higher education.
2. **United Nations Staff College 2023**
   [Certificate of completion United Nations Summer Academy](#)
3. **Nottingham Trent University Green Academy 2023**
   [Sustainability in Practice Certificate](#)
4. **Nottingham Trent University 2023**
   [PGR Lecturer Development Program](#)

ROLES AND GLOBAL DEVELOPMENT CONTRIBUTIONS

1. Postgraduate Member of the [Co(l)laboratory](#) PhD applicants interview panels **2025.**
   Provided feedback on Interviews, leading to candidate selection.
2. [STEM Learning](#) Supported by UKRI August **2024 - Date**
   Ambassador, Climate Trajectory
3. Global Chapters Facilitator, World Youth Parliament for Water **2019 - 2024**
   [Coordinated National/Regional Chapters Creation and Management](#)
4. Planning Committee, and British Mycological Society Rep **2024**
   [Early Career Mycologist Symposium, International Mycology Conference, Netherlands.](#)
5. International Secretariat for Water delegate, UN-Water Conference, New York **2023**
   Contributed to the global youth movement but didn't attend onsite due to a US visa delay.
6. Panellist UN DESA Global Policy Dialogue (UNTV). **2023**
   [Indigenous and Youth Solutions for Clean Water](#)
7. Contributor, Innovation Workshop on Water Quality, Netherlands. **2023**
   [Topic: Routine Monitoring of Antimicrobial Resistance in Water (WMO and UNEP).](#)
8. Nottingham Trent University Green Academy, UK. **2023**
   Student Sustainability Consultant, the Green Game Jam 2023.
9. UNICEF Youth Delegate and Panelist Dushanbe Water Process, Tajikistan. **2022**

10. Contributor, Water Generation Summit, organized by the International Secretariat for Water and Solidarity Water Europe (ISW-SWE) France.   2022

    Topic: Strategic evaluation of the water pathway with the International Secretariat for Water.

List of Appendix

Table 2.1: Properties of Mycelia Under Different Drying Conditions

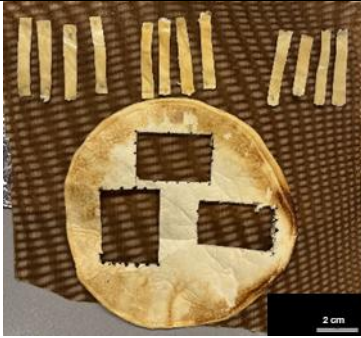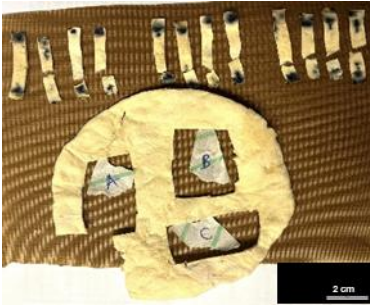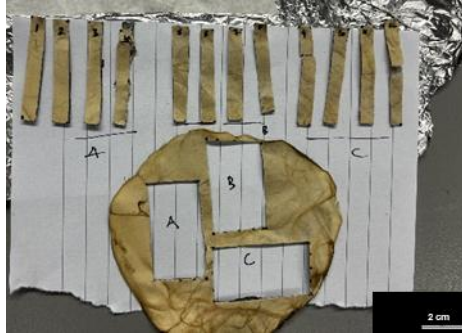| Drying condition	Dried Sample	Properties of sample
R. oryzae		
Air dry: 25 °C 8 h		The inner surface of the mycelia in contact with the Teflon is highly glossy, featuring a thin, shiny layer. The mycelia have turned a very light yellow, appearing thick yet fragile, and tend to break parallel to the inner surface, primarily around the middle area. No visible cracks.
Oven dry: 90 °C. 4 h		The inner surface in contact with the Teflon is highly glossy, featuring a thin, shiny layer. The mycelia have turned a deep yellow, appearing thicker but still fragile, and tend to break parallel to the inner surface, mostly near the end of the strip. There are no visible cracks.
Convectional freezing: -45 °C (8 h): then freeze dry		The mycelia retain their colour upon drying, exhibiting a fine surface with no visible cracks. They appear stretchier and tend to break parallel to the surface, primarily around the middle.
Cryogen freezing: -196 °C (3 min): then freeze dry		The colour remains intact upon drying, with a fine, rough surface and visible cracks around the outer edges. The texture is woolly and somewhat stretchy, tending to break parallel to the surface, primarily around the middle.

M. rouxii		
Air dry: 25 °C 8 h		The inner surface has a glossy appearance, with the mycelia becoming thin yet stretchy. The mycelia predominantly break parallel to the middle, with no visible cracks.
Oven dry: 90 °C. 4 h		The inner surface has a somewhat glossy appearance, with the mycelia becoming thick but less stretchy. The mycelia predominantly break parallel to the middle, with no visible cracks.
Convectional freezing: -44 °C (8 h): then freeze dry		The mycelia retain their colour upon drying, featuring a fine surface with no observable cracks. They are firm and predominantly break parallel to the middle.
Cryogen freezing: -196 °C (3 min): then freeze dry		The colour remains intact upon drying, with a fine surface and no observable cracks around the outer surface. It breaks parallel to the middle, with no visible cracks.

Table 2.2: Mechanical; Response of Mycelia under Different Drying Conditions

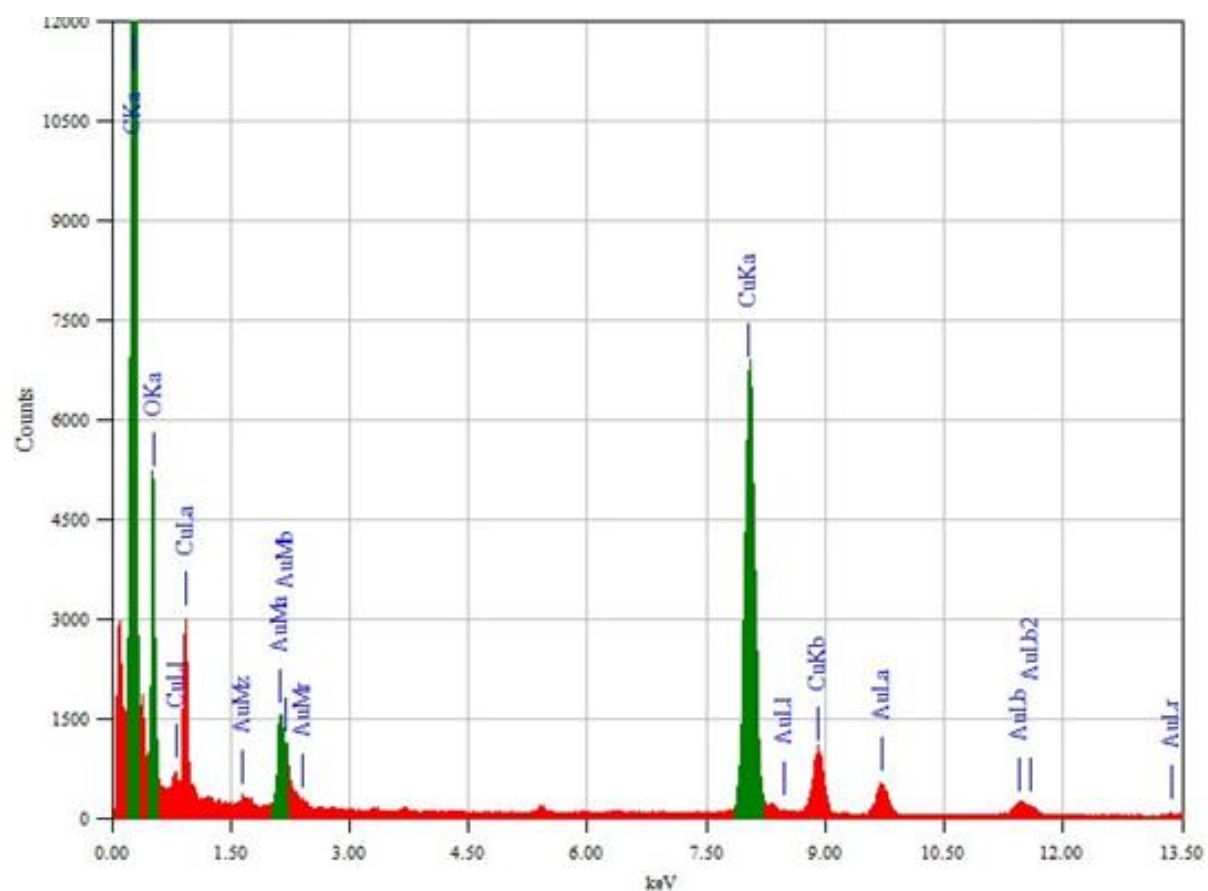| Drying condition	Sample mapping and breaking pattern
R. oryzae	
Air dry: 25 °C 8 h	
Oven dry: 90 °C. 4 h	
Convectional freezing: -45 °C (8 h): then freeze dry	
Cryogen freezing: -196 °C (3 min): then freeze dry	
M. rouxii	

| Air dry: 25 ºC 8 h | |
Oven dry: 90 ºC. 4 h	
Convectional freezing: -44 ºC (8 h): then freeze dry	
Cryogen freezing: -196 ºC (3 min): then freeze dry	

Appendix 3.1

Appendix Figure 3.1: Representative Energy Dispersive X-ray (EDX) result showing the Au peaks on typical AuNPs. Peaks from copper are due to the copper grids, and carbon peaks are from the carbon coating.
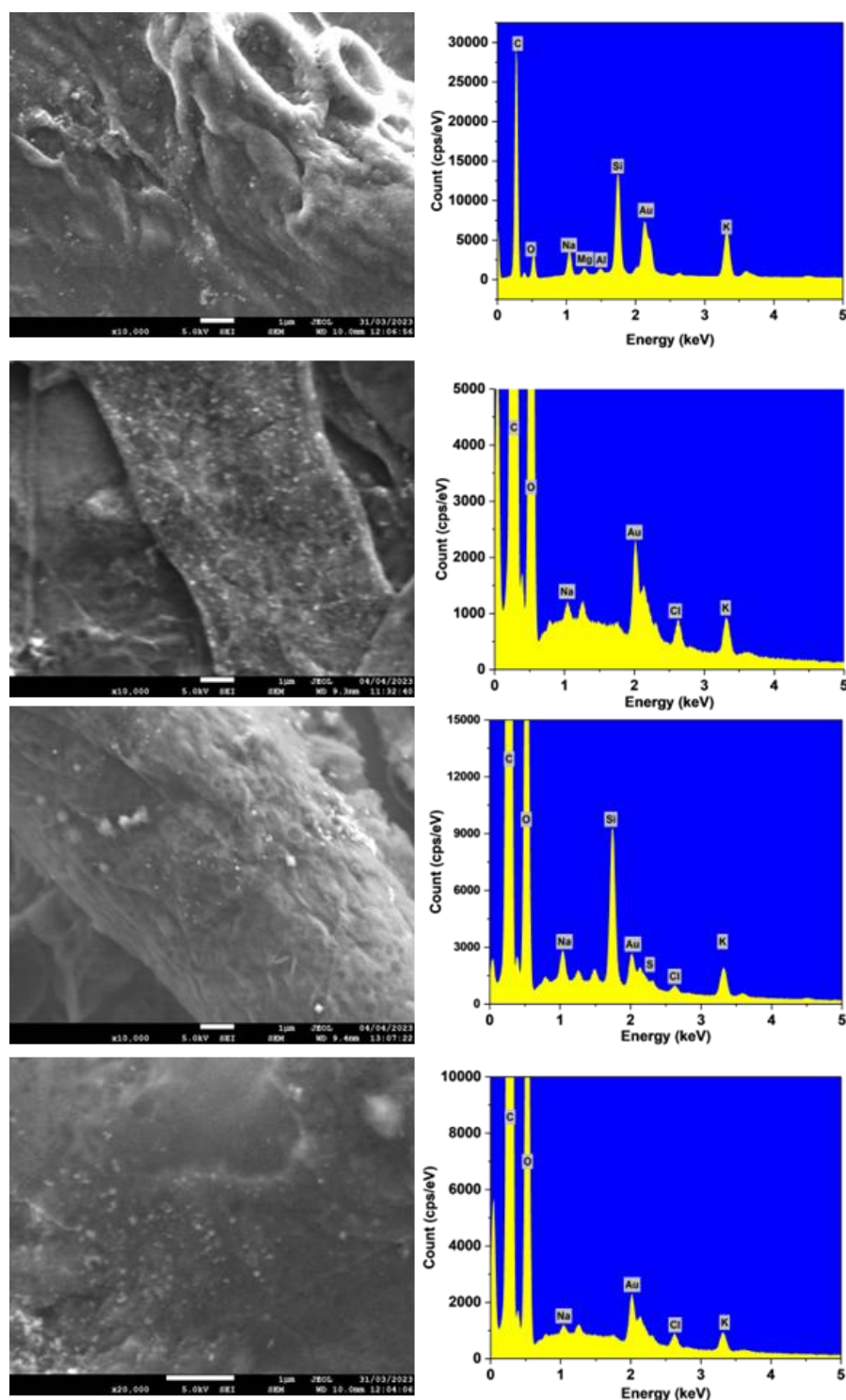
Appendix 4

The SEM/EDX images show the distribution of nanoparticles and elemental mappings on *A. niger* mycelia after either 7 or 10 days of growth. These images were taken with nitrate or glutamine as the nitrogen source.
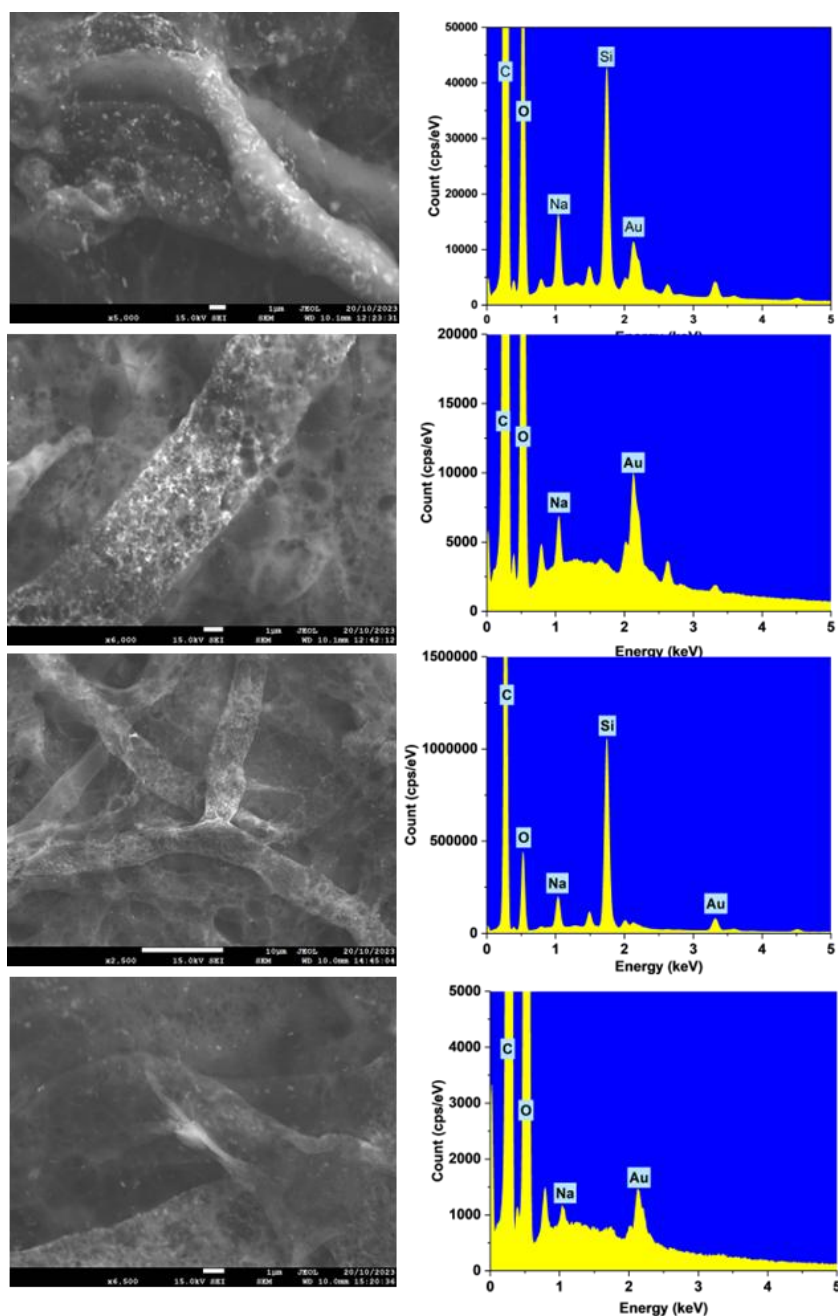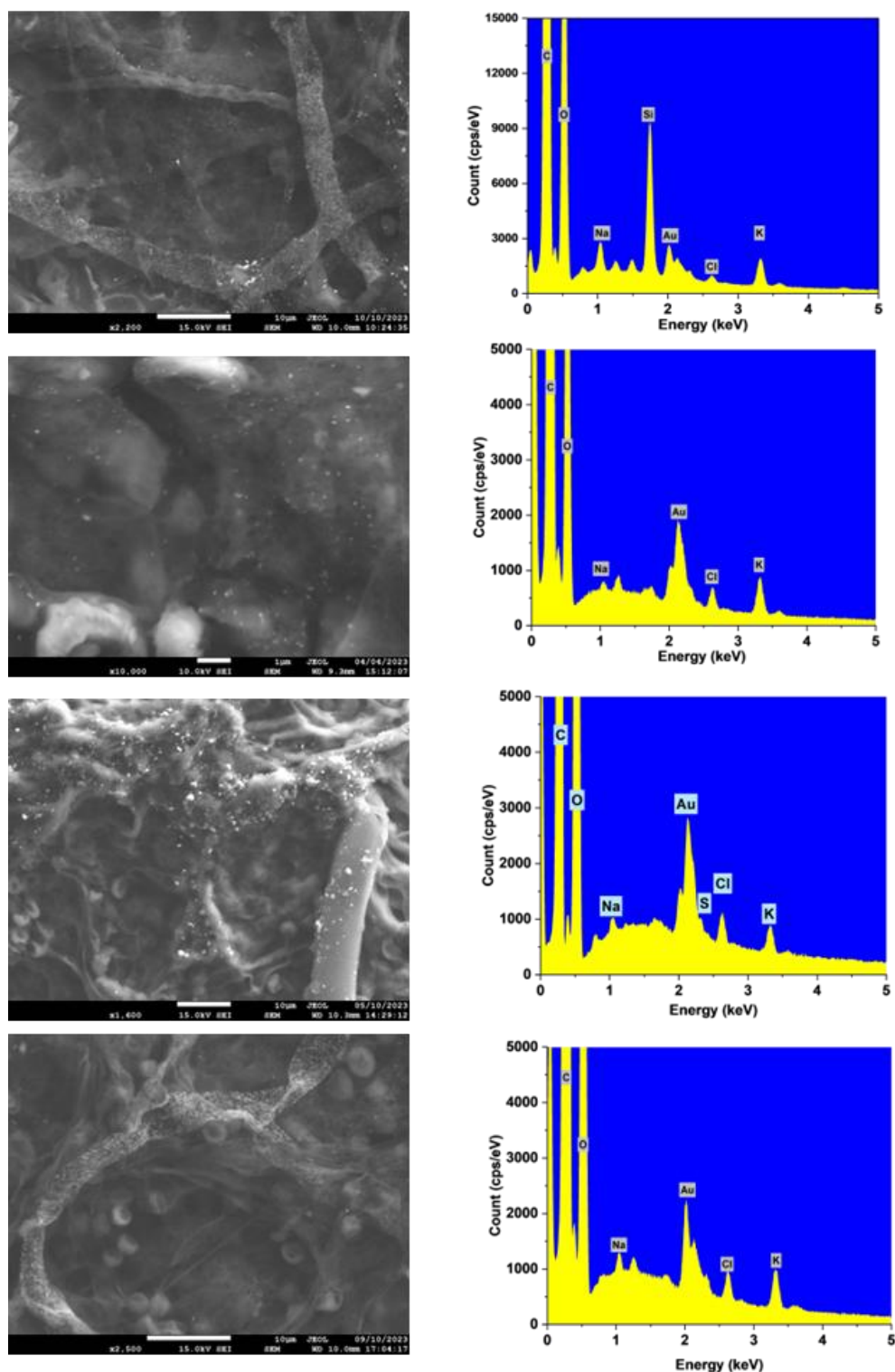

Appendix Figure 4.1A: Representative scanning electron microscopy (SEM) image, and elemental analysis (EDX) showing the distribution of (A): NaBH$_4$-AuNPs; (B): Glc-AuNPs; (C): Cef-AuNPs; (D): Cit-AuNPs; on *A. niger* hyphae at 20 µg/ mL after 7 days of growth (nitrogen source: nitrate).
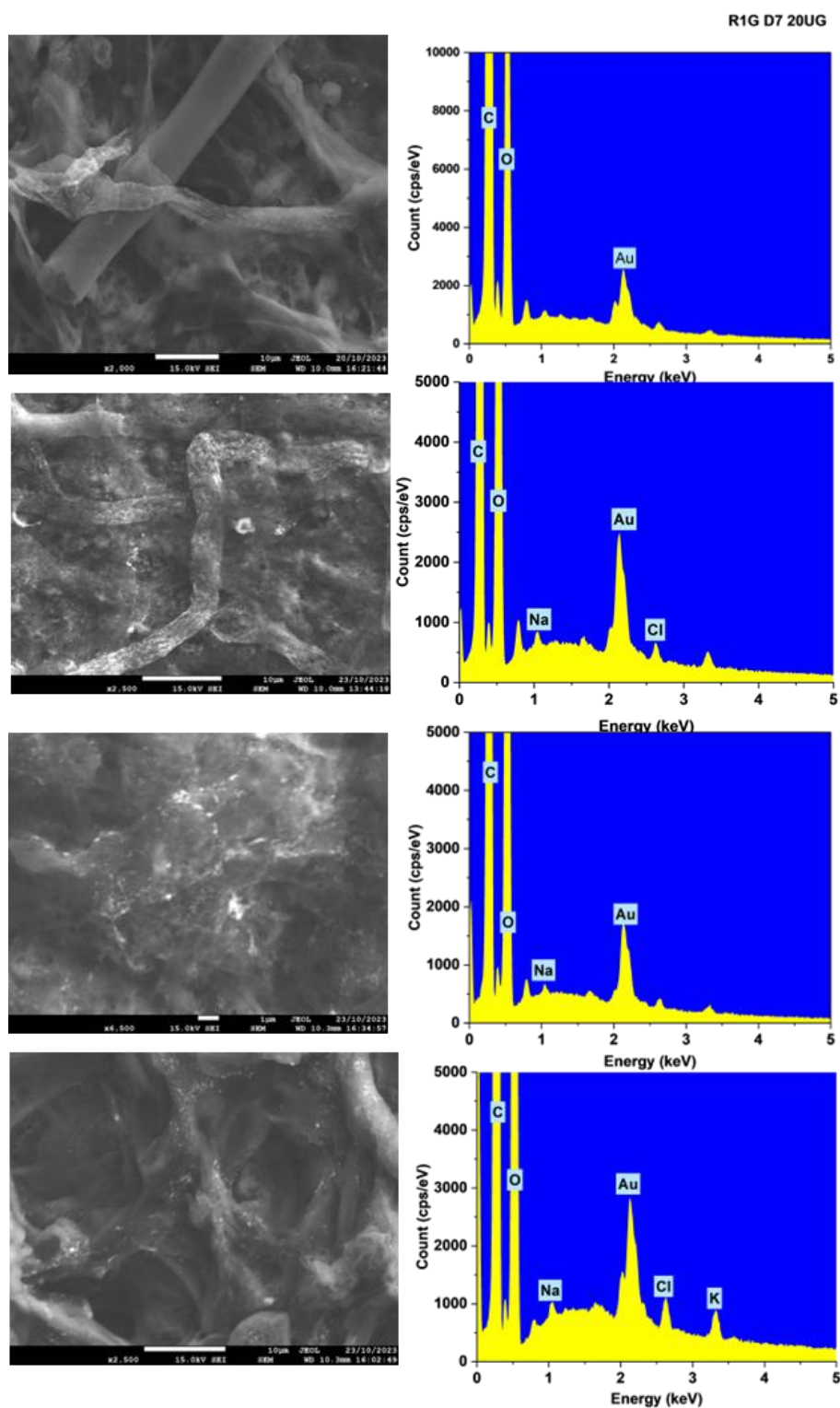
Appendix Figure 4.1B: Representative scanning electron microscopy (SEM) image, and elemental analysis (EDX) showing the distribution of (A): NaBH$_4$-AuNPs; (B): Glc-AuNPs; (C): Cef-AuNPs; (D): Cit-AuNPs; on *A. niger* hyphae at 20 µg/ mL after 7 days of growth (nitrogen source: glutamine).

Appendix Figure 4.1C: Representative scanning electron microscopy (SEM) image, and elemental analysis (EDX) showing the distribution of (A): NaBH₄-AuNPs; (B): Glc-AuNPs; (C): Cef-AuNPs; (D): Cit-AuNPs; on *A. niger* hyphae at 20 µg/ mL after 10 days of growth (nitrogen source: nitrate).

Appendix Figure 4.1D: Representative scanning electron microscopy (SEM) image, and elemental analysis (EDX) showing the distribution of (A): NaBH₄-AuNPs; (B): Glc-AuNPs; (C): Cef-AuNPs; (D): Cit-AuNPs; on *A. niger* hyphae at 20 µg/ mL after 10 days of growth (nitrogen source: glutamine).

Appendix 5

Table 5.1: Experimental Conditions for Evaluating the Impact of Varying Sugar Concentrations on Mechanical Properties and Surface Wettability in Five Fungal Strains.

Fungal Strain	Temp. (ºC)	Growth Period (Days)	Cond. A	Cond. B	Cond. C	Cond. D
R. oryzae	25	7	PDB	Minimal Medium (MM)	60 mM Glucose in MM	120 mM Glucose in MM
S. commune	22	15	PDB	Minimal Medium (MM)	30 mM Fructose in MM	60 mM Fructose in MM
T. versicolor	30	15	PDB	Minimal Medium (MM)	30 mM Fructose in MM	60 mM Fructose in MM
B. cinerae	30	15	PDB	Minimal Medium (MM)	60 mM Sucrose in MM	120 mM Sucrose in MM
A. niger	25	15	PDB	Minimal Medium (MM)	60 mM Glucose in MM	120 mM Glucose in MM

Table 5.2: Minimal media and nitrogen source for the germination of *Aspergillus* (MM1) adapted from Ijadpanahsaravi et al., 2021. The pH was corrected to 4.5 with 1M HCl

MM2 C0 + N	**Final concentration**	**Mass (g) for 500 mL**
KH_2PO_4	0.1% (w/v)	0.5 g
$NaNO_3$	0.3 (w/v)	1.5 g
KCl	0.05% (w/v)	0.25 g
$MgSO_4.7H_2O$	0.05% (w/v)	0.25 g
$FeSO_4.7H_2O$	0.002% (w/v)	0.01 g
in ddH_2O		Make up to 500 mL

Table 5.3: - Minimal media and nitrogen source for germination of *B. cinerea* (MM2). Adapted from Schumacher et al., (2008)**.**

MM2 C0 + N	Final concentration	Mass (g) for 500 mL
KH_2PO_4	0.1 % (w/v)	0.5 g
$NaNO_3$	0.3 % (w/v)	1.5 g
KCl	0.05 % (w/v)	0.25 g
$MgSO_4.7H_2O$	0.05 % (w/v)	0.25 g
$FeSO_4.7H_2O$	0.002 % (w/v)	0.01 g
in ddH_2O		Make up to 500 mL

Table 5.4: Minimal media and nitrogen source for germination of *S. commune* & *T. versicolor* (MM3*).* Adapted from Leem et al., (1999) and |Kim et al., (2022)**.**

- Magnesium chloride (CAS 7786-30-3) final concentration is 4.8 g/ L (or 2.4 g in 500 mL)
- Manganese sulphate monohydrate (CAS 10034-96-5) final concentration is 1.23 g/L (or 0.615 g in 500 mL)
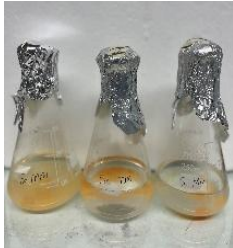
MM3 C0 +N	Concentration	Mass (g) for 500 mL
KNO_3	2 g/L	1 g
Trace element solution	40 mL/L	20 mL
Salt solution	25 mL/L	12.5 mL
in ddH_2O	Make up to 1 L	Make up to 500 mL
Trace Element Solution	**Concentration**	**Mass (g) for 500 mL**
$CaCl_2$	2.73 g/L	1.365 g
$MgCl_2.6H_2O$	10.25 g/L	5.125 g

FeCL$_3$.6H$_2$O	1.33 g/L	0.665 g
MnSO$_4$	1.1 g/L	0.55 g
ZnSO$_4$	1.0 g	0.5 g
In ddH$_2$O	Make up to 1 L	Make up to 500 mL
Salt Solution	**Concentration**	**Mass (g) for 500 mL**
Ammonium tartrate	20 g/L	10 g
KH$_2$PO$_4$	40 g/L	20 g
Na$_2$HPO$_4$	90 g/L	45 g
Na$_2$SO$_4$	11.2 g/L	5.6 g
in ddH$_2$O	Make up to 1 L	Make up to 500 mL

Table 5.5: Minimal media and nitrogen source for the germination of *R. oryzae* (MM4). Adapted from Wu et al., (2021).

MM4 C0 + N	**Concentration**	**Mass (g) for 500 mL**
MgSO$_4$.7H$_2$O	0.5 g/L	0.25 g
KH$_2$PO$_4$	0.6 g/L	0.3 g
FeSO$_4$.7H$_2$O	0.0088 g/L	0.0044 g
Urea	2 g/L	1 g
ZnSO$_4$.7H$_2$O	0.11 g/L	0.055 g
in ddH$_2$O	Make up to 1 L	Make up to 500 mL

Table 5.6: Autoclaving changes the media (fructose) from colourless) to dark brown compared to the ordinary minimal media

Media	*T. versicolor*	*S. commune*
Minimal media		
Minimal media (30 mM Fruc)		
Minimal media (60 mM Fruc)		
Potato Dextrose Broth		